Transactions of the ASME

Journal of Fluids Engineering

Published Quarterly by The American Society of Mechanical Engineers

VOLUME 107 • NUMBER 2 • JUNE 1985

FLUIDS ENGINEERING DIVISION
Technical Editor
FRANK M. WHITE (1989)
Executive Secretary
L. T. NELSON (1989)
Calendar Editor
M. F. ACKERSON

Associate Editors
Fluid Machinery
AWATEF A. HAMED (1985)
RICHARD F. SALANT (1987)
Fluid Measurements
ALEXANDER DYBBS (1987)
Fluid Mechanics
J. A. MILLER (1987)
HUGH W. COLEMAN (1987)
THOMAS J. MUELLER (1985)
HASSAN M. NAGIB (1986)
Fluid Transients
GEORGES L. CHAHINE (1986)
Multiphase Flow
JOHN T. JUREWICZ (1985)
Review Articles
RICHARD A. BAJURA (1985)

FOREIGN CORRESPONDENTS
Europe and Russia
JACQUES CHAUVIN
Europe and Russia
JOHN H. HORLOCK
India and Middle East
ARUN PRASAD
Japan and China
YASUTOSHI SENOO

BOARD ON COMMUNICATIONS
Chairman and Vice President
K. N. REID, Jr.

Members-at-Large
W. BEGELL, J. T. COKONIS, W. G. GOTTENBERG,
D. KOENIG, M. KUTZ, F. LANDIS,
R. E. NICKELL, J. ORTLOFF, C. PHILLIPS,
H. C. REEDER

President, **G. KOTNICK**
Executive Director
PAUL ALLMENDINGER
Treasurer,
ROBERT A. BENNETT

PUBLISHING STAFF
Mng. Dir. Publ., **J. J. FREY**
Dep. Mng. Dir. Publ.,
JOS. SANSONE
Managing Editor,
CORNELIA MONAHAN
Editorial Production Assistant,
MARISOL ANDINO

The Journal of Fluids Engineering (ISSN 0098-2202) is published quarterly for $100 per year by The American Society of Mechanical Engineers, 345 East 47th Street, New York, NY 10017. Second class postage paid at New York, NY and additional mailing offices. POSTMASTER: Send address changes to The Journal of Fluids Engineering, c/o THE AMERICAN SOCIETY OF MECHANICAL ENGINEERS, 22 Law Drive, Box 2300, Fairfield, NJ 07007-2300. **CHANGES OF ADDRESS** must be received at Society headquarters seven weeks before they are to be effective. Please send old label and new address. **PRICES:** To members, $24.00, annually: to nonmembers, $100. Add $6.00 for postage to countries outside the United States and Canada.

STATEMENT from By-Laws. The Society shall not be responsible for statements or opinions advanced in papers or . . . printed in its publications (B7.1, Par. 3), **COPYRIGHT** © **1985** by The American Society of Mechanical Engineers. Reprints from this publication may be made on condition that full credit be given the TRANSACTIONS OF THE ASME, JOURNAL OF FLUIDS ENGINEERING and the author, and date of publication be stated.

INDEXED by the Engineering Index, Inc.

Papers From The 1983 WAM Symposium on Uncertainty Analysis – Theory and Practice of Experimental Control

Additional Technical Papers

(Contents continued on page 152)

Downloaded 03 Jun 2010 to 171.66.16.159. Redistribution subject to ASME license or copyright; see http://www.asme.org/terms/Terms_Use.cfm

Contents
(Continued)

Announcements and Special Notices

S. J. Kline
Professor of Mechanical Engineering,
Stanford University,
Stanford, Calif. 94305
Fellow ASME

The Purposes of Uncertainty Analysis

Introduction

This symposium has four major sections.

I. Basic concept and questions
II. Procedures for estimating uncertainties, including proposed ASME/ANSI standards
III. Use of uncertainty analysis to reduce errors in experiments
IV. Panel discussion of issues

This paper deals with the item I and covers the following topics:

A. Why a symposium on uncertainty analysis?
B. The concept of uncertainty in experiments.
C. The uses of uncertianty analysis.
D. Is uncertainty analysis worthwhile; if so, when?

In addition, Appendix I covers:

- some simple examples and case histories;
- conclusions;
- remarks on the ideal experiment, from the view of uncertainty.

A. Why a Symposium on Uncertainty Analysis?

Uncertainty analysis has been a topic of much research and thought by a dedicated group of workers for many years; in the United States this includes particularly R. B. Abernethy of Pratt & Whitney and co-workers, and Churchill Eisenhart and co-workers at the National Bureau of Standards. This work has resulted in two recent ASME/ANSI Standards [1, 2] and several related basic publications by NBS [3-5]. International agreements on the topic are also being created, and are well advanced toward completion.

At the same time, both the teaching and the use of uncertainty analysis remains in a highly ambiguous state. A survey of twenty-five first-year Mechanical Engineering graduate students at Stanford in early 1983 showed that just half of these students had been given any materials or asked to do any problems on uncertainty analysis in their undergraduate engineering studies. Some current texts on laboratory work discuss uncertainty analysis, and some do not. Those that do often still reference as a primary basis the thirty-year-old paper of the writer and F. A. McClintock [6]. Some societies and journals routinely demand presentation of uncertainties as a portion of any experimental data (e.g. *Jour. Fluids Engrg.*, APS journals), but other do not (e.g. AIAA, SAE, International Combustion Symposia; but see closure regarding a new reference book).

Thus, while a great deal of work has been done on the "trees" of procedure, it would seem that there is no general recognition that a "forest" called uncertainty analysis exists as a valid part of engineering experimental work.

This paper accordingly discusses the broad general questions needed in order to decide the place and importance of uncertainty analysis (items IA, IB, IC, ID) since no discussion seems to be available in current publications. The material in this symposium next summarizes the procedures for uncertainty analysis becoming available as ASME/ANSI Standards and related publications (item II). The discussions in this symposium on item II are not intended to be replacements of the new ASME/ANSI Standards nor the related references, but rather to summarize them and provide a guide for persons not familiar with the details.

To make the remarks on the new ASME/ANSI Standards more concrete, an excellent, thorough example of their application is provided in this symposium in the paper by Smith and Wehofer. This paper is noteworthy for illustrating the relation between costs and specified accuracy of test.

The symposium next takes up some questions that appear in need of further study. Particularly noteworthy is the distinction between procedures for estimating uncertainty in an existing experiment and optimal procedure for reducing the errors by using uncertainty analysis in the planning and in the checkout stages of a new, never-before-performed experiment. Such procedures have been developed in the recent past largely by R. J. Moffat, and are presented next in the symposium. In the writer's view, these new procedures are an important advance in the available arsenal of tools for dealing with the difficult problem of providing reliable experimental results of requisite accuracy for given purposes.

The assumptions that underline the mathematics of conventional uncertainty analysis, including the new ASME/ANSI Standards, are not often discussed carefully. As one might expect, when these assumptions are violated, a need to modify procedures may arise. This problem was discussed by G. Lassahn in the current symposium, and Dr. Lassahn's remarks are summarized in the closure.

B. The Concept of Uncertainty

Since no measurement is perfectly accurate, means for describing inaccuracies are needed. It is now generally agreed that the appropriate concept for expressing inaccuracies is an "uncertainty" and that the value should be provided by an "uncertainty analysis." An uncertainty is not the same as an error. An error in measurement is the difference between the

---

Contributed by the Fluids Engineering Division and presented at the Symposium on Uncertainty Analysis, Winter Annual Meeting, Boston, Mass., November 13-19, 1983. Manuscript received at the ASME Headquarters, March 22, 1985.

true value and the recorded value; an error is a fixed number and cannot be a statistical variable. An uncertainty is a possible value that the error might take on in a given measurement. Since the uncertainty can take on various values over a range, it is inherently a statistical variable. Uncertainty can be thought of as a histogram of values. In any experiment that is under adequate control, this histogram must peak at or near the central value and decrease toward zero as the measurement gets further away from the central value on either side. Hence, uncertainty can be thought about in terms of statistical concepts and often can be calculated using well verified statistical procedures. These questions are discussed in some detail in reference [6] using nonstatistical language. Since statistics is today much more broadly known among engineers, it seems appropriate to summarize the ideas briefly in statistical terms.

In a broad sense, the value reported for a measurement describes the central tendency, usually the mean (see Example 1); the uncertainty describes the dispersion usually in terms of a measure associated with a stated probability level such as the standard deviation (see Example 3). Ideally, this measure of uncertainty is calculated from repeated trials, but it may need to be taken from estimates in whole or part in many engineering tests or research experiments. Further discussion on this and related points is deferred until the uses of uncertainty analysis have been delineated to take the discussion substantive.

C. Uses of Uncertainty Analysis[1]

Uncertainty analysis can do, and has done, all of the following:

1. Enforce a complete examination of the experimental procedure, including the potential sources of troubles and errors. Steps or components of procedure cannot be easily forgotten, because gaps then occur in the uncertainty analysis that prevent completion of the work; see Cases A, F, G,
2. Advise, specifically, when improved instruments and/or improved procedures must be found to obtain a given output accuracy; see Case E.
3. Minimize instrument cost for a given output accuracy.[2]
4. Identify those instruments and/or procedures which control accuracy. (Usually this is one or at most a few from the total set.) This identification focuses attention on points where care is particularly important in experimental procedure in order to obtain accurate results, and also identifies the specific points where improvements in instruments must be made to improve accuracy; see Case E.
5. Inform us beforehand, during the design of an experiment, when the experiment cannot meet desired accuracy and therefore is "hopeless," in a sense. Such experiments can then be redesigned or abandoned, as appropriate. Obviously, redesign or abandonment is less painful in the design stage than after some years of failing attempts to make the experiment behave as desired; see Case A.
6. Provide the only known, approptiate basis for deciding whether (*a*) computations agree with data or lie outside acceptable limits, (*b*) data sets on one phenomenon or situation from two or more laboratories agree or disagree, and (*c*) tests on a given item of hardware in separate facilities, for example in acceptance of jet engines for aircraft, agree or disagree; see Cases D, F, G.
7. Advise when more accurate experiments must be provided to further "calibrate" approximate theory, e.g., in turbulence modeling; see Case D.
8. Provide the basis for guarantees of accuracy in commercial tests of large equipment, such as power plants; allow estimates of cost as function of accuracy demanded; see paper by Smith and Wehofer.
9. Allow design of probes (and instrument procedures) for minimum uncertainty (e.g., multiple hot-wire probe geometry and orientation in a flow; see Cases B, E.
10. Provide a check against unknowingly taking data in some odd corner of the test-parameter hyperspace where uncertainties become very large (e.g., when two numbers, say x and y, are subtracted from each other in the reduction procedure approach the same value. This will happen, for example, whenever $x \rightarrow y$; see examples in Appendix I and Moffat's paper in this symposium.
11. Provide a stronger, better integrated grasp of how to run a given experiment than any other procedure known to the writer. This follows from item 4 above; once controlling uncertainties are known, one can think more clearly about the experiment, consider instrument improvements, and take special care in obtaining readings at critical measuring stations. See Cases B, C, E.
12. Provide the only known basis for deciding whether a closure check has been achieved, based on a governing equation (e.g., continuity or comparison of PL & PR in a momentum equation; see Case G).

D. Is Uncertainty Analysis Worthwhile?

The question posed by the title of this section is largely answered by the list of uses in Section C. A procedure that supplied methods for any half of the functions listed in Section C would obviously be very important in science and in engineering. Given the list of uses, it is clear that uncertainty analysis is very worthwhile indeed! Examples and cases in Appendix I substantiate the reality of the items in Section C. A prolonged discussion on the question of the title of this section is not necessary. This section thus needs to ask more refined questions.

These include:

(i) Is uncertainty analysis always necessary, or only sometimes in experimental work?

(ii) Is there a single universal procedure for uncertainty analysis, or are various procedures needed for various applications?

While there is complete agreement among the members of this panel and other workers in uncertainty analysis concerning the importance of the topic under many circumstances, there is some apparent disagreement on the subsidiary issues represented by questions (i) and (ii) of the preceding paragraph. The following remarks therefore represent the writer's view on these subsidiary questions, and are given as a point of departure for the symposium.

In order to understand whether uncertainty analysis is always necessary in experiments, it is vital to be clear about the true extent of types of experiments performed in science and engineering. In particular, one needs to distinguish four classes of experiment which I shall call: (*a*) quick-sort; (*b*) report of field test, development test, or acceptance test; (*c*) report of research; (*d*) calibration test.

(*a*) Quick-sort experiments are used for a number of purposes. I shall give one science and one engineering example to indicate quick-sort experiments are real and significant. In fluid mechanics one often wants to establish the global nature of a flow pattern; flow visualization is the standard method for this purpose. The visual results are then used to determine where to place probes and what type of probes to use in order to obtain meaningful results of adequate quantitative accuracy. In many cases one only wants the general pattern in flow visualization work, and in such a case uncertainty

---

[1] Information on uses not covered by this list will be appreciated by the author.

[2] The mathematical structure of this problem is essentially the same as that for uncertainty analysis. However, the details lie beyond the scope of this paper.

analysis is not essential. In engineering development work one often needs to know whether something will work: what is needed is a yes/no answer in a very short time at low cost. It would be counterproductive in such work to do a highly accurate, fully-documented experiment with a full uncertainty analysis; indeed, it would defeat the basic purpose which is to get an answer quickly at low cost so that one can move on in the work.

(*b*) The meaning of field-development or acceptance tests is generally understood by engineers. It is important to note that such tests are usually carried out using well-established test procedures or even formalized codes. Much experience is usually available on the types of instruments used, the pitfalls, and the expected uncertainty levels.

(*c*) Reports on research projects on topics of concern to engineers are more like papers in what T. Kulm called "normal science" than like reports of tests of type (*b*). In such work, special new instruments are often necessary. Also, it is usually too costly to repeat such experiments completely. For both these reasons, little or no prior experience will be available to estimate uncertainties on at least some parts of the experiment.

(*d*) The term "calibration experiment" is used in this paper to denote an experiment which: (i) calibrates an instrument or a thermophysical property against established standards; (ii) measures the desired output directly as a measurand so that propagation of uncertainty is unnecessary.

Calibration expriments are vital to engineering experimental work but usually are not in and of themselves complete engineering experiments. Rather, they are background information that is crucial to and employed in engineering experiments. Three facts about calibration experiments are implied immediately by this understanding of their purpose in engineering.

(i) They need to be as accurate as possible.

(ii) Very complete information on their accuracy needs to be recorded and transmitted to potential users.

(iii) The information transmitted from calibration experiments into a complete engineering experiment on engineering systems or a record experiment on engineering research needs to be in a form that can be used in appropriate propagation processes. (See remarks in Appendix I.)

Before ending this discussion of the necessity for uncertainty analyses in record experiments, we should ask, "Are there any disadvantages involved in formal uncertainty analysis?" The answer seems to be that leaving aside the work involved, none are apparent provided only that the procedure is handled reasonably well. As a former professor of the writer liked to emphasize, "There is no procedure so foolproof that a really good fool cannot louse it up." That was, and unfortunately remains, true. It is possible to do such a bad job of estimating uncertainties that the results are misleading. Barring such really foolish work, the only disadvantage is the labor involved. Hence the question reduces to another, "Is uncertainty analysis worth the effort?" Thirty years experience in our laboratory convinces the writer that the answer to this question is a clear unambiguous, "Yes!" We have almost never performed an uncertainty analysis on an experiment of any complexity whatsoever in which we did not obtain vital, unobvious information. In many cases, we have saved much time and cost (see Case A); in others we have vastly improved the accuracy of output (see Cases B, C, E); in still other instances we have sharpy focused the need for and developed new instruments and/or mensuration techniques (see Case C). Moreover, when computer data reduction is employed, the task becomes nearly trivial; see paper by Moffat below.

In sum, there is no alternative to uncertainty analysis in experiments of types (*b*), (*c*), and (*d*), presuming only that we are serious in stating that we are trying to produce accurate quantitative results. Uncertainty analysis is the sine qua non for record experiments and for systematic reduction of errors in experimental work. Uncertainty analysis is the heart of quality control in experimental work, and wider use of the methods needs to be a part of current U.S. effort to improve quality control.

Several professional divisions of ASME have asked if uncertainty analysis should be used as part of publication procedure for experimental results. The answer is an absolute, clear "YES!" for any experiment of class (*b*), (*c*), or (*d*). This is the central and most important conclusion for this symposium; all questions of procedure are clearly subsidiary to this central conclusion. All members of the panel have been polled on this point and are in agreement.

The preceding remarks are not intended to imply uncertainty analysis is always easy. Difficult and subtle questions can and do exist that need thought and continuing discussion. The remarks are intended to imply that any reasonable procedure is infinitely better than none so long as the procedure is made clear for future users of the results.

We then turn to the question, is there one universal procedure of uncertainty analysis, or is more than one needed for various purposes? This question almost answers itself. There are few topics of any complexity where one procedure is sufficient or only one is viable. In uncertainty analysis, several useful procedures have been developed and can be used.

Particulary noteworthy is the distinction between procedures for estimating uncertainty in standard tests, such as codes, and procedures needed to improve and control accuracy in new experiments of either a scientific or engineering type. As noted above, these experiments typically generate quite different conditions and hence need different uncertainty procedures. Additional remarks on this point appear in the closure.

Another noteworthy distinction is between estimating uncertainty in a completed experiment and in the planning stage of an experiment. In the completed experiment, it is usually possible and extremely desirable to use calibrations and repeated trials to obtain statistically valid estimates of uncertainty in each output variable. In the planning stage, as W. A. Wilson [7] noted long ago, this is clearly impossible, and one must use prospective, that is, estimated values of uncertainty without a statistical data base. Nevertheless, the use of formal uncertainty procedure in the design stage often determines the difference between an accurate and useless result. See Moffat's paper for a more complete discussion; see also Ref. [1].

Other distinctions exist, but these are sufficient to warn against a simple assumption that any one procedure covers all cases and circumstances. To repeat the main point, the use of some appropriate uncertainty analysis is indispensable in record experiments, and any appropriate analysis is far better than none so long as the procedure is explained for the user.

A final comment is in order to avoid potential misunderstanding. Uncertainty analysis is *not* a replacement for calibrations, cross-checks, closures using governing equations, nor for sound careful technique. See Moffat's paper and closure. Nor is uncertainty analysis a substitute for understanding the problem and the physics underlying the mensuration techniques. But this is not unique; no methodology is useful without underlying content. Uncertainty analysis is: (i) a procedure that provides a powerful framework inside which the other checks just mentioned as well as other information can be used much more effectively; (ii) an additional powerful cross-check and procedure for ensuring that requisite accuracy is actually obtained with minimum cost and time.

References

1 Abernethy, R. B., "Fluid Flow Measurement Uncertainty," 3rd Draft of ISO/DIS 5168 for International Organization for Standardization Committee, ISO TC30 SC9.

2 Abernethy, R. B., Benedict, R. P., and Dowdell, R. B., "ASME Measurement Uncertainty," (current symposium paper).

3 Eisenhart, C., "Expression of the Uncertainties of Final Results," NBS paper, Jan. 1983.

4 Ku, H. H., "Expressions of Imprecision, Systematic Error, and Uncertainty Associated with Reported Value," NBS paper, Jan. 1983.

5 Eisenhart, C., and Colle, R., postcript to references [3 and 4], July 1980, reissued Jan. 1983.

6 Kline, S. J., and McClintock, F. A., "Describing Uncertainties in Single-Sample Experiments," *Mechanical Engineering*, Jan. 1953.

7 Wilson, W. A., "On the Use of Uncertainty Analysis in Experimental Design," in *Symposium on Accuracy and Errors*, TASME, Vol. 77, No. 4, May 1955, p. 408.

8 Moffat, R. J., "Contributions to the Theory of Single-Sample Uncertainty Analysis," ASME JOURNAL OF FLUIDS ENGINEERING, Vol. 104, June 1982, pp. 250-260.

APPENDIX I

Contents

This Appendix contains:

I. Examples of Procedures for:

A. describing uncertainties in measurands.
B. propagating uncertainties in measurands into uncertainties in the results.

These examples include comments on a number of questions that arise in describing uncertainties and propagation of uncertainty into results.

The examples also illustrate alternative procedures that are useful in various types of problems.

II. Case Histories illustrating what can be gained by use of uncertainty analysis in various types of problems.

III. Summary

IV. The Ideal Experiment From the View of Uncertainty Control

Comment

The elements I and II are intended to make procedures and ideals clear by concrete example. These examples are chosen to be very simple, for clarity. They do not consitute a stand-alone discussion of uncertainty analysis, for two reasons: (*a*) they are illustrative but not exhaustive, since a larger variety of problems arises in uncertainty than can be treated here; (*b*) they need to be read in conjunction with the references cited to complete the theory.

I. Examples of Procedure

A. Description of Uncertainty in Measurands

Example 1

For concreteness consider the following example. The pressure in a tank is to be measured. The tank is charged by a compressor running with an automatic shutoff that nominally stops charging at 100 psig (689.46 kpa). It is desired to estimate the uncertainty of the pressure in the tank at shutoff.

Before we can make a rational assignment of uncertainty in the measurand of concern (pressures), we must take note of the fact that several levels of replication exist in this innocuous-looking example.

At the lowest level of replication, we could concern ourselves with the uncertainty while using one tank, one compressor, one charging, and one reading of a single pressure gage. To put this operationally, we would take a tank, charge it up once and measure pressure with a single pressure gage; let us say the gage is a Bourdon type with a full scale reading of 200 psig and a smallest interval between scale markings (least count) of 5 psi. Let us also say that no calibration on this gage is available; it is a new off-the-shelf gage.

Table 1 Some terms used in uncertainty analysis

Current Usage	Precision
Older Usages	• Random component of uncertainty. • Random error. • Repeatability.
These elements can be sampled with the available procedures and apparatus, and should be based on statistical estimates from samples whenever possible.	
Current Usage	Bias
Older Usages	• Fixed component of uncertainty. • Fixed error. • Systematic error.
These uncertainties cannot be sampled (via replication) within available procedures and/or apparatus and therefore must be estimated if required. Their existence is what mandates the need of cross-checks and closures via theory.	

Comments:

1. In some older discussions, reproducibility denotes the total uncertainty (precision and bias).
2. The distinction between precision and bias is operational (not absolute), since it depends on the procedures and apparatus. By broadening procedures and/or acquiring more apparatus, one can systematically move elements from the bias to the precision category.

Notice in this example we have no repeat measurements (replications) of anything. This is what Moffat [8] calls a zeroth-order estimate. (The word "estimate" is used in this paper in the COMMON LANGUAGE SENSE of a mental estimate, and NOT IN THE STATISTICAL SENSE of the value of parameter of a population "estimated" from a statistic measured on a sample of data. This common usage for the word "estimate" will be employed uniformly in this discussion since no other suitable words exists in the common language.) In such an estimate, we cannot distinguish between bias and precision (because the semantics of uncertainty analysis have not been uniform until recently, some synonyms are indicated in Table 1), and therefore can do no better than estimating the total uncertainty interval for given probability based on experience with such instruments and/or the manufacturer's specification including least count. We therefore interrogate our experience (and perhaps the experience of others) with such gages, and assign a value of twice the least count as a rough estimate of the uncertainty: we would therefore report:

$$p = 100 \pm 10 \text{ psig } (P = 0.95)$$

Comment

All assignments of uncertainty in this discussion are made in the framework of confidence intervals in the statistical nomenclature. That is, the interval assigned is to be understood as a RANGE within which the true reading would lie the fraction of time suggested at the probability indicated. When this framework is understood, it does not matter whether one gives probability, odds or frequencies, since they can be converted and carry the same information. Thus $P = 0.955$ is equivalent to an odds of 20 to 1 or a frequency of 20 times out of 21. In some cases, the value of the assigned RANGE (the uncertainty interval) will be taken from sample statistics, in other cases from estimates based on experience or other prior information. The accuracy of the assigned RANGE will be different in the two cases, but the underlying meaning of the RANGE is the same; it is the range within which variations of the measurand are expected to lie on repeated measurements stated for an appropriate probability level, odds, or frequency.

A zeroth-order estimate of uncertainty interval is a very poor basis for description of inaccuracy in data. The purist, the gage-lab person, or the conservative worker might well say it is a hopeless situation and should not be reported at all. Nevertheless, it is a situation we often face in engineering work. Suppose, in the tank example, we need to know simply if the compressor system is working and we need to know this within one minute, to guarantee cooling air to a critical part. Under these conditions an uncertainty of 10 psi is acceptable; a delay to calibrate the gage is not.

Let me be clear to minimize misunderstanding. I am not recommending using uncalibrated gages in record experiments, nor am I recommending use of uncertainty estimates this crude for normal purposes. I am saying there are some situations in which crude estimates of uncertainty are all we can get for a variety of reasons, and such estimates are sometimes good enough for the purposes in hand. The classic instance in which we cannot obtain any statistical information about uncertainty (through replication) is in the planning stage of a new experiment. Furthermore, as Wilson [7] pointed out long ago, use of uncertainty analysis in the planning stage often is the difference between success and failure in an experiment, particularly in an experiment of a new, never-previously-performed type. A second important case where little if any replication is possible is large-scale field tests where only limited time and money are available for testing and types of instruments are constrained by the field situation.

The tank example thus serves to illustrate two important matters we must understand if we are to use uncertainty analyses intelligently. First, there are levels of replication, and we must account for these levels in a rational uncertainty analysis, for several reasons. Second, the percentage accuracy needed on the estimate of uncertainty can often be much less than the uncertainty in the value of the measurand itself and still provide the information needed.

Some other important levels of replication that may need consideration in the example of the pressure tank charged by a compressor are discussed next.

Example 2

A second level of replication that is frequently important Moffat calls FIRST ORDER. At first order, we let time run forward and repeat measurements; calibration information on instruments will usually be included. What might we estimate for uncertainty at first order in the tank charging example? Suppose we have calibrated the bourdon gage using a deadweight tester with a precision uncertainty of 0.0080 psi and negligible bias. Suppose further that this establishes a precision uncertainty interval for the gage in hand of 2.5 psia at a probability level of $P = 0.95$ with negligible bias since we have calibrated against a standard with much smaller uncertainty and negligible bias.

We would then report the measurement as:

$$p = 100 \pm 2.5 \text{ psig precision;}$$
$$0 \text{ bias } (P = 0.95)$$

This report follows the current practice of reporting precision and bias uncertainties separately. This practice is a clear improvement on older recommendations of reporting a single value whenever sufficient information is available. Notice that the zero for bias implies only that the bias is very small value compared to the precision. Also notice that if we did not calibrate, but did repeat the measurement a number of times (using the same gage but only one charging of the tank), we would find measurements varying about the mean of 100 by less than 2.5 psia in 20 out of 21 readings. The uncertainty interval for the precision could also have been found by carrying out these repeated measurements, but we would not have known the uncertainty was unbiased, and would have had to report an appreciable uncertainty interval for the bias as well as the precision. Calibration reduces bias.

Example 3

There is still another important source of uncertainty in the experiment described that has so far been left out of consideration. Suppose we use some air from the tank and then allow the compressor to recharge, and again measure pressure using the calibrated gage. Now we repeat this operation a number of times. We will than probably find that the measurements give a higher value of uncertainty at $P = 0.95$ than before, say, 5.3 psia, because the compressor shut-off control is not accurate to 2.5 psi. The details of how to find this value of 5.3 psia from a series of such readings using the "t" Table are given by R. B. Abernethy in his course, in the current papers of this meeting and in the curent ASME/ANSI standards. We would then report the uncertainty

$$p = 5.3 \text{ psia precision; } 0 \text{ bias } (P = 0.95)$$

(The bias is still zero, because we calibrated the gage.)

This "reset" uncertainty occurs in many experiments, whenever we must shut down from time to time and then reset nominal values for further running. This example shows a large reset value to make the point clear. Reset is peculiarly important in fluid mechanics, in which small changes in value settings or in fits where pieces are reassembled can alter location of laminar-turbulent transition, flow separation, etc. The example also illustrates one of many elements that can be replicated but were not at either the zeroth or first level. The example thus moves part way to what Moffat has called the *N*th level of replication.

At the *N*th level, one uses more than one type of instruments on each measurement, more than one observer, more than one laboratory, and more than one physical realization of the test apparatus or equipment under study. To put this differently, the *N*th level of replication would sample and make statistics available on all elements of the experiment contributing to uncertainty. The *N*th level is an ideal experiment from the viewpoint of assigning uncertainty; it is a state we can approach, but probably never completely realize, in practice. The *N*th level is important not only because it is a theoretical limiting goal of experimental design but also because it gives the value of uncertainty that must be used for several important cases; these include:

(i) instances where we need to compare experimental results with theory;

(ii) instances where we need to compare two experimental results from two or more distinct laboratories or test facilities.

In both (i) and (ii), all possible sources of uncertainty must be taken into account if a meaningful estimate is to be realized concerning whether agreement between the results from the various sources has been achieved.

This movement toward the *N*th level of replication can be described in several ways. Abernethy describes the changes in terms of "reclassification" of the uncertainties from the bias to the precision category. Moffat explicitly describes the level of replication being used. Kline and McClintock described them in terms of a "thought" experiment in which one visualized all possible sources of uncertainty and combined the components by the rms rule (see section B). Eisenhart, Ku, and co-workers in the current papers [3-5] describe only the *n*th level because as Ku says the papers refer to the work of a "calibration laboratory" and hence to calibration experiments in the sense described in the body of this paper. In any of these methods it is important to recognize two things: (i) at the *N*th level, there are many potential sources for error and hence of uncertainty even in an experiment as simple as the example of the charged pressure-tank; (ii) nearly always, some fraction of these uncertainties will have been sampled and the remainder will not have been.

In the worst experiment, from the view of uncertainty control, none of the sources of uncertainty will have been sampled, and hence no *statistical* estimates of sample standard deviations can be made. That very undesirable case is sometimes forced upon us in engineering practice, and it is this situation that Kline and McClintock [6] called a single-sample experiment.

In the best experiment, from the view of the uncertainty control, all elements of uncertainty are sampled so that standard deviations from sample data can be calculated for all elements. This "best" condition is an ideal limit that we approach in calibration experiments, but may never actually reach in practice. Clear recognition of the various level are important not only in providing understanding for statements of precision and bias, but also as Moffat [8] shows for two other purposes:

(i) development of systematic methods for reduction of errors through use of uncertainty analysis;

(ii) for understanding the appropriate estimates to be used at various stages in experimental design and development in new experiments.

It is important to note that the example given above is a case where calibration can be used to drive bias to a very small value compared to precision. In some cases, for example in measurement of viscosity, this would not be possible owing to instrument limitations, and appreciable values of bias would need to be reported even though instrument calibrations were done. The four possible cases of the relative magnitudes of precision and bias are carefully discussed in the current paper by Eisenhart [2] and will not be repeated here.

B. Propagation of Uncertainties Into Results

In calibration experiments, one measures the desired result directly. No problem of propagation of uncertainty then arises; we have the desired results in hand once we complete measurements. In nearly all other experiments, it is necessary to compute the uncertainty in the results from the estimates of uncertainty in the measurands. This computation process is called "propagation of uncertainty."

Propagation of uncertainty is not a trivial exercise as the following examples illustrate.

Example 4

Suppose one wants to find the density of air from measurements of pressure and temperature.

Using the methods of section A, suppose

$$p = 100 \text{ psia} \pm 2.5 \text{ psia precision;}$$

$$\text{zero bias } (P = 0.95)$$

$$T = 500 \text{ deg R} \pm 0.1 \text{ deg precision}$$

$$1 \text{ deg bias } (P = 0.95)$$

Using the perfect gas equation of state, we then write:

$$\rho = P/RT \tag{B1}$$

Differentiating, we obtain

$$d\rho = \frac{dp}{RT} - p\frac{dT}{T^2} \text{ (assuming negligible uncertainty in R)} \tag{B2}$$

Dividing equation (B2) by equation (B1) gives

$$\frac{d\rho}{\rho} = \frac{dp}{p} - \frac{dT}{T} \tag{B3}$$

We now replace the differentials in equation (B3) with the uncertainty estimates in the measurands, P and T, and combine to obtain the uncertainty in the results.

$$\frac{d\rho}{\rho} = \sqrt{\frac{2.5^2}{100} + \frac{0.1^2}{500}} \pm \frac{1}{500}$$

$$\frac{d\rho}{p} = \pm\sqrt{6.25 \times 10^{-4} + 4 \times 10^{-8}} = 6.2504 \times 10^{-4} \pm \frac{1}{500}$$

$$\frac{d\rho}{\rho} = \pm 2.50008 \times 10^{-2} = 2.5\% \text{ precision} \pm 0.2\% \text{ bias}$$

$$(P = 0.95)$$

Combining precision and bias using rms summing gives

$$\left.\frac{d\rho}{\rho}\right|_{\text{total}} = \sqrt{6.250404} = 0.02500808 = 2.5\% \; (P = 0.95)$$

(Two methods of combination are possible: linear and rms. The choice between these two combination methods has been much discussed. There now seems to be agreement that rms combination should be used for each of the precision uncertainty and bias up to the final step, where either method is acceptable provided one states the basis. The rms method is employed here.) Unwarranted figures have been retained in the arithmetic to illustrate forcefully that only the larger sources of uncertainty affect the answer when rms summing is used.

Two rules of thumb are useful. When to uncertainties are combined and one is three or more times larger than the other, the smaller uncertainty has negligible effect. When a large number of uncertainties, say six or more, are combined, any uncertainty less than one-fifth of the largest uncertainty will have negligible effect. Negligible here implies 5 percent or less in the uncertainty reported, which is generally more accurate than the value with which uncertainty is known. These rules have a very important bearing on how one designs and troubleshoots an experiment. If significant reductions in inaccuracy are to be actually realized, one must find and focus on reducing the large uncertainties. The small ones do not count. This argument is given a more complete basis in reference [6].

The generalization of equations (B2) and (B3) in algebra are as follows: Let R be a result computed from n measurands $X_1, \ldots . x_n$ and W denotes an uncertainty with the subscript indicating the variable. Then, in dimensional form, we obtain:

$$W_R = \sqrt{\left(\frac{\partial R}{\partial x_1} W_{x_1}\right)^2 + \left(\frac{\partial R}{\partial x_2} W_{x_2}\right)^2 + \ldots \left(\frac{\partial R}{\partial x_n} W_{x_n}\right)^2} \tag{B4}$$

In fractional, nondimensional form, we have:

$$\frac{W_R}{R} = \sqrt{\left(\underbrace{\frac{\partial \ln R}{\partial \ln x_1}}_{C_1} \frac{W_{x_1}}{x_1}\right)^2 + \left(\underbrace{\frac{\partial \ln R}{\partial \ln x_2}}_{C_2} \frac{W_{x_2}}{x_2}\right)^2 + \ldots \left(\underbrace{\frac{\partial \ln R}{\partial \ln x_1}}_{C_3} \frac{W_{x_n}}{x_n}\right)^2} \tag{B5}$$

Equations (B2), (B3), (B4), and (B5) apply strictly only to small values of the uncertainties W_n. However, this restriction is easily removed in data reduction when required. One simply inserts the appropriate perturbations into equation (B1) or the equivalent equations, graphs, tables, or computer codes and calculates the changes that ensue, taking care to retain sufficient significant figures.

Equation (B5) is a particularly useful form, since it makes explicit the influence coefficients (C's) that connect a one-percent uncertainty in a given measurand to the percent uncertainty in the result. In Example 1, both C_p and C_T are unity, but this is by no means general. The value of an influence coefficient can approach zero or ∞, as is demonstrated in Examples 5 and 6, which follow.

Example 5

Consider a result R found from two measurands through the equation

$$R=x-y$$

Then

$$\frac{W_R}{R}=\sqrt{\left(\frac{x}{x-y}\frac{W_x}{x}\right)^2+\left(\frac{y}{x-y}\frac{W_y}{y}\right)^2}$$

Suppose $x = 1$ and $y = 0.98$ and the uncertainty in each of x and y is one percent; then the uncertainty in R is

$$\frac{W_R}{R}=\sqrt{\left(\frac{1}{0.02}0.01\right)^2+\left(\frac{1}{0.02}0.01\right)^2}=0.707=71\%$$

An intolerable uncertainty for most purposes thus is generated by measurements that seem accurate at first glance.

Example 6

As another example, consider a Result R found from a measurand z through the formula:

$$R=\sqrt{\frac{1}{1+z}}$$

Let the value of z be 0.1 and the uncertainty in z be 20 percent; then the uncertainty in R, by perturbation, is

$$R_R=\sqrt{\frac{1}{1+0.1}}-\sqrt{\frac{1}{1+0.12}}$$

$$=\sqrt{0.9090909\ldots}-\sqrt{0.8928571}$$

$$=0.9534626-0.9447112=0.0085514$$

$$\frac{W_R}{R}=\frac{0.008551}{0.9534}=0.89\%$$

In Example 5, the influences coefficient $C_x = C_y = 50$. In Example 6, the influence coefficient $C_z = 0.89/20 = 0.044$. These two illustrations demonstrate forcefully that one cannot assume low uncertainties in the measurands will always provide low uncertainty in results, nor conversely that high uncertainties in the measurands will always give high uncertainties in the result. Propagation is not a trivial exercise since:

(i) the relations between uncertainty in measurands and in the results are usually not a priori obvious;

(ii) the differences between the uncertainty in the measurands in the results can be large;

(iii) the differences between the uncertainties in the measurands and in the results often depend on the values of the measurands as well as the values of uncertainties. It is for this reason that the computer "'jitter package" (given by Moffat in [8] and below) is an important precaution in data reduction. One can easily take data in some odd corner of the test space where uncertainties become very large and not be aware of this difficulty without some precaution of this sort.

A final comment on propagation is needed as part of these examples. Kline and McClintock [6] showed that the use of linear combination for several measurands leads to a rapid increase in the effective level of probability. To put this concretely, suppose we combine three uncertainties each at 20 to 1 odds. If these three estimates are combined *linearly*, the odds associated with the computed uncertainty in the result rise to more than 8000 to 1 (provided the uncertainties are functionally independent on each other and the underlying probability distribution that would be generated in repeated trials is of any reasonable form). For this reason, the use of quasi-absolute bounds for examples in estimates on bias errors may be satisfactory for calibration experiments, but created an unsolved and significant difficulty if used for propagating uncertainties into the results whenever more than one measurand enters the computation for the given result: see conclusions in closure.

II. A Few Case Histories of the Uses of Uncertainty Analysis

A few case histories from actual experience are given as illustrations in this section. The cases are all actual history. However, they are given succinctly and do not give the full details of the experiences. Despites this, they do make concrete the values of uncertainty analysis as indicated in the body of this paper.

Case A—A Hopeless Experiment Avoided. An experiment was considered using a lumped-parameter heat-transfer technique. The models to be used were expensive. It was therefore proposed to make one model and test the effects of Reynolds number by successively removing the rear sections of what would be initially a long test specimen. When the uncertainty analysis was carried out, in the design stage, it was found that the experiment could not give accurate results because the reduction of data would appear in the form of the Example 2 of the prior section, where

$$R=x-y$$

Consequently, this form of experiment was not carried out.

Since it seemed that the experiment would save much time and expense when initially proposed, the experiment actually would have been carried out if the uncertainty analysis had not made clear the fundamental design flaw.

Case B—Uncertainty in a Probe System Minimized. A three-wire hot-wire probe was designed in order to measure three components of mean and fluctuating velocities simultaneously in real time. An analysis of uncertainty for the principal mean and fluctuating quantities was carried out in the design stage, using a computer analysis in order to find a configuration of wires that would minimize uncertainty for measurements in shear flows. In this way, uncertainties at $P = 0.95$ of about 2 percent in u' (streamwise fluctuations) and 3 percent in v' and w' (cross-stream fluctuations) were anticipated and later realized.

The computer analysis of uncertainty was then applied to a probe manufactured in a second laboratory, where the geometry had been set apparently to minimize difficulty of manufacture. The uncertainty in u' resulting was of the order of 3 percent; however, the typical uncertainty in v' was 65 percent and in w' 75 percent. Insofar as we know, the second laboratory was not aware of the difficulty and had published results without mention of the excessive uncertainties in v' and w'.

Case C—Controlling Uncertainty Located, Reduced. A test bank had been installed by professional engineers for testing a variety of pumps. Considerable effort had been expended in order to calibrate the flow gages using gravimetric techniques to a claimed uncertainty of 0.25 percent. Large-sized, calibrated Bourdon gages were used to measure differences in head. No uncertainty analysis was done during the original construction nor for some years afterward. At a later time, an uncertainty analysis was performed. It was found that, for low and moderate heads, the Bourdon gages created uncertainties in the results of at least ten times those arising from the flow meters. A more precise "pressure-weighing" instrument was installed to measure head. The new instrument created an uncertainty in the results equivalent to those in the flow meters. Test results immediately showed far less scatter, and details of the performance that had never before been seen in the test bank became visible.

Case D—Calibration of Computer Model Improved. A theory for computation of flow in the transitory stall region of straight-walled, planar diffusers was being constructed. It was found to be very consistent, but it needed values of parameters in the equations set from data. The only available data happened to have been taken in the same group at an earlier time, so it was known that a 15-20 percent uncertainty existed in this very unsteady flow to regime. As a result, another apparatus was designed for further tests, with careful attention to the control of uncertainty in this flow regime. The resulting data were used for final calibration of the parameters in the computer model. These results were compared with the mean values that would have been found had the more uncertain earlier data been used; the comparison showed that errors of 7-10 percent would have been generated had the more uncertain data been used.

Case E—Need for More Accurate Instruments Identified. In an experiment on transition in a round tube, it was desired to measure pressure drop to obtain friction coefficient and thereby locate the laminar, transitional, and turbulent regimes. An analysis of uncertainty showed that sufficient precision could not be obtained using any then-existing commercial instrument for measurement of pressure difference. Work was therefore initiated with an instrument manufacturer to develop the necessary instrument. As a result, the experiment not only gave the desired results with excellent accuracy, but also provided data corroborating, for the first time, already developed theory on the effect of density on friction factor.

Case F—Closure of Theory With Data Demand Uncertainty Values. In a conference to evaluate computer models for turbulent flows, it was found that closure between theory and data could not be established without reasonable estimates of uncertainty. The data for this conference came from several fields of engineering. In some of these fields, it is routine to provide estimates of uncertainty for the data; in other fields, uncertainty had not usually been given for data. As a result, the data evaluators were forced to estimate uncertainties in cases for which they were not provided. This procedure is much less satisfactory than estimates by the observers reporting the data, since the observers always have far more information than anyone else concerning the test situation and its behavior under varying conditions of operation.

Case G—Apparent Disagreements Resolved Between Theory and Data. In a conference evaluating methods for computation of turbulent boundary layers, a check on the data base utilized a procedure in which the left- and right-hand sides of a complete momentum equation were compared and the difference recorded. This procedure worked well for flow far from detachment. However, near detachment many flows showed more differences between the two sides of the momentum equation than desired, and checks with computer output seemed to be lacking. An analysis of uncertainty by one of the workers in the conference showed that the uncertainties in the data for flows nearing detachment are inherently very large for the data procedures that had been employed in nearly all instances. An appropriate reevaluation of the data in this region and an appropriate comparison with computer models then became possible.

III. Summary

The examples and discussion above, taken with published papers and standards (references [1-7]), show several points concerning assigning uncertainties in the measurands. First, there is no single way to describe uncertainties in measurands; there are many different situations that demand somewhat differing descriptions. The Kline-McClintock description for example is appropriate for single sample experiments and experiments still in the design stage. The recommendations of Eisenhart et al. contain some methods that are useful in calibration experiments. The recommendations of Abernethy, Dowdell and Benedict in current ASME/ANSI Standards are appropriate for use when field, development, or acceptances tests are concerned. Moffat's methods seem most appropriate for systematic reduction of error using uncertainty analysis and hence in research-type experiments that occupy much of the space in journal publication. Hence, it would seem that insistence on a single method at this point in time would be counterproductive.

The second major point is that the distribution of uncertainty between precision and bias is arbitrary in the sense that it depends on what has been sampled by replication and what has not, and that use of levels of replication is an explicit and useful way for describing this set of facts.

Finally, it is important and timely to reiterate that any differences of opinion over which method is to be used in a given case is decidely secondary to the major point: that journals of record require that uncertainties be reported in some appropriate way and that the report include the methods employed. There seems to be general agreement that this report on methods whenever possible should cover four items:

(i) components of bias and precision in the measurands;

(ii) the number in the sample on which estimates of precision are based;

(iii) if bias and precision are combined into a single number, the combination method used should be reported;

(iv) the combined final value of the uncertainties in results and the ranges to which they apply.

IV. The Ideal Experiment From the View of Uncertainty Control

The summary above plus the contents of Table 1 provide a basis for consideration of what an "ideal experiment" would be from the point of view of uncertainty control. This question seems not to have been explicitly addressed in published materials. What follows is therefore a first attempt to provoke further discussion. The remarks refer to engineering experiments [class (*b*) and (*c*)] and not to a quick-sort or calibration experiment where conditions and desiderata may be different.

In an ideal record experiment:

1. All sources of uncertainty are sampled, and measurements repeated a sufficient number of times to provide valid statistical measures of confidence intervals on each measurand.
2. The bias is systematically driven toward zero, and this process is carried sufficiently far that bias is negligible compared to the precision of item 1. This negligible bias is based on traceable standards in a form suitable for propagation computations. The word "traceable" here denotes standards traced back to a calibration experiment based on known physical principles with negligible bias.
3. Available physical theory based, for example, on closure of an energy balance and/or other well-established scientific principles) are employed in quantitative form to cross-check the negligible bias. Cross-checks by two independent methods are made for at least a few points in the test space.

We shall seldom, if ever, completely reach this ideal state in a real-world experiment. However, explicit recognition of the ideal is useful as a basis for discussion of procedures of uncertainty analysis and as a standard of comparison for consideration of the "believability" of data reported in the literature.

R. B. Abernethy
Pratt & Whitney Aircraft Company,
West Palm Beach, Fl. 33408
Mem. ASME

R. P. Benedict
Westinghouse Electric Corporation
Fellow ASME

R. B. Dowdell
University of Rhode Island,
Kingston, R.I.
Mem. ASME

ASME Measurement Uncertainty

The purpose of this paper is to introduce the new ASME measurement uncertainty methodology which is the basis for two new ASME/ANSI standards and the ASME short course of the same name. Some background and history that led to the selection of this methodology are discussed as well as its application in current SAE, ISA, JANNAF, NRC, USAF, NATO, and ISO Standards documents and short courses. This ASME methodology is rapidly becoming the national and international standard.

Background

The accuracy of test results has always concerned engineers and scientists, but for decades this subject has been plagued by controversy, argument, confusion and even emotion. The absence of an uncertainty calculation standard made significant comparison of test results between facilities, companies and laboratories almost impossible. Still there was good attempts. H. H. Ku of NBS relates the following [1]:

> "Dan Johnson, an old time at the Bureau, told me this story. In the 1930's, P. H. Myers at NBS and his colleagues were studying the specific heat of ammonia. After several years of hard work, they finally arrived at a value and reported the result in a paper. Toward the end of the paper, Myers declared:
>
> "We think our reported value is good to one part in 10,000; we are willing to bet our own money at even odds that it is correct to two parts in 10,000; furthermore, if by any chance our value is shown to be in error by more than one part in 1000, we are prepared to eat our apparatus and drink the ammonia!"

History

In the research that led to the JANNAF (formerly ICRPG) [2] and the USAF [3] handbooks, a powerful statistical tool, Monte Carlo simulation, was used to select the best methods from the many available. J. Rosenblatt, H. H. Ku, and J. M. Cameron of NBS provided excellent constructive criticism of these documents and have continued to support industry in this effort. The references to the NBS publications are particularly recommended to the reader [1, 4, 5, 6].

By the late seventies, the only major argument that remained was over how to combine the bias error limit with the precision error. Addition of the two components is recommended in [2, 3, 4, 7, 12, 13, and 15]. Combination by the root-sum-square method is recommended in [8, 9, 10, 16, and 18]. This argument could not be solved completely by Monte Carlo simulation as it is largely a matter of opinion. However, these simulations aided significantly in evaluating the statistical characteristics of the two uncertainty intervals. The argument as to how to combine bias and precision errors raged over many committees in several societies, and most participants believed it would never be settled. A compromise was suggested by the NBS group [6] in late 1980. It was suggested that (1) if the bias and precision components are propagated separately from the measurements to the final test result and (2) the method of combination is clearly stated, then either the addition or root-sum-square method should be accepted as it is the last step in the calculation and can easily be undone. Shortly thereafter, the ASME, SAE and ISA committees approved this compromise of allowing the analyst to decide and state which uncertainty model (ADD or RSS) was to be used.

Current Activities

1. *ASME*. The two ASME committees are:

ANSI/ASME PTC 19.1 – 1983 – Measurement Uncertainty –

ANSI/ASME MFC – 2M – 1983 – Uncertainties in Flow Measurement –

In addition, the ASME Short Course on Measuring Uncertainty was given at the 1983 ASME – WAM.

The status of these ANSI/ASME documents is described in later sections of this paper.

2. *SAE*. Committee E33 on "Aircraft In-Flight Propulsion Measurement and Uncertainty," is drafting an SAE Aerospace Information Report (AIR 1678) titled, *In-Flight Thrust Measurement Uncertainty*, which they hope to distribute for industry review in 1984. This document uses the same uncertainty methodology as that of this paper. The activities of this committee are described in [11].

Contributed by the Fluids Engineering Division and presented at the Symposium on Uncertainty Analysis, Winter Annual Meeting, Boston, Mass., November 13-18, 1983. Manuscript received at ASME Headquarters, March 20, 1985. Paper No. 83-WA/FM-3.

3. *ISA*. The Instrument Society of America provides a short course titled, *Test Measurement Accuracy*, at the International Instrumentation Symposium and other locations several times a year. This course is identical to the ASME Short Course. ISA also has formed a Measurement Uncertainty Committee to encourage and promote the use of measurement uncertainty analysis. *The United States Air Force Handbook* [3] has been reprinted as the *ISA Measurement Uncertainty Handbook* [13].

4. *ISO*. ISO TC30 SC9 approved the method described herein at their meeting in Leningrad in May 1982 and requested a revision of the existing world standard ISO 5168 [11]. The second draft was reviewed at their recent meeting in Washington, D.C. at the National Bureau of Standards in November 1982.

5. *MIDAP*. The British Ministry Industry Drag Analysis Panel published their report, Agardograph 237, in 1979 [10]. In a joint meeting held with SAE Committee E33 in England in May 1982, the uncertainty methodology was coordinated between these two groups.

6. *ASQC*. The ANSI Committee Z11 has commissioned an ASQC Writing Group on Calibration Assurance. This Writing Group is drafting a national standard on assuring the quality of calibration [15]. Although this standard treats only calibration error, it is consistent with the methodology recommended herein.

7. *NRC*. At the Idaho National Engineering Laboratory, a report titled, *Semiscale Uncertainty Report: Methodology* [14], has been written for the United States Nuclear Regulatory Commission. This document uses the uncertainty methodology described herein. *Nuclear Material Control, Mass Calibration Techniques*, ANSI N15.18-1975, also is consistent with the recommended methodology.

8. *NATO*. NATO AGARD PEP 15 Committee on Uniform Engine Testing is conducting an interfacility test of two jet engines at NASA-LEWIS, USAF AEDC, USN NAPC, Britain's NGTE, France's SACLAY facility and a Turkish facility. This committee, selected the recommended uncertainty methodology as their standard for this program at their meeting in Toulouse, France in May 1981.

9. *CRC*. The Coordinating Research Council has decided to re-evaluate the test data from their Atlantic City test program on engine exhaust emissions using the recommended uncertainty methodology.

Brief Description of Methodology

Measurement Error. It is a well-accepted principle in engineering that all measurements have errors (δ_k). These errors are the differences between the measurements and the true value (see Fig. 1). Furthermore, the total error is usually expressed in terms of two components: a fixed (bias) error (β), and a random (precision) error (ϵ_k) such that

$$\delta_k = \beta + \epsilon_k . \tag{1}$$

Precision Index. The precision error is determined by taking N repeated measurements from the parameter population, the characteristics of which can be approximated by the precision index (S) defined by the familiar

$$S = \frac{\sum_{k=1}^{N} (X_k - \bar{X})^2 \quad 1/2}{N-1} . \tag{2}$$

where $\bar{X}$ is the average value of X.

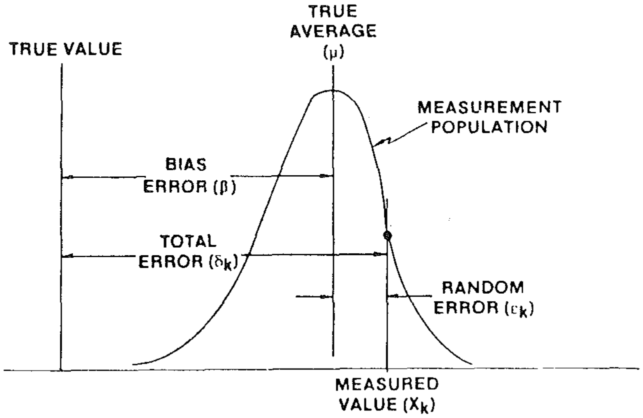

Fig. 1 Measurement error

The precision index of the average of a set of measurements is always less than that of an individual measurement according to

$$S_{\bar{x}} = \frac{S}{\sqrt{N}} . \tag{3}$$

Bias Error. The bias error is the systematic error which is considered to remain constant during a given test. Thus, in repeated measurements of a given set, each measurement has the same bias. There is no statistical equation, as (2) or (3), to define the bias limit, B. Instead, it must be estimated, and this is not an easy matter since the true value is not known. Calibrations help, as does a comparison of measurements by independent methods, but in general the estimate of bias must be based on judgment.

Combining Errors. Errors arise from many sources. These are divided arbitrarily into three categories: calibration errors, data acquisition errors, and data reduction errors. For each of these sources of error there will be bias and precision components.

To obtain the precision of a given parameter (like temperature, pressure, or flow rate), the root sum square (RSS) method is used to combine the precision indices from the K sources of error. Thus

$$S = [S_1{}^2 + S_2{}^2 + \ldots + S_K{}^2]^{1/2} . \tag{4}$$

Similarly, the bias of a given parameter is given by

$$B = [B_1{}^2 + B_2{}^2 + \ldots + B_K{}^2]^{1/2} . \tag{5}$$

Uncertainty of a Parameter. If a single number (U) is needed to express a reasonable limit of error for a given parameter, then some model for combining the bias and precision errors must be adopted, where the interval

$$\bar{X} \pm U \tag{6}$$

represents a band within which the true value of the parameter is expected to lie, for a specified coverage.

While no rigorous confidence level can be associated with the uncertainty (U), coverages analogous to the 95 percent and 99 percent confidence levels can be given for the two recommended uncertainty models. Thus

$$U_{\mathrm{ADD}} = B + tS_{\bar{x}} \text{ provides} \simeq 99 \text{ percent coverage,} \tag{7}$$

and

$$U_{\mathrm{RSS}} = [B^2 + (tS_{\bar{x}})^2] \text{ provides} \simeq 95 \text{ percent coverage.} \tag{8}$$

The Student t value is a function of the degrees of freedom (ν) used in calculating $S_{\bar{x}}$. For large samples, (i.e., $N > 30$), t is set equal to 2, otherwise the Welch-Satterthwaite formula is used to provide ν, according to

$$\nu = \frac{\left(\sum_{j=1}^{3}\sum_{i=1}^{K}\frac{S_{ij}^{2}}{N}\right)^{2}}{\sum_{j=1}^{3}\sum_{i=1}^{K}\frac{S_{ij}^{4}}{N^{2}\nu_{ij}}} . \qquad (9)$$

where S_{ij} represents the precision indices of the various error sources involved, and V_{ij} represents the degrees of freedom of these same error sources.

Uncertainty of a Result. Errors in measurements of various parameters (P) are propagated into a derived result (r) through the functional relationship between the result and its independent parameters. The relationship provides the sensitivity factors (θ_i), which indicate the error propagated to the result because of unit error in the parameter. Thus if

$$r = f(P_1, P_2 \ldots . P_J) \qquad (10)$$

where J is the number of parameters involved, then

$$\theta_i = \frac{\partial r}{\partial P_i} . \qquad (11)$$

The bias and precision errors of the parameters are kept separate until the last step of computing the uncertainty of a result. Thus, the precision index of a result is given by

$$S_r = \left[\sum_{i=1}^{J} (\theta_i S_{P_i})^2\right]^{1/2} \qquad (12)$$

and the bias limit of a result is given by

$$B_r = \left[\sum_{i=1}^{J} (\theta_i B_{P_i})^2\right]^{1/2} . \qquad (13)$$

The uncertainty of a result is again given by the two models according to

$$\underset{\text{ADD}}{U_r} = B_r + tS_r @ 99\% \qquad (14)$$

and

$$\underset{\text{RSS}}{U_r} = [B_r^2 + (tS_r)^2]^{1/2} @ 95\% . \qquad (15)$$

The Student t value is a function of the degrees of freedom used in calculating S_r. For large samples of all parameters, (i.e., $N > 30$), t is set equal to 2, otherwise the Welch-Satterthwaite formula is used to provide ν_r according to

$$\nu_r = \frac{S_r^4}{\sum_{i=1}^{J} \frac{(\theta_i S_{P_i})^4}{\nu_{P_i}}} . \qquad (16)$$

ASME PTC 19.1, Measurement Uncertainty

This committee was formed in 1979 to provide the Performance Test Codes Board with an authoritative Supplement on which to base Measurment Uncertainty Analyses. This was for the use of the various Code and Supplement writing committees.

This committee has endorsed and contributed to the methodology of this paper, and has just completed a draft for the PTC Board and Industry approval [16].

The document includes a nomenclature and a glossary of terms that are in agreement with the various International Standards. A detailed review of the methods of this paper is included, as is a strong section on Applied Considerations. This latter includes: multiple test uncertainty, long versus short term tests, comparative versus absolute tests, spacial variations, outlier treatment, regression uncertainty, weighting method, pre- and post-test analyses, and number of measurements required. A step-by-step calculation procedure is given, as well as worked-out examples applying the method. All in all, we expect to satisfy the PTC requirements for an authoritative document on measurement uncertainty that is easily understood and applied.

ASME MFC, Fluid Flow Measurement Uncertainty

The ASME Standards Committee on the Measurement of Fluid Flow in Closed Conduits (MFC) was formed in 1973 as a result of the recognition by those actively working in the field that there was a need for a single national standard on this subject. In most Western European countries, national standards on flow measurement have been in use for many years. These are usually promulgated by government supported agencies such as the British Standards Institute in the United Kingdom, AFNOR in France, VDI in West Germany etc. The first International Standard on Flow Measurement ISO/R541 was published in January 1967.

This country has had no national standard, but many authoritative documents on flow measurement existed such as the ASME Report "Fluid Meters, Their Theory and Application" [17], PTC 19.5 on Flow Measurement, AGA Report #3 on Gas Flow Measurement, etc. For the most part, these documents were in agreement on their methodology, coefficient values, required upstream lengths, and calculation procedures.

This was not true on the international scene, and the initial ISO document contained many compromises between USA procedures and those in use throughout Western Europe. Differences in required upstream lengths and coefficient values have not yet been resolved.

All of these publications, those within the USA, the European national standards, and the international standards, address the question of the accuracy of a flow measurement. However, each document created its own procedures for estimating the uncertainty and values given were based on human judgment usually biased by the individuals involved.

The first publication of a standard devoted entirely to the estimation of uncertainty of a flow rate measurement was ISO/DIS 5168 published in 1976.

Recognizing the importance of this subject matter, the ASME Standards Committee MFC set up its first subcommittee, i.e., SC1 with the charge to prepare a USA standard on Uncertainties in Flow Measurement. It has taken many years, 10 to be exact, and much effort by the people involved, to produce the first ANSI/ASME MFC – 2M Standard on Uncertainties in Flow Measurement which was published in 1983 [18]. The methodology follows that of the preceding section of this paper and should form the basis of some further, more applied, or working documents on flow measurement.

Summary

Engineering judgment and experience is still required when estimating bias or systematic errors but this is clearly stated in [18] and all parties to a contract can agree beforehand to the values that should be used.

Unfortunately we are still left with many unanswered questions that must be resolved in the not-too-distant future. For instance: How do we interpret statements by the manufacturers of industrial instrumentation that claim a device to be "accurate to within ±0.5 percent of full scale"? That is: How much of this is bias error and how much should be attributed to random or precision error? Similarly, when dealing with meter coefficients: How do we interpret values given in [17] for the 2σ tolerance on the discharge coefficient? It is necessary that the concepts of this paper be adopted throughout all segments of industry and one day we will have a uniform, unambiguous method of estimating the uncertainty of not only a flow measurement, but measurements of all kinds.

References

1 Ku, H. H., "Uncertainty is NBS's Business," presented to the NBS Advisory Panel, October 9, 1975.

2 Abernethy, R. B., et al., *ICRPG Handbook for Estimating the Uncertainty in Measurements Made With Liquid Propellant Rocket Engine Systems, JANNAF* (formerly ICRPG) Performance Standardization Working Group Report CPIA No. 180 (AD 851 127), April 1969.

3 R. B. Abernethy, et al., *Handbook Uncertainty in Gas Turbine Measurements*, USAF Arnold Engineering Development Center, Report AEDC-TR-73-5, Feb. 1973.

4 Ku, H. H. Editor, *Precision Measurement and Calibration*, NBS Special Publication 300, Volume 1, 1969.

5 Rosenblatt, J., and Spiegelman, C. H., NBS, Discussion, *Technometric*, Vol. 23, No. 4, Nov. 1981.

6 NBS Postscript to Special Publication 300, Nov. 1980.

7 Hersey, M. D., "A Development of the Theory of Errors With Reference to Economy of Time," British Association for the Advancement of Service, 1913, Reprinted by Churchill Eisenhart, NBS, *Journal of Research*, 1965.

8 Kline, S. J., and McClintock, F. A., "Describing Uncertainties in Single-Sample Experiments," *Mechanical Engineering*, Vol. 75, 1953.

9 MIDAP Study Group, "Guide to In-Flight Thrust Measurement of Turbojets and Turbofans," Agardograph AG-237, Jan. 1979.

10 ISO 5168, Measurement of Fluid Flow—Estimation of Uncertainty of a Flow-Rate Measurement, 1976.

11 Abernethy, R. B., "SAE In-Flight Propulsion Measurement Committee E33: Its Life and Work," SAE in *Aerospace Engineering*, Vol. 1, No. 1., July 1981.

12 Abernethy, R. B., et al., Instrument Society of America Measurement Uncertainty Handbook, ISBN: 87664-483-3 Revised 1980.

13 Golden, R. W., "Semiscale Uncertainty Report: Methodology," prepared for U.S. Nuclear Regulatory Commission, NUREG/CR-2459, Sept. 1982.

14 Schumacher, R. B. F., "Systematic Measurement Errors," *ASQC Journal of Quality Technology*, Jan. 1981.

15 ASQC Writing Group Draft, American National Standard for Calibration Systems, 1983.

16 ANSI/ASME PTC 19.1, 1983, "Measurement Uncertainty."

17 *Fluid Meters, Their Theory and Application*, 6th Edition, 1971, published by ASME.

18 ANSI/ASME MFC-2M, 1983, "Measurement Uncertainty For Fluid Flow in Closed Conduits."

R. E. Smith, Jr.
Chief Scientist & Director.

S. Wehofer
Engineering Specialist.

Aeropropulsion Program Dept.,
Sverdrup Technology, Inc.,
AEDC Group,
Arnold Air Force Station, Tennessee 37389

From Measurement Uncertainty to Measurement Communications, Credibility, and Cost Control in Propulsion Ground Test Facilities[1]

In the past several years significant advances have been made in altitude ground test facilities with respect to measurement accuracy and measurement cost control. To a large measure, the advances have been the result of the application of comprehensive measurement uncertainty evaluation programs. This paper discusses the specific measurement evaluation process used in the Engine Test Facility, Arnold Engineering Development Center. To explain this process, the reader is guided through the measurement process for engine thrust, an extremely critical parameter for propulsion performance testing. Although this paper focuses on the measurement of engine thrust, the overall objective is the general measurement evaluation process and its uses. The approach presented can be applied to any type measurement system. First, an overview of the measurement uncertainty methodology and its application in altitude engine test cells is presented. The paper concludes with a discussion of how measurement uncertainty results can be utilized to improve measurement understanding and presents the means to identify factors that must be controlled to achieve a reliable and accurate measurement assessment.

Introduction

One of the most important questions that an engineer must answer is "How good are your results?". Unfortunately, this is an area of engineering often not emphasized. A large part of the problem has been the lack of clearly established engineering standards for measurement accuracy assessments. The ability to resolve and understand measurement accuracies in propulsion ground test facilities improved immensely when in the early 1970's Abernethy and Thompson introduced an engineers' measurement uncertainty[2] methodology to the aircraft turbine engine industry [1]. The Abernethy-Thompson method is based on the Interagency Chemical Rocket Propulsion Group (ICRPG) efforts [2] and was one of the first methods that enabled the engine measurement processes to be audited on an elemental error source basis. Since its introduction, the method has gained wide acceptance by the aircraft turbine engine industry and is presently being considered as a standard by several engineering technical societies [3, 4].

The Abernethy-Thompson methodology served as the basis for the measurement uncertainty quality program adopted in 1971 at the Engine Test Facility (ETF), Arnold Engineering Development Center (AEDC). This program has been instrumental in both developing procedures for determining engine performance measurement uncertainties and in improving engine measurement techniques and practices. Since engine internal performance evaluations involve buyer/seller obligations, results from the AEDC/ETF program have been closely scrutinized by the aerospace propulsion community.

The intent of this paper is to provide an overview of the AEDC/ETF measurement evaluation program and to discuss the utilization of the measurement uncertainty results. In this paper, for the purpose of describing the program, the reader is guided through the engine thrust measurement process. The first part of the paper deals with the definition of measurement uncertainty. This then is followed by a discussion on procedures for identifying and quantifying measurement error sources. Since this latter part requires some understanding of the measurement system, the discussion is preceded by a cursory description of a propulsion test cell and engine thrust measurement system. The next part of the paper discusses the measurement validation process which is a form of using unlinked, measurement self-consistency checks to preclude gross error omissions. Finally, the results and findings which evolve from

---

[1] The research reported herein was performed by the Arnold Engineering Development Center (AEDC), Air Force Systems Command. Work and analysis for this research were done by personnel of Sverdrup Technology, Inc./AEDC Group, operating contractor for the AEDC propulsion test facilities. Further reproduction is authorized to satisfy needs of the U.S. Government.

[2] The terms measurement uncertainty and measurement accuracy are often used interchangeably when quantifying measured values. In this paper the more precise term measurement uncertainty, which is defined as the maximum inaccuracy or error that may be expected, will be used.

Contributed by the Fluids Engineering Division and presented at the Symposium on Uncertainty Analysis, Winter Annual Meeting, Boston, Mass., November 13-18, 1983. Manuscript received at ASME Headquarters, March 20, 1985.

the measurement uncertainty assessment are reviewed, and the principal organizational requirements for implementing a measurement uncertainty evaluation program are addressed.

Measurement Uncertainty Methodology

Communications of measurement uncertainty numbers require a precise definition of what is meant by measurement uncertainty. Unless this is accomplished, any communications pertaining to absolute measurement uncertainty values or comparative results between two parties will be ambiguous. In the Abernethy-Thompson method, measurement error is defined as the difference between the measured value and the value that would be obtained by the National Bureau of Standards (NBS) (Fig. 1). Measurement uncertainty is defined as

$$\pm U = \pm (B + t_{95} S)$$

and has two components: a random or precision error (S) [Fig. 2(a)] and a fixed or bias error (B) [Fig. 2(b)]. The t_{95} is the Student's-t statistical parameter at the 95-percent confidence level and is a function of the number of degrees of freedom or the number of data samples used in calculating the precision index.

There are numerous error sources that must be considered to determine the total uncertainty of a given measurement system. In the AEDC/ETF measurement quality program, uncertainty analysis is performed using a building-block concept starting with a base calibration of the measurement transducer provided by a standards laboratory. Transfer errors are added to the base calibration to account for the installation and environment errors associated with the characteristics of the measurement transducer and the transducer data-conditioning equipment. Finally, to complete the error source audit, elemental errors from the data acquisition and data-processing systems are evaluated and combined with the above error values.

Measurement Error Identification/Quantification

Identifying and quantifying measurement error sources requires both historical experience with the measurement system involved and a significant amount of engineering judgment and understanding. The logic used in this process can be exemplified by reviewing the AEDC/ETF turbine engine thrust measurement methodology. To understand the methodology, however, some descriptive background in propulsion test cell hardware configurations and thrust stand hardware is first in order. A detailed discussion of turbine engine thrust measurement has been presented by the authors in previous papers [5, 6].

Test Configuration. In this paper, only thrust measurements in the so-called direct-connect test configuration are considered. This particular test configuration derives its name from the fact that the engine inlet is directly connected to a controlled-air-supply system, and the engine exhaust exits into a separately controlled environment.

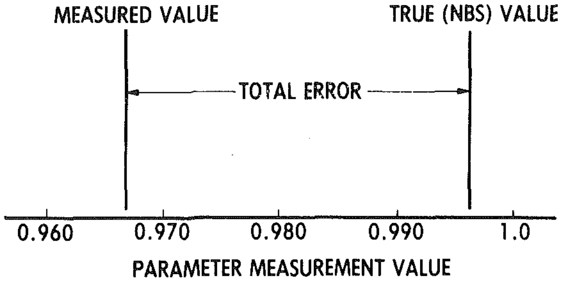

Fig. 1 Definition of measurement error

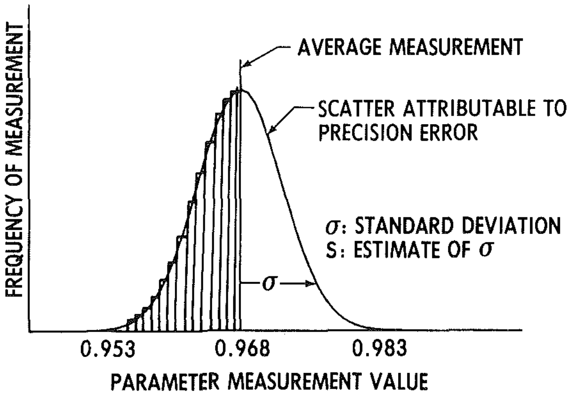

(a) Precision error (S)

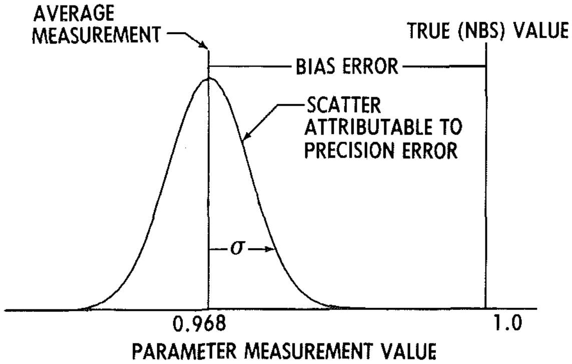

(b) Bias error (B)

Fig. 2 Classes of measurement errors

The direct-connect configuration provides the best opportunity for the measurement of the steady-state behavior of the axial component of thrust produced by a turbojet or turbofan engine. The essential features of the direct-connect configuration are shown in Fig. 3. Although there are a number of hardware options available to implement each of the key functions in a direct-connect test configuration, it is nevertheless essential that each of the functions represented by these specific hardware items identified in Fig. 3 be successfully implemented.

Nomenclature

B = bias error
df = degrees of freedom or sample size
F = thrust
FNC = corrected net thrust
F_s = measured scale force
$f(\ )$ = function of argument within ( )
N2C = corrected high-pressure compressor rotor speed
S = precision error
SFCC = corrected specific fuel consumption
t_{95} = Student's-t statistical parameter
U = uncertainty
σ = standard deviation

Subscript

i = elemental
G = gross

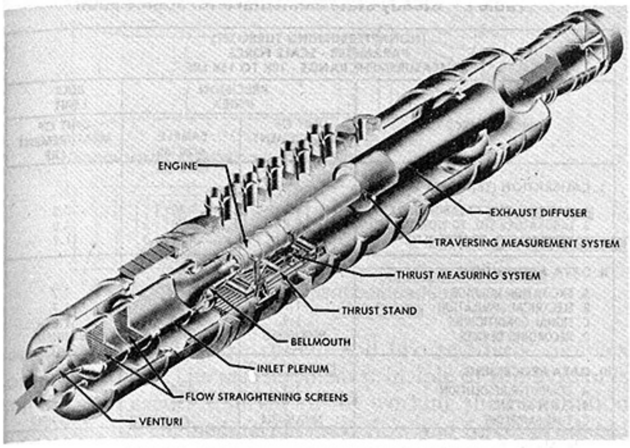

Fig. 3 Direct-connect engine installation

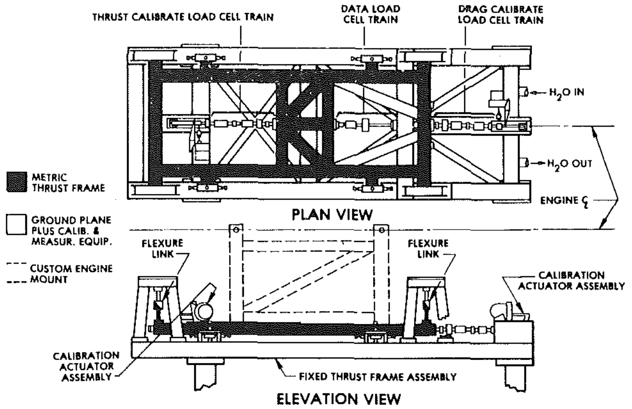

Fig. 4 Carriage thrust stand

Table 1 Scale force steady-state elemental error sources

I. LOAD CELL CALIBRATION
- NATIONAL STD. TO LAB STD.
- LAB STD. TO WORKING STD.
- WORKING STD. TO MEAS. STD.

II. DATA ACQUISITION
- LOAD CELL BRIDGES
- SIGNAL CONDITIONING EQUIPMENT
- RECORDING SYSTEM

III. DATA PROCESSING
- COMPUTER RESOLUTION
- CURVE FITTING/TABLE LOOK-UPS
- TIME SAMPLING

IV. INSTALLATION/ENVIRONMENTAL
- LOAD CELL PRESSURE EFFECTS
- TARE LOADS
- TEST CELL PRESSURE EFFECTS
- UTILITY LINE PRESSURE EFFECTS
- THRUST STAND THERMAL EFFECT
- CELL COOLING AIR
- LABYRINTH SEAL MISALIGNMENT/BALANCE
- CENTERLINE LOADING

First, the flow of air through the engine must be known very precisely. The venturi shown in Fig. 3 represents one of the devices available to accomplish this measurement. After the flow of working fluid into the engine is carefully measured, it is then necessary to condition the temperature, pressure, and velocity profiles of the air entering the engine; this conditioning is often accomplished with flow-straightening screens, as shown in Fig. 3. It is important to note that frequently the test will require nonuniform aerodynamic profiles entering the engine. In a like manner, these properties are generally obtained by the use of flow "un-straightening" devices such as nonuniform screens or air injection systems. An inlet plenum is then provided to permit installation of the engine inlet bellmouth.

Finally, for control of the exit environment into which the engine exhaust is discharged, it is necessary to utilize some type of exhaust diffuser to collect the engine exhaust gases and direct them away from the test cell.

The test cell ambient environment can be extremely demanding from a measurement standpoint. Engine inlet air temperatures can be minus 100°F while the exhaust gases read 3500°F. The test cell acoustic levels may be as much as 130 decibels, and engine vibrational displacement amplitudes may be as much as 10 mils (0 to 1000 Hz), peak to peak. The impact of all these conditions on the measurement process must be included in the uncertainty analyses.

Scale-Force Measurement Method. The most commonly used procedure for making engine force measurements in propulsion test cells is the scale-force measurement method. The essential characteristic of this method is that the engine is installed so that it may be handled as a free body, and the net forces acting around the free body provide a measurement of the engine gross thrust. The most complex piece of test equipment required by this method is the thrust stand. The thrust stand attaches directly to the engine mounting hardware and provides for the measurement of the net excess force acting on the engine free body. The essential functions of the thrust stand are shown schematically in Fig. 4. The example chosen in this schematic is for a carriage thrust stand configuration, i.e., the fixed frame (ground) and metric frame are located below the engine. However, the same elements and approximately the same relationships are required for an overhead thrust stand designed for use with pylon-mounted engines and other engines for which it is desired to use an overhead mounting configuration except that the fixed frame (ground) is located above the metric frame. The basic design requirements for the thrust stand are that (1) both the ground fixed frame and the metric thrust frame be dimensionally stable at all engine and environmental operating conditions, (2) all connecting linkages between the metric plane and the ground plane behave as elastic pivots (flexures), and (3) the thrust stand be capable of measuring bidirectional forces, i.e., forces acting in both the thrust and drag directions. The force applied by the engine to the thrust stand (i.e., engine scale force) is measured directly with a calibrated load cell.

After the engine and thrust stand installation is complete, the measurement of scale force appears straightforward. However, as with any measurement system, there are a number of errors present in th scale-force measurement system which must be identified and quantified if the measurement is to be totally understood, and if the tester is to establish measurement **Credibility.**

The scale-force steady-state elemental error sources are identified in Table 1. The errors are divided into four categories: (1) calibration, (2) data acquisition, (3) data processing, and (4) installation/environmental. The load cell calibration errors are those involved in the transfer of standards down through the hierarchy to the data load cells. The data acquisition effects reflect the errors present in the electronic portions of the force measurement system. The data processing errors are associated with the data sampling rate and data display device (computer, strip chart, oscilloscope, . . .). The final category, installation and environmental errors, are the result of mechanical, aerothermodynamic, and thermal effects on the measurement equipment.

Generally, calibration, data acquisition, and data processing errors are fairly well understood, and procedures have been developed to quantify these types of error. Installation and environmental effects however, are much more difficult to recognize and evaluate. For instance, after an engine installation is completed, the thrust stand assembly may be viewed as an engine restraint system which reacts to the engine thrust and drag by the deflection of a group of springs acting in parallel, with each spring deflecting within its elastic range. The primary spring is, of course, the data load cell itself; however, other springs are typically (1) the connecting engine service lines, (2) the axial-force component

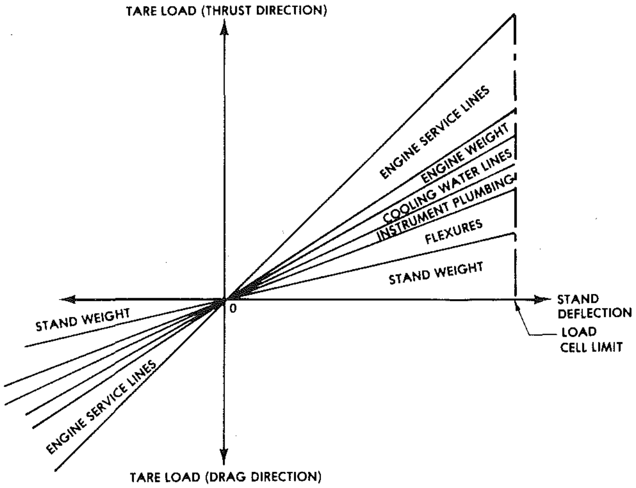

Fig. 5 Thrust stand force calibration (typical deflection-tare stacking)

produced by the weight of the engine itself acting through the flexure link deflection, (3) the flexures which support the weight of the engine and the stand, (4) the weight of the stand itself, and finally, (5) the test cell service lines which provide the cooling water, instrumentation, and other test services to the engine. A typical thrust stand force calibration is shown in Fig. 5 for all of the thrust and drag restraints except for the load cell itself. Such calibration data are obtained incrementally during an engine installation period as the various components are added to the test unit installation.

It should be noted that the data load cell train, which provides the actual force measurement during testing, is located off the centerline of the engine (Fig. 4). This characteristic feature results in a centerline offset loading effect which produces bending of the engine thrust stand and the engine mounting system.

There are several other scale-force error sources which also must be evaluated using an inplace calibration approach. The flow nonuniformity existing at the labyrinth seal which separates the ground plane from the engine free body mounted on the metric thrust frame displays the net influence of streamline curvature on force measurement. These streamline curvature effects are generated by flow through the inlet contraction upstream of the labyrinth seal plane, by the forward-facing effects of flow around the engine bulletnose or spinner, and by the radial mass-flow characteristics of the compressor blade rows downstream of the seal plane. The thrust stand thermal effect shows the force generated because of changes in level and gradients of the temperatures in the metric thrust frame as well as in the ground plane. The cell cooling-air effect measures the forces generated by the extremely low-velocity airflow maintained through the engine compartment to scavenge vapors and to provide cooling of the test cell interior. The load cell thermal effect reflects the influence of small variations in temperature gradient through the thermally conditioned load cell units. In a similar manner, the load cell pressure effect reflects the influence of variations in ambient pressure on the data load cell.

As can be noted throughout this section, there is no magic involved in identifying error sources. The error source determination process described above involves engineering studies and engineering analysis from personnel experienced in many different disciplines. As will be shown in a later section on measurement validation, there are, however, analytical checks that can be made to assist in the error identification process.

The specific procedures and methods used to quantify error sources vary depending on the type error being evaluated. The general guidelines, however, are very similar for most measurement systems and are discussed in Ref. [1]. Generally, several common-type checks are used to assess error sources and consist of instrument "end-to-end" tests, inplace calibrations, response and environmental tests, data repeatability, linearity and hysteresis checks, and redundant checks with computer test codes and historical data.

Table 2 Steady-state elemental error source audit

(NONAFTERBURNING TURBOJET) PARAMETER - SCALE FORCE MEASUREMENT RANGE - 10K TO 15K LBF			
ERROR SOURCE	PRECISION INDEX		BIAS LIMIT
	UNIT OF MEASUREMENT ± LBF	SAMPLE SIZE (df)	UNIT OF MEASUREMENT ± LBF
I. CALIBRATION (TRANSFER ERROR)			
A. NATIONAL STD. TO LABORATORY STD.	4.1	>30	3.5
B. LABORATORY STD. TO WORKING STD.	5.8	>30	4.0
C. WORKING STD. TO MEAS. STD.	8.4	>30	11.9
II. DATA ACQUISITION			
A. EXCITATION VOLTAGE	1.7	>30	1.7
B. ELECTRICAL SIMULATION	1.7	>30	1.7
C. SIGNAL CONDITIONING	1.9	>30	1.8
D. RECORDING DEVICES	NEGLIGIBLE		NEGLIGIBLE
III. DATA PROCESSING			
A. COMPUTER RESOLUTION	1.3	>30	1.2
B. CURVE FITTING	1.5	>30	1.5
C. TIME SAMPLING	NEGLIGIBLE		NEGLIGIBLE
IV. INSTALATION/ENVIRONMENT			
A. LOAD CELL AMBIENT PRESSURE EFFECTS	5.5	>30	8.0
B. TARE LOADS	14.7	>30	18.7
C. CENTERLINE LOADING	9.0	>30	14.0
D. THERMAL EFFECTS	4.6	15	9.5
E. CELL COOLING AIR	2.0	>30	2.0
F. LABYRINTH SEAL MISALIGNMENT	2.8	12	5.0

Table 3 Scale-force steady-state error source audit summary

ERROR SOURCE	PRECISION (S) INDEX		BIAS (B) LIMIT
	UNIT OF MEASUREMENT, LBF	SAMPLE SIZE (d_f)	UNIT OF MEASUREMENT, LBF
I. LOAD CELL CALIBRATION	±11	>30	±13
II. DATA ACQUISITION	±3	>30	±3
III. DATA PROCESSING	±2	>30	±2
IV. INSTALLATION/ ENVIRONMENT	±19	>30	±27

$S_{TOTAL} = \sqrt{\Sigma S_i^2} = \pm 22$ LBF $\qquad B_{TOTAL} = \sqrt{\Sigma B_i^2} = \pm 30$ LBF

UNCERTAINTY = $\pm [30 \text{ LBF} + (2.0)(22 \text{ LBF})] = \pm 74$ LBF (OUT OF 15,000 LBF)

Once the error sources are identified and the magnitude of the errors determined, an elemental error audit, which is the **Credibility** basis for all measurement uncertainty analyses, can be accomplished. An example of a completed error audit for a scale-force measurement system on a nonafterburning, turbojet engine test is contained in Table 2. Table 2 identifies the individual error sources and the magnitude of the precision index, the bias limit, and the measurement sample size. Usually, it is informative to summarize the magnitude of the error by group (i.e., calibration, data acquisition, data processing, installation/environmental) to determine the relative influence of each error group on the final measurement uncertainty. Such a summary is shown in Table 3 where it can be seen that the installation/environmental errors are ±65 lbf [i.e., ±27 + (2.0)(19)] out of a total scale force error of ±74 lbf; which says, "if you want to reduce scale force errors, concentrate on installation and environmental effects".

Measurement Validation

In addition to the scale-force measurement method, there are two other methods which can be used to evaluate engine thrust. For convenience, these methods are called (1) the momentum balance method and (2) the component performance stacking or computer model simulation method. The essential features of each of these methods are shown schematically in Fig. 6.

The momentum balance method requires the use of a

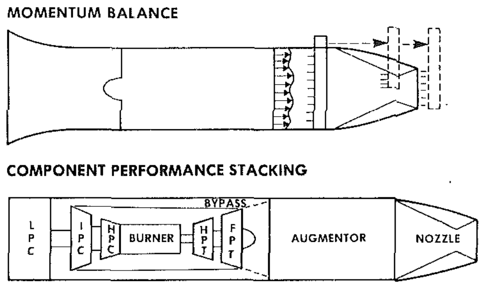

Fig. 6 Thrust measurement comparison methods

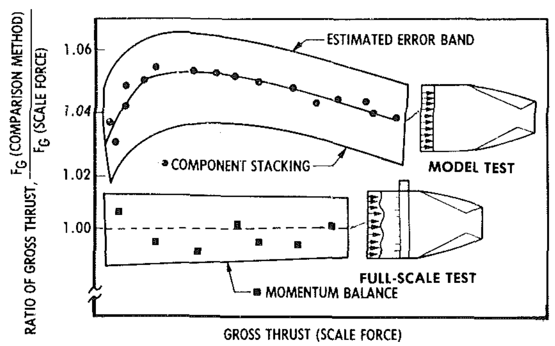

Fig. 7 Thrust redundancy checks

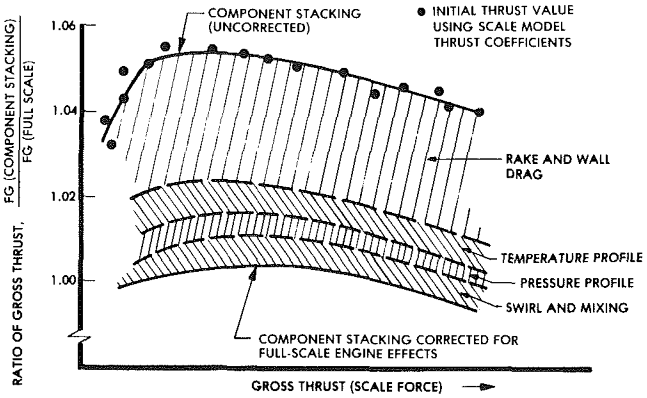

Fig. 8 Resolution of scale model and full-scale engine thrust data (nonafterburning turbojet)

complex traversing rake system and two relatively complex computer codes. The measurement principle of this system is that with an accurate survey of the working fluid stagnation properties, the engine internal mass flow and forces produced by the flow field as it exits the engine tailpipe nozzle can be resolved to determine the engine airflow rates and gross thrust.

The component performance stacking method is basically a full computational method and depends on the proper accounting of the mass, momentum, and energy of the working fluid as it passes through each of the components within the engine. The computer code must be amply supported by the data from component rig tests and model component tests early in the development of the code, and in these early stages the computer code is referred to as an uncorrected model (i.e., no full-scale data corrections). Later in the life cycle of the engine development and code development, substantial reductions in the uncertainty of the code values are possible if the results of full-scale engine tests are used to tailor the characteristics of the code. In the code, several elements such as compressors, turbines, and burner, for example, in the gas path and the several components in the control system are stacked together to provide an overall solution of the controlled engine behavior. The code inputs can be as simple as the aircraft flight conditions and engine throttle setting or could include mechanical rotor speeds and intercomponent flow property values.

A thorough discourse on the momentum balance and component stacking method can be found in Ref. [5]. For the purpose of this paper, it is only important to note that there are other means of evaluating engine thrust independent of the scale-force method. The maximum value of any measurement comes into play when two or more measurements of the same quality can be employed simultaneously. Because of the relatively weak coupling between both inputs and outputs of the scale-force, momentum balance method, and component stacking method, substantial diagnoses and understanding of the individual factors which make up the overall thrust performance of an engine can be obtained from the simultaneous determination of thrust by multiple methods. The overall resolving power of these combined methods is easily demonstrated with test data obtained from an engine development program.

Engine gross thrust obtained by the scale-force method is compared (Fig. 7) with the gross thrust obtained from the momentum balance method, and component stacking method (uncorrected model). In this particular approach to thrust measurement, the gas properties at the exhaust nozzle inlet were measured experimentally during test operation. These values of gas properties were then used in combination with the momentum balance method and with thrust coefficients from the component stacking method to obtain a gross thrust value independent of most of the parameters used to obtain a gross thrust value by the scale-force method. As shown in Fig. 7, the thrust values from the scale-force and momentum balance methods agree within the measurement uncertainty bands of these methods. The agreement (or disagreement) with the uncorrected model data, however, is well outside the quoted uncertainty bands for each of the methods.

The thrust data from the component stacking and scale force methods were analyzed and compared one against the other in an attempt to quantify the term-by-term differences and to analyze and resolve the differences shown in Fig. 7. The results of this effort are shown in Fig. 8. The initial values of the two sets of thrust measurements are repeated along the top line shown in Fig. 8. The detailed analysis of the thrust information showed that from two to three percent of the differences in the thrust values were caused by improper accounting for the rake drag and wall drag in the engine tailpipe. Another one percent of the difference was related to improper accounting for the substantial profile variations of total pressure and total temperature at the nozzle inlet. And, finally, another one percent of the difference was related to the gas swirl and mixing losses produced by the turbine and exhaust sections of this particular engine. When all of these factors were properly placed into the component stacking method, the results from all the methods agreed within approximately ±0.5 percent, as shown by the bottom line in Fig. 8. Thus, this resolution of what was initially an unacceptable variation in experimental measurements has now become a single value of measured thrust *and* a series of explicit values of second-order engine flow effects which were initially unidentified error sources.

Another valuable measurement check is facility-to-facility comparisons. Interfacility comparisons can be an extremely effective means for both evaluating and validating measurement results and should be periodically conducted to determine whether significant differences in measured values exist. On most turbine engine performance test programs, the engine will be tested on a sea-level test stand prior to being tested in an altitude test facility. It is, therefore, standard practice to compare engine sea-level stand thrust data with the

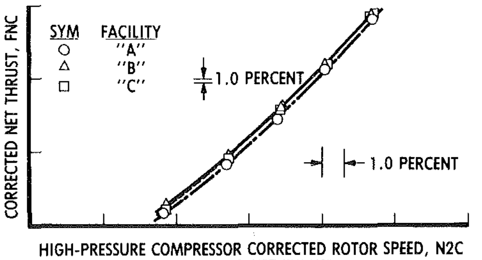

CORRECTED NET THRUST

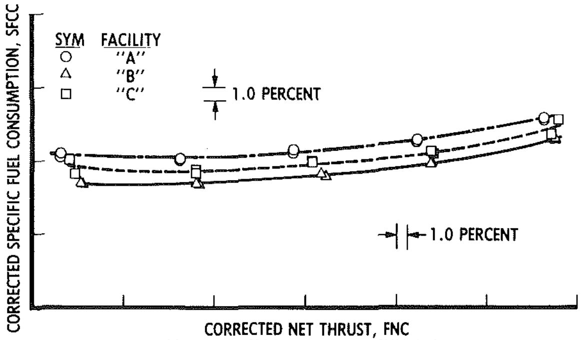

CORRECTED SPECIFIC FUEL CONSUMPTION

Fig. 9 Interfacility data comparison

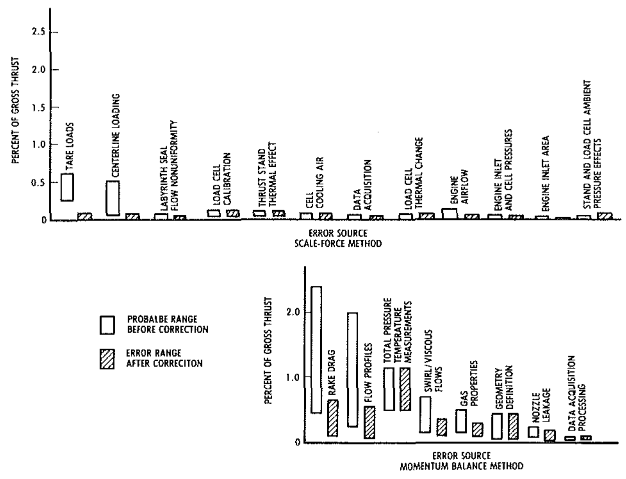

(a) Nonafterburning turbojet, military power setting, sea-level-static

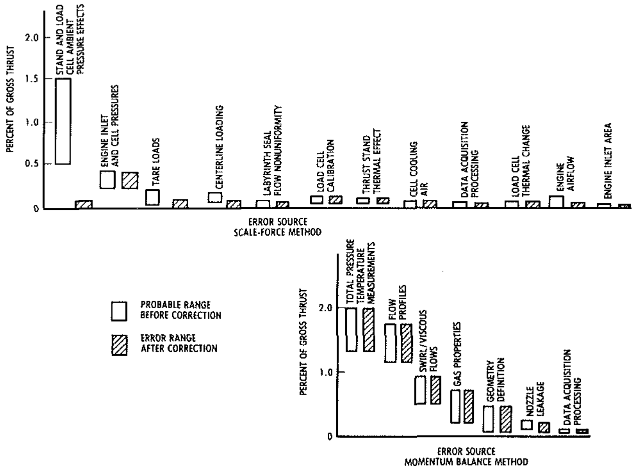

(b) Afterburning turbojet, maximum power setting, altitude = 40,000 ft. Mach Number = 1.2

Fig. 10 Thrust measurement elemental error charts

corresponding sea-level thrust data from the altitude test facility. Results from one such correlation test using a low-bypass turbofan engine and involving three different ground test facilities are presented in Fig. 9 [7]. Facilities "B" and "C" net thrust and specific fuel consumption values agreed to within one percent, which was within the quoted interfacility measurement uncertainty band of 1.5 percent. Facility "A" values were greater (approximately 2 to 2.5 percent) than both "B" and "C" values. This difference was traced to an inaccuracy in Facility's "A" bellmouth flow coefficient and omission of an inlet momentum term in the calculation of gross thrust. As a result of this interfacility comparison, Facility "A" was able to identify two unaudited error sources and upgrade their measurement system.

Measurement Uncertainty Utilization

One of the challenges that befalls the engine ground tester is the task of matching the measurement system to the program requirements in order to control resource expenditures – **Cost Control**. In order to accomplish this task, the engineer must

1. make pretest measurement uncertainty estimates to ensure that an acceptable measurement system will be selected,
2. identify the measurement factors that must be controlled in order to meet the program uncertainty requirements, and
3. estimate the manhour resources required to meet the test program uncertainty objectives.

To generate the required information, historical data relating measurement system uncertainties to measurement factors are compiled in the form of error charts.

Error charts provide two major benefits: they enable the tester to (1) make pretest estimates of measurement accuracies for a specified level of effort and (2) identify the measurement system error sources that can most effectively be worked to improve the test results. An example of a thrust error chart is shown in Fig. 10. The chart abscissa lists the error sources that influence the measurement of the performance parameter. The chart ordinate specifies the level of this influence. An open or unhatched bar depicts the nominal range of the systematic errors, and the cross-hatched bar depicts the error range that can generally be achieved with a normal effort to account for correctable errors. Thus, the magnitude of the cross-hatched bar corresponds to the magnitude of combined error sources which are considered random in nature and not readily correctable in the measurement system. The Fig. 10 error charts quantify the various gross thrust error sources for the scale-force and momentum balance methods. The magnitude of the individual error terms will vary as a function of the engine cycle and operating condition. In order to show this effect, an error chart is presented for both a nonafterburning turbojet engine operating at military power and sea-level altitude [Fig. 10(*a*)], and for a turbojet engine operating at maximum (afterburning) power at an altitude of 40,000 ft [Fig. 10(*b*)].

The largest correctable error for the scale-force method nonafterburning, low-altitude case is the tare load effect. The tare load shown reflects the stiffness of the thrust stand support systems and service systems. The centerline loading error quantifies the effect of the bending of the thrust stand and engine mounting system because the data load cell is not located on the engine thrust centerline. However, the tare loads and centerline loads can be established with such a high degree of precision that the overall effect of each of these errors is less than ±0.1 percent of the measured gross thrust. Similarly, with additional effort, the probable error range for the other primary sources of scale-force error can also be established with a high degree of precision.

The largest correctable error for the scale-force method for

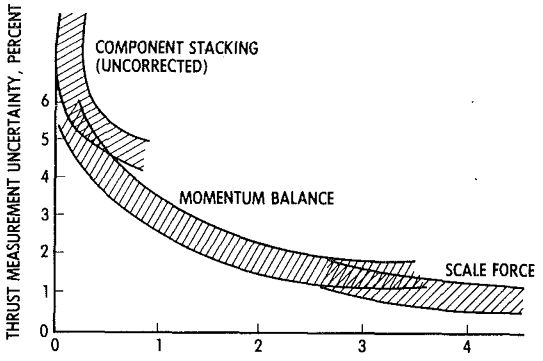

Fig. 11 Impact of thrust measurement uncertainty on program measurement resources (nonafterburning turbojet engine)

the afterburning, high-altitude case is the effect of varying test cell ambient pressure on the data load cell and thrust stand. For present-day equipment the magnitude of this effect typically lies in the range of 0.5 to 1.5 percent of full scale of the scale-force measuring system. However, the load cell and thrust stand response to changing pressures can be established with such a high degree of precision that the overall effect of this error is less than ±0.1 percent of the measured force.

The largest error sources in the momentum method are the drag of the survey rake (although this will vary in each application depending upon the particular rake design) and errors from nonuniform flow profiles of total pressure, total temperature, static pressure, and angularity in the flow. These types of errors, however, can be corrected using theoretical and experimental treatment. Other error sources such as flow swirl and viscous effects, gas properties, and nozzle leakage can be controlled by careful design of the experiment.

For the afterburning case, a direct measurement of the tailpipe pressure and temperature profiles is generally not practical. Therefore, bulk values of the tailpipe flow properties are estimated based on a tailpipe heat and momentum balance or a value is obtained from the engine math model simulation for the particular test conditions. Obtaining a value in this manner, however, results in a larger error for the pressure, temperature, and gas property values and means that profile effects are not correctable.

Once the test program performance uncertainty requirements have been defined and the measurement uncertainty error charts have been generated, the tester can use the charts and test requirements to arrive at a measurement system selection and a test measurement cost estimate. The measurement selection is made by reviewing the individual error charts to determine which systems can meet the test requirements. Having defined the measurement system, the hardware and software requirements can be defined, and the work efforts required to address the correctable error sources can be estimated. An example of an engine thrust measurement uncertainty and resources tradeoff curve for different measurement approaches is shown in Fig. 11. It can be seen as the thrust measurement uncertainty requirements are reduced, the proposed measurement method changes and resource requirements increase exponentially as the uncertainty requirements approach the current state-of-the-art.

The resource trend curve in Fig. 11 applies to a nonafterburning turbojet engine and assumes that a component stacking model adjusted to sea-level test stand data is available for thrust predictions. Since the component stacking method is basically an analytical effort, this is the least costly approach. However, for measurement uncertainties less than 5 to 10 percent, full-scale altitude test data are required to further refine the model, and at this point, the momentum balance method becomes a more economical choice. As the measurement uncertainty requirements are further reduced, the momentum balance, tailpipe rake sampling requirements and the supporting analytical analysis requirements reach a level where it becomes more economical to use the scale-force method. For thrust measurement uncertainty requirements less than nominally 0.5 percent, additional thrust measurement technology must be developed, and this will be costly to accomplish and difficult to schedule.

Measurement Uncertainty Implementation

Implementation of a measurement uncertainty program primarily requires three actions:

1. adopting a measurement uncertainty methodology,
2. establishing a measurement uncertainty overview committee, and
3. assigning a measurement uncertainty assessor and historian.

The primary consideration for adoption of a measurement uncertainty methodology is industry acceptance. The measurement uncertainty methodology used within the aerospace propulsion industry (i.e., the Abernethy-Thompson method) has gained acceptance by several engineering technical societies [3, 4, 8, 9]. The procedures defined by the Abernethy-Thompson methodology are sufficiently general so that they may be applied to virtually any type of measurement system. In the AEDC/ETF the same uncertainty methodology is used for research experiments, development testing, and testing of production propulsion systems.

Once a measurement uncertainty methodology is adopted, it is necessary to convene some type of committee to establish specific measurement uncertainty practices within your company's operation that meet the measurement uncertainty methodology guidelines. In the AEDC/ETF this committee is made up of members from each of the disciplines involved in the measurement activities: measurement installation, calibration, data acquisition, data processing, and analysis. The committee has the requirement to establish measurement practices consistent with the adopted methodology. This includes instrument calibration practices, instrument installation requirements, error source identification and type (i.e., precision or bias), measurement evaluation practices, and the measurement error evaluation procedures.

Finally, someone must be tasked to continuously monitor the ongoing test programs to ensure that the measurement uncertainty requirements are being met. This task primarily consists of reviewing test calibration data and taking random measurement samples and evaluating measurement precision and bias errors while the test is being conducted. At the completion of the test, the measurement uncertainty assessor must make the final evaluation of the measurement uncertainty levels achieved for the test and report his findings in the form of an error audit table such as Table 2. The measurement uncertainty assessor also uses the findings from each test to establish a measurement uncertainty data base (error charts being one means) from which to make future pretest predictions.

The first thought entering the reader's mind at this point is that a measurement uncertainty evaluation program can be expensive and time consuming. At the AEDC/ETF the measurement uncertainty effort discounting the initial program start-up efforts consumes less than two percent of the company's manhour resources: certainly a small investment for such a significant payoff.

Summary

Measurement uncertainty analysis is not only a means for quantifying measurement goodness but also a means for measurement control. The measurement uncertainty program described in this paper addresses three of the more difficult areas which confront the measurement engineer.

Communications. Communications of measurement uncertainty values requires a precise definition of the means used to derive the measurement uncertainty values. Using the Abernethy-Thompson methodology, a systematic approach for evaluating and reporting measurement results has been developed. This same methodology can also be used to bring measurement uncertainty results derived using different methodologies to a common basis.

Credibility. The basis for measurement credibility espoused in this paper is the elemental error audit. The error audit reports three pieces of information: (1) the error source, (2) the bias and precision error values, and (3) the method used to quantify each error value.

Cost Control. By developing measurement error charts and measurement uncertainty-resource plots, the engineer can compile the necessary data to (1) make accurate pretest measurement uncertainty predictions, (2) match measurement hardware and software requirements to the test measurement uncertainty requirements, and (3) identify measurement tasks and systems that are cost-efficient with respect to the test program objectives.

References

1 Abernethy, R. B., and Thompson, J. W., Jr., "Handbook—Uncertainty in Gas Turbine Measurements," Technical Report No. AEDC-TR-73-5 (AD-755356), Mar. 1973.

2 JANNAF "ICRPG Handbook for Estimating the Uncertainty in Measurement Made with Liquid Propellant Rocket Engine Systems," CPIA Publication 180, 1969.

3 International Organization for Standardization (ISO), ISO TC30 SC9, "Fluid Flow Measurement Uncertainty," Dec. 1981.

4 Abernethy, R. B., et al., "ASME Measurement Uncertainty," American Society of Mechanical Engineers, Winter Annual Meeting, Nov. 1983, ASME Paper No 83-WA/FM-3.

5 Smith, R. E., Jr., and Wehofer, S., "Measurement of Engine Thrust in Altitude Ground Test Facilities," AIAA Paper 82-0572, AIAA 12th Aerodynamic Testing Conference, March 22–24, 1982.

6 Smith, R. E., Jr., and Wehofer, S., "Uncertainty of Turbine Engine Performance Measurements in Altitude Ground Test Facilities," *Proceedings of the 29th International Instrumentation Symposium*, Vol. 29, 1983.

7 Couch, B. D. and Hinds, H. S., "Turbine Engine Performance Correlation Between Three Ground Test Facilities," AEDC-TR-79-70 (AD-B048371), June 1980.

8 Adams, G. R., et al., "Uncertainty Methodology for In-Flight Thrust Determination," Presented at the Society of Automotive Engineers, Aerospace Congress and Exposition, Oct. 1983, SAE Paper No. 831438.

9 *Instrument Society of America (ISA) Measurement Uncertainty Handbook*, revised 1980.

Using Uncertainty Analysis in the Planning of an Experiment

R. J. Moffat
Professor of Mechanical Engineering,
Stanford University,
Stanford, CA 94305

A simple example using convection heat transfer is used to illustrate the use of uncertainty analysis in PLANNING experiments. Major points made are: (i) the choice of test and data-reduction procedure can have important impact on the accuracy of the results, with one procedure better for some conditions and the other better in other ranges; (ii) it is important to specify carefully the level of replication (what is held constant and what varied in a given test), since otherwise an inappropriate value of uncertainty may be generated; (iii) reliable means for cross-checking and/or externally validating the results of an experiment are necessary if predicted uncertainties are to be confirmed; (iv) in experiments where data are reduced by computer, uncertainty analysis can be done by sequential perturbation, using the main data-reduction program itself.

Introduction

Uncertainty Analysis of a proposed experiment can pay big dividends in the planning stage of an experiment, providing guidance for both the overall plan and for the execution of the details.

When two or more approaches are available for the same task, a question frequently raised is, "Which of these methods will produce the best data?" If the word "best" is interpreted to mean "least uncertain," the question can be answered before the experiment is ever run, using the techniques of Uncertainty Analysis. In the present paper, two different techniques are considered for a hypothetical experiment, either of which could apparently be used. Uncertainty Analysis provides important input to the selection process by pointing out the uncertainty which would result from each method.

The application of Uncertainty Analysis to a proposed test program is called a priori Uncertain Analysis in the author's laboratory, and "pre-test analysis" in other works (Abernethy et al. 1981). These two terms may be synonymous and are only subtly different, at most.

This paper describes the use of a priori Uncertainty Analysis in choosing between two proposed techniques for measuring the heat transfer coefficient from a cylindrical rod to an air stream.

The analysis starts with the data-reduction equations for each method (the equations by which the result will be computed from the raw data), along with estimated values of the uncertainty in each piece of input data. The uncertainties in the results are then calculated for representative points across the domain of the proposed experiment by each of the two methods. Once the uncertainties of the two methods are displayed, the choice between the methods is obvious.

In the present paper, the focus is on the use of Uncertainty Analysis as an aid in decision making, not on the technique of Uncertainty Analysis itself. Those techniques have been discussed in previous publications (Kline and McClintock, 1953; Abernethy et al. 1981; Moffat, 1978; Moffat, 1982.

The main body of the paper proceeds as though the appropriate value for the uncertainty were known for each measurement, and as though the mathematical procedures of Uncertainty Analysis could be applied to the data-reduction equations with no special difficulties. As a supplement to the main text, there are two appendices which treat these issues in more detail: (I) Identifying the Uncertainty in a Measurement, and (II) Computerizing Uncertainty Analysis.

The Physical Situation and Energy Analysis

This experiment involves measuring the convective heat transfer coefficient from an existing test specimen (a cylindrical rod) in an airstream over a range of velocities. The objective is to produce a reference-quality data set describing the "constant properties" heat transfer coefficient over a range of Reynolds numbers. The test is to be designed to achieve the minimum uncertainty which can be realized using available instruments and equipment. All testing is to be conducted at approximately ambient conditions of temperature and pressure, using an existing test tunnel, but the velocity can be varied over a wide range.

Figure 1 shows the test specimen and illustrates the energy-flow terms recognized as "possibly important" in establishing its thermal response.

Considering a control volume which includes all of the test specimen but is infinitesimally outside its surface, an energy balance yields equation (1):

$$hA(T-T_\infty)+\sigma\epsilon A(T^4-T_w^4)+2K_e(T-T_\infty)+Mc\frac{dT}{d\theta}-W=0 \quad (1)$$

In this equation, it is assumed that the temperature is

Contributed by the Fluids Engineering Division and presented at the Symposium on Uncertainty Analyses, Winter Annual Meeting, Boston, Mass., November 13-18, 1983. Manuscript received at ASME Headquarters, March 20, 1985.

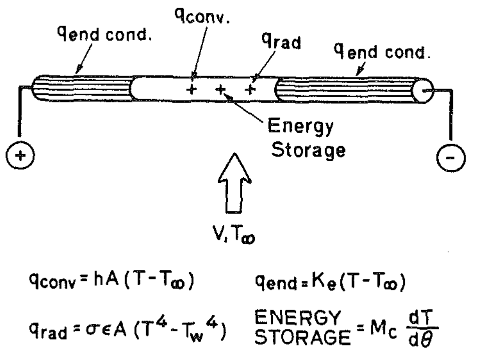

Fig. 1 The test specimen and the energy flows

uniform inside the rod, so that the single symbol, T, represents both the surface temperature and the average internal temperature. This assumption limits the test range to relatively low "h" values, those for which the internal temperature gradient is negligible compared to the temperature difference used in defining h. The usual method is to calculate the Biot number hr/k, and require that it be 0.01 or less (depending on how critical is the experiment).

This energy-balance equation is the basis for both of the techniques considered for the present experiment—the steady state and the transient methods.

The Steady-State Method. Equation (1) can be solved for h by simply rearranging it. If, at the same time, a linearized approximation is substituted for the radiation term and the temperature of the tunnel walls is assumed to be the same as that of the tunnel air, a particularly helpful form emerges:

$$h = \frac{W}{A(T - T_\infty)} - 4\sigma\epsilon T_m^3 - 2K_e - \frac{M\bar{c}}{A}\frac{dT/d\theta}{(T - T_\infty)} \tag{2}$$

In equation (2), the first term is a first approximation to h, and the following terms are the corrections which should be applied to account for radiation ($4\sigma\epsilon T_m^3$), end conduction ($2K_e$), and unsteady test conditions ($M\bar{c}\ dT/d\theta)/(A(T - T_\infty)$).

Equation (2) is the data-reduction equation for the Steady-State tests. For simplicity in illustrating the use of Uncertainty Analysis in the planning of the experiment, only the first term is used in the following calculations. Thus, for the present purpose, equation (3) is the data-reduction equation:

$$h = \frac{W}{A(T - T_\infty)} \tag{3}$$

The Transient Method. In the transient method, the specimen is first heated above the air temperature and then quickly inserted into the flow. (The intent is to produce the equivalent of a "step-change" in temperature of the surrounding. There are several ways to accomplish this goal, some of which do not involve actually moving the test piece.) The temperature of the specimen is recorded during the cooling interval, and the heat transfer coefficient deduced from the time-temperature history. Typically, there is no power applied during the cooling transient; hence $W = 0$.

The data-reduction equation for the transient method is derived from equation (1) by linearizing the radiation term and collecting all heat transfer terms using an "overall h" defined as:

$$h_0 = h + 4\sigma\epsilon T_m^3 + \frac{2K_e}{A} \tag{4}$$

With the use of h_0, equation (1) becomes:

$$h_0 A(T - T_\infty) + M\bar{c}\frac{dT}{d\theta} = 0 \tag{5}$$

If h_0 remains constant throughout the transient, this equation has a simple solution.

Values of $(T - T_\infty)$, on semi-log coordinates versus time, are shown in Fig. 2. The "characteristic time" of the sytstem is found from:

$$\tau = \frac{\theta_2 - \theta_1}{\ln\left(\frac{T_1 - T_\infty}{T_2 - T_\infty}\right)} \tag{6}$$

Any two points within the linear portion of the curve can be used as points 1 and 2. This method is preferred over the use of a single measurement of the 0.632 completion time, because it uses more information from the test, is less susceptible to error, and is self-validating. (In cases where the thermal response of the system cannot be described by a simple linear, first-order equation such as equation (5), the line will not be straight. Curvature in the plot of $(T - T_\infty)$, in these coordinates, is evidence that the proposed procedure is not applicable and some other procedure should be sought.)

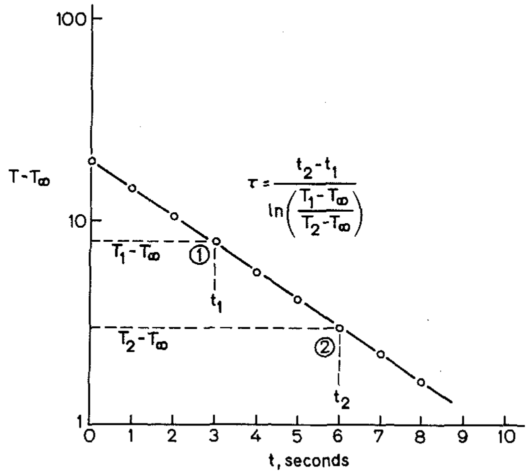

Fig. 2 Typical data from a first-order system during cooling

The value of h_0 is found using the definition of "characteristic time" and h found from h_0 by subtracting the terms originally embedded in it:

$$h = \frac{M\bar{c}}{\tau A} - 4\sigma\epsilon T_m^3 - \frac{2K_e}{A} \tag{7}$$

In illustrating the use of Uncertainty Analysis for the

Nomenclature

A = heat transfer area
c = specific heat of test specimen
D = specimen cylinder diameter
h = heat transfer coefficient
k = thermal conductivity of test specimen
K_e = effective end conductance
L = length of test specimen
M = mass of test specimen
R = result of experiment; calculated from x_i's
T = temperature on heat transfer surface, assumed uniform
T_m = effective mean temperature for radiation
T_w = temperature of enclosure walls
T_∞ = ambient air temperature
W = power supplied to specimen
x_i = the ith variable measured in the experiment
θ = time
σ = Stefan-Boltzmann constant
ϵ = emissivity of body; parameter of incremental variation in App. II
τ = time constant of system

present paper, only the first term will be used. Thus the data-reduction equation for the transient method is:

$$h = \frac{M\bar{c}}{\tau A} \tag{8}$$

Uncertainty Analysis—General Forms

Execution of an Uncertainty Analysis requires reporting of the uncertainty in each measurement, as well as the value itself. Each recorded piece of data is considered to be: (1) an independent observation, (2) from a Gaussian population of possible values, and (3) the uncertainty interval quoted for each variable must be quoted at the same "odds." A complete entry is:

$$x_i = \hat{x}_i \pm \delta x_i \quad (20/1) \tag{9}$$

Equation (9) means: "The observed value was $\hat{x}_i$, and 19 of 20 readings of x_i are expected to lie within ± δx_i of that value, if repeated readings are taken, following a prescribed replication pattern." It is important that δx_i accurately reflect the uncertainty in x_i for the considered level of replication. This topic is discussed in Appendix I.

For a result, R, calculated from a set of input data ($x_1, x_2, x_3, \ldots, x_N$), the uncertainty is:

$$\delta R = \left\{ \left(\frac{\partial R}{\partial x_1} \delta x_1 \right)^2 + \left(\frac{\partial R}{\partial x_2} \delta x_2 \right)^2 + \ldots \left(\frac{\partial R}{\partial x_N} \delta x_N \right)^2 \right\}^{1/2} \tag{10}$$

For the special case where the result R can be written as a product of terms, each raised to some power, the Relative Uncertainty, $\delta R/R$, can be found by equation (12); i.e.,

if $$R = x_1^a x_2^b x_3^c \ldots x_N^N \tag{11}$$

then

$$\frac{\delta R}{R} = \left\{ \left(a \frac{\delta x_1}{x_1} \right)^2 + \left(b \frac{\delta x_2}{x_2} \right)^2 + \ldots \left(N \frac{\delta x_N}{x_N} \right)^2 \right\}^{1/2} \tag{12}$$

This form is particularly useful if the uncertainties in the input values are known as "percent of reading" or can easily be put in that form before the Uncertainty Analysis is done.

Uncertainty Analysis—The Steady-State Method

In the steady-state method, h is found using equation (2), but for illustration of the Uncertainty Analysis, equation (3) will be used. This is in the form of equation (11) and allows a simple, relative uncertainty calculation.

Applying equation (12) to the data-reduction equation for the Steady-State case yields the following equation for the relative uncertainty in h, using the steady-state method:

$$\frac{\delta h}{h} = \left\{ \left(\frac{\delta W}{W} \right)^2 + \left(\frac{\delta D}{D} \right)^2 + \left(\frac{\delta L}{L} \right)^2 + \left(\frac{\delta \Delta T}{\Delta T} \right)^2 \right\}^{1/2} \tag{13}$$

For the instruments available, the uncertainty estimates were assumed to be:

$\delta W = 0.5$ W
$\delta D = 0.025$ mm
$\delta L = 0.125$ mm
$\delta \Delta T = 0.2$ C

The effect of these uncertainties will depend on the values of W, D, L, and ΔT, and some of those values will change with test conditions. To estimate the uncertainty before the test is run, some decisions must be made about the conduct of the test.

In the present case, the specimen is assumed to exist; therefore D and L cannot be changed: $D = 0.0254$ m and $L = 0.254$ m.

In heat transfer measurements, it is good practice to keep the surface temperature constant throughout the test, in order to eliminate the effect of changes in fluid properties. If ΔT is chosen to be 20 C, the relative uncertainty in ΔT will be 1 percent, an acceptable level. The overall uncertainty of the measurement of h will then depend on the power level, W, which will change as the air velocity changes. To estimate this effect, only an estimate of the range of expected h is needed. The uncertainty in h can then be calculated as a function of h.

Based on the results of related or similar tests, it was judged that h would probably lie between 10 and 1000 W/m^{2}C. For the given geometry, for several possible values of h, the power, W, was calculated using equation (3). Then, for each of those values of h, the relative uncertainty was estimated using equation (13). The results are shown in Fig. 3.

The Relative Uncertainty in h is largest at low values of h, where the uncertainty in W dominates the calculation. As h increases, the uncertainty decreases.

Uncertainty Analysis—Transient Method

In the transient method, h is found using equation (7), but for illustration of the uncertainty analysis, only the first term will be used, i.e., equation (8).

Once again, the form allows a simple determination of the Relative Uncertainty, $\delta h/h$, following equation (12):

$$\frac{\delta h}{h} = \left\{ \left(\frac{\delta \tau}{\tau} \right)^2 + \left(\frac{\delta \bar{c}}{\bar{c}} \right)^2 + \left(\frac{\delta M}{M} \right)^2 + \left(\frac{\delta D}{D} \right)^2 + \left(\frac{\delta L}{L} \right)^2 \right\}^{1/2} \tag{14}$$

The data list is quite different from that of the steady-state method, and some new uncertainty estimates are needed. The following values were used.

$\delta \tau = 0.0025$
$\delta M = 0.001$ kg
$\delta c = 0.004$ kJ/kgC
$\delta D = 0.025$ mm
$\delta L = 0.125$ mm

For the range of h already defined, values of τ were calculated, using equation (8), and used to predict the relative uncertainty in h at each point in the operating domain of the experiment. The results are shown in Fig. 3.

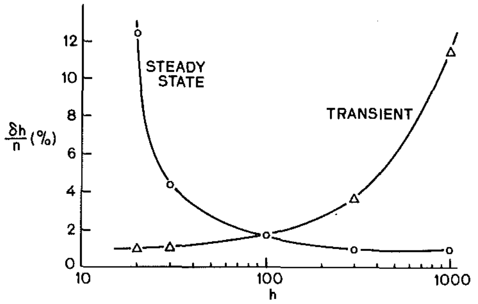

Fig. 3 Comparison of the uncertainty intervals of the two methods proposed – Nth order

Comparison and Interpretation

Figure 3 shows the cross-over point to be h = 100 W/m^{2}C. For tests where h is expected to be above that value, the Steady-State method would be specified, while for tests below that, the Transient method would yield lower uncertainties.

In the present illustration, the scope of the experimental variations was limited in order to channel the development quickly toward a single solution. In a more general case, one might find that the dimensions of the test specimen, the test velocity, the operating temperature difference, and other degrees of freedom exist. It may begin to appear that the possibilities are endless. The important point to remember is that desk-time is cheaper than test-time. Uncertainty analysis will frequently reveal that an apparently plausible test program simply cannot deliver the required precision.

What Does the Calculated Uncertainty Interval Mean? The uncertainty intervals used as input for the Steady-State method were dW, dD, dL, and $d\Delta T$, while for the Transient method, the inputs were $d\tau$, dD, dL, dM, and $d\bar{c}$. The individual estimates included allowances for both the reading uncertainties and the calibration uncertainties in the instruments involved; they are Nth Order Uncertainty Interval estimates (following the material in Appendix I). The calculated uncertainty interval for the result is thus an estimate of the standard deviation of the population of all possible experiments like this one: any person, in any lab, using any set of instruments, should produce results which agree with these predictions. This is the type of uncertainty interval which should be quoted in reporting the work to the outside world.

The results of repeated trials with the same specimen and the same instruments will display much less scatter than the prediction just made. This is called a First-Order replication; only reading uncertainties are sampled. For repeated trials with the same specimen in the present case, the input list of uncertainties reduces to dW and dT for steady State and $d\tau$ alone for the Transient tests. Further, the uncertainty intervals for these variables are smaller for the First-Order replication, since they now reflect only the reading uncertainties. The calibration uncertainties of the instruments do not introduce scatter at this level of replication. Figure 4 shows the First-Order uncertainty results for the two methods, assuming that one-half of the uncertainty originally quoted was due to instrument-calibration uncertainty. The effect is primarily at the low-uncertainty end of each testing range.

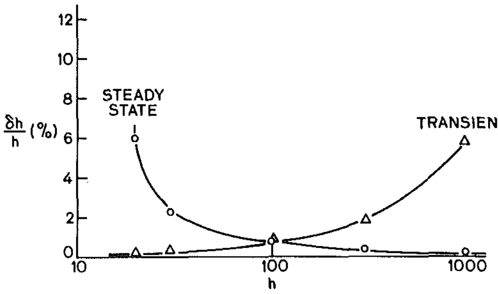

Fig. 4 Comparison of the uncertainty intervals of the two methods proposed – first order

Experimenters frequently calculate the Nth-Order uncertainty interval for their tests and then are "pleased" that their results on repeated trials lie well within the calculated uncertainty! This does not have much meaning. The scatter on repeated trials should not be judged against the Nth-Order uncertainty, but against the First-Order interval, which is always smaller and sometimes much smaller.

The First-Order uncertainty interval is used mainly in the "debugging" phase of an experiment, in which unusually large scatter can signify trouble with the experiment.

The Nth-Order uncertainty interval should be reported with the data for external users. It is this value which relates to the agreement which others may expect to find with the reported data.

Cross-Checking the Experiment. If possible, an experiment such as this should be equipped for both methods, thus providing a good opportunity for validating the experiment by cross-checking the two methods. In the vicinity of the cross-over point, both methods are equally certain; therefore, agreement of the results by the two methods constitutes strong evidence that the results are correct. Since the two methods have no data in common except the surface area of the specimen, there is no other single parameter which can affect both methods in the same way: if they agree, they are probably correct.

One simple test for agreement between two uncertain results which should be the same but don't appear to be is to compare the observed difference with the calculated uncertainty interval for the difference $(R_1 - R_2)$. This is the interval within which the observed difference would lie, 19 times out of 20, by chance alone, if the mean of many differences was zero (given the uncertainties in each of the terms). If the observed difference lies outside this interval, there is only one chance in 20 that the difference is not significant.

Since the relative uncertainty in each result is already known, the calculation is simply:

$$\delta(R_1 - R_2) = \left\{ (\delta R_1)^2 + (\delta R_2)^2 \right\}^{1/2} \tag{15}$$

Conclusions

Uncertainty analyses should be done as a routine part of the planning for experiments, not simply as go/no-go tests on the plan, but as contributory to the decision process concerning the test methods and objectives.

The uncertainty interval for most experiments is dominated by the behavior of a few terms—frequently one or two. For planning purposes, it is generally sufficient to work with these only.

Uncertainty estimates should be made at both First and Nth-Order, to provide proper guidance in debugging and proper evaluation for reporting.

References

1 Kline, S. J., and McClintock, F. A., "Estimating the Uncertainty in Single-Sample Experiments," *Mechanical Engineering*, Jan. 1953.

2 Moffat, R. J., "Planning Experimental Programs," Stanford University, Thermosciences Division Lecture Notes, 1978.

3 Abernethy, R. B., et al., "Handbook on Uncertainty in Gas-Turbine Measurements," USAF AEDC-TR-73-5, AD 755356. Also available through the Instrument Society of America as "Measurement Uncertainty Handbook, Revised 1980," IS&N: 87664-483-3.

4 Moffat, R. J., "Contributions to the Theory of Single-Sample Uncertainty Analysis," ASME JOURNAL OF FLUIDS ENGINEERING, Vol. 104, June 1982, pp. 250–260.

5 Moffat, R. J., "The Measurement Chain and Validation of Experimental Measurements," Paper B-103, ACTA IMEKO, 1973.

APPENDIX I

Identifying the Uncertainty in a Measurement

There is no single value of uncertainty associated with a particular measurement in an experiment. The value which should be assigned as δx depends on the objective of the analysis, as well as the characteristics of the experiment.

The uncertainty assigned to a given variable represents an estimate of the scatter which would be observed if that variable were measured many times *under prescribed conditions* and depends on what factors of the experiment are allowed to vary during those repeated trials.

The difference between the true value and the recorded result of an experiment includes measurement errors and apparatus-dependent errors [5], but only measurement errors are dealt with here. The apparatus may have produced a bad example of the desired situation, in which case the results would be "wrong" even though the measurement uncertainty is low.

First-Order Uncertainty Estimate. Consider a series of repeated measurements made over a short (but representative) time interval, using the same set of instruments, on a system nominally at a steady state. The only components in the scatter will be those introduced by short-term instabilities in the process being studied and in the instrumentation. This is the most closely controlled form of replication. An uncertainty estimate aimed at predicting this scatter will be called a First-Order uncertainty estimate [4].

The term First-Order uncertainty is synonymous with "Precision" as used by Abernethy et al. (1981). The First-Order uncertainty estimate, as used here and in references [2 and 4], makes no allowances for any "fixed errors' in the experiment; it accounts only for the errors which were random as the experiment was conducted. Since the First-Order uncertainty estimate is used only to evaluate the significance of the scatter in repeated trials with the same equipment and the same instruments, the omission of "fixed errors" causes no problem; this is purely a "precision" issue.

To estimate the First-Order uncertainty interval for a given measurement, a temperature, for example, one must operate the entire test apparatus at steady state long enough to take 30 readings of the temperature in question, over a representative interval of time. The First-Order uncertainty interval for that measurement is taken to be twice the standard deviation of the sample of 30 readings. If the operating range of the apparatus is large, the First-Order estimate for each instrument should be checked at several points over the range of the apparatus to be certain that a representative value has been obtained.

First-Order uncertainty estimates predict the scatter which would result from repeated trials using the same apparatus and instruments. They are used to evaluate the significance of the scatter which does result when the actual test is repeated: if the actual test data show more scatter than predicted by the First-Order analysis, the experiment is not well controlled.

Nth-Order Uncertainty Estimates. When the intent of the uncertainty analysis is to estimate the total measurement uncertainty in an experiment, instrument calibration errors must be considered in addition to the random errors introduced by unsteadiness and by reading errors. In a usual experiment, the instruments remain in place throughout the test series, and their calibration errors introduce "fixed errors" or "biases" to the result, but do not introduce scatter. If the instruments used on a real experiment were changed with each reading, the scatter in recorded results would undoubtedly go up.

Instrument calibration defects can be incorporated into the present framework of uncertainty analysis by imagining a hypothetical replication pattern in which every instrument was exchanged for another (of similar type) after each reading. This hypothetical replication pattern would introduce instrument calibration as a random variable. The actual, single-sample experiment which is done is simply one member of the population of hypothetical replications.

The uncertainty estimate appropriate for this hypothetical replication is called the *N*th-order uncertainty. It represents an outer bound for measurement errors due to uncertain calibration, system unsteadiness, and reading errors. The results of a single-sample experiment may still contain fixed errors due to system/sensor interactions, system disturbance effects, and conceptual errors [5]. These residual fixed errors can frequently be spotted by comparing experimental results with carefully qualified baseline results: if they differ by more than the *N*th-order uncertainty interval, there is probably a residual fixed error.

The *N*th-order uncertainty estimate, for each measurement, is calculated from the observed First-Order estimate and the (assumed known) uncertainty in the instrument calibration. The two must be expressed in the same units, for the same odds, and are then combined using the Root-Sum-Square form. The result is an estimate of the most likely total uncertainty in that measurement. It is assumed that all known errors (i.e., calibration curves, etc.) have been accounted for so that all that is left is the uncertainty in the calibration. This approach makes no allowance for any other class of "Fixed Errors." The resulting estimate is the smallest uncertainty interval which must be acknowledged for that one measurement. If *N*th-Order estimates are used for all the variables in a calculation, the uncertainty in the result is the smallest which must be acknowledged to exist, consistent with the known properties of the input data. For precision in identifying the significance of an experiment, one wants to know the smallest uncertainty interval which must surround the data—not the largest; large uncertainty intervals render comparisons meaningless.

Summary of Appendix I

First Order: Record 30 readings from the instrument over a short but representative time interval. Find the standard deviation, σ, of the 30 readings. The First-Order uncertainty for that variable, at those operating conditions, is 2σ. The test should be conducted at more than one point inside the operating range and should be repeated at regular intervals to recertify the apparatus.

Nth-Order: The Root-Sum-Square combination of the uncertainty in the instrument calibration and the First-Order result calculated above. The calibration uncertainty interval must be for the same "odds" as the First-Order uncertainty, typically 20/1.

APPENDIX II

Computerizing the Uncertainty Analysis by Sequentially Perturbing the Data-Reduction Program

With the advent of computerized data reduction (including even the use of programmable hand calculators), it has become easy to do uncertainty analysis, on even the most complex programs.

The most difficult part of uncertainty analysis is the determination of the partial derivatives shown in equation (10), which are central to the whole operation. Computerized data reduction makes this simple, however, if one examines the definition of the partial derivative operation:

$$\frac{\partial R}{\partial x_i} = \lim_{dx_i \to 0} \frac{\left(R_{x_i + dx_i} - R_{x_i}\right)}{dx_i} \tag{16}$$

From the above definition, it follows that the contribution from each of the *i*th variables to the total uncertainty in *R* is:

$$\left(\frac{\partial R}{\partial x_i}\,\delta x_i\right) = (R_{x_i+\delta x_i} - R_{x_i}) \tag{17}$$

These terms can be calculated by running the data-reduction program $n + 1$ times, once with the baseline data set (the recorded values of the x_i) and once more for each variable, with the value of that variable increased by its uncertainty interval (and all of the other *x*'s returned to their baseline values). The method is thus one of sequential perturbation, using the main data-reduction program as the calculator.

The process is illustrated in Fig. 5 for calculation of *h* given the heat flux (W/m^2) and two temperatures. The input block shows that the data are accompanied by estimates of their uncertainties. On the first pass, run "0," the baseline value of *h* is calculated: h_0. This is stored as the value of *h* and also for future use in each successive calculation. Next, the program increases the value of *q* by the amount δq and recalculates *h*: h_q. The difference $(h_q - h)$ represents the contribution to the uncertainty in *h* introduced by the uncertainty in *q*. The value of *q* is then reset to its baseline value, and another loop run for T_1 and then for T_2. The contributions are squared, summed, and the square root taken. The uncertainty in *h* is displayed for each value of *h*.

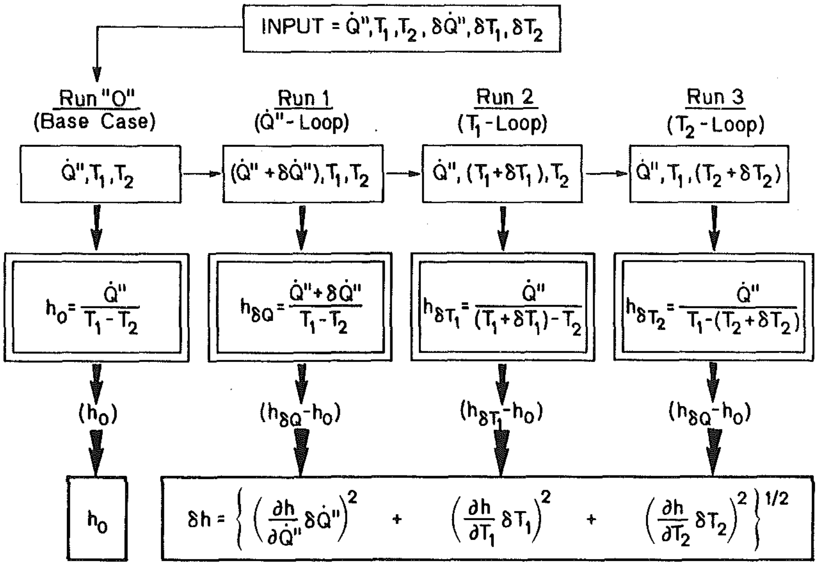

Fig. 5 Illustrating the method of sequential perturbation using the uncertainty intervals directly

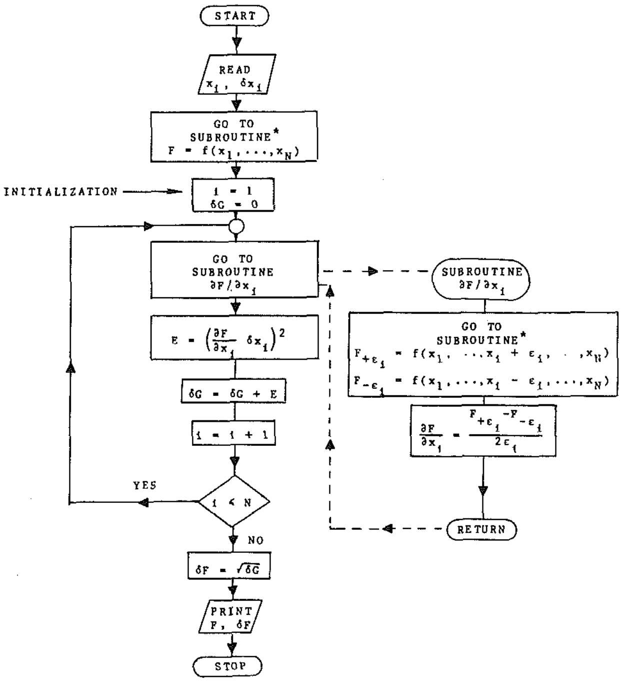

*EXISTING DATA-REDUCTION ROUTINE FOR CALCULATING PARAMETER F.

Fig. 6 A flow diagram for the perturbation method using a small parameter ϵ to find the partial derivatives

This method is far superior to the separate evaluation of uncertainty using a specially derived computer program for that purpose. For one thing, such special programs are uneconomical to write, being tedious in the extreme. For another, the uncertainty program would have to be updated with every change in the main program—a formidable task and one not likely to be done. By using the data-reduction program itself to compute the uncertainties, the program is automatically kept up to date.

Large computers are not necessary; programmable hand calculators will do. Figure 6 shows a flow diagram for a "jitter package" which operates on a TI-59 programmable hand calculator and does the uncertainty analysis for a data-reduction program involving ten variables (Siebers, 1982).

This flow diagram shows a more rigorous process than the one shown in Fig. 5. In Siebers' work, the true value of the partial derivative is estimated using a separate parameter ϵ, whereas in Fig. 5, the value of the uncertainty interval itself was used. Either method is acceptable in most cases.

With the computerized uncertainty analysis so easy, it seems hard to justify not requiring it as an adjunct to every print-out which might be used for design or decision making.

UNCERTAINTY DEFINITION[1]

G. D. Lassahn[2]

The importance of uncertainty analysis is finally becoming widely recognized, thanks mainly to a handful of diligent and dedicated individuals, most of whom are authors of other reports on uncertainty analysis in this volume. There is a natural inclination to feel that the task of developing and promulgating the theory and practice of uncertainty analysis is finished, and that we can now move on to new problems. However, there remains one not very noticeable but very important point to be resolved before uncertainty analysis can be considered a mature discipline. This point is the formal definition of uncertainty.

In order to understand what is needed and why, we must have clearly in mind the difference between (1) the definition of a quantity, (2) the correct numerical value of that quantity in a particular application, (3) the value estimated by measurement or calculation in a particular application, and (4) a qualitative description or an intuitive understanding of the meaning of the quantity. Consider as an example the hydrostatic pressure of a stagnant fluid. This pressure might be defined as the force per area on a surface in contact with the fluid, assuming that force and area are already well defined and understood quantities. After such a definition is agreed on, it implies that there is some correct value of the pressure in any application; without a definition, it does not make sense to talk about a correct value. Various schemes might be proposed to measure the pressure with hardware or to predict it with theory in particular applications; we hope that the estimates resulting from these measurements and predictions will be at least close to the correct value, but we realize that there will usually be differences (errors) and we keep well in mind that there is a difference in principle between the correct value implied by the definition and the estimated value obtained from a measurement. The intuitive understanding of pressure, including for example the difference between pressure and force, might be built solely on a study of the definition but more often relies at least in part on experience and observation of examples. This intuitive understanding is usually more qualitative than quantitative. In any case, the intuitive understanding is not a substitute for the formal definition and should not be confused with a definition.

Sometimes definition, correct value, measured value, and intuitive notions are confused with one another, especially in the developmental stages of a new concept, often unavoidably. One can imagine a tinkerer of long ago building and playing with a widget that responds to what we now understand as pressure. He might show the widget's operation to his friends, who would find it an amusing if useless toy:

"What it is good for?"

"It measures pressure."

"What is pressure."

"Pressure is what the widget measures"

"That's nice. You have a widget that's good for nothing but measuring pressure, and pressure is good for nothing but stimulating your widget."

The next natural step is for the inventor (he used to be a tinkerer) to define pressure in terms of the readings from his widget. But, this still leaves pressure and widget separate and removed from the practical, useful world of the engineer. Pressure and widget will remain useless until the scientist-inventor-tinkerer shows the connection between his new concept and the rest of the world, until he understands and explains and DEFINES pressure in terms of other things that are already understood.

The current status of uncertainty analysis, as presented by the most widely accepted methodology in this country, is much like the tinkerer-inventor stage of the pressure widget. There is a prescribed procedure for calculating the uncertainty (use the widget to measure the pressure), and the uncertainty is not defined except as the result of using the procedure (the pressure is whatever number you get from the widget). This leaves unanswered questions of great practical importance: What does the uncertainty mean? What is it good for? What can I use it for? How can I use it, and what good is it to me, if I don't know what it means? Are there other ways to determine the uncertainty when the prescribed procedure is not applicable? How do I know what other procedures might be acceptable if I don't know what uncertainty is, if uncertainty has not been defined? These questions have obvious analogs in the pressure widget example, and I believe that the concept of uncertainty can be as useful and important and precise as the concept of pressure has become. But, we are not there yet. First, there are qualitative statements of intuitive meaning of uncertainty, but these statements are not a good substitute for a definition and they cannot adequately answer the questions that arise for the serious uncertainty analyst. Secondly, the uncertainty values produced by the popular methodology do not have a consistent, quantitative meaning. (Contrary to the common assumption, they do not necessarily represent either a 95% or a 99% proability interval.) The meanings of the uncertainty values are different in different applications, and no one knows (without a separate analysis) the meaning in any one application. Third, two analyses of the same application can and usually do result in two different values for the uncertainty; this is analogous to two widgets giving different values for the pressure of a single fluid. As long as the uncertainty (or the pressure) is defined to be the result of a procedure (or the widget reading), having two different results for one application is a serious dilemma. On the other hand, if we define the uncertainty in terms of other quantities that we already understand, and we recognize that the prescribed procedure is one imperfect way of obtaining an estimate of the correct value implied by the definition, then different results from different analyses are acceptable and expected.

Thus, even though uncertainty analysis is very important, the popular methodology is not acceptable to the critical, thinking scientific community because of a lack of definition and the resulting lack of meaning of the uncertainty. Defining uncertainty is very easy and would require little or no change in the practical procedures in most applications. Various aspects of defining uncertainty have been discussed in several reports [1-4]. Let us take this final, simple step and make uncertainty analysis a complete, useful discipline.

References

1 Lassahn, G. D., *LOFT Experimental Measurements Uncertainty Analyses, Volume I, Methodology and Summary*, NUREG/CR-0169, EGG-2037, Vol. I, Mar. 1983.

2 Lassahn, G. D., "LOFT Uncertainty Analysis Methodology," ASME Paper 83-HT-107, 21st ASME-AIChE National Heat Transfer Conference, Seattle, Washington, July 24-28, 1983.

3 Lassahn, G. D., "Thermal-Hydraulic Uncertainty Analysis and Measurement Techniques," *Transactions of the American Nuclear Society*, Vol. 44, June 1983, pp. 610-611.

4 Lassahn, G. D., "Requirements for Uncertainty Analysis Standards," Guest Column, *Heat Transfer and Fluid Flow Digest*, Vol. 17, No. 6, June 1984.

---

[1] Presented at the Symposium on Uncertainty Analysis, Winter Annual Meeting, Boston, Mass., November 13-18, 1983. Manuscript received at ASME Headquarters, March 20, 1985.

[2] EG&G Idaho, Inc., Idaho Falls, ID 83415

Discussion of Symposium on Uncertainty Analysis

Edited by T. Heidrick[1]

Question from the Audience

If you were the editor of the Journal of Fluids Engineering, what would you demand regarding an uncertainty analysis?

All panelists were in agreement that some kind of an uncertainty analysis should be required. Individual other comments were:

R. Abernethy:

I would require estimates of precision, bias, and sample size (i.e., is it a small sample?)

R. J. Moffat:

I would like to see a large (> 20) set of initial repeat tests as a baseline check and demonstration of good precision.

S. Wehofer:

First, I think that any properly qualified uncertainty measurement information is preferable to no information. At the other end of the spectrum, I would ask for an estimate of the following features: measurement range, level of the bias errors, level of the precision errors, the sample size, and a reference to the methodology and tests used to estimate the error levels.

Comment

An appeal was given by the panel and audience for instrument vendors to provide uncertainty data with any of their instruments.

Question from the Audience

Do you think that there's a single uncertainty procedure that will handle the analysis of all types of experiments?

R. B. Abernethy:

The new ASME/ANSI standards now being printed should cover all cases. We have good experience over two decades applying this method to all types of experiments.

R. J. Moffat:

I'm concerned primarily with single-sample type experiments and don't require many of the features of the ASME procedures. I need only a few specific parts.

For "once off" experiments that can't be repeated, I recommend the use of the methods outlined by R. B. Abernethy. However, if a series of tests is to be done on the same test rig, I would recommend that a series of about 30 repeated tests be initially done to establish the repeatability statistics for the apparatus. Thirty tests should be sufficient (based on a Student's t distribution), so long as the range of the test matrix for subsequent experiments does not change completely.

S. Wehofer:

At the AEDC Engine Test Facility we use the same measurement uncertainty methodology for turbine engine tests, rocket tests, and research experiments. The type of checks used to identify and quantify error sources of each of these tests varies, of course, depending on the available data base and the particular measurement process.

G. D. Lassahn:

I am also primarily interested in single-sample data, and hence methods requiring averages are not applicable. No method is totally satisfactory, since most data have generally questionable distributions. I believe ones needs look on uncertainty value and a statement of the meaning of uncertainty in publishing experimental results.

---

[1] Alberta Research Council, Edmonton, Alberta, Canada.

1983 Symposium on Uncertainty Analysis Closure

S. J. Kline
Professor of Mechanical Engineering,
Stanford University,
Stanford, CA 94305
Fellow ASME

This symposium contains more comprehensive presentations and discussions of uncertainty procedures than has previously been available. Since these materials extend our understanding in several ways, it is important to recap the results and summarize appropriate conclusions. In drawing these conclusions I will also draw on remarks by Ted Heidrick and Hugh Coleman in the correspondence concerning the Symposium.

When I wrote the initial paper in the symposium, I set up three categories of experiments as they relate to uncertainty analysis. The presentations and discussions convinced me that a division into four categories was more useful. I have modified the initial paper to reflect this change. A fifth, relatively rare situation is mentioned below. These categories are quite important in understanding what procedure should be used in a given instance, and therefore should play an important role in reaching any conclusions concerning requirements for uncertainty analysis as part of publication standards. Since these categories are newly introduced, the reader may need to refer to the initial paper in the collection to gain understanding of what the categories include.

In the first paper, I indicated that there was a paucity of good text materials. Since then an excellent recent text has come to my attention: It is:

An Introduction to Error Analysis
by John R. Taylor, 1982
Publ: University Science Books,
20 Edgehill Road,
Mill Valley, Ca. 94941

This text can be recommended for any engineer or scientist concerned with learning more about uncertainty analysis.

As a part of the work of the symposium, I also polled the contributors regarding several basic questions. On one point there was strong unamimity of opinion in the responses and in the symposium. It is therefore stated as the first conclusion.

CONCLUSION I

UNCERTAINTY ANALYSIS IS AN ESSENTIAL INGREDIENT IN PLANNING, CONTROLLING AND REPORTING EXPERIMENTS. THE IMPORTANT THING IS THAT A REASONABLE UNCERTAINTY ANALYSIS BE DONE. ALL DIFFERENCES OF OPINION ABOUT APPROPRIATE METHODS ARE SUBSIDIARY TO THIS CONCLUSION.

As pointed out forcibly in the paper by R. J. Moffat in this Symposium, the word PLANNING in Conclusion I needs emphasis. I can do no better in this regard than to quote from a letter to me by Hugh Coleman, who remarks:

> "I agree wholeheartedly with your statement that 'The important thing is that some appropriate uncertainty analysis be done . . . ' " Coleman adds, "All experimentalists should be taught that an uncertainty analysis PERFORMED IN THE PRELIMINARY DESIGN PHASE OF AN EXPERIMENT will often yield results and insights far out of proportion to the relatively small investment of time required for the analysis." (emphasis Coleman's)

It is appropriate to stress this remark as a second conclusion.

CONCLUSION II

IT IS PARTICULARLY IMPORTANT TO USE AN UNCERTAINTY ANALYSIS IN THE PLANNING AND CHECK OUT STAGES OF AN EXPERIMENT!

Since there is no published paper in the collection covering the contribution by Gordon D. Lassahn to the Symposium, it will be useful to indicate what his remarks covered.

Mr. Lassahn has been particularly concerned with defining the meaning or "uncertainty" carefully and with situations where very careful estimates of uncertainties are necessary concerning events of very large impact but very low probability (nuclear applications). In such cases, there is an unusual amount of knowledge needed about the details of the statistical situation, particularly about the tails of the probability distributions. For example, whether or not these tails are symmetric may be of importance. It is very rare that one has enough information to be knowledgable about the tails of the distribution; it requires a really vast amount of careful data to gain such knowledge. Fortunately, most of the time these details are irrelevant to the uncertainty analysis needed. Thus the situations of concern to Mr. Lassahn form what should be considered a fifth class of experiment that occurs relatively rarely, but when it does needs special mathematical considerations. For these reasons Mr. Lassahn has paid particular attention to the underlying mathematical assumptions of the usual forms of uncertainty analysis, and has suggested procedures for study of problems where there is special importance in the tails of the probability distribution or other conditions that violate the usual mathematical assumptions (specifically: Gaussian distribution functions and independence among the variables). Individuals with applications of this type would do well to consult the report by Mr. Lassahn, in LOFT Experimental Measurements Uncertainty Analysis Vol I, EGG-2037, or EGG-M-08983. Write EG&G Idaho, Idaho Falls, Idaho 83415.

The third major point that emerges from the presentations and discussions of this symposium concerns what type of uncertainty analysis is appropriate in given situations. Since its establishment, the JFE has required an uncertainty analysis for all experimental papers that appear in the Journal. The procedure suggested when inquiries were made of the Journal has usually been that owing to Kline and McClintock (reference in first paper). Currently two ASME/ANSI standards suggesting somewhat different procedures are printed, have been adopted by some societies, and are being considered by other national and international societies. (See paper by Abernethy, Benedict and Dowdell). A still different set of procedures has been recently reiterated by Churchill Eisenhart and his co-workers at the US National Bureau of Standards. In addition, recent work by R. J. Moffat (see the

1982 JFE paper) adds onto the Kline-McClintock procedure and clarifies long-standing problems concerning fixed errors and the appropriate uncertainty estimates for various points in time in the development of an experiment. At the time the Kline-McClintock paper was published no other applicable procedure for what they called "single-sample" experiments was known. But now there are several others, and a reconsideration is in order.

For this reason, the Fluids Engineering Division of ASME has established a Committee to study this question. The Committee is chaired by Dr. T. Heidrick. Dr. Heidrick would welcome suggestions from interested workers. His current address is Oil Sands Research Department, Alberta Research Council, 11315-87th Ave., Edmonton, Alberta, T6G 2C2 Canada.

It would be inappropriate for the writer to anticipate the conclusions of Dr. Heidrick's Committee, but several remarks seem appropriate as input for the Committee.

A review of the four types of experiments outlined in the Opening paper, plus the remarks above about a fifth type suggested by the work of Gordon Lassahn (and also the remarks in the discussion) suggest quite strongly that most of the past, sometimes rancorous, debates about what method ought to be used in uncertainty analysis appears to stem from unstated assumptions about the type of experiment being discussed by various workers. For example, the remarks of Eisenhart and co-workers seem appropriate for a calibration experiment type (d) of the first paper. However, these recommendations include no procedure for propagation since calibrations normally measure the desired output. And, unfortunately, these recommendations are stated in a form that make their use for treating the problem of propagation in later experiments difficult or even impossible. The ASME/ANSI proposed standards suggested in the paper by Abernethy, Benedict and Dowdell, appears quite viable for experimental tests of type (b) of the first paper. But there were objections in the discussion from researchers about the use of such a procedure in experiments of type (c) where the kind of information used to estimate bias in the procedure by Abernethy et al. is often not available. The use of the Kline-McClintock procedure and the additions suggested by Moffat are both specifically designed with research experiments containing single-sample element, class (c) of the first paper in mind. They are therefore inappropriate where one intends to gather statistics from many experiments and estimate uncertainty via statistical procedures.

Thus one major point the writer would like to see Dr. Heidrick's committee address is the question of what type of uncertainty analysis ought to be required for specific named types of experiments. It really does appear from this Symposium that much of the arguments of the past have arisen from a failure to make clear implicit assumptions about the type of experiment various workers have had in mind.

There are two other questions, that the writer would like to see Dr. Heidrick's Committee consider with care. First, should the materials on uncertainty sent to the receiver of an experimental paper be the same as those that appear in the final paper? We can probably all agree that a central task of the reviewer is to ascertain, insofar as possible, that the data given do in fact represent what the author intends them to be. A detailed uncertainty is particularly useful for such a determination. On the other hand, a detailed uncertainty analysis will usually be too long for a published article, and most readers only need to see the uncertainty bands on the data. Thus the use of different materials for the reviewer from those of the published paper might well be worth consideration.

Second, a point made in the paper by R. J. Moffat needs to be repeated. All parties concerned (the author, the reviewer, and the readers) need an answer to the question, "To what degree do these data really represent the situation intended?" That is, what is a reasonable estimate for the bias uncertainty, and what has been done to make sure the bias is sufficiently small. As Moffat notes, a believable answer to these questions, requires the use of some external standard. There are several types of such standards that one can use: (i) overall checks (for example: continuity, momentum and/or energy); (ii) comparison with an independent experiment of known quality; (iii) the use in at least some places of the test domain of two independent methods to ascertain if they agree to within the expected uncertainties (see the example in Moffat's paper). These elements are not sufficiently emphasized in the current suggestions for methodology in the writer's view. Full understanding and use of such procedures needs to be informed by the idea of levels of replication developed by Moffat.

In summary, the symposium presentations and discussions suggest that different types of experiments need different procedures for uncertainty analysis and that sufficient knowledge has been developed about the various types to make timely a reconsideration of the standards of uncertainty analysis required for publication in JFE.

S. M. Fraser
Senior Lecturer.

C. Carey
Lecturer.

Department of Thermodynamics and
Fluid Mechanics,
University of Strathclyde,
Glasgow, U.K.

G. Wilson
National Engineering Laboratory,
East Kilbride, Glasgow, U.K.

Behavior of Air in the Rotor of a Model Mixed-Flow Pump Operating at Peak Efficiency

The behavior of air in a model of a mixed-flow bowl pump has been investigated using a laser-Doppler anemometer. Velocity measurements were obtained at a number of sections within, upstream and downstream of the rotor. All three components of velocity were determined, and related to the rotating frame of reference using a computerised data acquisition method. The results provide useful data relevant to some complex problems of incompressible flow in turbomachines, including annular casing boundary layer growth.

Introduction

The need for manufacturers to improve the performance and efficiency of pumps is greater than ever, because of global financial and energy problems, and the highly competitive nature of the pump industry. Techniques for hydrodynamic design of pumps have reached a high level of sophistication, and the use of computer aided methods is becoming commonplace. Unfortunately, it is not easy to assess the accuracy of predictions of fluid behavior in and near to rotating components, because the amount of experimental data available for specific types of machine is limited. Indeed, some of the more complex phenomena which occur in rotor flows are not well understood even qualitatively.

Laser-Doppler anemometry (LDA) provides an accurate method of velocity measurement, which, owing to its nonintrusive and rapidly responsive nature, is well suited to a study of the flow within moving blade rows. This paper describes the results of a detailed investigation of the velocity distribution through the impeller of a model mixed-flow pump. The flow survey was performed using a conventional two colour LDA system, connected to a special data acquisition system. The model was operated at the flow rate giving maximum total efficiency, and three-dimensional velocities obtained relative to the rotating blade positions at a large number of axial and radial stations.

The results show the generally inviscid behavior of the fluid in the mainstream flow; they also reveal some interesting features of the flow phenomena occurring close to the annular casing endwall related to the development of the boundary layer. As quantitative data from the latter region are particularly rare, the results should be of great interest to researchers working on advanced numerical methods for turbomachinery flows. Of course, it is impossible to present all of the measurements in the limited space available here; however, a complete set of data will be produced in due course, including a full description of the research facility and the geometrical coordinates of the model [1, 2].

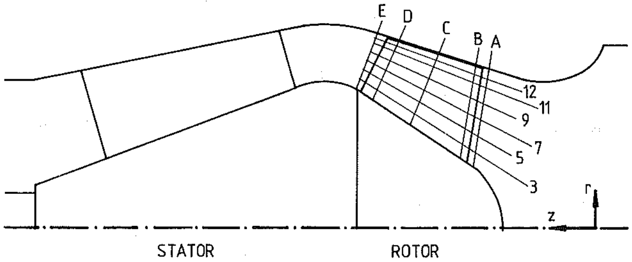

Fig. 1 Section through model pump in meridional plane, showing measuring station positions

Research Facility

The flow survey was conducted in a model of a mixed-flow bowl pump of specific speed 2.5 (SI units), working in air. The machine has five rotor blades mounted on a conical hub, and nine stator blades in a diffuser which brings the diagonally outward flow from the impeller back to the axial direction. The maximum internal diameter of the model is 536mm, and the rotor blade chord length approximately 280mm at mid-span. During the course of experimental work described in this paper, the model was operated at the best efficiency point of its performance characteristic, with a rotor speed of 1200rpm and volume flow rate of 1.01 cu.m/s. The corresponding flow and head coefficients were $\phi = 0.344$ and $\psi = 0.282$, respectively, and the total efficiency of the model 87 percent. The Reynolds Number based on blade chord length was 8×10^5.

The model is fitted with a very large transparent window to provide optical access for the LDA from rotor inlet to stator outlet. The window was moulded in two sections to conform to the rotor and stator casing profiles, from 2.5mm thick Perspex. The width of the stator window in the circumferential direction is a 90 degree arc, covering two full

---

Contributed by the Fluids Engineering Division of THE AMERICAN SOCIETY OF MECHANICAL ENGINEERS and presented at the Joint Applied Mechanics Bioengineering, and Fluids Engineering Conference, Albuquerque, New Mex., June 24-26, 1985. Manuscript received by the Fluids Engineering Division, December 13, 1983. Paper No. 85-FE-7.

stator blade pitches. The rotor window has a width of only 20 degrees, as the space between the two blade rows is so large that there are no measurable circumferential variations in the flow field in the rotor casing induced by the stator. The stator window assembly is easily removable, so that the internal surfaces of the windows can be cleaned if contamination by deposition of LDA seeding particles degrades the optical signal quality. This problem occurs only after several hours of operation with direct injection of oil droplets into the annular casing boundary layer.

The velocity survey grid is shown in Fig. 1. The grid consists of six streamwise grid lines (SGLs) and five transverse grid lines (TGLs) in a meridional plane, the intersections of which form the measuring station positions. Each SGL is described by R = constant.

LDA System

The LDA is a DISA two-channel three-beam colour separation system, with confocal backscatter collection optics. The laser light source is a 2W Spectra-Physics 165 argon-ion laser operating at 488nm (blue) and 514.5nm (green). The front lens has a focal length of 310mm, and forms an optical probe volume of length 1.4mm by diameter 80μm, based on the $1/e^2$ intensity points. The probe volume contains orthogonal sets of blue and green fringes (approximate spacing 4.2μm and 4.7μm, respectively), used to measure both components of velocity normal to the optical axis of the instrument. A Bragg Cell is used to apply frequency shift to the mixed-colour beam; the effective velocity of blue and green fringes can be independently varied using separate photomultiplier signal mixers.

The complete optical system is mounted on a traversing table allowing movement in a horizontal plane in two perpendicular directions, one of which is parallel to the model shaft axis (i.e., z-direction). The table itself can be traversed vertically on its support column. The relationship between the (z, r) coordinate system of the model, and the (z, d, h) cartesian coordinate system of the traversing mechanism is shown in Fig. 2. Since the optical axis of the LDA is always horizontal and normal to the vertical plane of the shaft axis, displacing the optical axis from the horizontal plane of the model shaft by distance h is equivalent to inclining the optical axis to the radial direction in the model at angle ξ (= arcsin(h/r)). This is helpful in minimizing the size of the region in which velocity measurements are impossible because of obstruction of the laser beams by the twist of the rotor blades. The inclination of the optical axis to the radial direction also allows the radial velocity component to be determined, as explained below. The model is mounted in a duct between two spigoted flanges, and the complete casing can be rotated about the shaft axis using a screw jack, allowing the position of the optical window in the rotor casing to be adjusted in accordance with the vertical position of the optical axis.

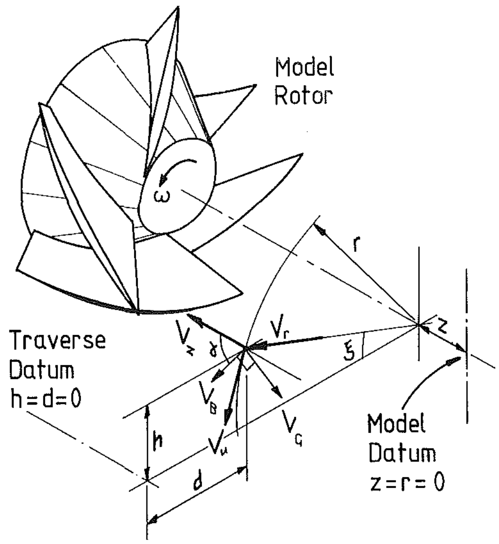

Fig. 2 Relationship between model and traverse coordinate systems, and measured velocity components

Data Acquisition System

When a seeding particle crosses the probe volume fringes, the signal frequencies from blue and green channels are measured by a pair of DISA counter-type processors. The digital output lines from the counters are connected to a computer controlled data acquisition system. The data acquisition hardware was described for a single-channel LDA application in reference [3]. The main components of the

Nomenclature

A-E = transverse grid lines
d = traversing system coordinate
h = vertical displacement of LDA optical axis
N = pump specific speed
n = number of individual velocity measurements in sample
r = radius
R = distance from the hub in the meridional plane, measured along the normal to the annular passage centerline (SGL7), expressed as a fraction of the distance from hub to casing
s = blade pitch, degrees
Q = volume flow rate
SGL = streamwise grid line
TGL = transverse grid line
U_t = blade trailing edge velocity, mid radius
V = mean velocity
$|\underline{V}|$ = total velocity, = $(V_z^2 + V_u^2 + V_r^2)^{1/2}$
V' = rms velocity
W_u = relative tangential velocity
x = tangential co-ordinate relative to blade centerline; negative values, suction side of blade
X = tangential location, x/s
Z = distance from rotor inlet measured in meridional plane along SGL, expressed as a fraction of the distance from rotor inlet ot outlet
z = axial coordinate
α = absolute flow angle, = arctan(V_p/V_u)
β = relative flow angle, = arctan(V_p/W_u)
β' = blade angle
∂ = flow deviation, = $(\beta_t' - \bar{\beta}_E)$
ϵ = flow deflection, = $(\bar{\beta}_E - \bar{\beta}_A)$
ζ = flow incidence, = $(\beta_i - \bar{\beta}_A)$
δ = measured velocity component orientation angle with z-direction
ξ = angle between LDA optical axis and radial direction
ϕ = flow coefficient
ψ = head coefficient
ω = rotor angular velocity

Subscripts

A,E = transverse grid lines upstream and downstream of rotor
B,G = components measured by blue and green LDA channels
l = blade leading edge
n = component normal to SGL
p = component parallel to SGL
r = radial component
t = blade trailing edge
u = tangential component
z = axial component

Superscript

$\bar{\ }$ = denotes quantity averaged tangentially over blade pitch

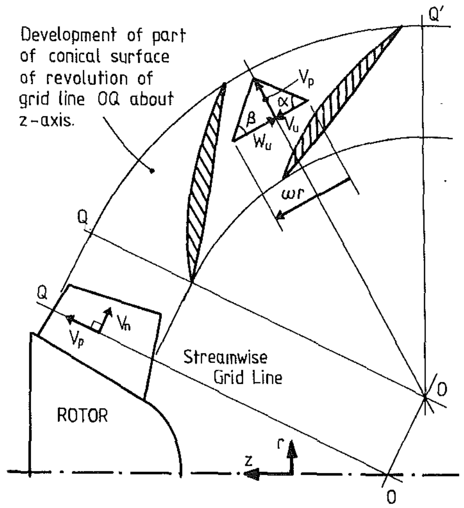

Fig. 3 Plotted velocity components, V_p, V_n, and W_u

system are the DISA Buffer Interface, a dedicated DEC MINC-11 minicomputer, and an optical encoder on the rotor shaft of the model pump. Before the start of a test run, the rotor is set to a datum position indicated by an index mark on the shaft. The Buffer Interface then receives an instruction from the computer to begin counting signal pulses from the encoder. Thus, after the machine has been started for a series of measurements, the Buffer Interface is able to determine when the rotor returns to its datum position. The Buffer Interface measures the time intervals between successive Doppler bursts and the occurence of this position in each revolution; from this information the computer calculates the relative shaft position associated with each burst. The time interval measurements are made with a high precision 10MHz clock; however, small inaccuracies of the rotor position measurement are introduced by the truncation error in the 12-bit floating-point digital representation of each time interval which is used in the Buffer Interface. The positional error is estimated to be less than 1 percent of the blade pitch. Whenever burst frequency measurements are made on both channels from a single particle, the computer records the two frequencies together with the angular position of the shaft rotor at the time of measurement.

Although an approximate (integer) analysis is performed on the data in real-time to generate a graphical display on the computer terminal, all of the collected data are stored on disk in batches, for full analysis after the run is complete. This procedure maximizes the efficiency of data collection and allows flexibility of data analysis methods.

Data Analysis

The data presented in this paper were analyzed using a data reduction program which operates as follows. The rotor blade pitch is divided into forty equiangular sectors. The burst data obtained at a single measurement station are read back from disk and the data sorted into the sectors according to rotor position. Within each sector, the arithmetic mean and standard deviation of the burst frequency observations from the two channels are calculated. Hence, the mean and root-mean-square (rms) velocity components normal to the fringes are determined. For the results presented in this paper the average number of two-channel observations obtained in each sector was 1000, and the minimum number approximately 400.

Many of the less well understood flow phenomena encountered in turbomachinery are three-dimensional in nature, so it is desirable to obtain estimates of all three velocity components in a flow survey of this type. This is especially important within the complex geometry of a mixed-flow machine, where the primary flow direction at any point is not clearly defined. Unfortunately, it is impossible to measure the radial component directly within the blade passages, because the LDA system can only detect velocities normal to its optical axis. Therefore an indirect method is used, as follows. When the optical axis of the LDA system is inclined at angle ξ to the radial direction using the traversing mechanism described above, the detected velocity components are V_B and V_a, shown in Fig. 2. δ is the angle between the normal to the blue fringes and the z-direction. The measured velocity components on the blue and green channels are given by the pair of equations

$$V_B = V_z\cos\delta + V_u\cos\xi\sin\delta - V_r\sin\xi\sin\delta$$

$$V_a = -V_z\sin\delta + V_u\cos\xi\cos\delta - V_r\sin\xi\cos\delta$$

Measurements are taken at each station with the optical axis at two different vertical displacements, producing two pairs of equations which are solved to give V_z, V_u, and V_r. One equation is redundant, allowing independent estimates of V_z to be obtained from each of the pairs, and used as a check on the repeatability of the data.

Because the meridional flow direction in the rotor is diagonally outward, the results are resolved into p, n, and u components (defined in Fig. 3) for presentation in this paper. The p and n directions lie in the meridional plane, and are, respectively, parallel and normal to the SGL on which the measuring station lies. Relative tangential velocity components were deduced from the measurements obtained in the stationary frame of reference, according to the expression $W_u = \omega r - V_u$.

Sources of Error

The sources of error associated with velocity measurement by LDA have been widely discussed in the literature in recent years. The error in measurement of the beam angles needed for conversion of fringe-crossing frequencies to velocities is within ±0.5 percent. The precision of measurement of a single frequency by the counter processor is to within 1 percent. However, the signal generated by the transit of a particle through the probe volume is subject to the influence of random optical and electronic noise. In a sample of frequency observations from a given sector, the individual values fluctuate due to this signal noise and also due to differences in the velocity of the seeding particles. Assuming the particles follow the fluid flow precisely, the differences in their velocities are caused by turbulence, large scale unsteadiness (including the effects of variations in the rotor shaft speed), and velocity gradients within the dimensions of the probe volume and sector. These factors all contribute to the standard deviation of the measurements in the sample. The uncertainty at 20:1 odds in the estimate of mean velocity for a sample of n observations is $\pm 2V'/(V\sqrt{n})$.

It is impossible to distinguish between the various contributions to the standard deviation, so it is not accurate to describe this quantity as the turbulent velocity component. However, in the measurements described here, the rotor speed was held constant to within ±2rpm and the LDA signal-to-noise ratio was high (typically better than 10:1). The distributions of the measured rms velocities are therefore presented as estimates of the overall unsteadiness of the flow.

Velocity samples produced by LDA counter systems are subject to statistical bias, which can be a significant source of error. Bias occurs because the probability of a seeding particle passing through the probe volume and giving rise to a valid frequency measurement is not independent of the fluid velocity in the probe volume; therefore, the arithmetic average of the individual measurements within the sample can yield a value different from the true time-averaged mean

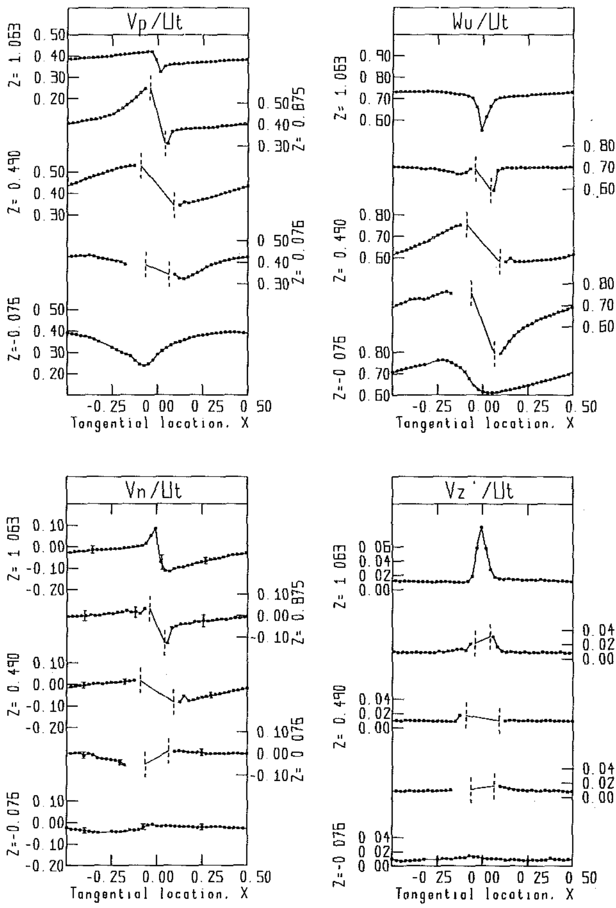

Fig. 4 Blade-to-blade distributions of velocity on SGL7, $R = 0.500$

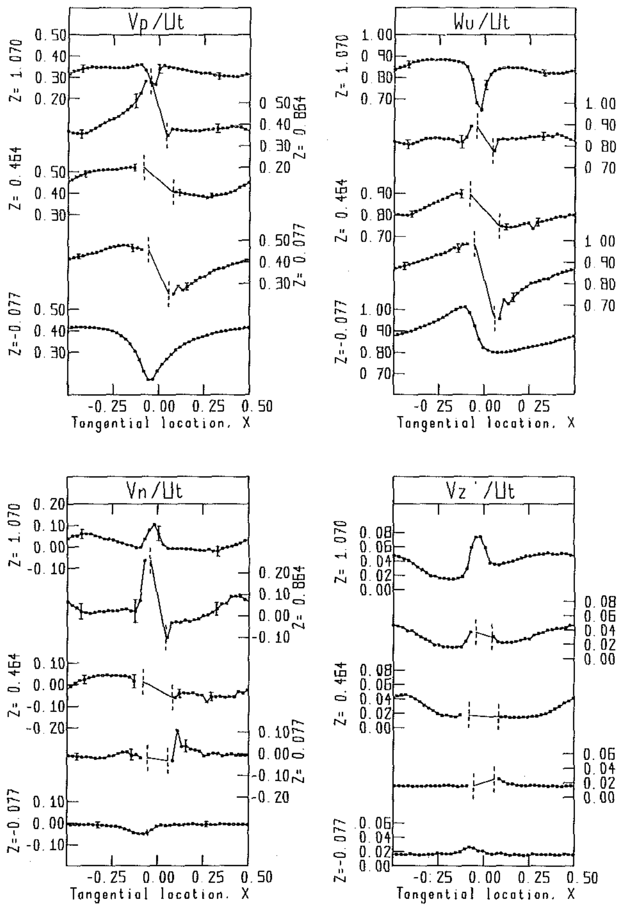

Fig. 6 Blade-to-blade distributions of velocity on SGL11, $R = 0.833$

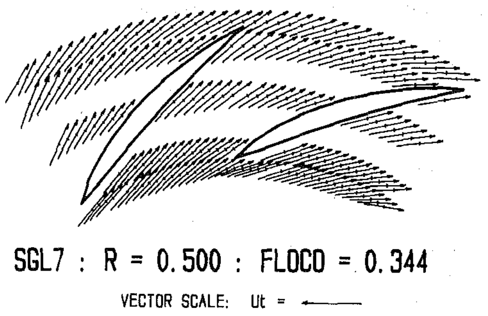

Fig. 5 Relative velocity vectors on development of conical surface of revolution of SGL7, $R = 0.500$

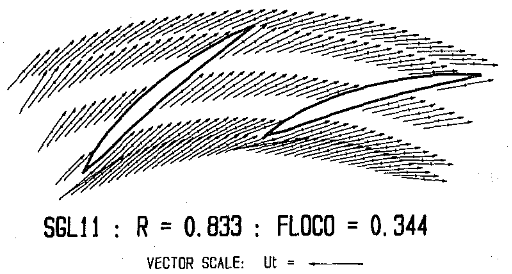

Fig. 7 Relative velocity vectors on development of conical surface of revolution of SGL11, $R = 0.833$

velocity, depending on the data-processing and sampling methods employed [4, 5].

A number of factors which affect the biasing problem have been discussed in the literature. In the data presented here, the measured values of the fluctuating velocity components were small; typically $V'/|\underline{V}| = 0.04$ in the mainstream flow, with a maximum value of $V'/|\underline{V}| = 0.15$ in mixing regions and wakes. For fluctuations of this order, the maximum errors in the arithmetic mean of a sample due to velocity bias [6] should be about 0.2 and 2 percent, respectively. Directional bias [6], comparator tolerance bias [7] and signal amplitude bias [8] are believed to be insignificant, not only because of the low level of the velocity fluctuations, but also because of the careful use made of frequency shift, which the quoted references have shown to be useful in minimising these effects.

The dynamic behavior of light-scattering particles in turbomachinery flows is important because of the tendency of the particles to be centrifugally separated from the flow. In this work, the flow was artificially seeded with 2μm diameter oil droplets from a blast atomiser. Order of magnitude calculations using Stokes Law [9] give a terminal radial velocity of these droplets relative to the air of 0.1 percent of their tangential velocity. Problems encountered in high speed turbomachines concerning particle relaxation times [10] are not important here. Thus, it seems likely that differences in velocity between seeding particles and air are not a major source of error.

The positional accuracy of the probe volume is important because of the need to take two sets of measurements at each station. The effect of refraction of the laser beams by the optical window in the casing of the model is therefore taken into consideration. The paths of the beams through the window are calculated by vector algebra methods using a computer program which takes as input the refractive index and geometry of the window material, the measuring station coordinates, and the laser beam angles. Hence, the true position of the probe volume (beam intersection) is calculated, and using an iterative procedure, the necessary traverse coordinates are obtained. Therefore, the only error in setting the station position is due to imprecision in the traversing mechanism itself, estimated to be within ± 0.2mm in each direction.

Estimates of the uncertainty in the plotted mean velocity components are shown as error bars on the graphs of results described below. The spanwise component, V_n, is subject to greater uncertainty than the other components, because of the effect of small values of ξ (typically 30 degrees or less) in error propogation from the measured to plotted components. The maximum usable values of ξ are restricted by the blade geometry.

As a check on the overall accuracy of the data, the measured velocity distributions were numerically integrated over the annular flow area to obtain an estimate of the total volume flow rate across each of the five transverse grid lines (see Fig. 1). The results were as follows: A, $Q = 0.990\text{m}^3/\text{sec}$; B, $Q = 0.971\text{m}^3/\text{s}$; C, $Q = 0.980\text{m}^3/\text{s}$; D, $Q = 1.016\text{m}^3/\text{s}$; E, $Q = 1.025\text{m}^3/\text{s}$. The flow rate was also estimated by measurement of the pressure drop at a calibrated inlet cone upstream of the model, which gave a reading corresponding to a flow rate of $1.010 \pm 0.015\text{m}^3/\text{s}$. The consistency of these results is remarkably high, in view of the limited number of LDA measurement stations (six on each TGL), and the absence of data from the regions close to the casing and hub.

Results – Mainstream Flow

Figure 4 shows, in graphical form, the velocity pattern along SGL7, mid-passage. Each frame contains five curves, representing the pitchwise variation of one component of velocity at the five stations on SGL7. The tangential location, X, is given as a fraction of the circumferential blade pitch. At those stations within the impeller, the central value $X = 0.0$ is at the blade centre, with negative values of X to the low pressure (suction) side of the blade. The blade surfaces are represented by vertical dotted lines. At the station downstream from the impeller ($Z > 1.0$), the value $X = 0.0$ is at a position corresponding to a line extrapolated from the blade trailing edge, at the exit blade angle. At the upstream station ($Z < 0.0$), $X = 0.0$ is similarly defined relative to the blade leading edge, and the inlet angle.

Figure 5 shows part of the same velocity pattern in vector form. Each vector is plotted with its centre at the point of measurement. The vectors are given on a development of the conical surface of revolution of SGL7 about the pump shaft axis. The spanwise component, V_n is therefore not represented.

Averaged across the blade pitch, the inlet and outlet angles of the flow on SGL7 are, with an estimated uncertainty of ± 0.9 deg: $\bar{\alpha}_A = 90.0$ deg (no prerotation of the fluid); $\bar{\beta}_A = 26.7$ deg; blade inlet angle, $\beta_i' = 30.7$ deg; incidence, $\zeta = 4.0$ deg; $\bar{\beta}_E = 28.5$ deg; blade outlet angle, $\beta_t' = 33.4$ deg.; deviation, $\partial = 4.9$ deg; deflection, $\epsilon = 1.8$ deg. The velocity distributions on SGL7 are largely characteristic of inviscid flow, and the axial rms velocity is small ($V_z'/U_t = 0.01$), indicating low levels of turbulence and unsteadiness. The only exception is in the blade wake, which can be seen near the center of the distributions of all velocity components for $Z > 1.0$. The wake is formed at the trailing edge, where the two blade surface boundary layers merge and interact. Unfortunately, these boundary layers were too thin to be resolved within the rotor.

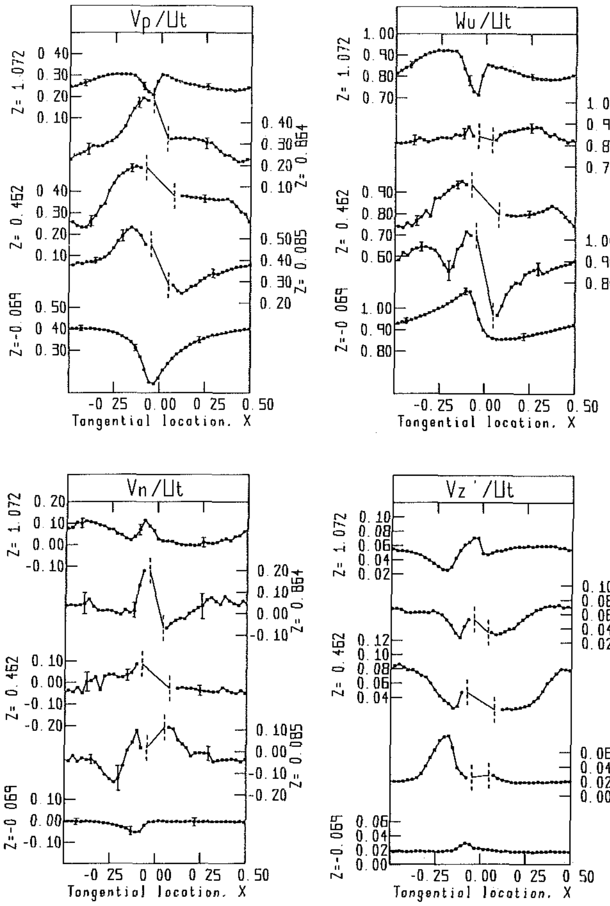

Fig. 8 Blade-to-blade distributions of velocity on SGL12, $R = 0.917$

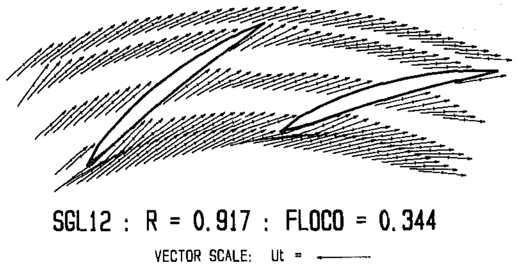

Fig. 9 Relative velocity vectors on development of conical surface of revolution of SGL12, $R = 0.917$

The results on SGL7 were typical of those obtained outside the casing endwall region. Because of the similarity between the measured velocity distributions, and the limited space available here, no data are presented from SGLs 3, 5, and 9.

Outlet Flow. Upstream of the rotor ($Z = -0.076$), large tangential variations of V_p and W_u can be seen in Fig. 4. This distortion of the inlet flow is produced by flow turning around the leading edge; the corresponding variations in absolute flow angle α are from 76 to 103 degrees, and in relative flow angle β from 18 to 30 degrees.

Flow Within Rotor. At $Z = 0.76$, twisting of the blades made measurements close to the suction surface impossible on SGL7, because the laser beams were shadowed by the blade tip; therefore the velocity distributions shown for this station do not extend closer to the blade surface than $X = -0.18$. Inviscid flow turning effects are mainly responsible for the tangential variations in the distributions of V_p and W_u; the accuracy with which the measured velocities follow the blade surfaces can be seen in the vector diagram (Fig. 5). The almost linear distributions of V_n at $Z = 0.490$ and $Z = 0.875$ appear to show the formation of a vortex caused by the through-flow component of the relative eddy [11], with positive spanwise velocities in the suction side of the blade passage and negative values on the pressure side.

Outlet Flow. Downstream of the rotor ($Z = 1.063$), the blade wake is clearly visible in the distributions of all components of velocity in Fig. 4. The spanwise velocities are particularly interesting. The through-flow vortex observed in the blade passage produces a trailing vortex with flow towards the hub to the pressure side of the wake. Additionally, in the suction side of the wake itself, a large positive value of V_n results from an imbalance in the radial pressure gradient and centrifugal forces. The spanwise mixing and high vorticity generated by these flows are influential in the transport, decay, and dissipation of the wake.

Results – Casing Region

Figures 6 and 8 describe the flow along SGLs 11 and 12, at $R = 0.833$ and $R = 0.917$, respectively. The graphs are complemented by the vector diagrams of Figs. 7 and 9. In contrast to the results from SGL7 described above, the velocity field in the casing region is very complicated. The complexity arises from the development and interactions of the annular casing boundary layer, the blade surface boundary layers and associated secondary flows, the rotor tip clearance leakage, and other blade tip effects. These phenomena originate very close to the casing, in a region where direct measurements were inhibited by laser "flare" from the Perspex window. However, spanwise mixing and propogation of turbulent, three-dimensional, viscous fluid behavior produce some very unusual velocity distributions on SGLs 11 and 12.

Averaged across the blade pitch, the inlet and outlet angles of the flow on SGL11 are, with an estimated uncertainty of ±1.6 deg: $\bar{\alpha}_A = 90.0$ deg (no pre-rotation of the fluid); $\bar{\beta}_A = 21.9$ deg; blade inlet angle, $\beta_l = 28.9$ deg; incidence, $\zeta = 9.1$ deg, $\bar{B}_E = 17.8$ deg; blade outlet angle, $\beta_l' = 29.0$ deg; incidence, $\zeta = 7.1$ deg; $\bar{\beta}_E = 21.5$ deg; blade outlet angle, $\beta_l' = 28.6$ deg; deviation, $\partial = 7.1$ deg; deflection, $\epsilon = 0.4$ deg. The corresponding figures for SGL12 are: $\bar{\alpha}_A = 90.0$ deg (no prerotation of the fluid); $\bar{\beta}_A = 19.8$ deg; blade inlet angle, $\beta_l' = 28.9$ deg; incidence, $\zeta = 9.1$ deg; $\bar{\beta}_E = 17.8$ deg; blade outlet angle, $\beta_l' = 27.6$ deg; deviation, $\partial = 9.8$ deg; deflection, $\epsilon = -2.0$ deg.

Inlet Flow. The velocity distributions at the stations upstream of the rotor (lowest curve in each frame), are of similar form to those obtained on SGL7, but the distortion of the flow field around the blade leading edge is greater on SGLs 11 and 12 because the angle of incidence of the flow increases towards the blade tip. The variations in relative flow angle across the pitch on SGL12 at $Z = -0.69$ are from $\beta = 8$ to $\beta = 23$ degrees. However, the circumferentially averaged absolute tangential velocity, $\bar{V}_u$, is zero, indicating no prerotation of the flow. The unsteady component of the flow is small, $V_z'/U_t = 0.02$ on SGL12. It appears that the annular casing boundary layer is too thin to include SGL12 in the region upstream of the rotor; this is to be expected as the inlet to the model has the form of a bell-mouth contraction.

Flow Within Rotor. The velocity distributions on SGL12 at $Z = 0.085$ (Fig. 8) have very interesting profiles, quite unlike those obtained on SGLs7 and 11. In the suction side of the passage the plotted components of velocity show the first signs of the influence of turbulent viscous effects. Centered at $X = -0.23$, there is a large peak in the unsteady component ($V_z'/U_t = 0.08$), a wake-like defect in W_u and a strong spanwise flow away from the casing. These features are probably caused by the tip leakage flow, which issues as a jet from the suction side of the clearance gap and produces a vortex close to the suction surface of the blade in the tip region. The tip clearance in this model is 1.1mm, approximately one percent of the blade span at mid-chord. The peak in V_z', caused by mixing of the leakage jet with the mainstream flow, is 10 mm from the casing wall and at a tangential distance of 40 mm from the suction surface.

Close to mid-chord, at $Z = 0.462$ on SGL12, the velocity distributions are dominated by the growth of the mixing region described above. Although the tip leakage vortex is less clearly identifiable in the V_n distribution, there is a broad peak in the unsteady component $V_z'/U_t = 0.09$, near the center of the blade-to-blade passage. The mixing processes cause loss of fluid momentum, creating large, wake-like defects in V_p and W_u centered at $X = -0.42$; the pressure side edge of the wake is sharply defined at $X = 0.35$. The effect of the wake on the relative flow direction is clearly seen in Fig. 9, near the center of the blade passage. The apparent movement of this turbulent region across the blade pitch away from the suction side of the blade (where it was observed near the rotor inlet), is due to the relative motion of the casing wall. It is possible that secondary flows within the rotor blade surface boundary layers are deflected towards the center of the blade passage by the casing wall and contribute to the mixing; however, these layers are very thin, and it seems likely that the clearance flow is the dominant feature. In the spanwise direction, the mixing region extends as far as SGL11; there is a broad peak in the distribution of V_z' at $Z = 0.464$ in Fig. 6, although the mean velocity components are unaffected.

Continuing growth of the mixing region on SGL12 can be seen at $Z = 0.864$. The V_z' profile has the form of a plateau, with a constant value of $V_z'/U_t = 0.07$ from $X = 0.25$ to $X = -0.2$. Close to the suction surface there is a narrow pocket of relatively low unsteadiness, although there are indications that the blade surface boundary layer and the mid-passage mixing region are growing toward each other. The wake-like defects in the profiles of V_p and W_u are wider; the minimum value of V_p is at $X = 0.45$, showing further relative motion of the mixing region towards the pressure surface. The pressure side edge of the velocity defect is much less clearly defined than at $Z = 0.464$. The increased size of the mixing region can be seen in the velocity vector diagram (Fig. 9). The results from SGL11 at $Z = 0.864$ (Fig. 6) also contain small defects in the mid-passage profiles of V_p and W_u, because of the spanwise growth of the mixing region.

An interesting feature of the flow is the spanwise movement of fluid towards the casing seen in the V_n component on SGL11 and SGL12 at $Z = 0.864$. Close inspection of the data shows, however, that near the pressure surface V_n is negative, showing spanwise movement away from the casing. These results imply that a large vortex has been formed against the pressure surface, probably caused by roll-up of the casing boundary layer into a "scraping vortex" [12]. Although the casing boundary layer is thin in the region adjacent to the pressure surface, the accumulation of slow moving fluid against the pressure tip forces the fluid outside the layer away from the casing. The residue of the tip leakage vortex is far enough from the suction surface to interact with the scraping vortex; this may account for the strength of the spanwise flow in mid-passage.

Outlet Flow. The velocity distributions downstream of the rotor, at $Z = 1.072$ on SGL12 and $Z = 1.070$ on SGL11, show the continuing influence of the mid-passage mixing region, and the presence of the blade wake. In view of the highly asymmetric V_p profiles seen at $Z = 0.864$, the variations in this component across the blade pitch are surprisingly small; however, the deflects in the V_p and W_u

profiles associated with the mid-passage mixing region are still clearly visible. On SGL12, the low pressure side of the blade wake is approximately twice as thick as the high pressure side, because of the greater boundary layer thickness on the suction surface of the blade, but on SGL11, the wake is more symmetrical, with a width of approximately 12 percent of the blade pitch. Outside the blade wake, the relative flow angle β is almost constant across the pitch. On both SGL11 and SGL12, the spanwise component, V_n, shows flow toward the casing in the blade wake, and at the centre of the blade-to-blade passage.

The continuing growth of the mid-passage mixing region is shown most clearly in the unsteady velocity component. On SGL12 the "plateau" in the V_z' profile observed at $Z = 0.864$ moves further from the suction side and merges with the pressure side of the wake by $Z = 1.072$. It is presumed that the growth of the scraping vortex described above is a contributory factor in this process.

Discussion

The behavior of fluid in the blade tip region is of considerable importance, as it accounts for a significant fraction of the total losses in the machine. The formation and propogation of the mixing region near the casing wall has the effect of generating turbulence in the flow, causing loss of fluid momentum and a relatively large deviation of the flow at the rotor outlet. Although this process apparently arises from localized phenomena occurring at the blade tip, it is equivalent to rapid growth of the annular casing boundary layer to include SGL11 ($R = 0.833$) by the impeller outlet.

Similar investigations into rotating turbomachinery passage flow phenomena have been performed at Pennsylvania State University by Lakshminarayana and his colleagues, using rotating and stationary hot-wire probes. Their work includes investigations into the flow in a rocket-pump inducer [13], and in an axial-flow compressor rotor [14]. These two machines have wide differences in design characteristics. The former operates at very low flow coefficients, has widely spaced but long blade channels, and as a consequence the boundary layer and mixing regions occupy a large proportion of the total flow area. The compressor, on the other hand, has a large number of blades and relatively thin boundary layers, giving a flow pattern in which the turbulent and viscous effects are important only near to the solid surfaces and in the blade wakes.

The behavior of the fluid in the mixed-flow machine described here shows some similarities to that in the two machines mentioned above. In particular, the formation of a mixing region in mid-pitch near to the casing wall is a feature common to all three machines. In the measurements given here, the blade surface boundary layers are very thin (and the secondary flow volumes within them presumably small), while the tip clearance vortex is established close to the impeller inlet. It therefore seems likely that most of the mixing and boundary layer growth is precipitated by the leakage vortex. Near the rotor outlet, however, roll-up of the casing boundary layer into a scraping vortex may contribute to the process. In the rocket-pump of [13] the blade surface boundary layers are seen to be of greater importance and the mixing occurs at a greater distance from the casing wall.

Conclusions

A conventional two-component laser-Doppler anemometer has been used to obtain an accurate map of the three-dimensional velocity field in the rotating passages of a mixed-flow rotor. Although the regions very close to the hub and casing walls could not be investigated because of the low signal-to-noise ratio caused by laser "flare," the range of measurements extended near enough to the casing wall to reveal important features relating to the growth of the casing wall boundary layer. The data should be of help in developing and testing advanced numerical flow models.

The mainstream flow in the rotor passages is largely inviscid in behavior. A through-flow vortex fills the blade-to-blade passage by the impeller outlet, but this is a fairly weak phenomenon, the velocity components in the spanwise direction remaining small. In this region, the blade surface boundary layers are very thin, resulting in the formation of small, narrow wakes downstream of the blades.

The flow in the casing region is much more complex. Although the casing boundary layer is thin at inlet to the rotor, turbulence, viscosity and three-dimensional effects assume increasing importance as the flow progresses through the machine. The results indicate the formation of a strong vortex against the suction surface of the blade near the blade tip, probably caused by the clearance leakage flow. The vortex migrates towards the blade pressure surface to create a large region of mixing against the casing wall at mid-chord, near the centre of the blade-to-blade passage. The boundary layer secondary flows may also contribute to the intensity of the mixing. This process is equivalent to a rapid growth of the casing boundary layer, blocking the flow passage, and giving rise to a very unusual circumferential distribution of meridional velocity component. Near the outlet of the rotor, the fluid in the casing boundary layer appears to roll-up against the pressure surface of the blade, forming a scraping vortex which further complicates the pattern of fluid behavior.

Downstream of the impeller, the blade wake within the casing boundary layer is influenced by the effects of the continuing growth of the mixing region.

The experimentally determined velocity distributions were numerically integrated across the annular flow passage at a number of stations, and the inferred flow rates were very close to the nominal flow rate metered by a calibrated inlet cone. This gives a favorable impression of the overall accuracy of the measurement techniques.

Acknowledgments

This work is sponsored by the U.K. Department of Industry, and the paper published with permission of the director of the National Engineering Laboratory. The information contained within the paper is Crown Copyright.

References

1 Carey, C., Fraser, S. M., Rachman, D., and Wilson, G., "Investigations into the Flow of Air in a Model Mixed-Flow Pump by Laser-Doppler Anemometry Part 1: Research Facility and Instrumentation," N.E.L. Report, National Engineering Laboratory, East Kilbride, Glasgow, U.K., in preparation.

2 Carey, C., Fraser, S. M., Rachman, D., and Wilson, G., "Investigations Into the Flow of Air in a Model Mixed-Flow Pump by Laser-Doppler Anemometry Part 2: Velocity Measurements Within Rotor," N.E.L. Report, National Engineering Laboratory, East Kilbride, Glasgow, U.K., in preparation.

3 Caspersen, C., "A Special Data-Processing Method for LDA Signals From Flow Near and Between Rotating Components," *Measurement Methods in Rotating Components of Turbomachines*, ASME, New York, 1980.

4 McLaughlin, D. K., and Tiederman, W. G., "Biasing Correction for Individual Realisation of Laser Anemometer Measurements in Turbulent Flows," *Physics of Fluids*, Vol. 16, 1973, p. 2082.

5 Edwards, R. V., and Jensen, A. S., "Particle-Sampling Statistics in Laser Anemometers: Sample-and-Hold Systems and Saturable Systems," *Journal of Fluid Mechanics*, Vol. 133, 1983, pp. 397-411.

6 Bucchave, P., "Biasing Errors in Individual Particle Measurements with the LDA-Counter Signal Processor," *Proceedings of the LDA-Symposium*, Copenhagen, 1975, pp. 258-278.

7 Flack, R. D., "Influence of Turbulence Scales and Structure on Individual Realisation Velocimeter Biases," *Journal of Physics E: Review of Scientific Instruments*, Vol. 15, 1982, pp. 1038-1044.

8 Durao, D. F. G., and Whitelaw, J. H., "Relationship Between Velocity and Signal Quality in Laser Doppler Anemometry," *Journal of Physics E: Review of Scientific Instruments*, Vol. 12, No. 1, 1979, pp. 47-50.

9 Durst, F., Melling, A., and Whitelaw, J. H., *Principles and Practice of Laser Doppler Anemometry*, 2nd Edition, Academic Press, 1981, p. 292.

10 Maxwell, B. R., "Tracer Particle Flow in a Compressor Rotor Passage with Application to LDV," *American Institute of Aeronautics and Astronautics Journal*, Vol. 13, No. 9, Sept. 1975, pp. 1141-1142.

11 Lewis, R. I., and Fairchild, G. W., "Analysis of the Through-Flow Relative Eddy of Mixed-Flow Turbomachines," *International Journal of Mechanical Engineering Science*, Vol. 22, No. 9, 1980, pp. 535-549.

12 Phillips, W. R. C., and Head, M. R., "Flow Visualization in the Tip Region of a Rotating Blade Row," *International Journal of Mechanical Sciences*, Vol. 22, No. 8, 1980, pp. 495-521.

13 Lakshminarayana, B., and Gorton, C. A., "Three-Dimensional Flow Field in Rocket Pump Inducers—Part 2," ASME JOURNAL OF FLUIDS ENGINEERING, Vol. 99, No. 1, 1977, pp. 176-186.

14 Lakshminarayana, B., Pouagare, M., and Davino, R., "Three-Dimensional Flow Field in the Tip Region of a Compressor Rotor Passage—Part 1: Mean Velocity Profiles and Annulus Wall Boundayr Layer," ASME *Journal of Engineering for Power*, Vol. 104, No. 4, Oct. 1982, pp. 760-771.

8 Durao, D. F. G., and Whitelaw, J. H., "Relationship Between Velocity and Signal Quality in Laser Doppler Anemometry," *Journal of Physics E: Review of Scientific Instruments*, Vol. 12, No. 1, 1979, pp. 47-50.

9 Durst, F., Melling, A., and Whitelaw, J. H., *Principles and Practice of Laser Doppler Anemometry*, 2nd Edition, Academic Press, 1981, p. 292.

10 Maxwell, B. R., "Tracer Particle Flow in a Compressor Rotor Passage with Application to LDV," *American Institute of Aeronautics and Astronautics Journal*, Vol. 13, No. 9, Sept. 1975, pp. 1141-1142.

11 Lewis, R. I., and Fairchild, G. W., "Analysis of the Through-Flow Relative Eddy of Mixed-Flow Turbomachines," *International Journal of Mechanical Engineering Science*, Vol. 22, No. 9, 1980, pp. 535-549.

12 Phillips, W. R. C., and Head, M. R., "Flow Visualization in the Tip Region of a Rotating Blade Row," *International Journal of Mechanical Sciences*, Vol. 22, No. 8, 1980, pp. 495-521.

13 Lakshminarayana, B., and Gorton, C. A., "Three-Dimensional Flow Field in Rocket Pump Inducers—Part 2," ASME JOURNAL OF FLUIDS ENGINEERING, Vol. 99, No. 1, 1977, pp. 176-186.

14 Lakshminarayana, B., Pouagare, M., and Davino, R., "Three-Dimensional Flow Field in the Tip Region of a Compressor Rotor Passage—Part 1: Mean Velocity Profiles and Annulus Wall Boundayr Layer," ASME *Journal of Engineering for Power*, Vol. 104, No. 4, Oct. 1982, pp. 760-771.

DISCUSSION

P. Hermann[1]

The authors are to be commended for their valuable addition to the skimpy amount of literature on this subject. They have presented the results of an excellent body of experimental data for a lightly loaded mixed-flow impeller used in pump and blower stages of moderately high specific speeds.

Since the blade loading is relatively low ($\Delta w/w < 0.4$ along mid-span SGL), it is not surprising that an extensive inviscid core dominated the flow pattern. The good guidance of the flow with this low solidity blading (see Figs. 5, 7, and 9) is undoubtedly the result of a good design system.

Although the paper is a very interesting one for the researcher, it will not have a noticeable impact on the design philosophy of pump and blower designs. However, it provides a substantial contribution for modelling loss mechanisms around an inviscid core flow. The tip-leakage-induced loss effects seem to be the predominant source of the hydraulic losses. The detailed reports will document a more detailed picture about these loss mechanisms and will, therefore, be even more helpful in establishing loss models.

It is hoped that the authors will continue their research work into highly loaded mixed-flow stages extending the results of their present investigation.

Authors' Closure

The authors would like to thank Dr. Hermann for his kind words about the paper and express general agreement with the comments contained in his contribution. The suggestion that the facility should be used to investigate the flow in highly-loaded rotors has been made by other parties interested in this research.

One of the difficulties associated with the design of pumps with highly-loaded blades is that of performance at low (off-design) flow rates. Pump manufacturers and their customers recognize the undesirability of machines which have a positively-sloped head-flow characteristic, because there is a possibility of unstable flow in an installation containing such a unit. The model described in the paper was one of a series of moderately-loaded machines designed with this problem in mind. The authors' most recent work has been directed at investigating the fluid behavior at flow coefficients in a positively-sloped portion of its characteristic, and it is intended to report the data which were obtained in due course. The next stage will be to investigate the off-design flow in a second rotor which is to be fitted in the same casing; it is known from previous model tests that the new combination exhibits an overall head characteristic with a continuous negative slope from the best efficiency point down to zero flow. Special attention will be paid to differences in the stall behavior of the two configurations, especially to the way in which separation and spanwise flow interactions develop as the flow coefficient is lowered.

In conclusion, it should be stated that there are no plans to study more highly loaded rotors in the immediate future; however, the intended programme of research described above deals with a strongly related problem. Of course, there is no technical reason why the facility should not be used to investigate more highly loaded rotors when the current programme has been completed.

---

[1] Chief, Turbomachinery Research Mechanical, Sundstrand Aviation Operations, Rockford, IL 61125-7002.

Correlation and Prediction of Rotating Stall Inception by Divergence Method

V. J. Zika
Burlington, Mass. 01803
Mem. ASME

An empirical correlation of rotating stall inception points of elementary compressors (isolated rotors, stages without prerotation, complete single stages, and multi-stage machines with repeating stages), modeled as equivalent diffusers, is presented. From it, two inception criteria for self-induced rotating stall are derived. Compressor blade rows are classified according to a geometric form parameter, $(L/A_\infty)_{cor}$, *into two groups, subcritical and supercritical. The subcritical geometries stall at a constant kinematic area ratio* A_E/A_∞, *in what appears to be a pure rotating stall mode, which occurs before the airfoil stalls. In supercritical geometries, the rotating stall is delayed until it is triggered by the airfoil stall. Thus, for the latter geometries, the airfoil stall and rotating stall are coincident. In contrast to other diffuser-analog methods, the divergence method determines the stall angle and the stalled flow coefficient rather than the stalled pressure rise.*

Introduction

A need for a reliable method of prediction of the compressor stall line is widely recognized by axial compressor specialists and designers. Recently, two new methods have been presented which precalculate, with a varied degree of success, the stalling pressure rise of an axial compressor stage and thus, indirectly, the stall point. A need still exists for a direct method, by means of which the stalled flow rate or stall angle could be predicted outright.

Several methods for the prediction of the inception of rotating stall had been published earlier, by Emmons [1], Nenni and Ludwig [2], and Takata and Nagano [3]. The first two are stability analyses, and the inception of rotating stall (R.S.) can be calculated if the complete compressor blade row characteristics, C_p versus β_1, and β_2 versus β_1, are known. The third one is a nonlinear analysis, by which the R.S. inception is obtainable if X_{ss} (loss coefficient) versus β_1, β_2 versus β_1, and τ (time lag) versus β_1 are known. All three methods then are actually "test analyzers" rather than "predictors," since no procedures are indicated how to calculate the R.S. inception in the absence of the above detailed performance characteristics.

Other analysts locate the inception of R.S. at the maximum of the C_p or ψ characteristic, whether measured or predicted (e.g. [4, 5], and [6]), which stems from the "classical" stability approach. This method, however, fails to distinguish between the stall modes (i.e., between R.S. and "airfoil stall"), presuming that both occur at the same point on the characteristic, which this writer disputes. Still others (e.g. [7 and 8]) use the surface diffusion limits of Lieblein [9] for stall inception. Again, no distinction is made between the possible modes of stall, although Lieblein's criterion applies strictly to airfoil stall.

The recently presented "finite discontinuity" method [10] predicts the inception of rotating stall from cascade geometry alone. It uses a semi-empirical inception criterion, $\cot\beta_i/\cos\lambda = \text{const}$, which is valid for higher solidities. That solution was derived from kinematic similitude. It will be shown later in this paper that the discontinuity criterion is valid, but limited to only some cascade geometries.

Let us return to the most recent "indirect methods" mentioned above. Koch [4] calculates the stalling pressure rise, and Schweitzer et al. [5] calculate the stall margin of the pressure rise from the maximum efficiency point. What is very attractive and common to both these methods is the modeling of the compressor cascade by a diffuser analog, formulated from the diffuser performance maps of Reneau et al. [11]. The present method is also based on the diffuser model, but all three methods use a different dependent variable while all use the same independent variable (normalized length).

In the present analysis the compressor blade passage is modeled as a two-dimensional asymmetric (curved) diffuser with a mitered entry, laid out at the rms radius (Fig. 1). A measure of the total diffusion done in such a "diffuser" is the area expansion ratio from approach to exit, or the "total divergence" (author's nomenclature). The exit area is fixed (in fixed stagger cascades), the inlet area is kinematic and thus variable with the flow rate or the inlet angle. As the inlet angle (and the incidence angle) increases (such progress is shown, from left to right, in Fig. 1), so does the kinematic area ratio, and with it the diffusion done by the blading. When the critical air angle (the stall angle) is reached, the diffusion

---

Contributed by the Fluids Engineering Division and presented as a longer version at the Symposium on Stability, Stall and Surge in Compressors and Pumps at the Winter Annual Meeting, New Orleans, La., December 9-14, 1984, of THE AMERICAN SOCIETY OF MECHANICAL ENGINEERS. Manuscript received by the Fluids Engineering Division, April 29, 1982; revised manuscript received April 2, 1984.

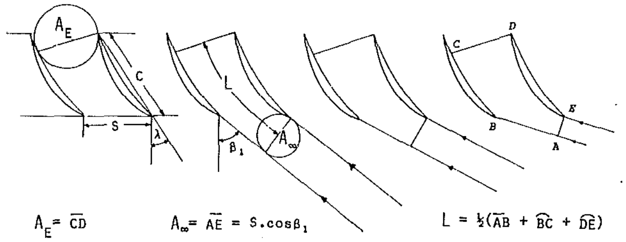

Fig. 1 Cascade layout and description

breaks down because of excessive (area) divergence, the flow becomes unstable and rotating stall commences. The present paper elaborates on these critical divergences which are signaling the inception of rotating stall. The data used for the present correlations are taken from references 2, and 12-25.

Let us pause at this point and discuss the various types of stalls. Apparently (per [4-6]) the multistage axial compressor stages encounter always the rotating stall at the onset of instability (stall line). Thus we may dispense with the discussion of the surge which has to do with the stability of the whole compressor-engine-ducting system, and concentrate entirely on the inception of rotating stall. According to technical literature, the rotating stall is triggered by either the *airfoil stall* (e.g. [4]; equivalent to 2-dimensional *diffuser stall*) or the *wall stall* (e.g. [4]). The airfoil stall occurs when the airfoil suction-surface diffusion exceeds the limit. The wall stall is caused by excessive wall boundary layers (in other words: deteriorated through-flow velocity profiles) entering higher compressor stages and the stall occurs prior to airfoil stall (i.e., airfoil stall is not due yet), a matter investigated and discussed in [4]. This paper is bringing attention to still another cause, which appears to be the *streamtube diffusion limit* (this streamtube occupying the whole blade channel volume). This may be actually a "pure rotating stall mode," triggered by neither airfoil stall nor wall stall.

Development of Stability Criteria

Diffuser Model and Stability Limit. Reneau et al. [11] formalized the presentation of 2-dimensional diffuser performance, a sample of which is shown in Fig. 2. The pressure recovery coefficient of parallel-wall diffusers is a function of geometric parameters and flow parameters. The diffuser stability line follows a sloping line of $C_p = .40$. More important to us is the sloping line passing through the points of maximum pressure recovery, which has been drawn into Fig. 2. This line of the maximum static pressure coefficient is presumed to be the compressor-stage stall line. Koch [4] and Schweitzer [5] have demonstrated that this equivalent-diffuser representation of the compressor stage is realistic, although their prediction ability is somewhat unreliable. The expected stall limit lines in terms of C_p and L/g_2 (=equiv. to N/W_1) are derived from Fig. 2 and similar, and are shown in Fig. 3, for various blockages. Both these methods, working with the pressure coefficients, encounter a great amount of difficulties because so many variables influence the pressure rise and thus have to be accounted for and corrected.

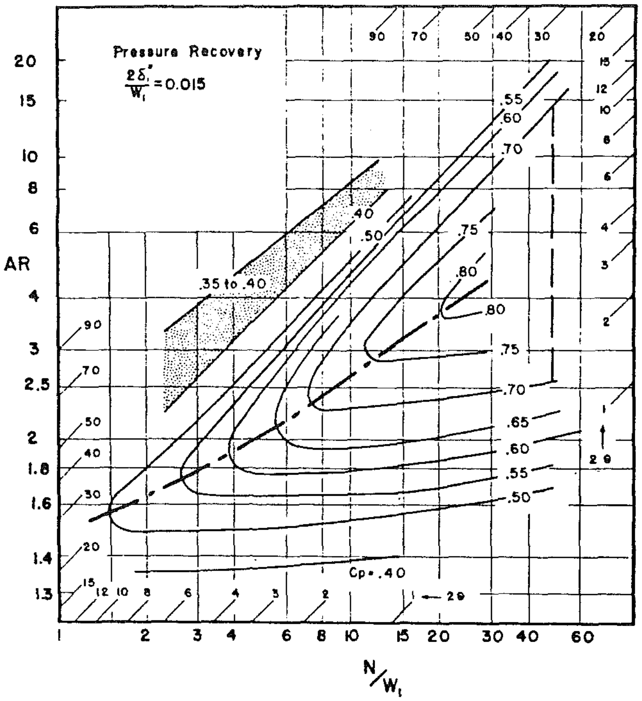

Fig. 2 Pressure recovery of two-dimensional diffusers with turbulent inlet boundary layers. (Copy of original Fig. 4(*b*) of reference [11].)

The present method bypasses most of these problems by selecting strictly geometric parameters as stall variables. Figure 4 shows the presumed compressor stability line taken out from Fig. 2 in terms of the area ratio against the nor-

Nomenclature

A = area
c = chord
C_{l_0} = camber coefficient (design lift coefficient)
$C_p = \Delta p / \frac{1}{2} \rho V_1^2$ = pressure coefficient
L = pathwise length of streamtube
Ma = Mach number based on relative entering velocity
N = length of straight diffuser
p = static pressure
Re = Reynolds number based on chord length
s = blade spacing
t = maximum airfoil thickness
V_1 = relative inlet velocity
X_{ss} = loss coefficient (steady-state)
W = width of 2-dimensional straight-wall diffuser
α = area coefficient
α_1 = angle of prerotation
β = air angle relative to rotor
δ^* = B.L. displacement thickness
ϕ = included cone angle
λ = stagger angle
$\psi = \Delta p / U^2 / g$ = pressure coefficient
$\sigma = c/s$ = cascade solidity
τ = time lag (response)

Subscripts

1 = inlet plane
2 = exit plane
∞ = approach
E = exit throat
i = incipient, inception, initial

Abbreviations

AR = area ratio
cor = corrected
crit = critical
eff = effective
lim = limit
R.S. = rotating stall (transverse mode)
rms = root-mean-square (geometric mean)

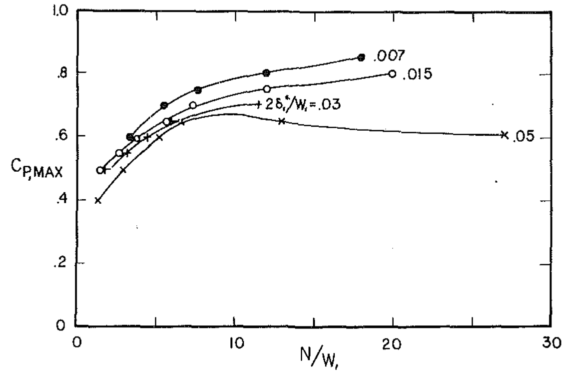

Fig. 3 Maximum pressure coefficient as affected by entering boundary layers (blockages)

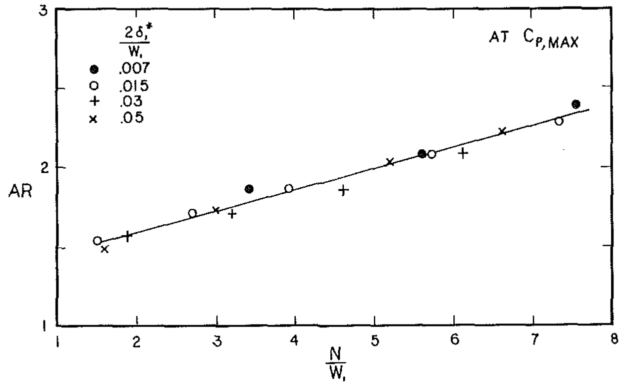

Fig. 4 Area ratio at max. pressure coefficient

malized length N/W_1, a single line for all four wall boundary layer thicknesses (blockages), suggesting (*a*) that the optimum area ratio is less affected by other geometry and flow variables, and as such (*b*) the area ratio is probably the truly controlling (independent) variable of stall and R.S. In any case, this stability line taken as a line of maximum pressure recovery of rectangular diffusers is a unique curve, independent of smaller blockages (up to 5 percent or so; for blockages of 10 percent or more the limiting area ratio is expected to be considerably reduced, perhaps proportionally with the blockage), and probably also independent of many of the variables that affect the pressure recovery itself. The limiting area ratio is expected to be a function of Ma, Re, significant (thick) blockages, equivalent length, camber and possibly stagger. There is no need felt to match the compressor area ratio vs. normalized length limit with the diffuser limit line of Fig. 4 because of the compressor-diffuser's curvature and sharp corner entry condition for which we have no equivalent among the tested diffusers. Instead, parameters A_E/A_∞ versus L/A_∞, as defined in Fig. 1, have been selected to construct a special limit line for rotor cascades. It is hoped that the result will still be a single correlation line, under the restricted conditions of a high Reynolds Number (100,000 or more), negligible Mach No. (incompressible), normal axial spacing (½ to 1 chord), small running tip clearance, and negligible blockage.

Rotating Stall Inception Criterion. The previous section defined a general stall or stability conditions for the compressor modeled as an equivalent diffuser of a particular kind, in terms of kinematic parameters A_E/A_∞ and L/A_∞. We now turn our attention to the inception of rotating stall specifically. We base the development of generalized R.S. criteria on a "classicial stability" solution of the problem recorded in technical literature.

Reference [1] shows that the inception of a small instability (small-wave fluctuations) due to rotating stall is conditioned by

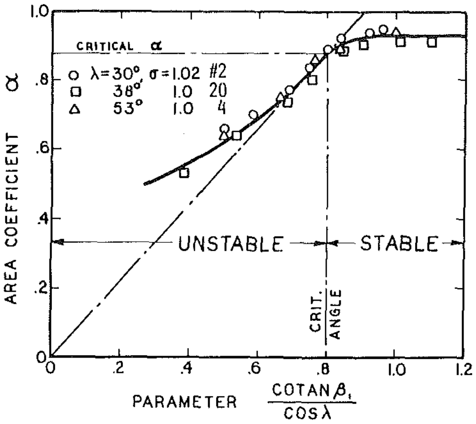

Fig. 5 Correlation of α function

$$\frac{d\alpha}{d\text{cotan}\beta_1} \geq \frac{\alpha}{\text{cotan}\beta_1} \tag{1}$$

where α can be defined as

$$\alpha \equiv A_{2,\text{eff}}/A_2, \tag{2}$$

where $A_{2,\text{eff}}$ is the geometric area at exit plane reduced by the wake blockage, and α can be evaluated from the definition of C_p, $C_p = 1-(A_1/A_2)^2 \rightarrow 1-(A_1/\alpha A_2)^2$, as

$$\alpha = (A_1/A_2)/(1-C_p)^{1/2}. \tag{3}$$

Figure 5 shows an α curve typical of isolated rotors in rotating stall. Here the unstable portion of α is initially linear, and thus the condition of instability (1) reduces into

$$\left(\frac{d\alpha}{d\text{cotan}\beta_1} \equiv\right)\frac{\alpha}{\text{cotan}\beta_1} = \text{const.} \tag{1a}$$

From this plot a critical value of the inlet air angle is obtained, at which the orifice coefficient becomes critical (where the α curve first becomes linear). Figure 5 is actually a composite curve of data on several rotors, normalized by means of the factor ($\cos\lambda$). Thus a single inception point of the R.S. instability also is suggested, coincident with the onset of a constant slope of the generalized α function, $\text{cotan}\beta_i/\cos\lambda \simeq .81$, which is the same as the inception criterion for high solidity cascades of reference [10].

Since the α is a ratio of two areas (the effective area over the geometric area at the passage exit plane), it is of interest to investigate also some other area ratios. One of them has been found quite useful and the two involved areas are shown in Fig. 1: the approach area A_∞ and the exit throat area A_E. The A_E is fixed by the cascade geometry (for fixed-stagger cascades, typical in rotors) but the A_∞ is kinematic, varying with the air angle. The ratio A_∞/A_E varies approximately linearly with $\text{cotan}\beta_1$ and can be normalized by the same ($\cos\lambda$) factor. The result is Fig. 6, A_∞/A_E versus $\text{cotan}\beta_1/\cos\lambda$ correlation. Because Fig. 5 and 6 have a common normalized abscissa,[1] the inception criterion can be marked in Fig. 6 also. The ordinate of Fig. 6 then suggests an alternate instability criterion $A_\infty/A_E \leq \text{lim}$, or $A_E/A_\infty \geq \text{lim}$, coincident with the point of criticality of Emmons' α function. The advantage is that the new function is strictly geometric, hence indifferent to the actual value of either the pressure or the loss coefficients. Not all the data on rotating stall inception contain the detail information (mostly β_2's of rotors) necessary to construct the α curves, and thus it is impossible to conclude whether the above inception criterion

---

[1] But not common coordinates. Figure 6 has strictly geometric variables, hence can be constructed all the way to the origin. Not so Fig. 5; c_p and β_2 on which α is based are available only to cotan values shown.

is valid in general, or is restricted to some cascade geometries. That question is addressed in the subsequent part.

Combined Stability Criteria. This concludes the preliminary analysis of the problem. Let us sum up our expectations. According to the modified diffuser analogy, the compressor stability line can be expected to be a single sloping line A_E/A_∞, above which (general) stall occurs and below which compressor elements are stable. From the tentative generalized analysis of R.S. inception, rotating stall should occur above the (single) line of $A_E/A_\infty = \text{const} \simeq 1.55$. The expectations are sketched in Fig. 7. The 2 stability lines intersect, and we are unable to resolve off-hand this dilemma analytically. The validation of these expectations must come from the correlation of experimental values of compressor stages and other elements at the onset of rotating stall.

Divergence Correlations For Elementary Compressors

Test data used for the correlations originate in [2] and [12] to [25]. All the pertinent original data as well as the calculated parameters are tabulated in Table 1 and refer to the rms radii. The correlation technique used here was developed in [13] where it is used to correlate cascade stall points (airfoil stall, not R.S.). It consists of plotting the area divergence ratio A_E/A_∞ against the form parameter L/A_∞. (All geometric variables are defined in Fig. 1.) Because rectangular diffusers have a straight axis and cascades do not, the cascade stall

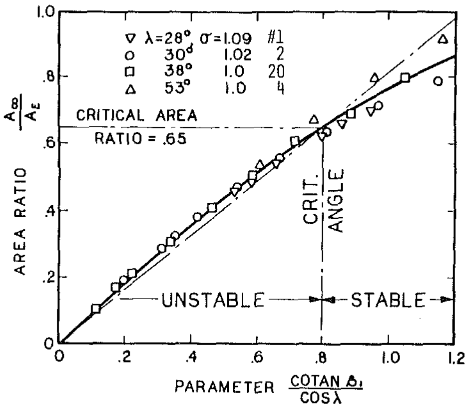

Fig. 6 Correlation of kinematic area ratio A_∞/A_E

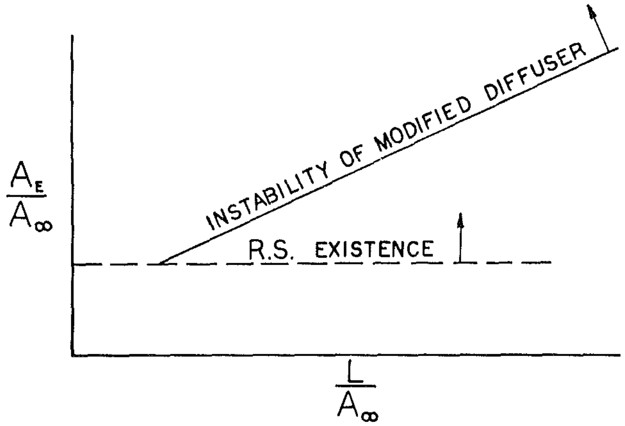

Fig. 7 Two instability lines indicated by preliminary analysis

Table 1 Geometry and performance data on some elementary axial compressors pertaining to rotating stall. (Sources: references [2, 12–25]; supplemented as listed in Notes below.)

No.	Year, Researcher, Institution, (ref.)	Element	Designation	$\frac{\text{hub}}{\text{tip}}$	Type	Airfoil	C_{l_o}	$\frac{t}{c}$	σ	λ	α_1	β_1	$\frac{A_E}{A_\infty}$	$\frac{L}{A_\infty}$	ΔL	$(\frac{L}{A_\infty})_{cor}$	$\frac{\text{cotan } \beta_1}{\cos\lambda}$
	Isolated Rotors:																
1	1955, Huppert, NACA, (16)	I.R.		.9	straight	65-010 *	1.2 ††	.1	1.09	28.5°	0°	53°	1.52	2.21	.3 + 0 = .3	2.51	.857
2	1956, Kriebel, MIT, (18)	I.R.	rotor A	.75	straight	65-010 *	1.2	.1	1.02	30°	0°	55°	1.56	2.24	.3 + 0 = .3	2.54	.810
3		I.R.	rotor B	.75	straight	65-010 *	1.2	.1	.51	30°	0°	70.7°	2.65	2.46	.3 + 0 = .3	2.76	.405
4		I.R.	rotor C	.75	straight	65-010 *	1.2	.1	1.02	53°	0°	66°	1.54	2.87	.3 + 0 = .3	3.17	.731
5	1973, Nenni, Calspan, (2,21)	I.R.	R1	.8	twisted	65-010 *	1.0 ††	.1	.85	50°	0°	65°	1.56	2.24	0 + 0 = 0	2.24	.725
6		I.R.	R1	.8	twisted	65-010 *	1.0 ††	.1	.85	40°	0°	61°	1.595	2.10	0 + 0 = 0	2.10	.724
7		I.R.	R1	.8	twisted	65-010 *	1.0 ††	.1	.85	30°	0°	55/65° ¶	1.54/2.10	2.63	0 + 0 = 0	2.63	.81/.54
8	1975, Tanaka, Osaka U., (22,23)	I.R.	#1 rotor	.85	F.V.twist	65-010	1.0	.1	1.03	51.5° †††	0°	73.7°	2.30	4.56	0 + 0 = 0	4.56	.47
9		I.R.	#1	.7	F.V.twist	65-010	1.0	.1	1.12	50° †††	0°	67.4°	1.71	3.36	0 + 0 = 0	3.36	.65
10		I.R.	#1	.5	F.V.twist	65.010	1.0	.1	1.21	48° †††	0°	67.9°	1.62	3.27	0 + 0 = 0	3.27	.605
	Stages without Prerotation (α_1=0°):																
11	1956, Huppert, NACA, (17)	R + G.V.	α_1 = 0	.9	straight	65-010 *	1.2 ††	.1	1.09	28.5°	0°	53.7°	1.55	2.25	.3 + 0 = .3	2.55	.836
12		Stage + G.V.	α_1 = 0	.9	straight	65-010 *	1.2 ††	.1	1.09	28.5°	0°	53.9°	1.56	2.26	.3 + 0 = .3	2.56	.830
13	1975, Tanaka, Osaka U., (22)	St.w/o G.V.	#1	.85	F.V.twist	65-010	1.0	.1	1.03	51.5° †††	0°	69.4°	1.88	3.70	0 + 0 = 0	3.70	.585
14		St.w/o G.V.	#1	.7	F.V.twist	65-010	1.0	.1	1.12	50° †††	0°	74°	2.36	4.40	0 + 0 = 0	4.40	.458
15		St.w/o G.V.	#1	.5	F.V.twist	65-010	1.0	.1	1.21	48° †††	0°	66.7°	1.74	3.52	0 + 0 = 0	3.52	.643
16	1977, Day, Cambridge U., (24,25)	Stage+G.V.	G(R), ϕ*=.71	.8	straight	C1 **	.8	.1	1 ***	35°	0° †	62.1°	1.74	2.64	-.3 + 0 =-.3	2.34	.65
17		Stage+G.V.	J, ϕ*=1.00	.8	straight	C1 **	1.65	.1	1 ***	20°	0° †	55.4°	1.73	2.52	1.0 + 0 =1.0	3.50	.73
	Complete Single Stages, α_1 > 0 :																
18	1954, Rannie, Caltech, (14)	1-stage	F.V.	.6	F.V.twist	65-010 *	.7	.1	..84	46°	22°	71.2°	2.10	3.04	-.45+.6= .15	3.19	.489
19		1-stage	solid body	.6	S.B.twist	65-010 *	.85	.1	.98	40°	30°	69.2°	2.19	3.45	-.22+.6= .38	3.83	.496
20	1955, Montgomery, MIT, (15)	1-stage		.75	F.V.twist	65-010 *	1.2 ††	.1	1.0	37.4°	24.4°	62°	1.76	2.63	.3 +.6= .9	3.53	.668
21	1956, Huppert, NACA, (17)	1-stage	α_1 = 0°	.9	straight	65-010 *	1.2 ††	.1	1.09	28.5°	0°	53.9°	1.56	2.26	.3 +0 = .3	2.56	.830
22		1-stage	α_1 = 22.5°	.9	straight	65-010 *	1.2 ††	.1	1.09	28.5°	22.5°	61.7°	1.94	2.89	.3 +.6= .9	3.79	.776
23		1-stage	α_1 = 40°	.9	straight	65-010 *	1.2 ††	.1	1.09	28.5°	40°	70.8°	2.78	4.25	.3 +.6= .9	5.15	.863
24	1958, Valensi, Marseille U., (19)	1-stage		.5	twisted	65-010 *	1.2 ††	.1	1.09	35°	23.5°	58.4°	1.62	1.62	.3 +.6= .9	2.52	.752
25	1961, Dunham, Cambridge U., (20)	1-stage		.4	twisted	65-010 *	.4	.1	.885	40°	29°	59.8° ¶¶	1.49	2.12	-.9 +.6=-.3	1.82	.759
26	1977, Day, Cambridge U., (24,25)	1-stage	A, ϕ*=.35	.8	straight	C1 **	.8	.1	1 ***	50°	40° †	69.9°	1.82	3.33	-.3 +.6= .3	3.63	.569
27		1-stage	C, ϕ*=.55	.8	straight	C1 **	.8	.1	1 ***	35°	25° †	59°	1.58	2.38	-.3 +.6= .3	2.68	.74
	Multistage Compressors (Repeating Stage):																
28	1954, Rannie, Caltech, (14)	3 stages		.6	F.V.twist	65-010 *	.7	.1	.84	46°	22°	64.6° ¶¶¶	1.60	2.28	-.45+.6= .15	2.43	.683
29	1977, Day, Cambridge U., (24,25)	3 stages	B, ϕ*=.35	.8	straight	C1 **	.8	.1	1 ***	50°	40° †	69.9°	1.82	3.33	-.3 +.6= .3	3.63	.569
30		2 stages	D, ϕ*=.55	.8	straight	C1 **	.8	.1	1 ***	35°	25° †	59°	1.58	2.38	-.3 +.6= .3	2.68	.74
31		3 stages	E, ϕ*=.55	.8	straight	C1 **	.8	.1	1 ***	35°	25° †	59°	1.58	2.38	-.3 +.6= .3	2.68	.74
32		3 stages	I(R), ϕ*=.71	.8	straight	C1 **	.8	.1	1 ***	35°	0° †	62.1°	1.74	2.64	-.3 + 0=-.3	2.34	.65
33		3 stages	L, ϕ*=1.00	.8	straight	C1 **	1.65	.1	1 ***	20°	0° †	55.4°	1.73	2.52	1.0 + 0=1.0	3.50	.73

Notes:

- * Assumed to be 65-010 or equivalent. (Circular arc camberline and 65 series profile mostly indicated.)
- ** Assumed to be C1 profile.
- *** Solidity not given, therefore taken as 1.0 for purposes of calculations. If actual value is within about .7 and 1.3, then the results should be unaffected.
- † Assumed equal to stator exit blade angle (a repeating stage).
- †† Corresponds to given camber angle; if not given, then found from turning, solidity and stagger.
- ††† Approximate value found from cascade performance charts, based on σ, C_{l_o} and β_1.
- ¶ Dual instability reported; strong R.S. at 65 deg, preceded by a weaker instability at 55 deg. The first instability is assumed here to be the more significant one, as it is expected to trigger stall in an actual machine.
- ¶¶ Mean angle corresponding to partial stall.
- ¶¶¶ Angle corresponding to partial stall.

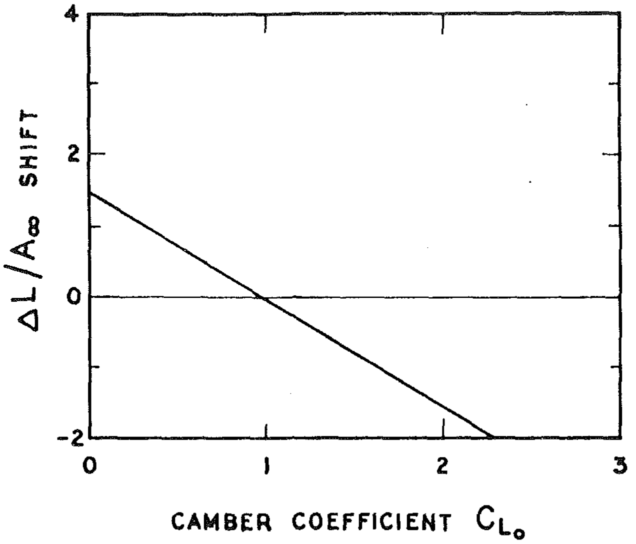

Fig. 8 Correction shifts for stalled rotor cascades

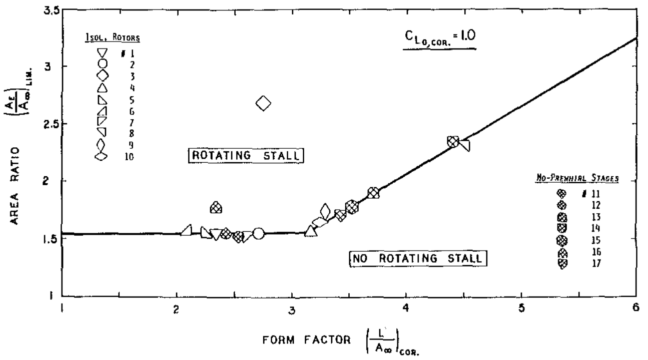

Fig. 9 Correlation of rotating stall inception for rotors

divergence limits vary with camber, and for a successful correlation equivalent to diffusers, all cascades would have to be corrected to zero camber. A consistent correlation may be obtained if all cascades are corrected to a constant camber. In the following correlations all the cascades were corrected to $C_{l_0} = 1.0$ by means of an empirical correction curve, Fig. 8.[2]

Isolated Rotors. The rotating stall inception points for numerous isolated rotors are plotted in Fig. 9. The points form two linear branches, fairly well correlated, one horizontal and the other sloping, as was anticipated. These two branches define two rotating stall inception criteria. The horizontal line apparently indicates a pure R.S. mode. The sloping line represents stall points that experience simultaneously airfoil stall and rotating stall. Apparently the rotating stall inception is delayed for these longer forms, until it gets triggered by airfoil stall. Without exception, all the stall points on the sloping line coincide with the onset of airfoil stall. Note that camber increases proportionally the effective length of the stalling passage. There appears to be no effect of solidity of order of 1 and larger. The same cannot be true for very low solidities (for example Pt.3, $\sigma = \frac{1}{2}$), but there is scarcity of low solidity data on R.S. inception and this effect must remain unresolved for the time being.

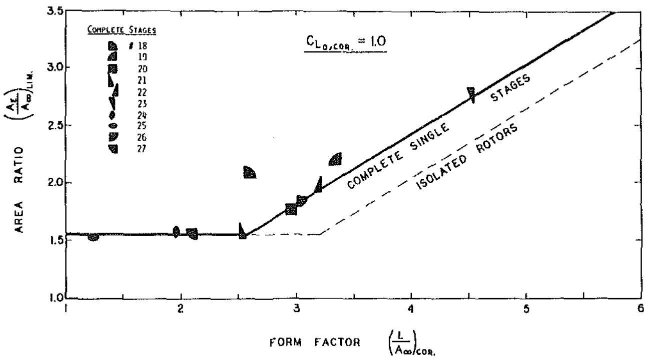

Fig. 10 Correlation of rotating stall inception points for complete single stages

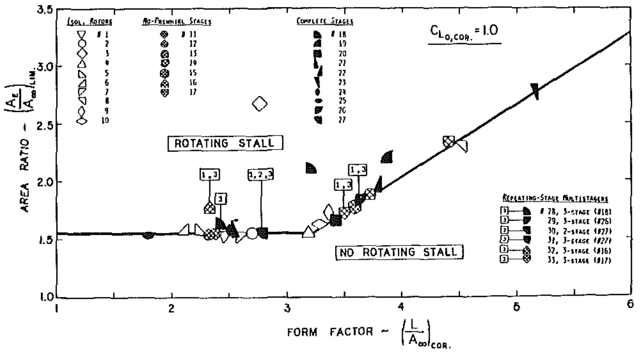

Fig. 11 Composite correlation of rotating stall inception for all elementary compressors

Stages Without Prerotation. Stages without guide vanes and stages with guide vanes imparting no prerotation ($\alpha_1 = 0^0$) behave exactly the same way as the isolated rotors. The rotating-stall inception points of these cases, corrected for camber, fall on either the horizontal or the sloping lines established by isolated rotors, and have been added as checkered points to Fig. 9.

Complete Single Stages. Staging has a definite effect on the divergence correlation and on the R.S. inception. Several complete stages, with guide vanes (here all imparting "positive" prerotation), are correlated in Fig. 10. The stall points again show the same trend, even the same slope, but the sloping line is offset horizontally by a shift of 0.6 of the normalized diffuser length, after all points were corrected for camber first. Thus it appears that staging has only one effect on the inception, namely, the addition of prewhirl guide vanes increases the effective length of the "diffuser" passage[3] by a fixed amount regardless of the prewhirl angle (as long as it is nonzero). Both corrections (for camber and for staging) are additive. This makes it possible to construct a composite correlation of R.S. inception points for all elementary compressors investigated in this study. The correction formula is

$$(L/A)_{cor} = (L/A)_{geom} - \Delta_{camber} + \Delta_{stage} \qquad (4)$$

Composite of Elementary Compressors. All elementary compressors listed in Table 1, isolated rotors, stages without prerotation, stages with guide vanes, and repeating-stage multistage compressors, are corrected and plotted together in Fig. 11. The result is a very good correlation, with only 3 points seriously off. The three culprit points are #3, 16, and

---

[2] Figure 8 was obtained by 3-dimensional curve fitting of area ratios versus normalized lengths at constant nominal lift coefficients, assuming linearity of area ratios at any constant C_{l_0} and proportionality of ΔC_{l_0} with $\Delta L/A_\infty$. Thus all lines of constant C_{l_0} are shifted until they collapse into one single sloping line (just like in Fig. 9) with minimum error. The resulting correction curve has provided satisfactory correlations (Figs. 9, 10, 11).

[3] The rotor is always controlling the inception of rotating stall. Thus the passage under scrutiny is the rotor passage.

18. No. 3 is an isolated rotor with a solidity of ½, which is very low. R.S. fails to materialize at solidities of 1/3 and lower, therefore #3 should have a very high area ratio limit. It is however the only case with a very low solidity, and therefore a trendline for low solidity effects cannot be established at this time. Point No. 16 is a high reaction stage design; it may be that extremal reaction has effect on the divergence limit also. Point No. 18 is a single stage of a very low hub/tip ratio with an extremal free-vortex blade twist. It may be that the rms radius does not represent correctly the average "diffuser conditions" in this case. Anyway, fewer than 10 percent of the cases fail to support this correlation, and thus the method appears to be fairly well justified.

Summary and Conclusions

Based on a successful correlation of about 30 cases of elementary compressors, two alternate criteria for inception of rotation stall have been established, subject to confirmation by additional experimental data: rotor cascades are classified into two groups, subcritical and supercritical, determined by the form parameter $(L/A_\infty)_{\mathrm{cor}}$ of the rotor. If, at the area ratio of 1.55, the corrected form parameter is less than 3.2, then the cascade is "subcritical" and rotating stall inception occurs when the area ratio is equal or larger than 1.55; if the form parameter is larger than 3.2, the cascade is "supercritical" and the area expansion ratio will surpass 1.55 until the airfoil stall is reached; at that point the R.S. is triggered. This has to be determined the long-hand way, because there are no greatly noticeable differences in the cascades on inspection alone.

The present understanding is that the rotating stall onset is governed by the rotor channel geometry (form, camber, stagger) and by staging. The horizontal stability line probably represents a "pure rotating stall mode," unrelated to either the suction surface deceleration (airfoil stall) or the excessive wall boundary layers (wall stall). This limit line is equivalent to the angular criterion of [10]. The sloping limit line means always a coincidence of airfoil stall and rotating stall. In this case, stable operation continues across the horizontal stability line until the airfoil stall is reached, which triggers the onset of R.S.

The correlations are corrected for camber ($C_{l_0} = 1.0$ is std.), and are applicable to solidities ≥ 0.8, high Reynolds numbers, negligible Mach numbers (i.e, incompressible), normal axial spacing (½ to 1 chord length), and negligible blockages (due to entering wall B.L.'s).

This solution of R.S. inception is obviously only a partial solution of a more general solution. To complete, more test data must be collected and correlated, particularly data on very low solidity, very thick wall B.L.'s (and large blockages), stage reaction, and run-of-the-mill multistage compressor stages. A careful use of this method is suitable for the prediction of rotating stall inception.

References

1 Emmons, H. W., Pearson, C. E., and Grant, H. P., "Compressor Surge and Stall Propagation," ASME Paper No. 53-A-65, 1953.

2 Nenni, J. P., and Ludwig, G. R., "A Theory to Predict the Inception of Rotating Stall in Axial Flow Compressors," AIAA Paper No. 74-528, June 1974.

3 Takata, H., and Nagano, S., "Nonlinear Analysis of Rotating Stall," ASME *Journal of Engineering for Power*, Vol. 94, Oct. 1972, pp. 279–293.

4 Koch, C. C., "Stalling Pressure Rise Capability of Axial Flow Compressor Stages," ASME Paper No. 81-GT-3, Mar. 1981.

5 Schweitzer, J. K., and Garberoglio, J. E., "Maximum Loading Capability of Axial Flow Compressors," AIAA Paper No. 83-1163, June 1983.

6 Moore, F. K., "A Theory of Rotating Stall of Multistage Axial Compressors: Part I—Small Disturbances," ASME Paper No. 83-GT-44, March 1983.

7 Greitzer, E. M., "REVIEW—Axial Compressor Stall Phenomena," ASME JOURNAL OF FLUIDS ENGINEERING, Vol. 102, June 1980, pp. 134–51.

8 Howell, A. R., and Calvert, W. J., "A New Stage Stacking Technique for Axial-Flow Compressor Performance Prediction," ASME *Journal of Engineering for Power*, Vol. 100, Oct. 1978, pp. 698–703.

9 Lieblein, S., "Loss and Stall Analysis of Compressor Cascades," ASME Paper 58-A-84, Dec. 1953; also: NACA Res. Memorandum E53D01, 1953.

10 Zika, V. J., "Approximation of Rotating Stall by Finite-Discontinuity Modeling," ASME Paper No. 81-WA/FE-15, Nov. 1981.

11 Reneau, L. R., Johnston, J. P., and Kline, S. J., "Performance and Design of Straight, Two-Dimensional Diffusers," ASME *Journal of Basic Engineering*, Vol. 89, Mar. 1967, pp. 141–50.

12 Herrig, L. J., Emery, J. G., and Erwin, J. R., "Systematic Two-Dimensional Cascade Tests of NACA 65-Series Compressor Blades at Low Speeds," NACA Research Memorandum L51G31, Sep. 1951.

13 Zika, V. J., "Affinity of Stalled Airfoil Cascades (Incompressible)," AIAA Paper No. 82-1005, June 1982.

14 Iura, T., and Rannie, W. D., "Experimental Investigations of Propagating Stall in Axial-Flow Compressors," *ASME Trans*, Vol. 76, Apr. 1954, pp. 463–71.

15 Montgomery, S. R., and Braun, J. J., "An Investigation of Rotating Stall in a Single Stage Axial Compressor," G. T. Laboratory Report No. 29, M.I.T., Cambridge, Mass., May 1955.

16 Costilow, E. L., and Huppert, M. C., "Rotating Stall Characteristics of a Rotor with High Hub-Tip Radius Ratio," NACA *Technical Note* 3518, Aug. 1955.

17 Costilow, E. L., and Huppert, M. C., "Some Effects of Guide-Vane Turning and Stators on Rotating Stall Characteristics of a High Hub-Tip Ratio Single-Stage Compressor," NACA Technical Note 3711, Apr. 1956.

18 Kriebel, A. R., "Stall Propagation in a Cascade of Airfoils," G. T. Laboratory Report No. 36, M.I.T., Cambridge, Mass., Aug. 1956.

19 Valensi, J., "Experimental Investigation of the Rotating Stall in a Single-Stage Axial Compressor," *Journal Aero. Sci.*, Vol. 25, Jan. 1958, pp. 1–10, and 72.

20 Dunham, J., "Observations of Stall Cells in a Single Stage Compressor," Aeronautical Research Council, C. P. No. 589, 1961.

21 Ludwig, G. R., Nenni, J. P., and Arendt, R. H., "Investigation of Rotating Stall in Axial Flow Compressors and the Development of a Prototype Rotating Stall Control System," Contractor Report AFAPL-TR-73-45, May 1973.

22 Tanaka, S., and Murata, S., "On the Partial Flow Rate Performance of Axial-Flow Compressor and Rotating Stall, 1st Report, Influences of Hub-Tip Ratio and Stators," *Bulletin of the JSME*, Vol. 18, March 1975, pp. 256–63.

23 Tanaka, S., and Murata, S., "On the Partial Flow Rate Performance of Axial-Flow Compressor and Rotating Stall, 2nd report, Influences of Impeller Load and a Study of the Mechanism of Unstable Performances," *Bulletin of the JSME*, Vol. 18, March 1975, pp. 264–71.

24 Day, I. J., Greitzer, E. M., and Cumpsty, N. A., "Prediction of Compressor Performance in Rotating Stall," ASME Paper 77-GT-10, 1977.

25 Day, I. J., and Cumpsty, N. A., "The Measurement and Interpretation of Flow within Rotating Stall Cells in Axial Compressors," *Journal of Mechanical Engineering Science*, Vol. 20, No. 2, 1978, pp. 101–14.

Kenjiro Kamijo
National Aerospace Laboratory of Japan,
Ohgawara, Miyagi 989-12,
Japan
Mem. ASME

Kunio Hirata
National Space Development Agency of Japan,
Minatoku, Tokyo, Japan

Performance of Small High Speed Cryogenic Pumps

Several small cryogenic pumps for a liquid rocket engine have been made and tested. These pumps have a small impeller and are characterized by high speed and high head. The main design characteristics of these pumps are as follows: stage specific speeds of from 0.0319 to 0.0766, flow rates from 0.016 to 0.0525 m^3/s, pressure rises from 4.9 to 26 MPa, rotational speeds from 16,500 to 80,000 rpm, and impeller diameters from 0.083 to 0.146 m. These pumps, when tested, showed higher efficiency even in the range of small stage specific speeds than any previously reported data on other pumps. This tendency was particularly striking with the two-stage pumps. With regard to pump efficiency measurement, it was made clear that adiabatic efficiency was utilizable for the present cryogenic pumps. The relationship between the adiabatic efficiency and ordinary efficiency was also confirmed by a brief calculation and test results.

Introduction

During over the past ten years, several small cryogenic pumps for liquid rocket engines have been made for purposes of research and development by the National Aerospace Laboratory of Japan (NAL) and the National Space Development Agency of Japan (NASDA). These pumps have very small impellers and are characterized by high speed and high head. The present paper focuses on the overall performance and efficiency measurements of these pumps.

In general, pump efficiency mainly depends upon the stage specific speed and flow rate [1]. Besides these factors, the efficiency of a pump having a relatively high specific speed and high flow rate seems to be influenced by suction specific speed [2]. A higher suction specific speed pump requires an increased inlet diameter, which results in poor geometry of the pump inlet. Furthermore, it is reported that, with small pumps, the diameter of the impeller has a strong influence on the pump efficiency [2, 3, 4]. In the authors' experience, however, the previously available technical data were not sufficient for designing small high speed pumps. For instance, some small high speed pumps which were made at NAL [5] showed considerably higher efficiency than that previously reported for such pumps [2, 3, 4].

The present small pumps were made for use with liquid oxygen (LOX) and liquid hydrogen (LH_2) feed pumps. They are single or two-stage centrifugal pumps with an inducer. The design characteristics of these pumps are as follows:

Stage specific speed: 0.0319 to 0.0766
Flow rate: 0.016 to 0.0525 (m^3/s)
Pressure rise: 4.9 to 26.0 (MPa)
Rotational speed: 16,500 to 80,000 (rpm)
Impeller diameter: 0.083 to 0.146 (m)
Impeller outlet blade angle: 25, 35, and 45 (deg)

These pumps were tested using water, LOX, liquid nitrogen (LN_2), and LH_2 as the pump fluid and overall performance factors such as efficiency and head/flow-rate characteristics were examined. The influence of rotational speed and pump fluid on the pump performance was also examined.

Furthermore, with regard to cryogenic fluids, adiabatic efficiency, which has previously been used to evaluate LH_2 pump efficiency [6], was investigated in more detail. A brief calculation was compared with the test results to clarify the relationship between the adiabatic efficiency and ordinary efficiency. It was made clear that the adiabatic efficiency obtained by measurement of fluid temperatures and pressures was suitable to obtain the efficiency of these cryogenic pumps.

Test Pumps and Test Procedures

A tabulation of major pump design parameters is presented in Table 1. Pumps A, B, C, and G were fabricated for LOX feed and the others for LH_2 feed. However, till now only an LN_2 test has been conducted with pump H. Design flow rate, Q_{d0}, and design head, H_{d0}, are exactly the same for pumps A and B but design rotative speed, N_{d0}, is quite different. Pumps C, D, D′, and E were made for use in development of the LE-5 engine of Japan's H-1 rocket. Pumps G and H are characterized by remarkably high discharge pressure.

All the test pumps have an inducer with three swept-back blades. Pumps F and H are two-stage centrifugal pumps, and all the others are single-stage centrifugal pumps. Pumps E, F, G, and H have vaned diffusers and the others have vaneless diffusers. All the test pumps have a closed impeller with two-dimensional, back-swept blades. Pumps D, D′, E, and H have impellers with splitter blades. The impellers of pumps A, B, C, and F were made of aluminum alloy, and those of pumps D, D′, and H were made of titanium alloy. Heat resisting alloy was used for pump G. Except for that of pump G, the impellers were made by machining. The backshroud

---

Contributed by the Fluids Engineering Division for publication in the JOURNAL OF FLUIDS ENGINEERING. Manuscript received by the Fluids Engineering Division, December 27, 1983.

Table 1 Main design characteristics of test pumps

Principal items	A	B	C	D	D'	E	F	G	H
Pump fluid	LOX	LOX	LOX	LH2	LH2	LH2	LH2	LOX	LH2
Number of stages	1	1	1	1	1	1	2	1	2
Flow rate, m^3/s	0.018	0.018	0.0172	0.0525	0.0525	0.0503	0.041	0.016	0.0439
Pressure rise, MPa	11.8	11.8	4.9	5.5	5.5	5.5	6.0	24.5	26.0
Rotational speed rpm	20,000	35,000	16,500	50,000	50,000	50,000	45,000	45,000	80,000
Pump head, m	1,051	1,051	439	8,000	8,000	8,000	8,500	2,230	37,240
Stage specific speed, n_s(non-dimensional)	0.0440	0.0766	0.0681	0.0408	0.0408	0.0401	0.0521	0.0529	0.0319
Stage specific speed; N_s, (m,m^3/min,rpm)	113	197	175	105	105	103	134	136	82
Required *NPSH* m	13	13	7.5	56	56	56	34	20	56
Inducer tip diameter, D_{i1}, m	0.065	0.060	0.0653	0.0682	0.0682	0.068	0.065	0.0473	0.063
Impeller diameter, D_{i2} , m	0.134	0.083	0.1112	0.146	0.134	0.1398	0.122	0.0863	0.1296
D_{i1}/D_{i2},	2.06	1.38	1.70	2.14	1.96	2.06	1.88	1.82	2.06
Inducer inlet tip blade angle deg.	10.3	8.0	10.0	9.9	9.9	9.0	9.9	8.5	7.0
Impeller inlet blade angle deg.	13.8	11.5	14.3	11.4	14.2	12.7	12.0	11.0	9.21
Impeller outlet blade angle deg.	25	25	25	35	45	35	35	25	45
Number of impeller blades	6	6	6	6+6	6+6+12	6+6	6+6	6	6+6+12
Impeller tip blade width m	0.0042	0.0092	0.0068	0.0038	0.0049	0.0036	0.0043	0.0038	0.0029
Diffuser type	A	A	A	A	A	B	B	B	B
Diffuser width m	0.014	0.0138	0.0152	0.0076	0.0099	0.0041	0.0053	0.0044	0.0034
Diffuser outlet to inlet diameter ratio	1.07	1.12	1.10	1.07	1.07	1.20	1.15	1.27	1.20
Number of diffuser blades	—	—	—	—	—	11	11	7	11
Diffuser inlet blade angle deg.	—	—	—	—	—	8.9	8.8	9.0	7.2
Diffuser outlet blade angle deg.	—	—	—	—	—	15.0	13.5	15.0	15.0

A = vaneless diffuser + volute. B = vaned diffuser.

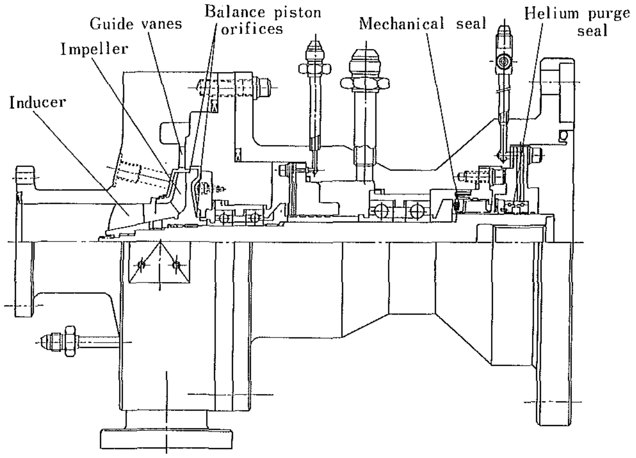

Fig. 1 Pump G

with the blades and the frontshroud were machined separately and joined by aluminum brazing or diffusion bonding. The impeller of pump G was made by precision casting. The surfaces of blades, shrouds, etc. were smoothly finished. Their surface roughness ranged from approximately 2 to 5 μm (R_{max}).

Pumps G and H are presented in Figs. 1 and 2, respectively. The axial thrust of the test pumps was balanced by balance holes machined in the backshroud of the impellers (pumps A, B, C, D′, and F) or by a balance piston mechanism as shown in Figs. 1 and 2. The balance piston orifices were formed by utilizing an impeller backshroud and a casing [7]. Ball bearings of all the test pumps were self-lubricated and cooled by pump fluid. A metal bellows mechanical seal was used to seal in pump fluid except for pump H in which floating ring seals were used because the seal pressure was considerably high. The details of the mechanical seals and floating ring seals are presented in references [8–10].

Table 2 Properties of pump fluids

	LOX	LN_2	LH2	WATER
Pressure (MPa)	0.1013	0.1013	0.1013	0.0023
Temperature (K)	90.2	77.4	20.3	293
Density (Kg/m^3)	1,140	808	70.8	998
Viscosity (N·s/m^2)	1.96×10^{-4}	1.63×10^{-4}	1.32×10^{-5}	1.01×10^{-3}
Kinematic viscosity (m^2/s)	1.72×10^{-7}	2.02×10^{-7}	1.86×10^{-7}	1.01×10^{-6}

The present tests were conducted using two test facilities. Testing of pump G as well as all the tests in which LH_2 was used as pump fluid, were performed at the NASDA LOX/LH_2 pump test facility. The remaining tests were conducted at the NAL LOX pump test facility, where water can be used as pump fluid. The test pumps were powered by a 880 KW d-c electric dynamometer at the NASDA facility and a 450 KW d-c electric dynamometer at the NAL facility. Measured torque and rotational speed were used to determine the brake horsepower of the test pumps. Torque was obtained by measuring the displacement of a balance of the electric dynamometer. Rotational speed was measured with a combination of a toothed wheel and a magnetic pulse pickup. A schematic diagram of the NASDA test facility, which is

Nomenclature

C = torque of pump shaft (N•m)
C_c = torque of friction at impeller shroud tip (N•m)
C_s = torque of friction at impeller shroud surface (N•m)
C_m = moment coefficient
D = diameter of impeller (m)
g = acceleration due to gravity (m/s^2)
h = enthalpy of pump fluid (J/Kg)
Δh = enthalpy change of pump fluid (J/Kg)
H = pump head (m)
H_i = inducer static head (m)
L_d = disk friction loss (w)
$\dot{m}$ = mass flow rate (Kg/s)
n = rotational speed (1/s)
N = rotational speed (rpm)
n_s = nondimensional specific speed ($n\sqrt{Q}/(g\bullet H)^{3/4}$)
N_s = specific speed (m, m^3/min, rpm)
p = pressure (MPa)
q = heat generated due to losses (J/Kg)
Q = flow rate (m^3/s)
Qd = flow rate determined by similar velocity triangles ($=Qd0(N/Nd0)$)
Re = Reynolds' number ($\omega\bullet(D_{i2}/2)^2/\nu$)
S = entropy of pump fluid (J/Kg)
T = temperature of pump fluid (K)
u = internal energy of pump fluid (J/Kg)
U_i = peripheral velocity of inducers (m/s)
U = peripheral velocity of impellers (m/s)
v = specific volume of pump fluid (m^3/Kg)
β = blade angle from tangent at impeller diameter (deg)
η_a = adiabatic efficiency
η_p = ordinary pump efficiency
ν = kinematic viscosity of pump fluids (m^2/s)
ρ = density of pump fluids (Kg/m^3)
Ψ_p = pump head rise coefficient ($g\bullet H/U^2$)
Ψ_i = inducer static head rise coefficient ($g\bullet H_i/U_i^2$)
Ψ_s = pump stage head rise coefficient
ω = angular velocity (1/s)

Subscript

1 = conditions of pump inlet
2 = conditions of pump outlet
is = isentropic compression process
act = actual compression process
$d0$ = design point

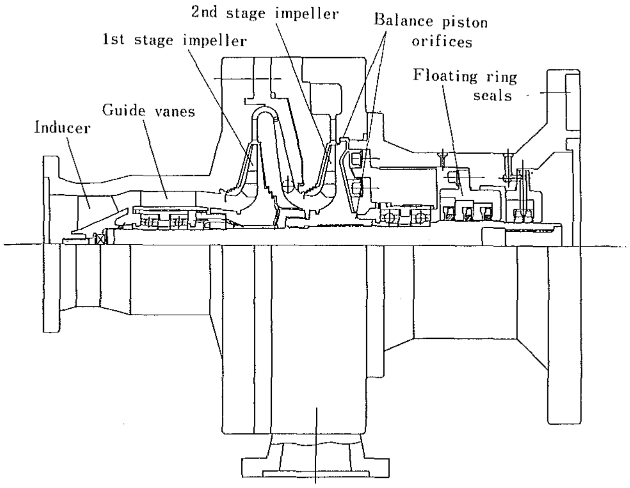

Fig. 2 Pump H

similar to the NAL test facility, is shown in Fig. 3. The test pumps were not insulated from their surroundings, which resulted in a slight heat flow through the pump casing, particularly in the LH_2 test. All the flow rates were measured by turbine type flow meters. Pressure measurements were carried out with strain-gage type pressure sensors. Cryogenic fluid temperatures at the pump inlet and outlet were measured with platinum resistance thermometers. Cryogenic fluid properties, which were necessary to obtain pump NPSH, adiabatic efficiency, etc., were obtained from various handbooks [11, 12, 13]. The main properties of the pump fluids are presented in Table 2. Viscosity of liquid hydrogen is much less than that of the other fluids. However, the kinematic viscosity of these three cryogens is almost the same.

Results and Discussion

Overall Performance. The relationship between the net positive suction head (NPSH) and the overall performance of the pump is presented in Fig. 4. Water was used as pump fluid. The test was carried out at the constant rotational speed and with the constant flow rate by reducing the pump inlet pressure. The overall performance of the pump was strongly affected by cavitation in the lower NPSH region. However, it is interesting to note that pump efficiency scarcely decreased even though remarkable inducer head degradation occurred. All the test results mentioned later were obtained at high NPSH values in order to eliminate the effects of cavitation on the overall performance of the pump. Suction performance of the present test pumps with cryogenic fluids is described in reference [14].

The overall performance of pump A, which was measured over a comparatively wide range of flow ratios, is shown in Fig. 5. Water was also used as pump fluid. Since the number of blades and the discharge angle of the main impeller were relatively small, a wide flow range with a negative $H-Q$ slope was obtained. The best pump efficiency was 68 percent, which seems to be a fairly high value for a small pump with an inducer. One of the most probable reasons for this high efficiency is the improvement of volumetric efficiency, which was accomplished by using plastic seal wearings that made possible quite small seal-clearances (less than 0.00005 m) of the wearing-ring seals. The influence of rotational speed on pump performance was very small over the range of speeds tested, as shown in Fig. 5. Incidentally, the ratios of calculated disk friction loss to brake horsepower were about 9.4 percent for 17,500 rpm and 10.1 percent for 12,500 rpm. The disk friction loss was estimated using the following equation [15], which takes into consideration the effect of the thickness of the impeller shroud at the tip.

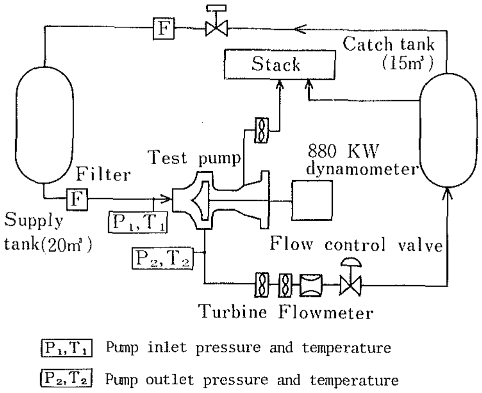

Fig. 3 Schematic diagram of LOX/LH_2 pump test facility

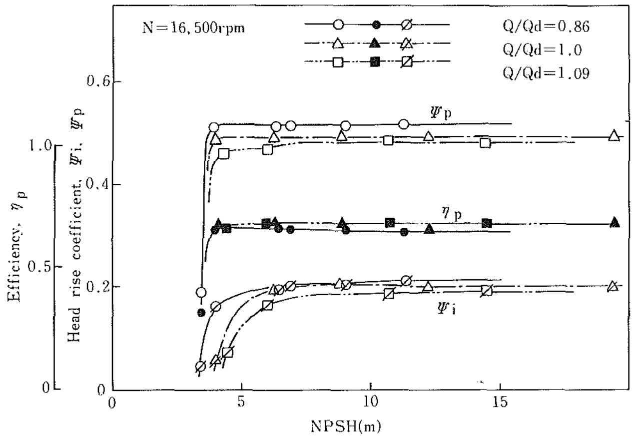

Fig. 4 Relationship between NPSH and overall performance of pump A (water test)

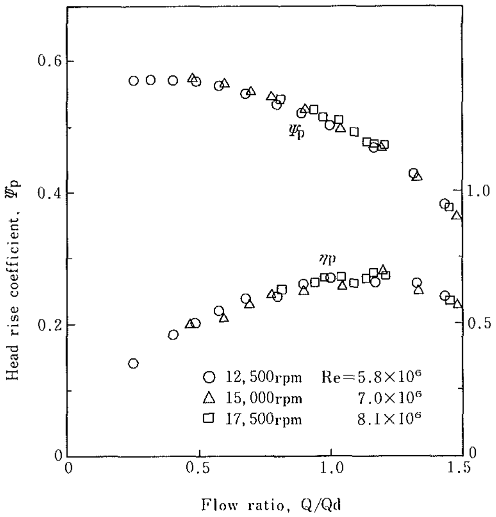

Fig. 5 Overall performance of pump A (water test)

$$L_d = \omega(C_s + C_c)$$

$$\cong \frac{1}{2} C_m \cdot \rho \cdot \omega^3 \cdot \left(\frac{D_{s2}}{2}\right)^5 \left(1 + \frac{5e}{D_{s2}}\right) \qquad (1)$$

where D_{s2} is the diameter of the impeller backshroud, e is the total of the shroud tip thickness, and C_m is the moment coefficient, which was determined by using data of reference [16] and in the case of high Reynolds' number, the extrapolation of these data. It was also confirmed that the influence of rotational speed on pump performance was small, with another higher speed pump (Fig. 13).

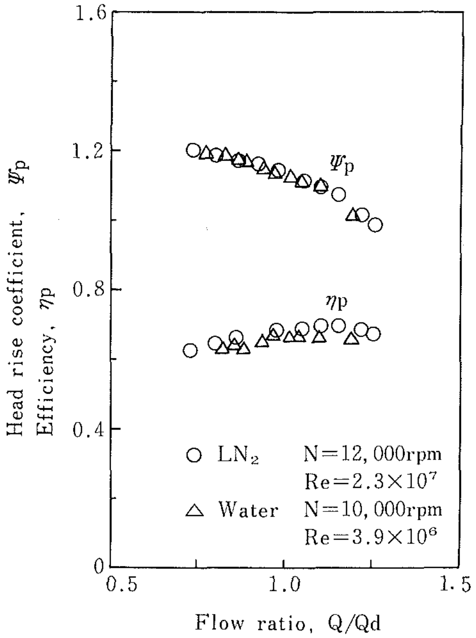

Fig. 6 Overall performance of pump F

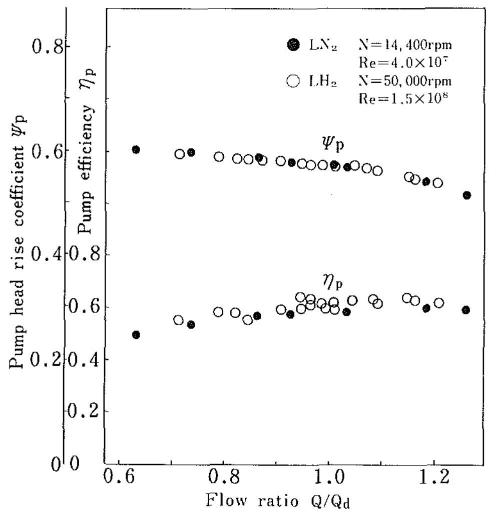

Fig. 7 Overall performance of pump D

In order to show the relationship between overall pump performance and pump fluids, a comparison of water and LN_2 tests with pump F is presented in Fig. 6, and the relationship of LN_2 and LH_2 tests with pump D is shown in Fig. 7. As shown in Fig. 6, almost the same head coefficients were obtained in both the water tests and the LN_2 tests, while LN_2 showed 2 ~ 3 percent higher efficiency than water. In Fig. 6 the decrease of impeller diameter in LN_2 was not taken into consideration. It was 0.4 percent of the diameter in the case of the water test. The efficiency difference in Fig. 6 is thought to be due to the difference of kinematic viscosity. The ratios of calculated disk friction loss to brake horsepower were 4.7 percent for LN_2 and 6.5 percent for water. Figure 7 shows the overall performance of pump D. The rotational speed of the LN_2 test was set at a level that would produce the same discharge pressure as that of the LH_2 test. There was extremely good agreement between the two tests regarding the pump head rise coefficient. It is well-known that LH_2 is much more compressible than LN_2. However, in the present test, the difference of LH_2 density between pump inlet and outlet, which was indirectly estimated using measured temperatures and pressures, was within about 1 percent. In Fig. 7, LH_2 showed about 4 percent higher efficiency than LN_2. The Reynolds' number of this LH_2 test was about 4 times larger than that of the LN_2 test. The ratio of calculated disk friction loss to brake horsepower of the LH_2 test was 2.2 percent lower than that of the LN_2 test.

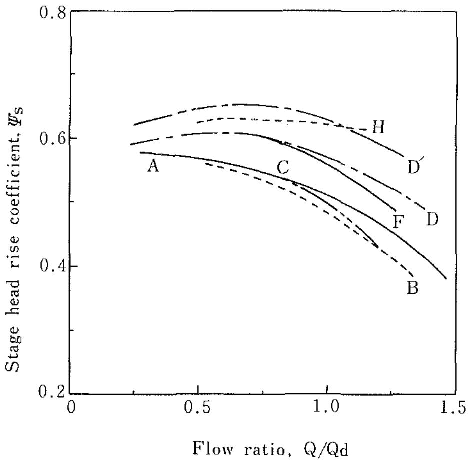

Fig. 8 Head/flow-rate curves of pump tested

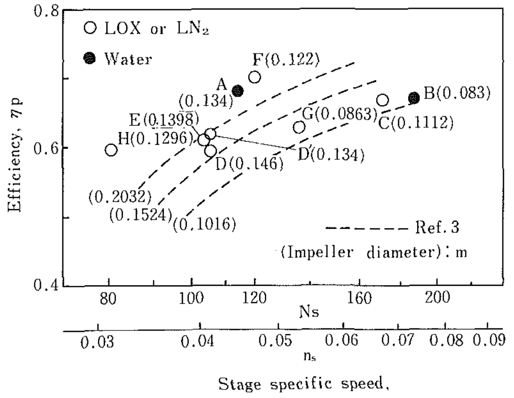

Fig. 9 Influence of impeller diameter on pump efficiency

Overall performance of almost all the test pumps in Table 1 is compared below. Firstly, the relationship between pump head rise coefficient and flow ratio is shown in Fig. 8. In this figure, the stage head rise coefficient, Ψ_s, is used with regard to pumps H and F. Figure 8 presents almost the same tendency as has been previously reported [17]. A bigger impeller discharge angle brought about the narrower range of flow ratio in which the slope of the $H-Q$ curve is negative. Pump A had a higher head rise coefficient than pump B though they both have the same impeller discharge angle, the same design flow rate and discharge pressure but a different design rotational speed and therefore a different specific speed. This difference in head rise coefficient was considered to be mainly due to the smaller blade length of pump B (smaller D_{i2}/D_{i1}) and secondarily to the higher volumetric efficiency of pump A.

The relationship between the stage specific speed and pump efficiency is shown in Fig. 9. In this figure, the influence of pump size on efficiency, which was presented in reference [2], is indicated by dotted lines. Figures in parentheses in Fig. 9 are impeller diameters. The efficiency of all the test pumps can be regarded as considerably higher than that indicated by the dotted lines. With the present test pumps, major components were precisely machined, and blade and shroud surfaces were smoothly finished. Furthermore, efforts were made in design to reduce leakage loss. These factors might explain the difference between the efficiency of these pumps and those previously reported on [2, 3, 4]. The influence of

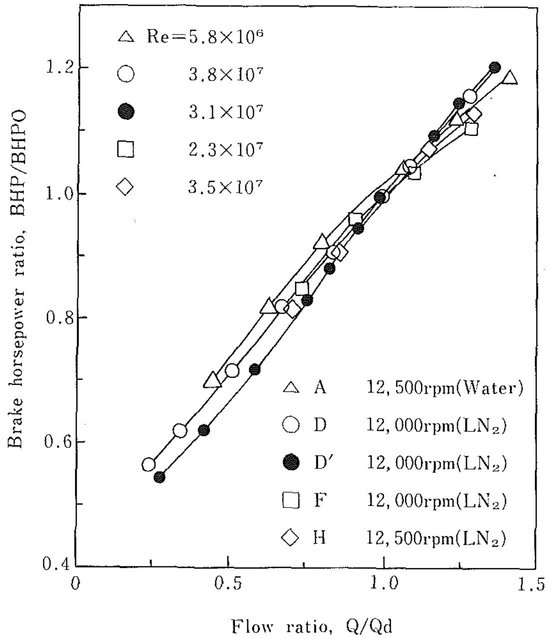

Fig. 10 Brake horsepower characteristics of tested pumps

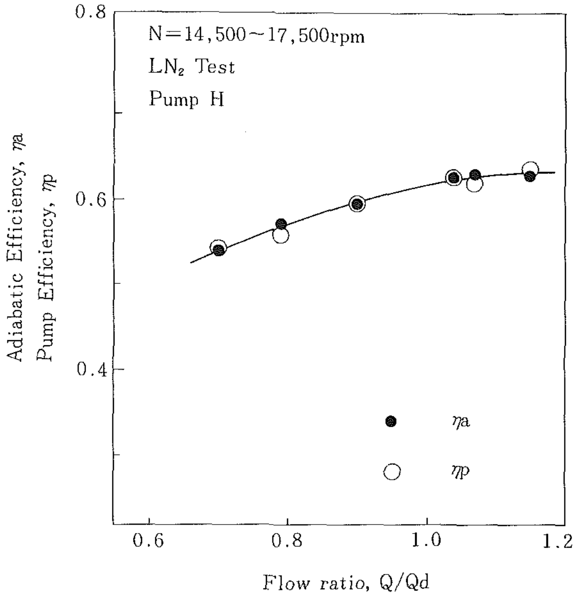

Fig. 12 Comparison of adiabatic efficiency and pump efficiency (pump H, LN_2 test)

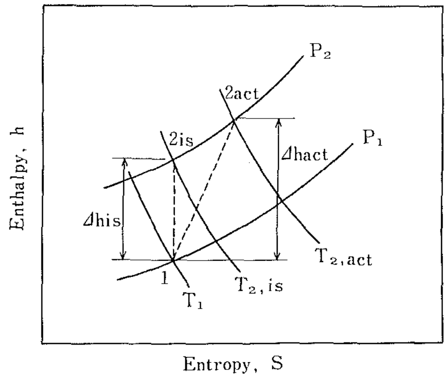

Fig. 11 Compression process of cryogenic fluids and efficiency

impeller diameters on pump efficiency was not so conspicuous in the present test. It seems that the efficiency differences among the present test pumps might be explained by the effect of factors other than impeller diameter. The high efficiency of the two-stage pumps F and H could be explained by the following. First, vaned diffusers functioned well, which was confirmed experimentally by pressure recovery in the diffuser vanes. The ratio of the pressure recovery in the diffuser vanes to the pump stage head was about 30 percent at the design point. Secondly, the pressure difference between the first-stage impeller outlet and the second-stage impeller inlet was small since an internal crossover passage was applied as shown in Fig. 2, which reduced leakage through the wearing ring seals between the backshroud of the first impeller and the frontshroud of the second impeller. The seal clearance of the wearing-ring seals was about 0.0001 m in the LN_2 test. Thirdly, the ratio of hydraulic loss between inducer and impeller to all the hydraulic losses became smaller than that of single-stage pumps. The high efficiency of pump A has been described in the discussion of Fig. 5. The comparatively low efficiency of pump E, which has vaned diffusers, was due to the deterioration of pressure recovery in the vaned diffusers at higher discharge pressures. The pressure recovery ratio decreased by about 5 percent. The lower efficiency of pump G is also thought to be mainly due to small pressure recovery in the vaned diffusers. The pressure recovery ratio was about 23 percent. The lower efficiency of pumps B, C, and D is thought to be mainly due to poor pressure recovery in the vaneless diffusers. Furthermore, the lower efficiency of pumps B, G, and C might also be due to their smaller impeller diameter.

Figure 10 shows the brake horsepower characteristics of the several pumps tested. BHPO in Fig. 10 is the brake horsepower at $Q/Q_d = 1$. These pumps had very similar brake horsepower curves. Pumps A and D showed slightly greater brake horsepower ratios in the low flow ratio ranges ($Q/Q_d < 1$) than the other pumps. This trend must be mainly due to the effect of the disk friction loss. Incidentally, the ratios of the calculated disk friction loss to the brake horsepower of pumps A, D, D′, F, and H are about 10.1, 8.5, 3.6, 4.7, and 8.1 percent, respectively, at the design point ($Q/Q_d = 1$). The greater disk friction loss of pump A is due to the higher kinematic viscosity of water. The greater disk friction losses of pumps D and H are due to greater impeller backshroud tip thickness, which is necessary to make the profile of the balance piston orifices appropriate, as shown in Fig. 2.

Adiabatic Efficiency. A typical compression process of cryogenic fluid is presented in Fig. 11. Enthalpy of fluid is given by equation (2).

$$h = u + p \cdot v \tag{2}$$

The change of enthalpy in the adiabatic compression process is represented by equation (3).

$$dh = du + p \cdot dv + v \cdot dp = dq + v \cdot dp \tag{3}$$

where dq is the heat generated due to various kinds of losses. The increases of enthalpy in the isentropic and actual compression processes are represented by equations (4) and (5), respectively.

$$\Delta h_{\text{is}} = \int_1^{2\text{is}} v \cdot dp \tag{4}$$

$$\Delta h_{\text{act}} = \Delta q_{12} + \int_1^{2\text{act}} v \cdot dp \tag{5}$$

The adiabatic efficiency is represented by equation (6).

$$\eta_a = \frac{\Delta h_{\text{is}}}{\Delta h_{\text{act}}} \tag{6}$$

On the other hand, the ordinary efficiency is given by

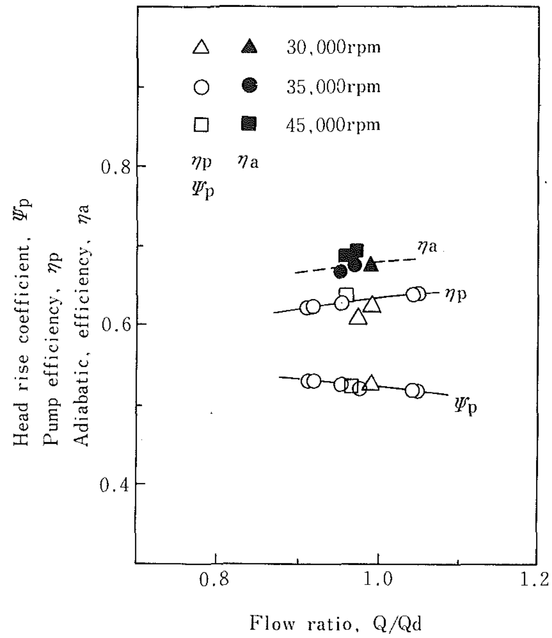

Fig. 13 Comparison of adiabatic efficiency and pump efficiency (pump G, LN_2 test)

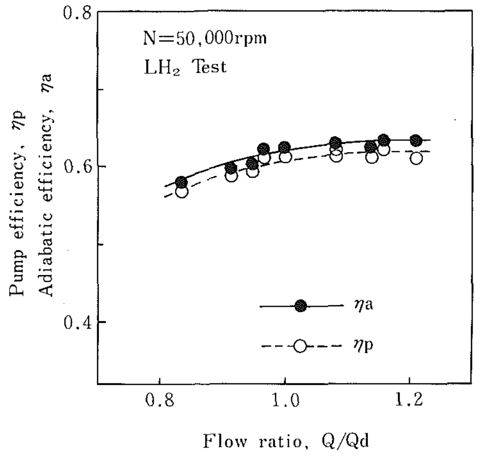

Fig. 14 Comparison of adiabatic efficiency and pump efficiency (pump D, LH_2 test)

equation (7) by neglecting both the kinetic head and the geodetic head.

$$\eta_p = \frac{\Delta p \cdot Q/\dot{m}}{C \cdot \omega/\dot{m}} = \frac{\Delta p \cdot v}{C \cdot \omega/\dot{m}} \qquad (7)$$

Here, the denominators of equations (6) and (7) are equal because they represent energy input to the pump. So, the difference between the adiabatic and ordinary efficiencies results from the numerators of equations (6) and (7), that is the difference between the term $\Delta p \cdot v$ and the change of enthalpy in the isentropic compression process. If the change of specific volume in the isentropic compression is negligibly small, it is expected that the adiabatic and ordinary efficiencies should be in good agreement. The authors would like to make clear this important point in order to know whether or not the measured adiabatic efficiency is utilizable for cryogenic pumps.

Figures 12, 13, and 14 present a comparison of measured adiabatic efficiency and pump efficiency. Figure 12 shows the results of the LN_2 test with pump H. Maximum discharge pressure was 14 MPa and maximum temperature rise of the pump fluid was 10.7 K. In Fig. 12, the adiabatic efficiency fairly well agreed with the pump efficiency. Estimations using equation (4) and the ordinary pump efficiency in Fig. 12 show that the maximum change of specific volume during the isentropic compression process was about 1.5 percent, which decreased the adiabatic efficiency by about 0.5 percent compared with the ordinary efficiency. However, this difference between the two kinds of efficiencies could not be confirmed in Fig. 12. Figure 13 shows the results of the LN_2 test with pump G. The adiabatic efficiency is 5 ~ 6 percent higher than the pump efficiency. In this test, the coolant of the self-lubricated ball bearings, which amounted to 4.5 percent of the total pump fluid, was allowed to escape into the atmosphere. This coolant, supplied from the impeller discharge, passed through the balance piston orifices, cooled the bearings and flowed out of the pump (see Fig. 1). When estimating the effect of this and other resultant effect, including mechanical and disk friction losses, on adiabatic efficiency, it was noted that the adiabatic efficiency shown in Fig. 13 must be lowered by about 6 percent in order to make a reasonable comparison of the two efficiencies. Consequently, it can be concluded that this adiabatic efficiency agreed with the ordinary pump efficiency within an error of a few percentage points. Figure 14 shows another comparison of the two efficiencies which were obtained by an LH_2 test with pump D. At the design point, it was $\eta_p = 60.5$ percent and $\eta_a = 62.0$ percent. The discharge pressure and temperature rise of the pump fluid at the design point were about 6 MPa and 7 K, respectively. When analyzing the result shown in Fig. 14, the effect of heat flow must be considered in addition to the coolant effect of about 4 percent on adiabatic efficiency because the pump casing insulation was not sufficient. The heat flow could be measured under conditions in which the pump rotating speed was zero, but pump fluid (LH_2) flowed inside the pump. Assuming that the heat flow during pump operation was the same as that mentioned above, the effect of the heat flow on the adiabatic efficiency could be estimated; it lowered the adiabatic efficiency by 1.5 percent at the design point ($Q/Q_d = 1$). This assumption seems to be fairly reasonable because the heat flow was almost completely determined by heat transfer at the pump casing surface, which was completely covered with liquid air. Therefore, the adiabatic efficiency shown in Fig. 14 must be lowered by 2.5 percent (= 4 percent − 1.5 percent). The change of specific volume in the isentropic compression process at the design point was 5.5 percent, which decreased the adiabatic efficiency by about 1.5 percent compared with the ordinary pump efficiency. The two efficiencies can be considered to be in comparatively good agreement.

Concluding Remarks

Several small cryogenic pumps have been made and tested for liquid rocket engine research and development. These pumps have small impellers and are characterized by high speed and high head. In this paper, the following two items were mainly described. Firstly, overall pump performance was compared with data available on other small pumps [2-4]. Secondly, adiabatic efficiency relative to cryogenic fluids was investigated in order to confirm its applicability to cryogenic pumps. Main findings in this study are as follows:

(1) Higher pump efficiency was obtained even in the range of small stage specific speeds compared with previously reported results. This tendency was particularly remarkable with the two-stage centrifugal pumps.

(2) Adiabatic efficiency which was obtained by measured pressures and temperatures agreed well with ordinary pump efficiency within an error of a few percentage points when the change of specific volume in the compression process was negligibly small.

Statement of Uncertainties

Uncertainties of the head rise coefficients and the flow ratios are about ±0.002 and ±0.005, respectively, in Figs. 4, 5, 6, 7, 8, 10, 12, 13, and 14. Uncertainties of the rotational speed and the torque are about ±0.002 and ±0.005, respectively. Uncertainty of the ordinary pump efficiency is about ±0.015 in Figs. 4, 5, 6, 7, 9, 12, 13, and 14. Uncertainty of the temperature is about ±0.1 K. Uncertainty of the adiabatic efficiency in Figs. 12, 13, and 14 is about ±0.01.

References

1 Stepanoff, A. J., *Centrifugal and Axial Flow Pumps*, 2nd ed., Wiley, 1967.

2 Anon., *Liquid Rocket Engine Centrifugal Flow Turbopumps*, NASA SP-8109, 1973.

3 Hidebrand, P., et al., "Centrifugal Pump (High Pressure) for Power Transmissions," Rep. No. AFAPL TR-66-12(AD-480108), The Garrett Corp., 1966.

4 Campbell, W. E., and Farquhar, J., "Centrifugal Pumps for Rocket Engine," *Proceedings of the Symposium on Fluid Mechanics, Acoustics and Design of Turbomachinery*," NASA SP-304, 1974, pp. 655-688.

5 Kamijo, K., Suzuki, A., Shimura, T., Hashimoto, R., Watanabe, M., Watanabe, Y., Iwabuchi, T., and Mori, Y., "Experimental Investigation of Small, High-Speed High-Head Oxygen Pump," Nat. Aerospace Lab. (Japan), NAL Rept. TR-415, 1975.

6 Diem, H. G., "Recent Progress on the Advanced Space Engine," AIAA Paper No. 78-940, 1978.

7 Zachary, A. T., Csomor, A. and Tignac, L. L., "Turbopumps for Cryogenic Upper Stage Engines," NASA CR-120193, 1973.

8 Nosaka, M., Miyakawa, Y., Kamijo, K., Suzuki, M. and Kikuchi, M., "Study on Sealing Characteristics of High Speed, Contacting Mechanical Seals for Liquid Hydrogen," *JSLE*, Vol. 29, No. 1, 1984.

9 Suzuki, M., Kamijo, K., Watanabe, Y., and Mori, M., "Seal Performance and Durability of Rotating Shaft Seals of Liquid Oxygen Turbopump," Nat. Aerospace Lab. (Japan), NAL Rept. TR-717, 1982.

10 Suzuki, M., Nosaka, M., Kamijo, K., Kikuchi, M., and Mori, M., "Research and Development of a Floating-Ring Seal for a Liquid Hydrogen Turbopump," Nat. Aerospace Lab. (Japan), NAL Rept. TR-710, 1982.

11 Hans, M. R., and Lloyd, A. W., "ASRDI Oxygen Technology Survey, Vol. 1: Thermophysical Properties," NASA SP-3071, 1972.

12 Angus, S., et al., *International Thermodynamic Tables of the Fluid States, 6 Nitrogen*, Pergamon Press, 1978.

13 McCarty, R. D., "Hydrogen Technological Survey—Thermophysical Properties," NASA SP-3089, 1975.

14 Kamijo, K., and Hirata, K., "Performance of Small High Speed Pumps," ASME *Symposium on Performance Characteristics of Hydraulic Turbines and Pumps*, Boston, Bk. No. H00280, 1983, p. 165-171.

15 Senoo, Y., "Internal Flows and Fluid Machineries (in Japanese)," Yokendo, Inc., 1981, p. 191.

16 Schlichting, H., *Boundary Layer Theory*, 6th ed., McGraw-Hill, 1968, p. 609.

17 Varley, F. A., "Effect of Impeller Design and Surface Roughness on the Performance of Centrifugal Pumps," *Proc. Inst. Mech. Eng.*, Vol. 175, No. 21, 1961, p. 955.

Statement of Uncertainties

Uncertainties of the head rise coefficients and the flow ratios are about ±0.002 and ±0.005, respectively, in Figs. 4, 5, 6, 7, 8, 10, 12, 13, and 14. Uncertainties of the rotational speed and the torque are about ±0.002 and ±0.005, respectively. Uncertainty of the ordinary pump efficiency is about ±0.015 in Figs. 4, 5, 6, 7, 9, 12, 13, and 14. Uncertainty of the temperature is about ±0.1 K. Uncertainty of the adiabatic efficiency in Figs. 12, 13, and 14 is about ±0.01.

References

1 Stepanoff, A. J., *Centrifugal and Axial Flow Pumps*, 2nd ed., Wiley, 1967.

2 Anon., *Liquid Rocket Engine Centrifugal Flow Turbopumps*, NASA SP-8109, 1973.

3 Hidebrand, P., et al., "Centrifugal Pump (High Pressure) for Power Transmissions," Rep. No. AFAPL TR-66-12(AD-480108), The Garrett Corp., 1966.

4 Campbell, W. E., and Farquhar, J., "Centrifugal Pumps for Rocket Engine," *Proceedings of the Symposium on Fluid Mechanics, Acoustics and Design of Turbomachinery*," NASA SP-304, 1974, pp. 655-688.

5 Kamijo, K., Suzuki, A., Shimura, T., Hashimoto, R., Watanabe, M., Watanabe, Y., Iwabuchi, T., and Mori, Y., "Experimental Investigation of Small, High-Speed High-Head Oxygen Pump," Nat. Aerospace Lab. (Japan), NAL Rept. TR-415, 1975.

6 Diem, H. G., "Recent Progress on the Advanced Space Engine," AIAA Paper No. 78-940, 1978.

7 Zachary, A. T., Csomor, A. and Tignac, L. L., "Turbopumps for Cryogenic Upper Stage Engines," NASA CR-120193, 1973.

8 Nosaka, M., Miyakawa, Y., Kamijo, K., Suzuki, M. and Kikuchi, M., "Study on Sealing Characteristics of High Speed, Contacting Mechanical Seals for Liquid Hydrogen," *JSLE*, Vol. 29, No. 1, 1984.

9 Suzuki, M., Kamijo, K., Watanabe, Y., and Mori, M., "Seal Performance and Durability of Rotating Shaft Seals of Liquid Oxygen Turbopump," Nat. Aerospace Lab. (Japan), NAL Rept. TR-717, 1982.

10 Suzuki, M., Nosaka, M., Kamijo, K., Kikuchi, M., and Mori, M., "Research and Development of a Floating-Ring Seal for a Liquid Hydrogen Turbopump," Nat. Aerospace Lab. (Japan), NAL Rept. TR-710, 1982.

11 Hans, M. R., and Lloyd, A. W., "ASRDI Oxygen Technology Survey, Vol. 1: Thermophysical Properties," NASA SP-3071, 1972.

12 Angus, S., et al., *International Thermodynamic Tables of the Fluid States, 6 Nitrogen*, Pergamon Press, 1978.

13 McCarty, R. D., "Hydrogen Technological Survey—Thermophysical Properties," NASA SP-3089, 1975.

14 Kamijo, K., and Hirata, K., "Performance of Small High Speed Pumps," ASME *Symposium on Performance Characteristics of Hydraulic Turbines and Pumps*, Boston, Bk. No. H00280, 1983, p. 165-171.

15 Senoo, Y., "Internal Flows and Fluid Machineries (in Japanese)," Yokendo, Inc., 1981, p. 191.

16 Schlichting, H., *Boundary Layer Theory*, 6th ed., McGraw-Hill, 1968, p. 609.

17 Varley, F. A., "Effect of Impeller Design and Surface Roughness on the Performance of Centrifugal Pumps," *Proc. Inst. Mech. Eng.*, Vol. 175, No. 21, 1961, p. 955.

DISCUSSION

B. Schiavello[1]

The authors have presented an extensive comparison of performance of several small high speed pumps of low specific speed. The data given in the paper, including the main geometrical design parameters of components, i.e., inducer, impeller, vaneless (vaned) diffuser of the various pump configurations are valuable information to pump designers.

All of this information gives a clear idea of both the matching of the various pump components and the distribution of losses in each test model and helps in analyzing and comparing the performance. In this regard it should be useful to have the values of surface roughness for vaneless or vaned diffuser and volute.

It is the writer's opinion that a so-called "efficiency-chart" does not give physical insights on pump performance as related to design. Firstly, these charts are based on statistical data with more or less broad scattering, which prevents us from using them as an absolute analysis tool for pump performance. Secondly, all the various charts which are published in the literature either correlate pump overall efficiency to: (*a*) specific speed and impeller diameter, (*b*) specific speed and capacity at b.e.p. (best efficiency point) references [1 and 3 of the paper] or correlate pump variable losses to specific speed and capacity [18]. This creates a problem since both pump efficiency and relative losses are nondimensional parameters which can be correlated [19] by the method of dimensional analysis to more than two nondimensional groups of parameters, e.g., specific speed (n_s), specific capacity ($q_s = Q/ND_2{}^3$), Reynolds number and relative roughness. For accurate prediction, the last two parameters have to be defined for each pump component.

We should note that both pump b.e.p. capacity and impeller diameter are dimensional parameters, which properly are subject to a size scaling effect and therefore can present good correlation with overall efficiency for homogeneous families of pumps, when predominant sources of losses are related to wall friction. However, it should be expected that losses from eddy viscosity and mixing and diffusion phenomena prevail in small, high speed pumps with impeller blades of high exit angle and high camber as well as smoothly finished surface, all of which are characteristic of the models presented in the paper. In addition, these models have high vane loading with consequent high secondary flow losses. All of these factors make the models more sensitive to Reynolds number than to impeller diameter, so that an efficiency chart based on n_s and D_2, as used by the authors, is not suitable to correlate the efficiency of their pump models.

Another reason to suspect the application of conventional charts for pump efficiency by the author is related to the special geometry of the authors' pumps. These pumps utilize inducers, and, in the majority of cases, special impellers with a large number of short blades with high exit angles, while efficiency charts for the same range of n_s are based on pumps without inducers and with impellers having a small number of long blades of logarithmic type and low exit angle. In any case, if the authors want to use efficiency charts based on n_s, the overall efficiency should be corrected for the inducer efficiency and the inducer head should be excluded from the calculation of n_s for consistency. To help the analysis, design values for both inducer efficiency and head should be given in the paper.

In the paper, the high efficiency of pump "A" is partially related to a reduction of leakage flow by using small clearance plastic seal wear rings. It is therefore desirable that the authors provide values of volumetric efficiency calculated at 17,500rpm and 12,500rpm as already calculated for disc friction losses.

For pump A, the authors have calculated the ratio of disc friction loss to brake horsepower at two different rotational speeds. If we assume that the brake horsepower varies with ω^3, we find that Cm varies with $\mathrm{Re}^{-1/2}$, which corresponds to a flow regime with laminar separated boundary layers [20]. As Reynolds numbers here are higher than 10^6, we would expect turbulent flow, and therefore Cm should vary as $\mathrm{Re}^{-1/4}$ for merged boundary layers or with $\mathrm{Re}^{-1/5}$ for separated boundary layers. I would like to ask the authors if they can give more information about the assumptions made to calculate the ratio of disc friction loss to the brake horsepower for pump A as well as pumps D, D1, F, and H (page 11), so that this apparent contradiction can be understood.

---

[1] Director of Hydrodynamics, Worthington Pump Division, Dresser Industries, Inc., Mountainside, N.J.

Additional References

18 Anderson, H. H., "Statistical Records of Pump and Water Turbine Efficiencies," Scaling for Performance Prediction in Rotordynamic Machines, I Mech E. Conference Publications 1977-7, pp. 1-6.

19 Schiavello, B., "Correlation for Maximum Efficiency of the Geometrical and Operating Design Parameters of Single Stage Centrifugal Pumps with Specific Speed," Graduation Thesis, University of Rome, 1974 (in Italian).

20 Daily, J. W., and Nece, R. E., "Chamber Dimension Effects on Induced Flow and Frictional Resistance of Enclosed Rotating Disks," ASME *Journal of Basic Engineering*, Mar. 1960, pp. 217-232.

Authors' Closure

The authors would like to express their gratitude to Mr. Schiavello for his discussions and comments to this paper.

First of all, the measured surface roughnesses of vaneless diffusers, vaned diffusers and volutes were from 5 to 10 μm, from 3 to 5 μm, and from 10 to 15 μm, (Rmax), respectively. With regard to efficiency charts, Mr. Shiavello's comments are well presented but Fig. 9 in this paper was also made in order to show that the influence of impeller diameters on pump efficiency was not so conspicuous with the present small high speed pumps. Regarding the comment of the pumps with inducers, design values of inducer efficiency were from 75 percent to 80 percent and design ratios of inducer head to pump head ranged from 3.5 percent to 10 percent. Therefore, it can be considered that the influence of inducers on the overall pump performance was comparatively small. The calculated volumetric efficiency of pump A was about 95 percent. With disk friction loss calculations, Cm was calculated with $R^{-1/5}$. The ratio of calculated disk friction loss to brake horsepower for 17,500 rpm of pump A was not 8.7 percent but 9.4 percent.

A Numerical Study of Pulsed Turbulent Pipe Flow

V. Reddy

J. B. McLaughlin

R. J. Nunge

Department of Chemical Engineering,
Clarkson University,
Potsdam, NY 13676

A numerical study of fully developed turbulent pipe flow due to a sinusoidally varying (with respect to time) axial pressure gradient was carried out using a nonlinear three-dimensional model. Pseudospectral methods were used to solve the model equations. The pulsation frequency was characteristic of the wall region eddies in steady turbulent flow. Attention was focused on the viscous wall region, and it was found that the mean profiles of axial velocity, fluctuation intensities, and turbulence production rate were essentially the same as in steady flow. The fluctuation intensities and the turbulence production rate showed a definite phase relationship to the pressure gradient. The turbulence production rate was the largest at the time in the pulsation cycle at which the largest adverse pressure gradient existed.

1 Introduction

The objective of the present study was to determine the effect of sinusoidal flow pulsations on turbulence structure and momentum transport. We were motivated, in part, by the experiments of Mizushina et al. [1, 2] who observed a resonance between the generation of turbulence and applied pulsations for sufficiently large pulsation frequencies. In addition, Lemlich [3] has suggested that high frequency pulsations might increase heat transfer rates significantly even for nonreversing flows.

The results to be reported were obtained by solving a three-dimensional, nonlinear model of turbulent pipe flow using pseudospectral techniques. We have previously used the model to study steady turbulent flow (see references [4, 5]) and we found good agreement with experimental results for the rate of production of turbulence as well as the intensities of fluctuating quantities. The model was modified to include a sinusoidally varying external pressure gradient superimposed on a steady external pressure gradient. The period of the pulsations was 100 in wall units (unit equal to ν/u_*^2, where the symbols ν and u_* are defined in the nomenclature) and the amplitude of the oscillations in the bulk velocity was 50 percent of the time averaged bulk velocity.

The choice of the pulsation period was motivated by the experiments of Hogenes and Hanratty [6] who found that the characteristic time scale associated with wall eddies is roughly 100 in wall units. In addition, Bakewell and Lumley [7] and Sirkar [8] have found that the median period of velocity fluctuations in the viscous wall region scales on wall variables and is equal to 110.

In our model the flow pulsations were imposed through a sinusoidally varying axial pressure gradient. The ensemble average[1] of the dimensionless[2] axial pressure gradient was expressed as

$$-\partial P/\partial X = G_s + P_{\text{amp}}\cos(2\pi t/T_p) \qquad (1)$$

where G_s is the pressure gradient associated with steady flow, P_{amp} is the amplitude of the pressure pulsations, and T_p is the time period of pulsations. In Fig. 1 we show a plot of $-\partial P/\partial X$ as a function of the pulsation phase angle $(2\pi t/T_p)$. For the calculations to be reported, the amplitude of the oscillatory part of the pressure gradient was approximately 400 times larger than the steady part.

2 High Frequency Behavior

At sufficiently high frequencies of pulsation the time taken for an eddy in the middle of the pipe to turn over would be larger than the time period of pulsations. Consequently, the turbulence in the middle of the pipe cannot respond to the pulsations. Brown et al. [9] termed this "frozen viscosity" (FV) behavior and experimentally determined the frequency range for FV behavior to be

$$S/\text{Re} > 0.1 \qquad (2)$$

where $S = \Omega R^2/\nu$, Ω is the angular frequency of pulsations, R is the radius of the pipe, and Re is the Reynolds number based on the bulk velocity and the diameter.

By assuming the typical eddy size in the middle of the pipe

Contributed by the Fluids Engineering Division for publication in the JOURNAL OF FLUIDS ENGINEERING. Manuscript received by the Fluids Engineering Division, March 27, 1984.

[1] The ensemble average is defined as:

$$f(t) = (1/N) \sum_{n=0}^{N-1} f(t + 2\pi n t/T_P).$$

When the frequency of pulsations is comparable to the frequency of turbulence fluctuations the ensemble average is more meaningful than the time average.

[2] In our model all variables are made dimensionless with the so-called wall variables, ν and u_*, where ν is the kinematic viscotity and u_* is the friction velocity. The unit of length is ν/u_* and the unit of time is ν/u_*^2.

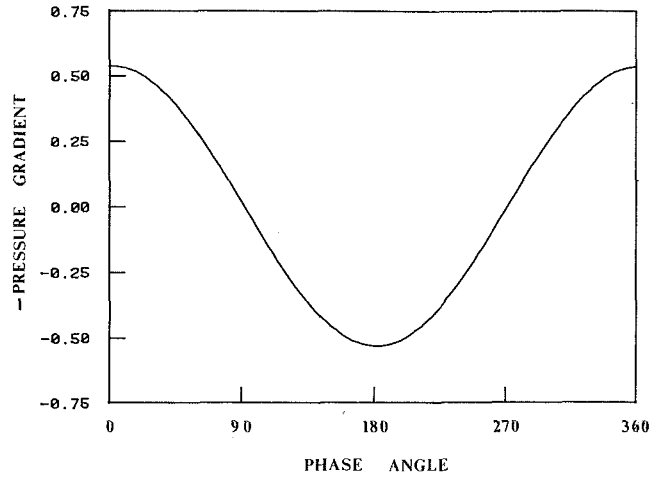

Fig. 1 Ensemble averaged axial pressure gradient in pulsed flow

Table 1 Relationship between inner and outer variables

Re	Z	R	Z/R
10,000	34.1	316	0.108
30,000	34.1	827	0.041
60,000	34.1	1520	0.022
100,000	34.1	2370	0.014

to be equal to the radius of the pipe and comparing the eddy turnover time to the time period of pulsations, Reddy [5] estimated the frequency range for FV behavior to be

$$T_p < R \tag{3}$$

For $10^4 < \mathrm{Re} < 10^5$, the estimates given by (2) and (3) are about the same.

The FV condition implies that the axial velocity in the middle of the pipe and the pressure gradient are 90 deg out of phase because of the fact that, for high frequencies, the ex-

Table 2 Grid points in the vertical direction

Grid Point	Z
1	∞
2	1005
3	246
4	106
5	56.8
6	34.1
7	21.8
8	14.5
9	9.75
10	6.57
11	4.35
12	2.79
13	1.67
14	0.897
15	0.386
16	0.0946
17	0.0

Nomenclature

$\mathbf{F} = \mathbf{V} \times \omega - (\partial P/\partial X)\hat{X}$
G_s = pressure gradient in steady flow
$i = \sqrt{-1}$
j,k = arbitrary integers
l,m = Fourier indices in the axial and spanwise directions
n = Chebychev index
N_X, N_Y, N_Z+1 = number of grid points in the axial, spanwise, and vertical directions
P = pressure
P_{amp} = amplitude of the pressure pulsations
P_r = rate of production of turbulent kinetic energy
p = fluctuating component of the pressure
R = radius of the pipe
Re = Reynolds number
$S = \Omega R^2/\nu$
T_p = time period of pulsations
T_n = Chebychev polynomial
t = time
u_* = friction velocity
U_{amp} = amplitude of oscillations in the free stream velocity
U_p = pulsating component of the axial velocity
U,V,W = axial, spanwise, and vertical velocities
$\mathbf{V}$ = velocity field
X,Y,Z = axial, spanwise, and vertical coordinates
Z_e = value of Z beyond which the horizontally averaged axial velocity is set equal to a known profile
Z_m = used in relating Z to ζ
$\alpha = 2\pi/\lambda_x$
$\beta = 2\pi/\lambda_y$
λ_x, λ_y = repetition lengths in the axial and spanwise directions
ω = vorticity
Ω = angular frequency of pulsations
π = dynamic pressure
ν = kinematic viscosity
ζ = transformed vertical coordinate
$< \ >$ = average with respect to X and Y

Subscripts

j = time step
$-$ = ensemble average
$=$ = long time average
$\tilde{}$ = mixed spectral (in X and Y) — physical (in Z) space
$\hat{}$ = fields at the end of the second fractional step
$\hat{\hat{}}$ = fields at the end of the second fractional step

ternally imposed acceleration dominates the nonlinear and viscous terms everywhere except the vicinity of the wall and, therefore, the pulsating component of the axial velocity can be estimated from

$$\partial U_p/\partial t = P_{\text{amp}}\cos(2\pi t/T_p)\,. \tag{4}$$

Reddy [5] carried out a series of computations using a one-dimensional model of pulsed flow. He found that if the frequency was chosen to satisfy (2) (or (3)) the computed phase shift, except very near the wall, was 90 deg and the amplitude of the oscillations in the axial velocity was equal to that calculated from equation (4).

In Table 1 we show the values of R at various Reynolds numbers. All our calculations were made at Re = 60,000 and T_p = 100 and therefore the flow was in the frozen viscosity regime.

3 Description of the Model

Our model focuses on the wall region which extends between $Z = 0$ and $Z = 30$ to 50, where Z is the dimensionless vertical distance measured from the wall. We were especially interested in studying the interaction between the imposed pulsations and the turbulence in the wall region. Furthermore, since we are in the FV regime the turbulence far from the wall cannot respond to the pulsations. Also, in summarizing previous experimental work on oscillating flows Simpson et al. [10] report that outside the wall region the turbulence structure is unaffected by the imposed oscillations. In Table 1 we show the values of Z/R for $Z = 50$ as a function of Reynolds number. Since the thickness of wall region at Re = 60,000 is only a small fraction of the radius we neglected curvature and used a Cartesian coordinate system. In this system the Y-axis points in the spanwise direction and the Z-axis is perpendicular to the wall.

Periodic boundary conditions were imposed in the axial and spanwise directions and the dimensionless repetition lengths were chosen to be 630 and 135, respectively. These values were chosen from the experimental results of Morrison et al. [11] and are further discussed by McLaughlin et al. [4].

In order to save computer time and storage, the following reflection symmetry in the spanwise direction was imposed on the velocity field:

$$U(X,Y,Z,t) = U(X,-Y,Z,t) \tag{5a}$$

$$V(X,Y,Z,t) = -V(X,-Y,Z,t) \tag{5b}$$

$$W(X,Y,Z,t) = W(X,-Y,Z,t) \tag{5c}$$

The disadvantage of the reflection symmetry was that it introduced an unphysical spanwise dependence into the time averages. When computing time or ensemble averaged quantities we also averaged with respect to X and Y. The average with respect to Y removed the spanwise dependence that was introduced by the reflection symmetry and the average with respect to X improved the statistics. It should be noted that our time and ensemble averages were essentially independent of X.

In order to obtain good vertical resolution near the wall, we used Chebyshev polynomial expansions in a transformed variable, ζ, which is defined as

$$\zeta = (Z - Z_m)/(Z + Z_m)\,.$$

The value of Z_m was chosen to optimize the grid spacing. In all our calculations $Z_m = 9.75$ which gives a high concentration of grid points in the vicinity of $Z = 10$ where the production of turbulence is highest. In Table 2 we show the values of Z at various grid points. It can be seen that the resolution far from the wall is very poor and in fact is larger than the Prandtl mixing length. In order to compensate for the poor resolution, the following extra condition was imposed on the horizontally (with respect to X and Y) averaged axial velocity:

$$<U> = (2.4\ln(Z) + b)\,(1 + U_{\text{amp}}\sin(2\pi t/T_p))\,, Z_e \le Z \le R \tag{6a}$$

$$<U> = U_\infty(1 + U_{\text{amp}}\sin(2\pi t/T_p))\,, R < Z \le \infty \tag{6b}$$

where < > denotes an average over X and Y will be used as such in the rest of the text, and $U_\infty = 2.4\ln(R) + b$. The conditions in equations (6*a*) and (6*b*) guarantee that, outside the viscous wall region, the horizontally and time-averaged velocity will be a good approximation to the experimental profile and that the bulk flow oscillations will have the desired amplitude. We set $Z_e = 34.13$ and, using a one-dimensional model, Reddy confirmed that for $Z > 34.13$ equation (4) was satisfied.

In all our calculations we used 16 grid points each in the axial and spanwise directions, and 17 grid points in the vertical direction. McLaughlin et al. [4] showed that this provided adequate resolution.

Since all quantities were made dimensionless using wall variables, we must impose the following condition for consistency:

$$\overline{\overline{<\partial U/\partial Z>}}\,|_{Z=0} = 1 \tag{7}$$

where the double overbar indicates a long time average over a number of pulse cycles. The constant b in equation (6*a*) was determined by an iterative procedure such that equation (7) was satisfied. It was found to be equal to 7.03. The condition in equation (7) follows from a force balance between the time average force due to the external pressure gradient and that due to the wall shear stress.

The Navier-Stokes equation and the equation of continuity are given by

$$\partial\mathbf{V}/\partial t = \mathbf{V}\times\omega - (\partial\bar{P}/\partial X)\hat{X} - \nabla\Pi + \nabla^2\mathbf{V} \tag{8}$$

$$\nabla\cdot\mathbf{V} = 0 \tag{9}$$

where $\mathbf{V} = (U, V, W)$ is the velocity field, $\omega = \nabla\times\mathbf{V}$ is the vorticity, $\Pi = p + (1/2)(\mathbf{V}\cdot\mathbf{V})$, p is the fluctuating component of the pressure, $\partial\bar{P}/\partial X$ is the ensemble averaged axial pressure gradient given by equation (1), and $\hat{X}$ is a unit vector in the X direction. In our model the velocity field was assumed to satisfy equations (8), (9), the extra conditions given by equations (6), and the reflection symmetry given by equations (5). The following boundary conditions were imposed on the velocity field:

$$\mathbf{V}(X,Y,0,t) = 0 \tag{10a}$$

$$\mathbf{V}(X,Y,\infty,t) = (U_\infty(1 + U_{\text{amp}}\sin(2\pi t/T_p)),0,0) \tag{10b}$$

$$\mathbf{V}(X + j\lambda_x, Y + k\lambda_y, Z, t) = \mathbf{V}(X,Y,Z,t) \tag{10c}$$

for all integer values of j and k

where λ_x and λ_y are the repetition lengths in the axial and spanwise directions.

In order to satisfy the periodic boundary conditions, the velocity field was represented by a Fourier series in the horizontal directions, and as mentioned earlier a Chebyshev series representation was used in the vertical direction:

$$\mathbf{V}(X,Y,Z,t) = \sum_{|l| < \frac{N_x}{2}} \; \sum_{|m| < \frac{N_y}{2}} \; \sum_{n=0}^{N_z} \tilde{\mathbf{V}}(l,m,n,t)\exp\{i(l\alpha X + m\beta Y)\}T_n(\zeta) \tag{11}$$

where N_X, N_Y, and $N_Z + 1$ are the number of grid points in the axial, spanwise, and vertical directions respectively, $\alpha = 2\pi/\lambda_x$, $\beta = 2\pi/\lambda_y$, and the expansion coefficients, $\tilde{\mathbf{V}}(l, m, n, t)$, are referred to as the representation of the velocity field in spectral space. In our calculations it was more convenient to use a mixed spectral (in X and Y) — physical (in Z) representation which is obtained by carrying out the summation over the n index in equation (11):

$$\mathbf{V}(X,Y,Z,t) = \sum_{|l|<\frac{N_x}{2}} \sum_{|m|<\frac{N_y}{2}} \tilde{\mathbf{V}}(l,m,Z,t)\exp\{i(l\alpha X+m\beta Y)\}. \tag{12}$$

From here on a $\tilde{}$ overline will be used to denote a mixed spectral (in X and Y) — physical (in Z) representation. The initial condition for the pulsed flow runs was specified by time-evolving a steady flow (no oscillatory pressure gradient) for 300 wall time units and then turning on the oscillatory pressure gradient. All of the Fourier components except $l = m = 0$, $|l| = |m| = 1$, and $|l| = 1$, $|m| = 2$ were zeroed at the beginning of the steady-flow run. At the end of a time equal to 300, the steady-flow run had reached a statistical steady-state in which all of the Fourier components (except those for $|l| = 8$ or $|m| = 8$ which were zeroed on each time step) were nonzero and no spatial symmetry other than the imposed spanwise reflection symmetry was detectable. Our estimate of the time transient for the steady-flow run is based on instantaneous horizontal averages of flow variables such as the x-component of the wall shear stress as well as short time averages over time intervals of length 100.

4 Solution Procedure

A modified version of a splitting method described by Orszag and Kells [12] was used to calculate the time evolution of the velocity field. The splitting method entails a fractional time stepping procedure. In the first step the velocity field is calculated by including only the $\mathbf{V} \times \omega$ and $\partial \bar{P}/\partial X$ terms. In the second step the $\nabla \Pi$ term is added and the Π field is calculated by demanding that the velocity field satisfy continuity. An invsicid boundary condition is imposed on the velocity field in the second step. In the third (final) step the $\nabla^2 \mathbf{V}$ term is added and the boundary conditions at $Z = 0$ and $Z = \infty$ are imposed. The solution procedure is very similar to that described by McLaughlin et al. [4] and only the main features are discussed in this paper. The details of the procedure can be found in a thesis by Reddy [5].

4.1 First Fractional Step. In this fractional step, we solve the equation

$$\partial \hat{\tilde{\mathbf{V}}}/\partial t + U_A(Z)\partial \hat{\tilde{\mathbf{V}}}/\partial \hat{X} = \tilde{\mathbf{F}} + U_A(Z)\partial \hat{\tilde{\mathbf{V}}}/\partial X \tag{13}$$

where $\hat{\mathbf{V}}$ is the velocity field at the end of the first fractional step, $\mathbf{F} = \mathbf{V} \times \omega - (\partial \bar{P}/\partial X)\hat{X}$, and the term, $-U_A(Z)\partial \mathbf{V}/\partial X$, is subtracted from both sides of the equation in order to reduce convective instability (see Orszag and Kells [12] and Reddy [5]).

$$U_A(Z) = U_L(1+U_p), Z<Z_e$$

$$U_A(Z) = <U>, Z_e \leq Z \leq \infty$$

where $<U>$ is given by equations (6), U_L is Laufer's [17] mean profile, and

$$U_p = \text{real part of } -iU_{\text{amp}}\{1-\cosh[(1+i)$$
$$(\sqrt{\pi/T_p})(Z_e - Z)]/\cosh[(1+i)(\sqrt{\pi/T_p})Z_e]\}\exp(i2\pi t/T_p).$$

The expression for U_p is the solution derived by Lamb [13] for a pulsating laminar boundary layer. Though Lamb's solution is strictly valid for laminar flow it worked quite satisfactorily in our case and we were successful in eliminating the convective instability. An Adams-Bashforth-Crank-Nicholson scheme was used to solve equation (13):

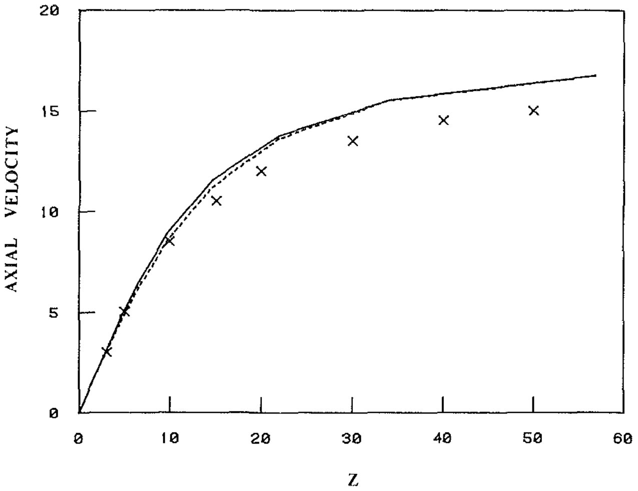

Fig. 2 Horizontal and time averaged axial velocity in pulsed flow (——) compared with steady flow (....) and Laufer's [17] data

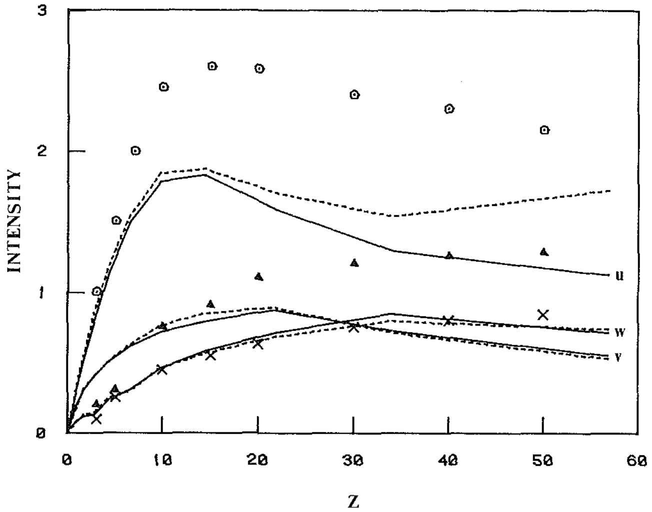

Fig. 3 Horizontal and time averaged fluctuation intensities of the three components of velocity in pulsed flow (——) compared with steady flow (....) and Laufer's [17] data, u(⊙), v(△), w(×)

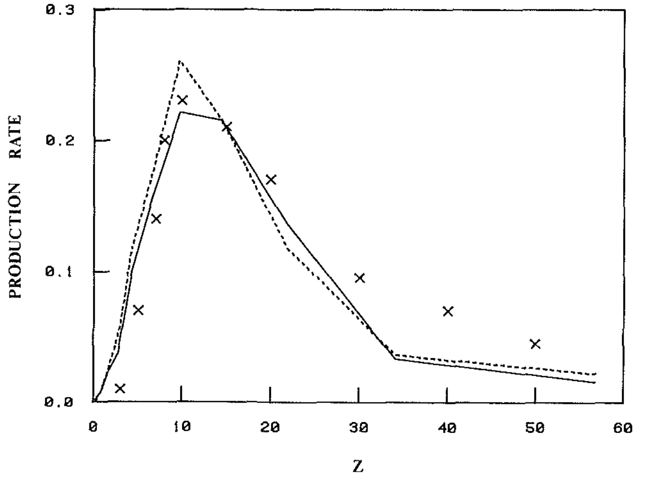

Fig. 4 Horizontal and time averaged production rate of turbulent kinetic energy in pulsed flow (——) compared with steady flow (....) and Laufer's [17] data

$$\hat{\tilde{\mathbf{V}}}_{j+1} = \{\tilde{\mathbf{V}}_j + (3/2)\tilde{\mathbf{F}}_j - (1/2)\tilde{\mathbf{F}}_{j-1} + (il\alpha U_A(Z)/2)(2\hat{\tilde{\mathbf{V}}}_j - \hat{\tilde{\mathbf{V}}}_{j-1})\} / \{1 + (il\alpha U_A(Z)/2)\Delta t\} \tag{14}$$

where the subscripts denote time steps.

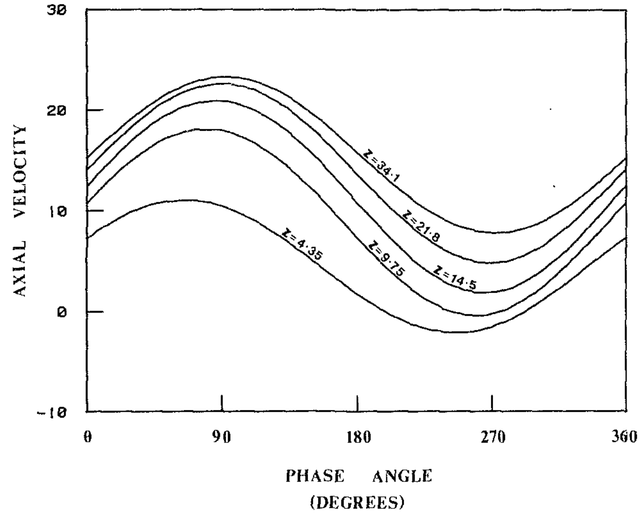

Fig. 5 Horizontal and ensemble averaged axial velocity for 0 < $Z \leq$ 34.1

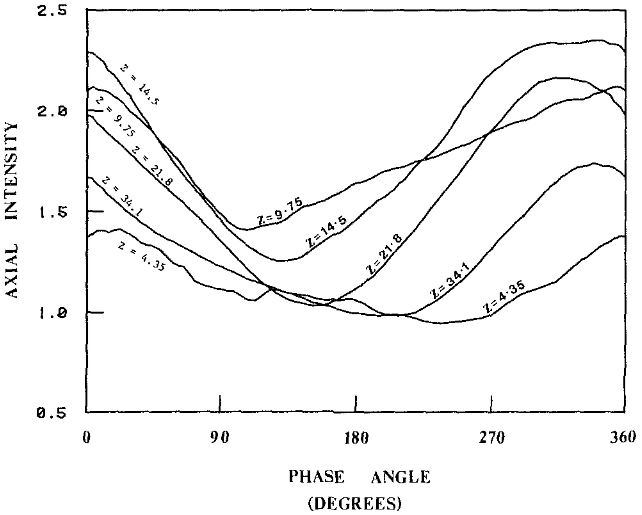

Fig. 6 Horizontal and ensemble averaged fluctuation intensity of the axial velocity for 0 < $Z \leq$ 34.1

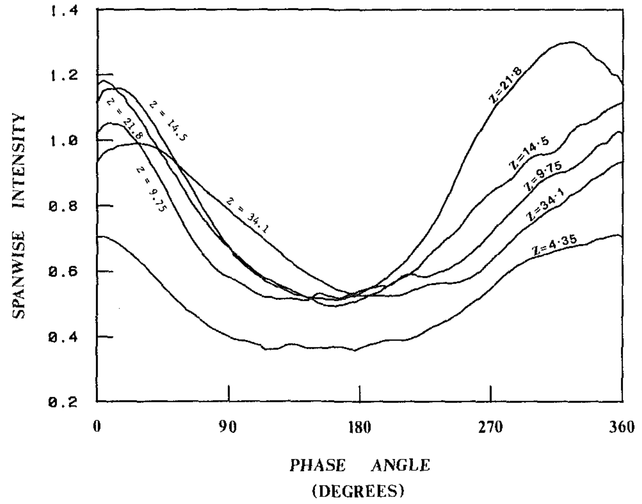

Fig. 7 Horizontal and ensemble averaged fluctuation intensity of the spanwise velocity for 0 < $Z \leq$ 34.1

4.2 Second Fractional Step. In the second fractional step, we include the effects of pressure.

$$\hat{\hat{\tilde{\mathbf{V}}}}_{j+1} = \hat{\tilde{\mathbf{V}}}_{j+1} - \Delta t \nabla \tilde{\Pi}_{j+1}. \quad (15)$$

The $\tilde{\Pi}$ field is calculated by imposing incompressibility on $\hat{\hat{\tilde{\mathbf{V}}}}_{j+1}$.

$$\nabla^2 \tilde{\Pi}_{j+1} = (1/\Delta t)\, \nabla \cdot \hat{\tilde{\mathbf{V}}}_{j+1} \quad (16)$$

subject to

$$\partial \tilde{\Pi}_{j+1}/\partial Z|_{Z=0} = \partial \tilde{\Pi}_{j+1}/\partial Z|_{Z=\infty} = 0$$

After calculating the Π field the velocity field is calculated from equation (15).

4.3 Third (Final) Fractional Step. Finally, we consider viscous effects. By treating the $\nabla^2 \mathbf{V}$ term implicitly using the Euler backward method we get

$$\tilde{\mathbf{V}}_{j+1} - (\nabla^2 \tilde{\mathbf{V}}_{j+1})\Delta t = \hat{\hat{\tilde{\mathbf{V}}}}_{j+1}. \quad (17)$$

For details concerning the evaluation of the spatial derivatives and the solution procedure for equations (16) and (17), the reader is referred to McLaughlin et al. [4] and Reddy [5].

In our calculations we used a time step (Δt) equal to 0.5. McLaughlin et al. [4] reported that the results obtained with $\Delta t = 0.25$ were virtually identical to those obtained with $\Delta t = 0.5$.

If the parameter $U_{\text{amp}} = 0$ and the steady-flow pressure gradient is used, the algorithm for the pulsed flow runs reduces to that used for the steady flow runs.

5 Results

The parameters used in this study were: $\lambda_x = 630$, $\lambda_y = 135$, $N_X = N_Y = N_Z = 16$, $T_p = 100$, $U_{\text{amp}} = 0.50$, and $\Delta t = 0.5$. In all calculations we used fifteen cycles of pulsation to compute the averages. This was sufficient since the averages computed over a lesser number of cycles were virtually the same.

Recently, Tu and Ramaprian [14, 15] and Shemer and Kit [16] reported experimental measurements in sinusoidally pulsed turbulent pipe flow. Unfortunately, we could not compare our results with their data. Tu and Ramaprian [14, 15] did not report measurements for $Z < 70$. Also, the highest pulsation frequency in their experiments was about an order of magnitude smaller than that used in the present study. Shemer and Kit [16] carried out their experiments using low frequency and low amplitude pulsations at very low Reynolds numbers (< 10,000). Their investigation was aimed at identifying a quasi-steady regime in pulsating flow while our flow was well into the FV regime.

In Figs. 2, 3, and 4 we compare the horizontal and time average of the axial velocity, fluctuation intensities of the three components of the velocity, and the production rate of turbulent kinetic energy to steady flow and Laufer's [17] data. The production rate was computed as

$$<\overline{\overline{P_r}}> = \overline{<\overline{UW}> <\overline{\partial U/\partial Z}>} \quad (18)$$

where the right-hand side is the average over a pulsation cycle of the product of the ensemble average Reynolds stress and the ensemble average velocity gradient. The profiles shown in Figs. 2, 3, and 4 are about the same for steady and pulsed flow and are in reasonably good agreement with experiment. The largest discrepancy between the calculated steady flow results and the corresponding experimental results occurs for the spanwise intensity. This discrepancy is probably primarily due to the spanwise reflection symmetry which forces the spanwise component of velocity to vanish at an infinite number of uniformly spaced points in the spanwise direction. The discrepancies between the calculated and experimental results increase with distance from the wall, and this is ascribable to the poor spatial resolution at large distances from the wall. The average wall shear stress in pulsed flow was only 3%

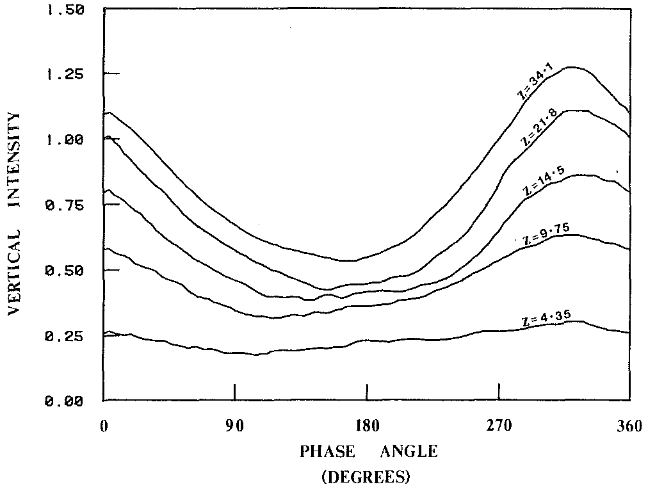

Fig. 8 Horizontal and ensemble averaged fluctuation intensity of the vertical velocity for $0 < Z \leq 34.1$

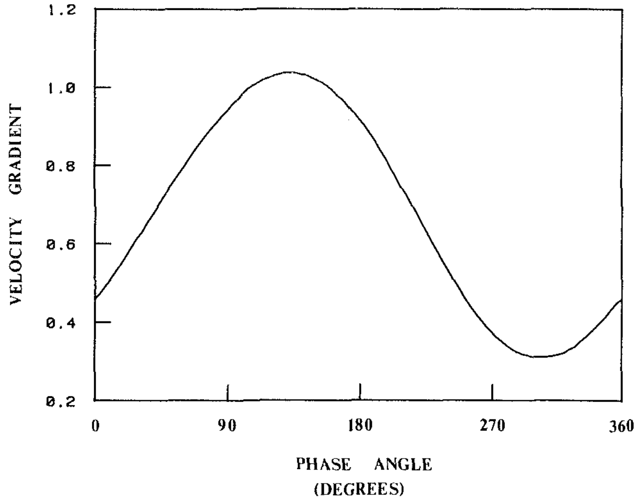

Fig. 10 Horizontal and ensemble averaged velocity gradient, $\partial U/\partial Z$, at $Z = 9.75$

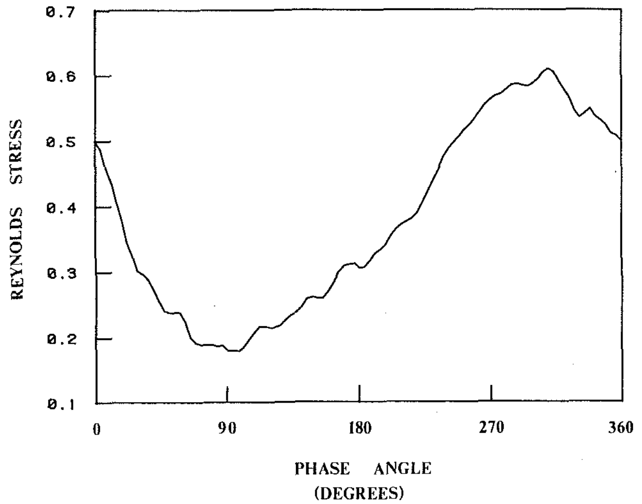

Fig. 9 Horizontal and ensemble averaged Reynolds stress, UW, at $Z = 9.75$

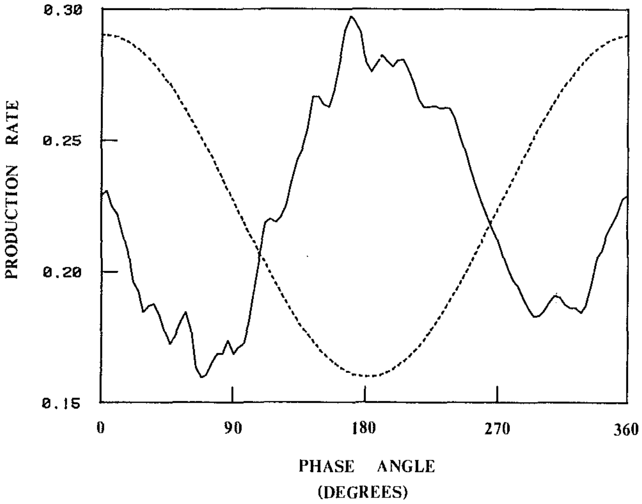

Fig. 11 Horizontal and time averaged production rate of turbulent kinetic energy at $Z = 9.75$. The dotted line is a scaled form of the pressure gradient.

higher than in steady flow which indicates that there was a negligible enhancement in momentum transport. The integrated production rate for $0 < Z < 34.1$ was 4.50 in steady flow and 4.40 in pulsed flow.

In order to determine the phase relationship between the flow variables and the pressure gradient, the ensemble average of the horizontally averaged flow variables was computed. In Fig. 5 the ensemble and horizontal average of the axial velocity for $0 < Z \leq 34.1$ is plotted as a function of the pulsation phase angle. The phase lag between the axial velocity and the pressure gradient is determined by comparing Figs. 1 and 5. For $Z > 34.1$ the phase lag is known to be 90 deg since it was imposed through equations (6). For $Z < 34.1$ the phase lag decreases with decreasing Z. This is to be expected since viscous effects become important close to the wall. At $Z = 0.095$, which is the grid point closest to the wall, the phase lag is about 50 deg.

In Figs. 6, 7, and 8 the ensemble and horizontal average of the fluctuation intensities are plotted as a function of the pulsation phase angle. It can be seen that the fluctuation intensities do show a dependence on the phase angle. When compared to Fig. 1, they are almost in phase with the pressure gradient. This implies that the turbulence is stronger during the part of the pulsation cycle when a favorable pressure gradient exists and weaker during the part of the cycle when an adverse pressure gradient exists.

A more important quantity to investigate is the ensemble averaged rate of production of turbulent kinetic energy since it will lead to a direct understanding of the phase relationship between the turbulence production and the imposed pulsations. The ensemble average of the horizontally averaged rate of production of turbulent kinetic energy was computed as

$$<\overline{P_r}> = <\overline{UW}> <\overline{\partial U/\partial Z}> . \qquad (19)$$

In Figs. 9 and 10 the Reynolds stress, $<\overline{UW}>$, and the velocity gradient, $<\overline{\partial U/\partial Z}>$, at $Z = 9.75$ are plotted as a function of the pulsation phase angle. The grid point, $Z = 9.75$, was chosen since the time average of the turbulence production rate was the highest at this point (see Fig. 4). The phase relationship between the Reynolds stress and the pressure gradient is similar to that of the fluctuation intensities. The velocity gradient, however, shows quite a different phase relationship to the pressure gradient. The production rate given by equation (19) is the product of Figs. 9 and 10. It is shown in Fig. 11 as a function of the pulsation phase angle. The dotted line in Fig. 11 is a scaled form of the pressure gradient. The production rate is at its maximum value when the pressure gradient is at its minimum. The maximum value is about 15 percent larger than the production rate in steady turbulent flow. Also, the production rate is larger than the mean value during the entire duration of the adverse pressure gradient which suggests that the adverse part of the pressure gradient enhances the rate of production of turbulent kinetic energy. A non-sinusoidal pulsation may in fact increase the mean production rate and we plan to investigate this in the future.

6 Conclusions

Our numerical simulation of pulsed turbulent pipe flow indicates a negligible change in momentum transport despite the fact that a large pulsation amplitude was used and the frequency was in the frozen viscosity regime. This result would appear to cast doubt on Lemlich's [3] speculation that heat transfer rates can be significantly enhanced by pulsing at high frequencies. On the other hand, we found that the ensemble averaged fluctuation intensities and turbulence production rate showed strong phase dependence. One of the more striking results was that the production rate was largest during the part of the pulsation cycle when an adverse pressure gradient existed.

Acknowledgments

This work was supported by the Department of Energy under contract DE-AC02-82ER12033.A000. The calculations were performed on the IBM 4341 computer at Clarkson University.

References

1 Mizushina, T., Maruyama, T., and Shiozaki, Y., "Pulsating Turbulent Flow in a Tube," *J. Chem. Eng. Japan*, Vol. 6, Dec. 1973, pp. 487-494.

2 Mizushina, T., Maruyama, T., and Hirasawa, H., "Structure of the Turbulence in Pulsating Pipe Flows," *J. Chem. Eng. Japan*, Vol. 8, June 1975, pp. 210-216.

3 Lemlich, R., "Vibration and Pulsation Boost Heat Transfer," *Chem. Eng.*, Vol. 68, May 1961, pp. 171-176.

4 McLaughlin, J. B., Reddy, V., and Nunge, R. J., "A Model of the Viscous Wall Region of Turbulent Shear Flows," (submitted to *Chemical Engineering Communications*).

5 Reddy, V., "A Study of Steady and Pulsed Turbulent Pipe Flow," Ph.D. thesis, Clarkson College, Jan. 1984.

6 Hogenes, J. H. A., and Hanratty, T. J., "The Use of Multiple Wall Probes to Identify Coherent Patterns in the Viscous Wall Region," *J. Fluid Mech.*, Vol. 124, Nov. 1982, pp. 363-390.

7 Bakewell, H. P., and Lumley, J. L., "Viscous Sublayer and Adjacent Wall Region in Turbulent Pipe Flow," *Phys. Fluids*, Vol. 10, Sept. 1967, pp. 1880-1889.

8 Sirkar, K. K., "Turbulence in the Immediate Vicinity of a Wall and Fully Developed Mass Transfer at High Schmidt Numbers," Ph.D. thesis, U. of Illinois, 1969.

9 Brown, F. T., Margolis, D. L., and Shah, R. P., "Small Amplitude Frequency Behavior of Fluid Lines With Turbulent Flow," ASME *J. Basic Engineering*, Vol. 91, Dec. 1969, pp. 678-693.

10 Simpson, R. L., Shivaprasad, B. G., and Chew, Y.-T., "The Structure of a Separating Turbulent Boundary Layer. Part 4. Effects of Free-Stream Unsteadiness," *J. Fluid Mech.*, Vol. 127, Feb. 1983, pp. 219-261.

11 Morrison, W. R. B., Bullock, K. J., and Kronauer, R. E., "Experimental Evidence of Waves in the Sublayer," *J. Fluid Mech.*, Vol. 47, June 1971, pp. 639-656.

12 Orszag, S. A., and Kells, L. C., "Turbulence in Plane Poisuelle and Plane Couette Flow," *J. Fluid Mech.*, Vol. 96, Jan. 1980, pp. 159-205.

13 Lamb, H., *Hydrodynamics*, 6th edition, Dover Publications, New York, 1945.

14 Tu, S. W., and Ramaprian, B. R., "Fully Developed Periodic Turbulent Pipe Flow. Part 1. Main Experimental Results and Comparison with Predictions," *J. Fluid Mech.*, Vol. 137, Dec. 1983, pp. 31-58.

15 Tu, S. W., and Ramaprian, B. R., "Fully Developed Periodic Turbulent Pipe Flow. Part 2. The Detailed Structure of the Flow," *J. Fluid Mech.*, Vol. 137, Dec. 1983, pp. 59-81.

16 Shemer, L., and Kit, E., "An Experimental Investigation of the Quasisteady Turbulent Pulsating Flow in a Pipe," Phys. Fluids, Vol. 27, Jan. 1984, pp. 72-76.

17 Laufer, J., "The Structure of Turbulence in Fully Developed Pipe Flow," NACA Tech. Note 1174, 1954, pp. 417-434.

Inviscid Shear Flow Analysis of Corner Eddies Ahead of a Channel Flow Contraction

R. N. Meroney
Professor,
Fluid Mechanics and
Wind Engineering Program,
Department of Civil Engineering,
Colorado State University,
Fort Collins, CO 80523

The steady rotational flow of an inviscid fluid in a two-dimensional channel toward a sink or a contraction is treated. The velocity distribution at upstream infinity is approximated by a linear combination of uniform flow, linear shear flow, and a cosine curve. The combinations were adjusted to simulate flows ranging from laminar to turbulent. Vorticity is assumed conserved on streamlines. The resulting linear equations of motion are solved exactly. The solution show the dependence of the corner eddy separation and reattachment on flow geometry and approach flow vorticity and velocity distribution typified by a shape factor.

Introduction

When a viscous fluid flows in a channel or pipe toward an abrupt contraction eddies form in the corners immediately preceding that contraction. The shape of the corner eddies and their upwind extent are said to be functions of the upwind profile, viscosity, and the state of the fluid (laminar or turbulent). Yet, surprisingly, viscosity is not required to reproduce the phenomenon of separation and reattachment! This paper will examine a variety of inviscid flow configurations during which corner eddies appear in a two dimensional channel flow contraction and relate the size of the eddy to different descriptors of the approach flow.

Because of the complex nature of separation dynamics realistic theoretical models including exact solutions for the separation flow are limited. There is an extensive literature on well separated flows about bluff bodies and subsequent wake development (Wu, 1972; Thwaites, 1960). To produce realistic flow patterns most analyses depend upon measurements to specify undefined base pressure, prespecification of separation or reattachment points, and almost all are limited to uniform or linear velocity gradient approach flows (Kiya and Arie, 1972; Frenkiel, 1961). Numerical solutions for more general profiles of inviscid shear flow over boundary obstructions have been performed by some authors (Taulbee and Robertson, 1972; Bouwmeester, Meroney, and Sandborn, 1978), but they are not exact and can suffer from numerical empericism.

An interesting exception is the solution obtained by Yih (1959) for the inviscid shear flow of a cosine velocity profile in a two dimensional channel flowing into a corner sink. The key to an exact solution of the inviscid shear flow problem is to find a flow where the vorticity is a unique function of the streamline along which it is convected (Taulbee and Robertson, 1972). In such a situation no singular surfaces occur in the flow, but the solution are unlikely to represent exactly the corresponding flow of a real fluid even at large Reynolds number. (As noted by Yih (1959) this is part of the penalty for ignoring viscous forces entirely in the search for an exact analytic solution.) Nonetheless the flow exterior to the corner eddy is strikingly similar to those in front of actual separation bubbles (Pande, Prakash, and Argarwal, 1980; Good and Joubert, 1968; Robertson and Taulbee, 1969; or Bradshaw and Galea, 1967), and the similarity justifies further examination of such exact solutions.

Two-Dimensional Channel Flow Into a Line Sink

In this section we shall consider steady two-dimensional flow in a long channel with half-width equal to unity terminating in a wall with a symmetrically placed line sink, with the centerline of the channel as the x-axis extending in the negative x direction.

Let ψ be Lagrange's stream function, then the equation governing steady two-dimensional inviscid flow is the Poisson equation or

$$\nabla^2\psi = \frac{\partial^2\psi}{\partial x^2} + \frac{\partial^2\psi}{\partial y^2} = -f(\psi) \tag{1}$$

where $-f(\psi)$ represents the vorticity and depends on the stream function alone. Ideally the velocity far upstream would be parabolic or logarithmic to represent the movement of a laminar or turbulent flow respectively in a long channel. Unfortunately the use of such profiles would make equation (1) nonlinear and preclude a simple solution. Instead we shall use a linear combination of uniform flow, a linear shear gradient, and a cosine distribution to create various nonuniform profiles. In terms of the centerline velocity $U_{\max}$ the dimensionless upstream profile is then

$$U/U_{\max} = u_0 + K_0(1-y) + 2(1-u_0-K_0/2)\cos(\pi y/2)/\pi \tag{2}$$

which vanishes at the walls ($y = \pm 1$) and is maximum at the centerline. The corresponding dimensionless stream function far upstream is

---

Contributed by the Fluids Engineering Division for publication in the JOURNAL OF FLUIDS ENGINEERING. Manuscript received by the Fluids Engineering Division, September 27, 1983.

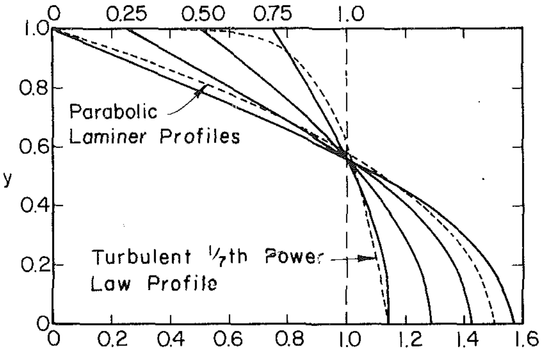

Fig. 1 Upstream velocity profiles, uniform plus cosine profiles

$$\psi = \int_0^y U/U_{\max} dy$$

$$= u_0 y + K_0(y - y^2/2)$$
$$+ (1 - u_0 - K_0/2)\sin(\pi y/2) \qquad (3)$$

such that at the walls ($y = \pm 1$) the values are ± 1. The vorticity function is then linear and equal to

$$f(\psi) = -K_0 - (\pi/2)^2(1 - u_0 - K_0/2)\sin(\pi y/2) \qquad (4)$$

Note that for consistency $u_0 + K_0/2 < 1$ is required.

The boundary conditions on equation (1) are

$$\text{(i)}\ \psi = \text{equation (3) as } x \to -\infty. \qquad (5)$$

$$\text{(ii)}\ \psi = \pm 1 \text{ for } y = \pm 1, \text{ and}$$

$$\text{(iii)}\ \psi = \pm 1 \text{ for } y \leq 0 \text{ and } x = 0.$$

Solution of equations (1) to (5) by the method of separation of variables yields

$$\psi = u_0 y + K_0(y - y^2/2) + (1 - u_0 - K_0/2)\sin(\pi y/2) \qquad (6)$$

$$+ \sum_{n=1}^{\infty} C1_n \sin(n\pi y) \exp(n\pi x)$$

$$+ \sum_{n=1}^{\infty} C2_n \sin(n\pi y) \exp((n^2 - 1/4)^{1/2} \pi x)$$

which satisfies boundary condition (i) and (ii), and the values of $C1_n$ and $C2_n$ are determined by Fourier expansion to satisfy boundary condition (iii) such that

$$C1_n = (2u_0 + K_0)/(n\pi) + 2K_0(\cos(n\pi) - 1)/(n\pi)^3 \qquad (7)$$

and

$$C2_n = 2(1 - u_0 - K_0/2)(1 + \cos(n\pi)/(4n^2 - 1))/(n\pi).$$

Equations (6) and (7) are the solution. The series solution has been evaluated out to sufficient terms such that the stream function is known to five significant places for different values of u_0 and K_0. Figure 2(a) and 2(b) are typical derived flow patterns for the half channel.

The stream function is specified to vary between -1 to $+1$ across the channel, but the flow may be distributed in a variety of profiles. Figure 1 suggests a possible set of profiles resulting from combinations of uniform and cosine functions. Alternatively, uniform and ramp functions were used. The dashed lines are parabolic and 1/7th power law profiles typical of laminar and turbulent channel flow distributions. Each profile is characterized by the magnitude of the slip at the wall, u_0, and the wall vorticity, ω_0. In addition one can characterize the velocity distribution by a displacement thickness, δ^*, and a momentum thickness, θ, which may be combined into a shape factor ratio, $H = \theta/\delta^*$, where

$$\delta^* = \int_0^1 (U_{\max} - U)dy/U_{\max}, \text{ and} \qquad (8)$$

$$\theta = \int_0^1 U(U_{\max} - U)dy/U_{\max}^2.$$

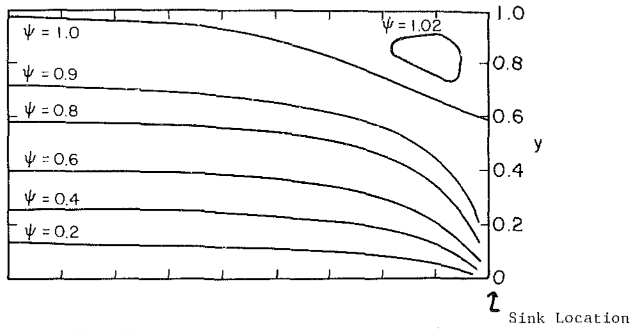

Fig. 2(a) Channel flow into a sink, $u_0 = 0.0$, $-u_0 = 2.47$

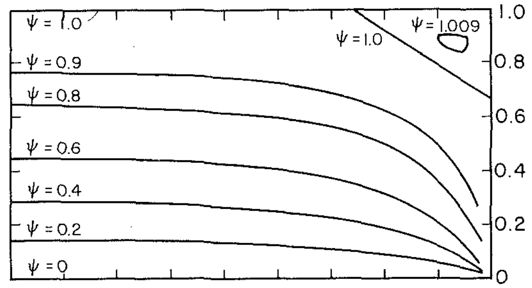

Fig. 2(b) Channel flow into a sink $u_0 = 0.25$, $-u_0 = 1.85$

Table 1 Influence of flow variables on separation and reattachment

u_0	K_0	$-\omega_0$	H	x_s	y_r
1.00	0	0	1.000	0	0
0	2.00	2.00	0.333	$-\infty$	0.40
0	0	2.47	0.376	$-\infty$	0.40
0.25	0	1.85	0.483	−0.51	0.33
0.50	0	1.24	0.619	−0.23	0.20
0.75	0	0.62	0.784	−0.06	0.04
0.25	1.50	1.50	0.425	−0.42	0.28
0.50	1.00	1.00	0.555	−0.18	0.13
0.75	0.50	0.50	0.735	−0.04	0.03
0.38	1.24	1.24	0.490	−0.32	0.20

Nomenclature

$C1_n$ = Fourier coefficient in infinite series
$C2_n$ = Fourier coefficient in infinite series
$f(\psi)$ = vorticity function
h = height of corner of contraction
h' = half width of contraction
H = shape factor
K_0 = gradient of linear shear profile
n = summation index in infinite series
U = velocity
$U_{\max}$ = velocity at $y = 0$
u_0 = slip velocity
x,y = Cartesian coordinates
x_s = distance of separation point from corner
y_r = distance to reattachment point from corner
ψ = stream function
δ^* = displacement thickness
θ = momentum thickness
ω_0 = vorticity at wall, $y = 1$

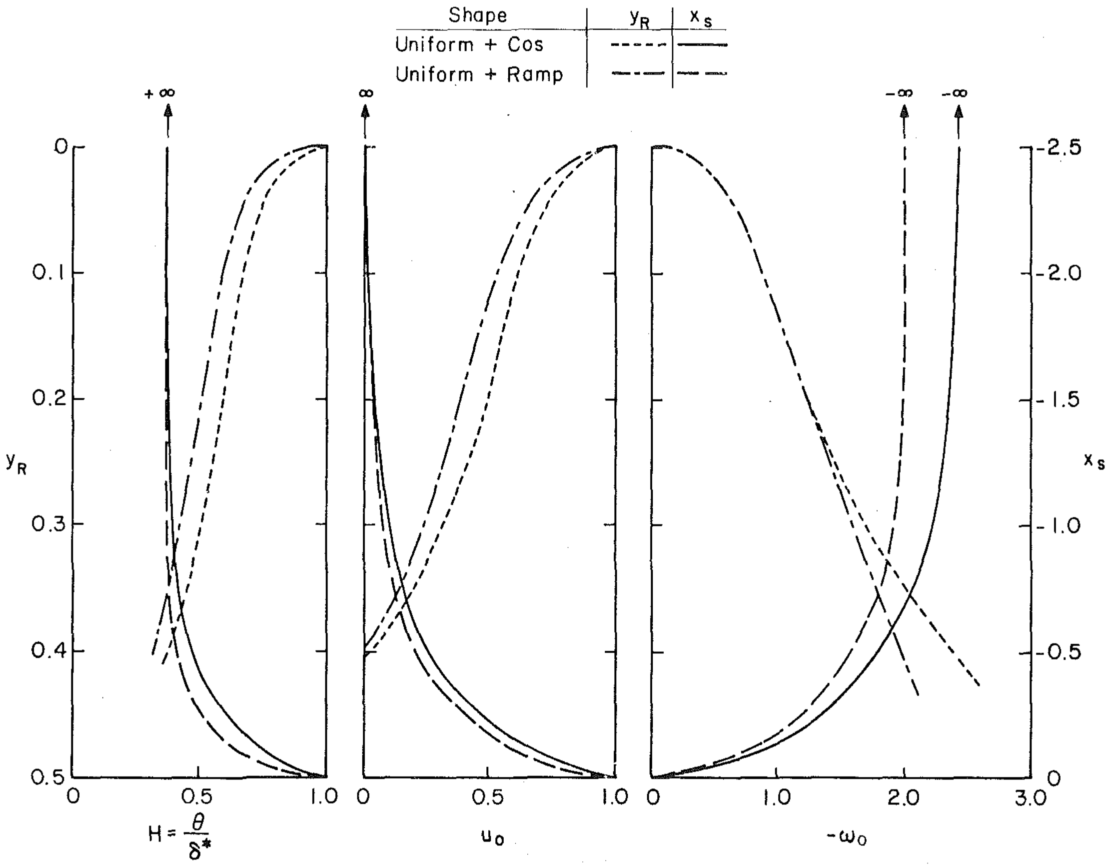

Fig. 3 Variation of separation distance and reattachment distance with profile parameters

Table 1 summarizes cases examined in this paper. Two flows are considered which maintain the same wall vorticity but different values of slip. Similarly one sees equal values of slip but different wall vorticity.

The size of the corner eddy is its most significant characteristic; hence, the distance to separation from the corner, x_s, and the location of the reattachment point, y_r, are also tabulated above. The variation of these variables with shape factor, slip velocity, and wall vorticity are plotted in Fig. 3.

As slip velocity approaches one, shape factor approaches one, or as vorticity decreases the corner eddy disappears. The rate of diminishing is not exactly the same for the various combinations of uniform, ramp and cosine flow, but they are very similar. As slip velocity decreases, shape factor decreases, and wall vorticity increases the reattachment point moves toward a value $y = 0.6$ ($y_r = 0.4$), but the separation point moves to $-\infty$. In the inviscid approach it appears a finite value of slip velocity is necessary to develop a finite separation point, x_s. Taulbee and Robertson (1972) also emphasized that the point of separation must be closely associated with the assumption about u_0. Indeed they conclude the entire inviscid flow field is sensitive to the choice of u_0.

Two-Dimensional Channel Flow Into a Contraction

In this section we will examine the effect of enlarging the hypothetical line sink into a finite width contraction. The new channel half width, h', may vary from 0.0 to 1.0. The channel contraction will confine the streamline pattern and result in larger exit velocities. When the contraction is abrupt the velocity profile will flatten and the flow will tend to separate at the corner. Since we will prespecify the exit profile the details of the post contraction eddy may not be realistic; nonetheless, the upstream corner eddy and flow field should be similar to measurements.

An exact solution can be obtained for two realistic exit profiles. The exit profile may be specified uniform such that $U_{x=0}/(U_{\max})_{x=-\infty} = 1/h'$. Alternatively the exit profile can be a partial cosine shape with slip at the outer wall, i.e., $U_{x=0}/(U_{\max})_{x=-\infty} = \pi/2 \ \cos(\pi y/2)/\sin(\pi h'/2)$. Neither of these profiles require that vertical velocities in the $x=0$ plane be zero (see Fig. 4).

Solutions for the contracted channel case can also be produced for an infinite combination of uniform, ramp, and cosine function upstream profiles. Since the sink solutions did not produce any unique perturbation resulting from the use of the ramp (linear shear flow) term the following solutions are limited to combinations of uniform and cosine profiles. As in the previous section the governing equations are (1) through (4), but with K_0 set to zero. The new boundary conditions for the uniform outlet flow case are

$$\begin{aligned} \text{(i)}\psi &= \text{equation (3) as } x \to -\infty \\ \text{(ii)}\psi &= \pm 1 \text{ for } y = \pm 1, \text{ and} \\ \text{(iii)}\psi &= y/h' \text{ for } -h' \le y \le h', \text{ or} \\ &= +1 \text{ for } h \le y \le 1, \text{ or} \\ &= -1 \text{ for } -1 \le y \le -h'. \end{aligned} \tag{9}$$

The final solution for the stream function is then

$$\psi = u_0 y + (1-u_0)\sin(\pi y/2) + \sum_{n=1}^{\infty} C1_n \sin(n\pi y)\exp(n\pi x) + \sum_{n=1}^{\infty} C2_n \sin(n\pi y)\exp((n^2 - 1/4)^{1/2}\pi x), \tag{10}$$

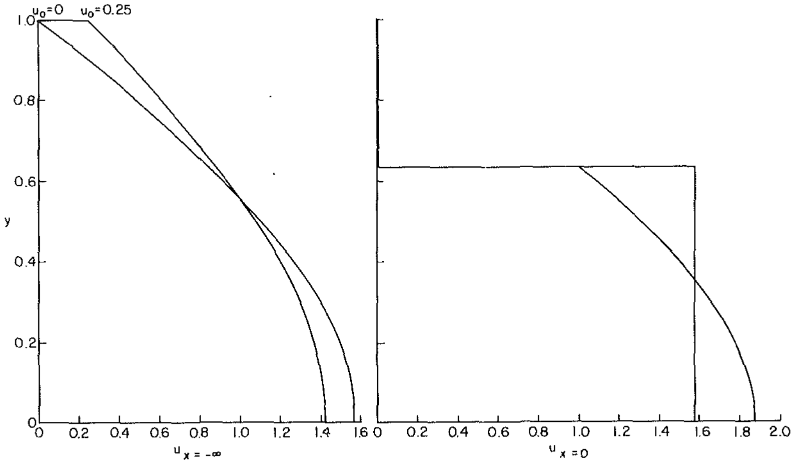

Fig. 4 Typical upstream and exit profiles for channel contractions, $h' = 2/\pi$

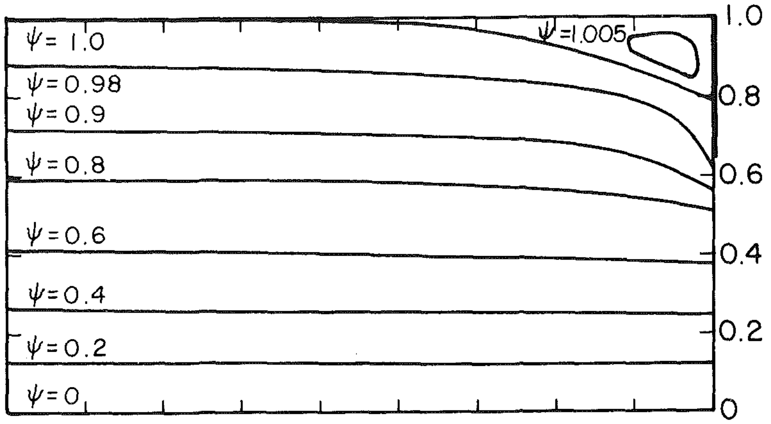

Fig. 5 Channel flow into a contraction, $u_0 = 0.0$, $H = 0.376$, $-u_0 = 2.47$, $h' = 2/\pi$, uniform flow outlet

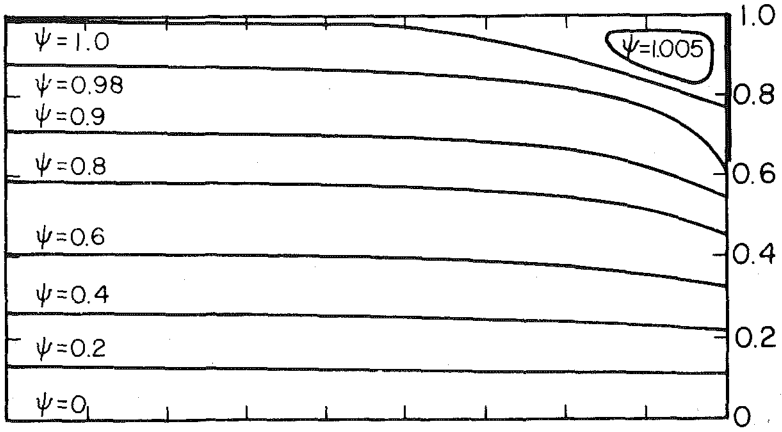

Fig. 6 Channel flow into a contraction, $u = 0.0$, $H = 0.376$, $-u_0 = 2.47$, $h' = 2/\pi$, cosine flow outlet

where

$$C1_n = 2u_0 \sin(n\pi h')/(n^2\pi^2 h'), \text{ and} \tag{11}$$

$$C2_n = 2(1-u_0)(\sin(n\pi h')/(n\pi h') + \cos(n\pi)/(4n^2-1))/(n\pi).$$

Similarly the new third boundary condition for the partial cosine velocity profile outlet case is

$$\text{(iii)}\quad \psi = \sin(\pi y/2)/\sin(\pi h'/2), \text{ for } -h' < y < h', \text{or} \tag{12}$$
$$= +1 \text{ for } h' \le y \le 1, \text{or}$$
$$= -1 \text{ for } -1 \le y \le -h'.$$

The final solution for stream function is the same as equation (9), but the Fourier coefficients are

$$C1_n = 2u_0/(n\pi)(\cos(n\pi h') - 4n^2 \cos(n\pi h')/(4n^2-1) + 2\sin(n\pi h')\cos(\pi h'/2)/(4n^2-1)/\sin(\pi h'/2), \text{and} \tag{13}$$

$$C2_n = 2(1-u_0)/(n\pi)(\cos(n\pi h') + \cos(n\pi)/(4n^2-1) - 4n^2\cos(n\pi h')/(4n^2-1) + 2n\sin(n\pi h')\cos(\pi h'/2)/(4n^2-1)/\sin(\pi h'/2)).$$

Equations (10) and (11) and equations (10) and (13) are the solutions for channel flow into a contraction with uniform

Table 2 Influence of contraction on separation and reattachment

u_0	Outlet Profile	$-\omega_0$	H	h	x_s/h	y_r/h
0	unif.	2.47	0.376	1.000	$-\infty$	0.40
0	unif.	2.47	0.376	0.500	$-\infty$	0.59
0	unif.	2.47	0.376	0.363	$-\infty$	0.58
0	unif.	2.47	0.376	0.200	$-\infty$	0.42
0.10	unif.	2.22	0.417	0.363	−1.21	0.52
0.25	unif.	1.85	0.485	0.363	−1.61	0.39
0.50	unif.	1.24	0.619	0.363	−0.25	0.15
0.75	unif.	0.62	0.784	0.363	−0	~0
1.00	unif.	0.00	1.000	0.363	0.00	0.00
0	cosine	2.47	0.376	1.000	$-\infty$	0.40
0	cosine	2.47	0.376	0.500	$-\infty$	0.61
0	cosine	2.47	0.376	0.363	$-\infty$	0.64
0	cosine	2.47	0.376	0.200	$-\infty$	0.66
0.15	cosine	2.10	0.439	0.500	−1.17	0.52
0.15	cosine	2.10	0.439	0.363	−1.15	0.53
0.15	cosine	2.10	0.439	0.200	−1.06	0.57
0.15	cosine	2.10	0.439	0.100	−0.98	0.51
0.25	cosine	1.85	0.485	1.000	−1.51	0.33
0.25	cosine	1.85	0.485	0.500	−0.74	0.44
0.25	cosine	1.85	0.485	0.363	−0.73	0.46
0.25	cosine	1.85	0.485	0.200	−0.62	0.40

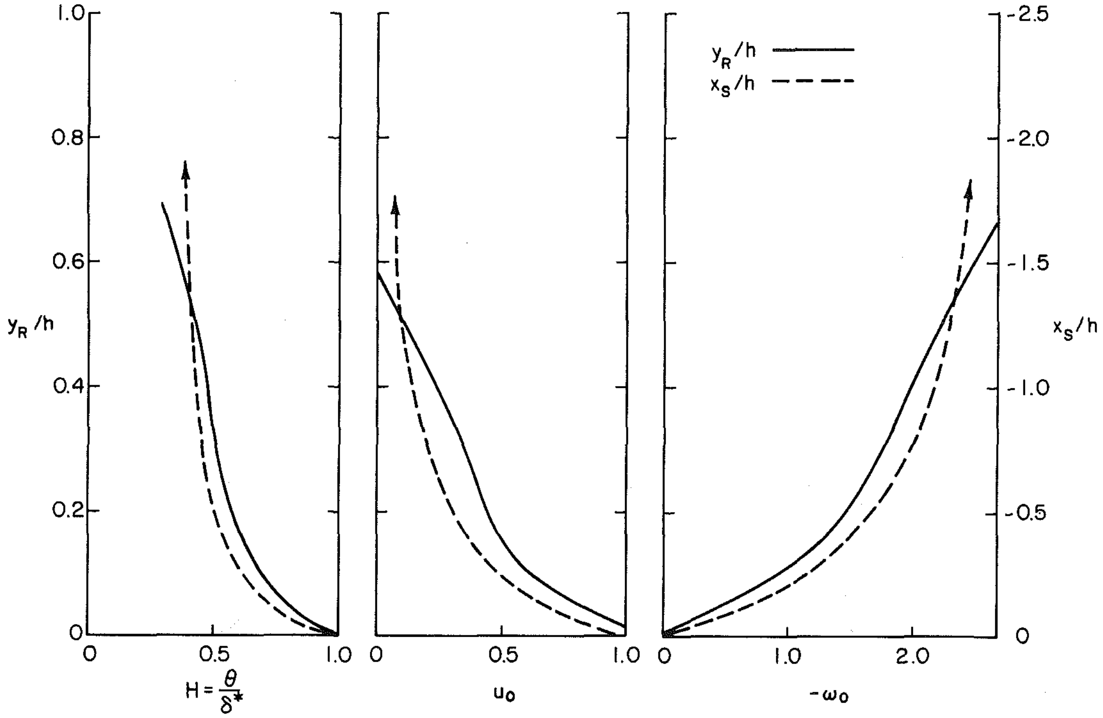

Fig. 7 Variation of separation distance and reattachment distance with profile parameters, $h' = 2/\pi$

and partial cosine output profiles respectively. The series solution has been evaluated out to sufficient terms such that the stream function is known to at least five significant places for different values of u_0. Figures 5 and 6 display derived flow patterns for the half channel. As before the stream function is specified to vary between -1 to $+1$ across the channel, but the flow may be distributed in a variety of profiles. Table 2 summarizes cases examined in this paper. Of interest is the relative location of the separation and reattachment points relative to the step height, h.

The size of the corner eddy and its variation with shape factor, slip velocity, and wall vorticity are plotted in Fig. 7 for a fixed size contraction. As slip velocity approaches one, shape factor approaches one, or vorticity decreases the corner eddy disappears. As slip velocity decreases, shape factor decreases, and wall vorticity increases the reattachment point moves toward a value of y_r/h near 0.6, but the separation point moves to $-\infty$.

Alternatively one can examine the variation of eddy size for fixed approach profile as the size of the contraction changes profiles. As the value of h' increases (or h decreases) it requires a larger number of terms from the series to produce a stable result. In general, the corner eddy occupies a larger proportion of the corner as the step increases.

It would be most interesting to compare the results developed here to experimental measurements or other analyses. Unfortunately most previous measurements upstream from a forward facing step are for relatively thin boundary layers developing independently from a constraining opposite wall (Bradshaw and Galea, 1967; Good and Joubert, 1968, Robertson and Taulbee, 1969; Pande et al., 1980). Some authors discuss measurements for large steps in channels but discuss downstream behavior only (Foss, 1962; Emery and Mohsen, 1968).

As noted by most authors, maximum pressures in the corner occur at the reattaching streamline. The separation bubble usually extends about one step height upstream and extends up about 60 percent on the upstream face of the

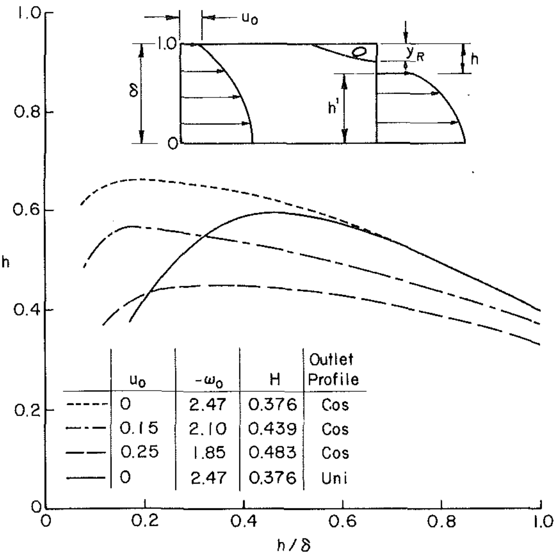

Fig. 8 Variation of reattachment distance with contraction size

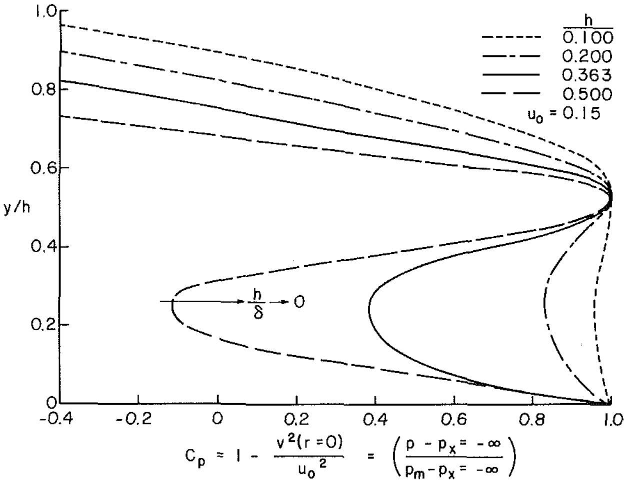

Fig. 9 Pressure distribution on forward facing step wall, $u_0 = 0.15$, $h = 0.1$ to 0.5, cosine flow outlet

contraction. Surface presssures upstream of the contraction on the channel wall begin to increase about 10 step heights upstream of the plate and become maximum on the corner. The pressure distribution displays a double maximum – one at separation, a decrease to reflect corner eddy velocities, and a second maximum on the wall (Bradshaw and Galea, 1967; Good and Joubert, 1968; Taulbee and Robertson, 1972). Sizeable back flow velocities were noted in the corner eddy during the present calculations. Foss (1962) mentioned a similar phenomenon during his channel flow measurements, but for the unconfined step most authors found eddy velocities were one-third or less in magnitude than the main stream velocities. Thus, whereas Taulbee and Robertson (1972) and Good and Joubert (1968) observed only about ten percent variation in the upstream face pressure coefficients over the bottom sixty percent of the corner, the more confined corners exhibited large pressure deviations as the contraction size varied. Good and Joubert (1968) noted that the pressure distribution flattened as the step height decreased, and the same behavior is seen in the exact channel flow contraction calculations (See Figure 9).

Taulbee and Robertson (1972) also observed that for thin boundary layers approaching tall steps choice of the wall vorticity and slip velocity did not seem crucial when predicting experimental measurements by numerical inviscid shear calculations, but that a large near wall vorticity seemed necessary to produce a corner eddy when the boundary layer to step height ratio became large. During the exact calculations considered here the corner eddy generally disappeared as the wall vorticity decreased.

Conclusions

This paper is concerned with deducing features of the corner eddy which forms in two-dimensional channel flow contractions from exact solutions of inviscid shear flow models for the flow motions. Corner eddy shapes are calculated for a line sink and various channel contractions when the upstream flow varied from uniform to a cosine shape. The separation distance from the corner is a direct function of the assumed slip velocity. The reattachment point occurred at 0.4 to 0.6 of the distance from the corner to the edge of the contraction.

References

Bradshaw, P., and Galea, P. V., "Step-Induced Separation of a Turbulent Boundary Layer in Incompressible Flow," *J. Fluid Mechanics*, Vol. 27, Part 1, 1967, pp. 111-130.

Emery, A. F., and Mohsen, A. M., "An Experimental Study of the Separated Flow of Very Thick Incompressible Turbulent Boundary Layers," ASME Paper 68-WA/FE-36, Winter Annual Meeting, December, 1968.

Foss, J. F., "Imcompressible Flow Over a Forward Facing Step," M. S. Thesis, in Mechanical Engineering, Purdue University, June 1962.

Frenkiel, L. E., "On Corner Eddies in Plane Inviscid Shear Flow," *J. Fluid Mechanics*, Vol. 11, Part 3, 1961, pp. 400-406.

Good, M. C., and Joubert, P. N., "The Form Drag of Two-dimensional Bluff Plates Immersed in Turbulent Boundary Layers," *J. Fluid Mechanics*, Vol. 31, Part 3, 1968, pp. 547-582.

Kiya, M., and Arie, M., "A Free-Streamline Theory for Bluff Bodies Attached to a Plane Wall," *J. Fluid Mechanics*, Vol. 56, Part 2, 1972, pp. 201-219.

Bouwmeester, R. J., Meroney, R. N., and Sandborn, V. A., Sites for Wind Power Installations, Wind Flow Over Ridges: Final Report, Dept. of Energy Contract Report No. RLO/243 8-77/1, Colorado State University, Civil Engineering Department CER77-78RJB-RNM-VAS51, 1978, pp. 206.

Miles, J. W., "Upstream Boundary-layer Separation in Stratified Flow," *J. Fluid Mechanics*, Vol. 48, Part 4, 1971, pp. 791-800.

Pande, P. K., Prakash, R., and Agarwal, M. L., "Flow Past Fence in Turbulent Boundary Layers," *J. Hydraulics Division, ASCE*, Vol. 106, No. HY1, 1980, pp. 191-207.

Robertson, J. M., and Taulbee, D. B., "Turbulent Boundary Layer and Separation Flow Ahead of a Step," *Developments in Mechanics*, Vol. 5, (Proceedings of the 11th Midwestern Mechanics Conference), 1969, pp. 171-190.

Taulbee, D. B., and Robertson, J. M., "Turbulent Separation Analysis Ahead of a Step," ASME *Journal of Basic Engineering* Vol. 94, 1972, pp. 544-550.

Thwaites, B., *Incompressible Aerodynamics*, Clarendon Press, Oxford, 1960, pp. 636.

Wu, T. Y., "Cavity and Wake Flows," "*Annual Review of Fluid Mechanics*," Vol. 4, 1972, pp. 243-284.

Yih, C. S., "Two Solutions for Inviscid Rotational Flow with Corner Eddies," *J. Fluid Mechanics*, Vol. 5, 1959, pp. 36-39.

I. Celik
Research Associate,
Institut für Hydromechanik,
Universtat Karlsruhe, FRG

V. C. Patel
Professor.

L. Landweber
Professor.

Department of Mechanical Engineering,
Iowa Institute of Hydraulic Research,
The University of Iowa,
Iowa City, Iowa

Calculation of the Mean Flow Past Circular Cylinders by Viscous-Inviscid Interaction

A method for the calculation of the mean flow past smooth circular cylinders is presented and evaluated. It utilizes an iterative procedure that couples a boundary-layer calculation method, by which the location of separation and the displacement thickness are predicted, and a new two-parameter irrotational-flow model, which predicts the pressure distribution. The displacement effect of the boundary layer is explicitly taken into account in the irrotational-flow model. The location of separation, drag coefficient, and pressure-distribution parameters are predicted at Reynolds numbers as high as 10^8. The results are compared with experiments in the subcritical and the supercritical flow regimes and with empirically developed design criteria for cylindrical structures at high Reynolds numbers.

1 Introduction

Information from the flow around circular cylinders is often used to predict the loads on engineering structures such as ocean pipelines, offshore-platform supports, bridge piers, smoke stacks, and cooling towers. The available information is primarily experimental and limited to Reynolds numbers less than 10^7. On the other hand, prototypes often operate at Reynolds numbers as high as 10^8. Therefore it is necessary to seek methods for the prediction of the basic flow parameters at high Reynolds numbers.

Although considerable advances have been made in the numerical solution of the complete Navier-Stokes equations for the flow past bluff bodies, the results are restricted to laminar flow at low Reynolds numbers. Extensions to higher Reynolds numbers are costly and present severe numerical problems. The alternative approach, which seeks numerical solutions of the Reynolds-averaged Navier-Stokes equations for turbulent flow, also involves excessive computing times and suffers from uncertainties in turbulence modeling, particularly in the region of separated flow. A practical and faster alternative is to develop an inviscid model that represents the most important features of the real flow. All such models involve some free parameters, usually the separation location and the base pressure, which have to be determined from other considerations. The existing models are briefly reviewed and a new model which takes explicit account of the boundary layer is presented. This is then combined with a boundary-layer calculation method, described earlier [1], to predict the key parameters associated with the mean flow around a cylinder over a range of Reynolds numbers.

2 Irrotational-Flow Models

The idea of modeling real flows past bluff bodies with an equivalent irrotational flow is not new. It has been the subject of many previous investigations.

Models which assume steady flow fall into one of three categories: (*a*) free-streamline models using conformal mapping, (*b*) surface-singularity models, and (*c*) free-streamline models with surface and wake singularities. In all of these, the flow field is decomposed into three sub-regions, namely the boundary layer on the body, the wake, and the flow exterior to the boundary layer and wake. The models differ primarily in their treatment of the wake region. Examples and discussions of potential-flow models in categories (*a*) and (*b*) can be found in [2]–[11]. In what follows, attention will be focussed on the more recently developed models in category (*c*). However, a brief account of the model of Parkinson and Jandali [5], which is of type (*a*), is useful since it was employed in the early stages of the present work.

Parkinson and Jandali [5] took a simple approach to specify the location of the free streamlines. They used two symmetric surface sources on the body in the wake region, with images at the center. The location and strength of the sources were found by satisfying some auxiliary conditions. The purpose of the sources is to model the effect of the wake region on the potential flow. The influence of the boundary layer and that of the flow between the separating streamlines is ignored. The position of separation and the base-pressure need to be prescribed. Güven [6] has made extensive comparisons with experiments on circular cylinders. His results indicated rather poor agreement between the theory and experiments, especially in the pressure-rise region, except in the case of cylinders with distributed roughness in the supercritical regime. Some calculations made by the authors also confirmed this conclusion (see Fig. 3).

Free-streamline models with surface and wake singularities (category *c*) assume that the vorticity in the wake is concentrated in relatively thin shear layers. The rotational wake is

---

Contributed by the Fluids Engineering Division of THE AMERICAN SOCIETY OF MECHANICAL ENGINEERS and presented at the Joint Applied Mechanics, Bioengineering, and Fluids Engineering Conference, Albuquerque, New Mex., June 24–26, 1985. Manuscript received by the Fluids Engineering Division, October 12, 1983. Paper No. 85-FE-1.

simulated by a pair of vortex sheets whose positions are not known a priori. Two typical studies in this category are those of Pullin [12] and Dvorak et al. [13]. Pullin presented a modified Riabouchinsky model, in which the wake is replaced by two variable-strength vortex sheets which are captured by an identical image obstacle, forming a closed wake bubble. The flow in the wake bubble was assumed to be inviscid and rotational with constant vorticity. This leads to a two-parameter model, involving the wake-bubble length (i.e., distance between the body and its image) and the base-pressure coefficient. Satisfactory results for flat plates were presented, but pressure distributions for circular cylinders have not been mentioned. A similar model has been introduced by Dvorak et al. The vorticity on the streamlines is assumed constant and equal to the value it attains at the separation point. The separating streamlines are allowed to develop freely, and their position is found by an iterative procedure. This method assumes an initial shape of the vortex sheets, finds the vorticity distribution which will satisfy the prescribed normal velocity condition on the body, finds the new free streamlines corresponding to the previous singularity distribution, and the procedure is iterated. Neither a convergence criterion nor the details of the numerical method are available. However, applications of the program developed by Dvorak et al. to the case of a circular cylinder showed that the results were greatly dependent on the wake fineness ratio which defines the wake length. This is a free parameter in the method and must be prescribed.

The models mentioned above are all steady, insofar as they treat only the mean flow past bluff bodies. When the time development of the flow about an impulsively started bluff body, or the vortex shedding behind it, is to be modeled, unsteady-flow equations must be solved with proper initial conditions. In modeling the vortex shedding behind circular cylinders, recently developed discrete-vortex models have gained popularity (see for example, Deffenbaugh and Marshall [14], Sarpkaya and Schoaff [15]). The principles, advantages and disadvantages of these models were described in detail by Sarpkaya and Schoaff. Such models also involve free parameters which have to be adjusted to ensure agreement with experiments. Also, calculations have thus far been restricted to the subcritical regime (Re $\leq 10^5$), presumably due to difficulties in passing through the critical regime or prescribing the initial conditions for the supercritical regime.

The foregoing review indicates that all irrotational-flow models involve some free parameters which have to be prescribed either from experiments or other considerations. The objective of the present study is to utilize boundary-layer theory to provide at least a part of this information so that the empirical inputs are minimized. Preliminary attempts at incorporating the influence of the boundary-layer displacement effects in the popular model of Parkinson and Jandali [5] had to be abandoned due to rather poor prediction of the pressure distribution beyond the pressure minimum (see Fig. 3), which is of critical interest in the calculation of the separation points. A new model, somewhat similar to that of Dvorak et al., was therefore developed. This is described below.

3 The New Irrotational-Flow Model With Boundary Layer Effects

3.1 Basic Assumptions. The real separated flow past a circular cylinder is approximated by the following assumptions (see Fig. 1(*a*)):

(i) The flow field is steady.

(ii) The boundary layer and the free shear layer are sufficiently thin, so that they can be represented by vortex sheets. The vorticity in the shear layer and in the boundary layer is assumed to be concentrated on the free streamline emerging from the separation point and on the body contour, respectively.

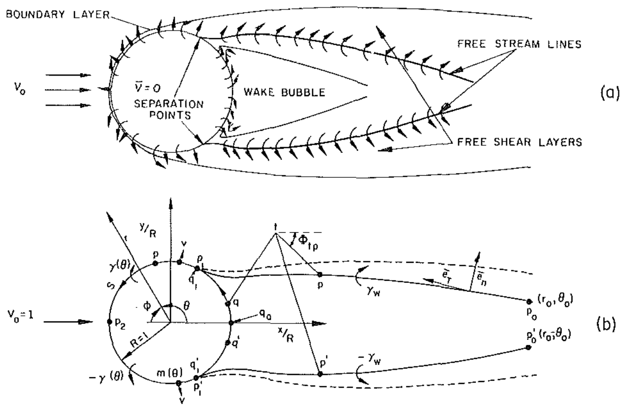

Fig. 1 Definition sketches; (*a*) mathematical model, (*b*) notation for integral equations

(iii) The wake bubble has negligible vorticity.

(iv) The vorticity strength on the free streamline is constant, at least in the near wake.

(v) There are stagnation points just downstream of the separation points on the body.

(vi) The influence of the boundary layer ahead of separation is represented by a source distribution on the surface such that the normal velocity is

$$v(\theta) = \frac{d}{d\theta}(2U_e\delta^*/D) \qquad (1)$$

where θ is the angle measured from the rear stagnation point, δ^* is the boundary-layer displacement thickness, U_e is the tangential velocity (outside the boundary layer), and D is the cylinder diameter. $v(\theta)$ is assumed to be negligible beyond separation.

3.2 Governing Equations and Solution. The above assumptions and boundary conditions pose a Neumann problem, the solution to which can be constructed by a system of singularity distributions composed of a source distribution $m(\theta)$ and a vortex sheet $\gamma(\theta)$, on the circle, a vortex sheet of constant strength γ_w on the shear layers, and a uniform stream of unit velocity $V_0 = 1$. The source distribution can be found to satisfy the inhomogeneous boundary condition $v_r = v$, and the vortex distribution can be determined such that the following conditions are satisfied:

(*a*) The normal velocity on the circle is zero.

(*b*) At the separation point, the vorticity is conserved, i.e., $\gamma_s = \gamma_w + \gamma_d$, where s and w refer to the upstream and downstream sides of the separation point on the exterior, and d refers to the downstream side in the interior.

(*c*) The tangential velocity at θ_d from the vortex distribution is equal and opposite to that of the source distribution (assumption (*v*) of Section 3.1).

The velocity at point t in the r-direction due to a unit source element and in the θ-direction due to a unit vortex element, at point p, in polar coordinates is given by (see Fig. 1(*b*) for notation)

$$G(p,t) = \frac{\partial \ln(r_{tp})}{\partial r_t} = [r_t - r_p\cos(\theta_p - \theta_t)]/r_{tp}^2 \qquad (2)$$

The boundary condition given by equation (1) can be satisfied by a source distribution $m(\theta_t)$ on the circle given by the integral equation

$$\pi m(\theta_t) + \int_0^{2\pi} m(\theta_q) G(q,t) d\theta_q = v(\theta_t) \tag{3}$$

Condition (*a*), which is equivalent to assuming that the fluid within the circle is at rest, yields the integral equation for the vortex sheets on the circle and the free streamlines:

$$\begin{aligned} & -\pi\gamma(t) + \int_{q_0}^{q_1} \gamma(q)[G(q,t) - G'(q',t)] d\theta_q \\ & \quad + \int_{p_0}^{p_2} \gamma(p)[G(p,t) - G(p',t)] ds_p - \sin\theta_t = 0 \end{aligned} \tag{4}$$

where $G(p', t) = G(r_p, -\theta_p, t)$ and s_p is the arc length at point p. This vortex distribution does not disturb the required outflow $v(\theta)$ at the circle, but the source distribution does contribute to the tangential velocity on the circle.

Since $G(q,t) = G(q',t) = 1/2$ on the circle, and $\gamma = \gamma_w =$ constant on the curve (p_0, p_1), equations (3) and (4) reduce to

$$m + M = v/\pi$$

or

$$m = (v - \bar{v}/2)/\pi \tag{5}$$

and

$$\pi\gamma + \sin\theta_t - \gamma_w Q = 0 \tag{6}$$

respectively. Here M and $\bar{v}$ are the mean values of m and v, defined as

$$M = \frac{1}{\pi}\int_0^{\pi} m(\theta) d\theta, \bar{v} = \frac{1}{\pi}\int_0^{\pi} v(\theta) d\theta \tag{7}$$

and Q is a wake influence function, which depends only on the geometry of the vortex sheets in the wake, defined as

$$Q(\theta_t) = \int_{p_0}^{p_1} [G(p,t) - G(p',t)] ds_p \tag{8}$$

At the stagnation point, we have $u_s = -2\pi\gamma_d$ and hence condition (ii) gives

$$\gamma_w = \gamma_s + u_s/2\pi \tag{9}$$

where u_s denotes the tangential velocity on the circle due to the source distribution. Equation (8) at $\theta = \theta_s$ and equation (9) can be used to obtain

$$\gamma_s = (2\sin\theta_s - u_s Q_s/\pi)/2(Q_s - \pi) \tag{10}$$

$$\gamma_w = (2\sin\theta_s - u_s)/2(Q_s - \pi) \tag{11}$$

Thus, given the location of the vortex sheet in the wake, the complete source and vortex distribution can be obtained from equations (5)-(11). The total tangential velocity on the circle, in particular, is given by

$$\begin{aligned} U &= -\sin\theta + u + \pi\gamma + \gamma_w Q \\ &= -2\sin\theta + u + \frac{(u_s - 2\sin\theta_s)Q}{(\pi - Q_s)} \end{aligned} \tag{12}$$

by equations (6) and (11). The first term on the right is the velocity due to the uniform stream, the second term is due to the boundary-layer displacement effect, and the third term is the combined effect of the boundary layer and the wake.

3.3 The Wake Length Parameter. Thus far, the positions of the vortex sheets have been assumed to be known. Since, initially, the streamlines emanating from the separation points are not known, the calculations must be started with a guess and the locations of the vortex sheets must be determined iteratively. Preliminary calculations with simple polynomials indicated that a second-degree curve (see Celik [16]), $r = r(\theta)$, gives rapid convergence. The boundary conditions of Section 3.1 require that the separating free streamlines must be tangent to the surface. Furthermore, due to a constant vorticity distribution (see assumption (iv), Section 3.1) on the vortex sheets, the streamlines must be terminated at some distance in the far wake although, in reality, the vorticity strength should decrease to zero far downstream. Thus, the constant-vorticity model requires the introduction of a wake-length parameter, w_l, which can be regarded as the effective wake length that represents the influence of the whole wake on the pressure distribution on the cylinder. The present model therefore involves two parameters, namely the separation angle θ_s and the wake length w_l. The former can be determined from boundary-layer calculations and the latter is determined by a trial-and-error procedure to match the calculated minimum pressure coefficient, C_{pm}; with a prescribed experimental value. In terms of the parameters θ_s and w_l, the second-degree curve in θ is given by

$$r = (w_l - 1)(\theta - \theta_s)^2/\theta_s^2 + 1 \tag{13}$$

The successive shapes of the streamlines are found by stepwise integration of the streamline equation with the initial condition: $r = 1$ at $\theta = \theta_s$. The new streamlines are calculated up to $x = w_l$ and they are not allowed to cross the vortex sheets since, if a streamline crosses a vortex sheet at a point where the local vorticity strength is nonzero, it can be deduced, from velocity considerations, that the streamline is refracted.

Thus, the pressure distribution on the cylinder can be determined iteratively, given the location of the separation point and the experimental value of the minimum pressure coefficient. Initial wake lengths chosen between 1.5D and 3D give rapid convergence. In the calculation of the new streamlines, singular or sharply peaked integrals are encountered. The singularities or the peaks can be eliminated as described by Celik [16].

3.4 Boundary-Layer Calculations and Overall Iterations. The information needed for the calculation of the source distribution from equations (1) and (5), and the location of separation has to be obtained from boundary-layer calculations. These, in turn, require the pressure distribution on the cylinder. Thus, the complete solution involves an iterative scheme which may be summarized as follows:

(*a*) Given Re and corresponding C_{pm}, take an initial guess for $\phi_s (= \pi - \theta_s)$.
(*b*) Determine the pressure distribution from the irrotational-flow model.
(*c*) Calculate δ^* and ϕ_s using the boundary layer method.
(*d*) Repeat steps (*b*) and (*c*) until some convergence criterion is satisfied.

The boundary-layer development is calculated using the method described in Celik and Patel [1]. This uses the numerical scheme and turbulence model of Cebeci and Smith [see 17] including the influence of surface curvature and low boundary-layer Reynolds numbers and empirical correlations for transition.

The overall iteration procedure converges quite rapidly provided the initial value of ϕ_s is larger than the final converged value. The convergence is slow in the supercritical regime and no convergence is obtained in the subcritical regime if the initial guess is lower than the experimentally observed values. Therefore, $\phi_s = 125°$ has been chosen for all calculations since it is larger than the values observed in all flow regimes except the critical regime. Since the latter is characterized by the presence of unstable separation bubbles, which the boundary-layer method cannot handle, calculations have not been performed in the critical regime.

3.5 The Base Pressure. The jump in the nondimensional total pressure head, H, across the vortex sheet is

$$\Delta H = U_i^2 - U_O^2 \tag{15}$$

where "i" and "o" denote the interior and exterior sides of the vortex sheet, U is the tangential velocity, made non-

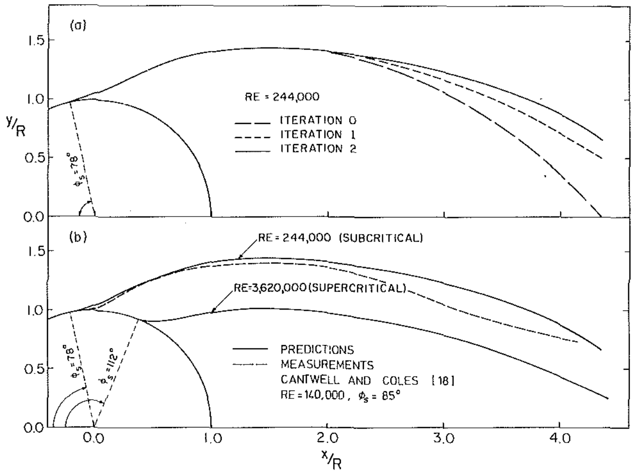

Fig. 2 Calculated wake shapes; (*a*) iterations, (*b*) converged solutions

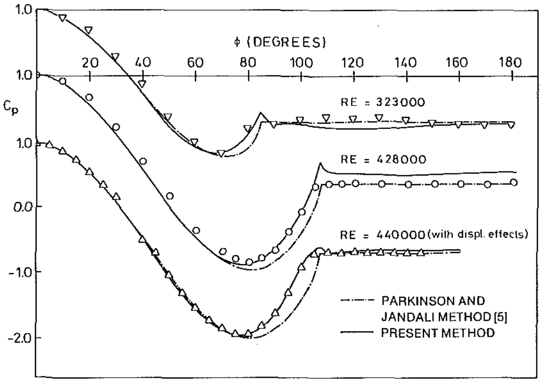

Fig. 3 Comparison of the present method and Parkinson and Jandali Method; Experiments: ▽ -Murphy [21], ○ -Achenbach [19], △ -Celik [16]

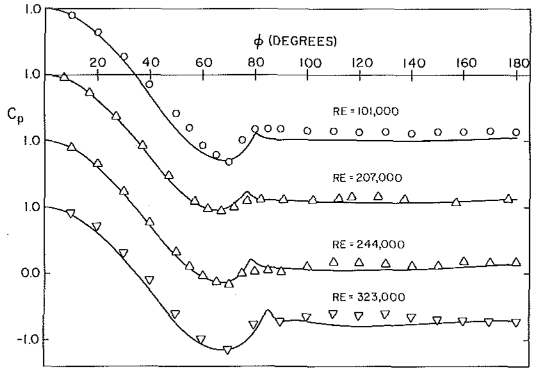

Fig. 4 Predictions in the subcritical regime. Experiments: ○ - Achenbach [19], △ -Güven et al. [20], ▽ -Murphy [21]; —— calculations (with or without displacement effects).

dimensional with the stream velocity V_o. With $2\pi\gamma_s = U_o - U_i$, equation (15) reduces to

$$\Delta H = 4\pi\gamma_s(\pi\gamma_s - U_O) \qquad (16)$$

Note that, because of assumption (iii) of Section 3.1, the total head must be constant in the wake bubble. Since the exterior flow is also irrotational, ΔH must be constant along the vortex sheets, contrary to assumption (iv) of Section 3.1. Nevertheless, since only a model of the real flow is considered, we shall allow ΔH to vary, and take its mean value as a constant total-head jump. That is

$$\overline{\Delta H} = 4\pi\gamma_s(\pi\gamma_s - U_O) \qquad (17)$$

In the calculations, the variation of U_o from its mean was

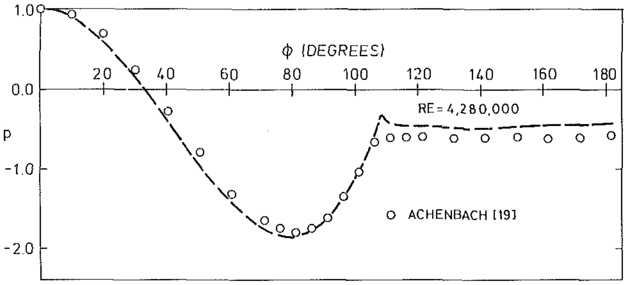

Fig. 5 Predictions in the supercritical regime. ○ -experiments, - - - - - calculations (without displacement effects).

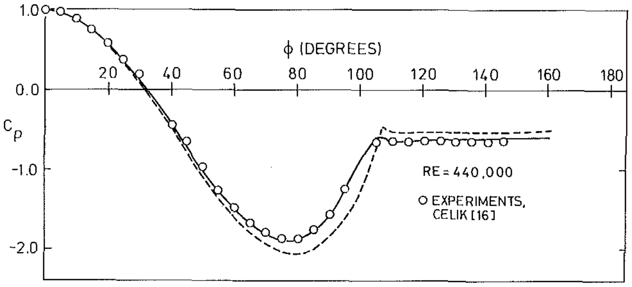

Fig. 6 Predictions on a cylinder with trip wires. Calculations: - - - - - without displacement effects, $C_{pm} = 1.1(C_{pm})_{\text{exp.}}$; —— with displacement effects $C_{pm} = (C_{pm})_{\text{exp}}$.

about ± 20 percent. The base pressure coefficient, C_{pb}, is then given by

$$C_{pb} = 1 - U^2 + \overline{\Delta H} \qquad (18)$$

4 Model Verification

The performance of the boundary-layer calculation method has been evaluated earlier [1] by comparisons with the available experimental data on circular cylinders. This aspect of the present method will not therefore be considered further.

Figure 2(*a*) shows the changes in the position of the vortex sheet during different wake iterations discussed in Section 3.3. The convergence criterion for these iterations was one percent difference between the calculated and prescribed values of C_{pm}. The final positions of the vortex sheets at two representative Reynolds numbers, one each in the sub- and super-critical regimes, are shown in Fig. 2(*b*). It is interesting to note that the shape of the separation streamline in the subcritical case agrees quite well with that determined from Cantwell and Cole's [18] measurements of the mean streamlines in the wake. However, it should be noted that the line calculated by the model represents the mean location of the separated shear layer rather than a physical streamline demarkating the wake bubble.

The results of the present irrotational-flow model, with and without boundary-layer displacement effects, are compared with those obtained with the model of Parkinson and Jandali [5] in Fig. 3. All experimental data shown here and later have been corrected for blockage. The same separation position is assumed in both models. However, the present model uses the minimum pressure coefficient whereas that of Parkinson and Jandali uses the base pressure. This is evident from the comparisons. We note that the present model gives a much better representation in the region of the pressure rise, a feature which is essential for the calculation of the boundary layer and the prediction of separation location. The small kinks in the neighborhood of the separation point in the present method arise due to the assumption of a constant total-head difference ΔH across the vortex sheet.

Figure 4 shows a comparison with the pressure distributions

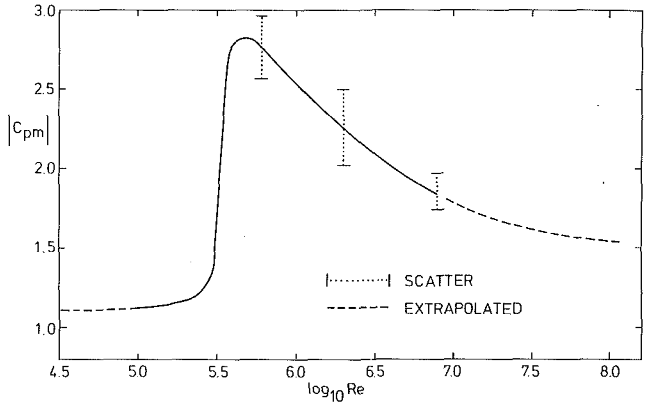

Fig. 7 Experimental correlation of C_{pm}

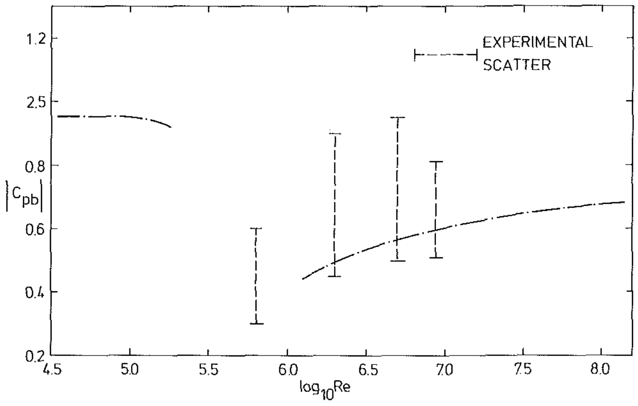

Fig. 8 Predicted base pressure coefficients

measured by several investigators [19–21] on nominally smooth cylinders at Reynolds numbers in the subcritical regime. Calculations in this regime indicated that the boundary-layer displacement effect is negligible, presumably because the laminar boundary layer remains thin all the way up to separation. Figure 4 shows that the pressure distribution is predicted satisfactorily although the calculated base-pressure coefficient is somewhat lower. However, the drag coefficients calculated by integrating the predicted pressure distributions agree with the experimenal values within three percent.

A similar comparison is made in the supercritical-flow regime with the high Reynolds number data of Achenbach [19] in Fig. 5. Here again the agreement is satisfactory. However, in this regime, the inclusion of the boundary-layer displacement effects leads to an approximately 10 percent decrease in the magnitude of C_{pm} (from that used in the wake iterations) and an increase in the magnitude of the base-pressure coefficient. Thus, in calculations without displacement effects, a 10 percent higher value is chosen for C_{pm} to demonstrate the displacement thickness effect (Fig. 6). The data were obtained by Celik [16], who studied the possibility of simulating supercritical flow at lower Reynolds numbers by fitting trip wires on a smooth cylinder. This particular case is chosen since the boundary layer development downstream of the trip wires was also measured. The calculations with the displacement thickness utilized laminar-flow calculation up to the wire and measured values beyond the wire so that any uncertainty in the turbulent boundary-layer calculation method is avoided. The effect of including the displacement thickness is clearly seen and the improvement in the agreement between the predicted and the measured pressure distribution is particularly noteworthy. A similar calculation for the case shown in Fig. 5 should also lead to an improvement in the base-pressure prediction.

5 Model Predictions

The irrotational-flow model described above and the boundary-layer calculation procedure of Celik and Patel [1] were combined, as discussed in Section 3.4, to predict the major mean-flow parameters over a range of Reynolds number in the sub- and supercritical flow regimes. The only parameter required to complete the inputs, namely C_{pm}, was obtained from the correlation of experimental data from several sources made by Güven et al. [20]. The variation of C_{pm} with Re is shown in Fig. 7 along with the scatter band. In order to continue the predictions beyond the largest Re for which data have been obtained, this correlation was extrapolated as shown. It should be noted that a parameter other than C_{pm}, for example C_{pb}, could have been chosen in the irrotational-flow model. However, C_{pm} has been used here since it is easily defined and it contains the smallest experimental scatter. Also, matching of C_{pm} ensures that the boundary-layer development in the important pressure-rise region is calculated realistically.

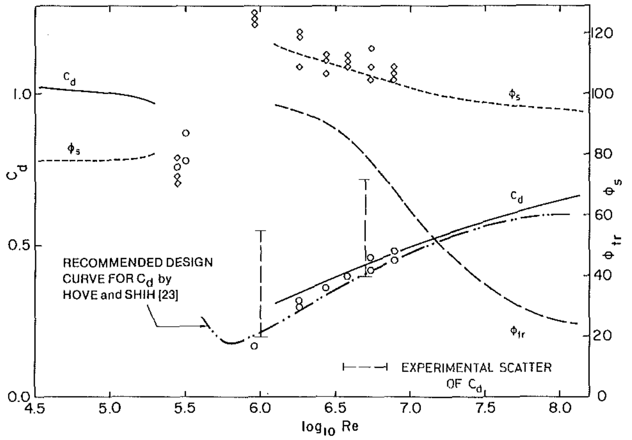

Fig. 9 Predicted C_d, ϕ_s, and ϕ_{tr}. Experiments: ○, ◇ -James et al. [22].

The results of the calculations in the Reynolds-number ranges $4.0 \times 10^4 < \text{Re} < 1.6 \times 10^5$ and $1.6 \times 10^6 < \text{Re} < 1.0 \times 10^8$ are presented in Figs. 8 and 9. Also shown in these figures are: (*a*) scatter bands of the available experimental data on the base pressure, C_{pb}, and the drag coefficient, C_d, (*b*) the recent data of James et al. [22] on the separation angle, ϕ_s, and the drag coefficient, and (*c*) a "design" curve for C_d recommended by Hove and Shih [23] for OTEC cold-water pipes on the basis of their evaluation of the experimental data from various sources. The data of James et al. are identified separately since they were obtained with the smallest relative surface roughness and, as discussed in [20] and [22], the scatter in the previous data is believed to be due to differences in the effective surface roughness. As noted earlier, all the data presented here have been corrected for blockage effects.

Figure 8 shows that the predicted base pressure is somewhat lower than the mean of the experimental data. However, it lies within the scatter of the data. From Fig. 9 it is evident that the calculated separation angles and drag coefficients are in good agreement with the data of James et al. The excellent agreement between the predicted drag coefficient and the design curve of Hove and Shih is particularly noteworthy and may be regarded as a theoretical verification of the empirical correlation. The fact that the calculated values lie at the lower end of the scatter band of the previous data, as in the case of the base pressure, appears to be due to unknown surface roughness effects in the earlier experiments. The calculated upstream shift in the location of transition, ϕ_{tr}, in the supercritical flow regime also appears to be reasonable.

6 Concluding Remarks

A new two-parameter irrotational-flow model, which takes into account the displacement thickness of the boundary layer, has been proposed and evaluated by comparison with experimental data. The boundary layer effect has been shown to be important in the supercritical flow regime. This is presumably due to the rapid thickening of the boundary layer in the extensive pressure-rise region in this regime.

In the early stages of this research, it was hoped to obtain the two model parameters by coupling the irrotational-flow model with a boundary-layer calculation procedure, and thus develop a model that would not require any empirical inputs. Unfortunately, the limitations of the potential-flow model with regard to the prediction of the complex real structure of the wake precluded the determination of a wake length parameter which, in turn, could be related to the base pressure or the minimum pressure coefficient. However, the location of separation could be predicted with some degree of confidence and therefore the complete solution procedure requires the specification of only one parameter. The calculations presented here utilize experimental values of C_{pm}, and therefore the results suffer from uncertainties in this parameter. The predictions for the high Reynolds numbers should therefore be regarded with some caution since they are based on an extrapolation of the correlation for the minimum pressure coefficient.

Finally, we note that the present calculations continue to show a Reynolds-number dependence even up to $Re = 10^8$ and do not indicate a Reynolds-number independent flow regime which has been conjectured on the basis of experimental information. This may of course be due to the way in which the available minimum pressure-coefficient data has been extrapolated (Fig. 7) to high Reynolds numbers. Another possible reason may be the increasing influence of surface roughness with increasing Reynolds number, which is not considered in the model. It would therefore be of interest to modify the boundary-layer method to incorporate roughness effects to study its influence as the Reynolds number is increased.

Acknowledgments

This research was performed at the Iowa Institute of Hydraulic Research under the sponsorship of the National Science Foundation Grant ENG-76-08849.

References

1 Celik, I., and Patel, V. C., "Boundary-Layer Development on Circular Cylinders," *Boundary-Layer Meteorology*, Vol. 24, 1982, pp. 281–293.

2 Roshko, A., "A New Hodograph for Free-Streamline Theory," NACA TN-3168, 1954.

3 Lin, A., and Landweber, L., "On a Solution for the Lavrentiev Wake Model and its Cascade," *Journal of Fluid Mechanics*, Vol. 79, 1977, pp. 801–823.

4 Wu, T. Y., "Cavity and Wake Flows," *Annual Review of Fluid Mechanics*, Vol. 4, 1972, pp. 243–284.

5 Parkinson, G. V., and Jandali, T., "A Wake Source Model for Bluff Body Potential Flow," *Journal of Fluid Mechanics*, Vol. 40, 1970, pp. 577–594.

6 Güven, O., "An Experimental and Analytical Study of Surface Roughness Effects on the Mean Flow Past Circular Cylinders," Ph.D. thesis, Mechanics and Hydraulics, Univ. of Iowa, Iowa City, Iowa, 1975.

7 Bearman, P. W., and Fackrell, J. E., "Calculation of Two-Dimensional and Axisymmetric Bluff-Body Potential Flow," *Journal of Fluid Mechanics*, Vol. 72, 1975, pp. 229–241.

8 Bhateley, I. C., and Bradley, R. G., "A Simplified Mathematical Model for the Analysis of Multi-Element Airfoils Near Stall," AGARD Conference Proceedings, No. 102, Fluid Dynamics of Aircraft Stalling, 1972.

9 Jacob, K., "Berechnung der abgeloesten inkompressiblen Stroemung um Tragfluegelprofile und Bestimmung des maximalen Auftriebs," *Zeitschrift für Flugwissenschaften*, Vol. 17, 1969, pp. 221–230.

10 Jacob, K., "Weiterentwicklung eines Verfahrens zur Berechnung der abgeloesten Profilstroemung mit besonderer Beruecksichtigung des Profilwiderstandes," Deutsche Forschungs- und Versuchsanstalt für Luft-und Raumfahrt, DLR-FB-76-36, Institut für Stroemungsmechanik, Goettingen, FRG, 1976.

11 Jacob, K., and Steinbach, D., "A Method for Prediction of Lift for Multi-Element Airfoil Systems with Separation," AGARD Conference Proceedings, No. 143, V/STOL Aerodynamics, 1974.

12 Pullin, D. I., "A Constant Vorticity Riabouchinsky Wake Model," Dept. of Mech. Engng., Univ. of Melbourne, Parkville, Victoria, Australia (unpublished), 1980.

13 Dvorak, F. A., Maskew, B., and Rao, B. M., "An Investigation of Separation Models for the Prediction of $C_{l\max}$," Final Technical Report, Contract DAAG29-76-C-0019, Analytical Methods, Inc., Bellevue, Wash., 1979.

14 Defenbaugh, F. D., and Marshall, F. J., "Time Development of the Flow about an Impulsively Started Cylinder," *AIAA Journal*, Vol. 14, 1976, pp. 908–193.

15 Sarpkaya, T., and Schoaff, R. L., "Inviscid Model for Two-Dimensional Vortex Shedding by a Circular Cylinder," *AIAA Journal*, Vol. 17, 1979, pp. 1193–1200.

16 Celik, I., "Mean Flow Past Circular Cylinders," Ph.D. thesis, Mechanics and Hydraulics, Univ. of Iowa, Iowa City, Iowa, 1980.

17 Cebeci, T., and Bradshaw, P., *Momentum Transfer in Boundary Layers*, Hemisphere Publishing Corporation, Washington, 1977.

18 Cantwell, B., and Coles, D., "An Experimental Study of Entrainment and Transport in the Turbulent Near Wake of a Circular Cylinder," *Journal of Fluid Mechanics*, Vol. 136, 1983, pp. 321–374.

19 Achenbach, E., "Distribution of Local Pressure and Skin Friction around a Circular Cylinder in Cross-Flow up to $Re = 5 \times 10^6$," *Journal of Fluid Mechanics*, Vol. 34, 1968, pp. 625–635.

20 Güven, O., Farell, C., and Patel, V. C., "Surface-Roughness Effects on the Mean Flow Past Circular Cylinders," *Journal of Fluid Mechanics*, Vol. 98, 1980, pp. 673–701.

21 Murphy, J. C., "The Effects of Nonsteady Flow on the Pressure Distribution About a Circular Cylinder," Thesis, United States Naval Postgraduate School, Monterey, Calif., 1966.

22 James, W. D., Paris, S. W., and Malcolm, G. N., "Study of Viscous Crossflow Effects on Circular Cylinders at High Reynolds Numbers," *AIAA Journal*, Vol. 18, 1980, pp. 1066–1072.

23 Hove, D. T., and Shih, W. C. L., "Hydrodynamic Loads on the Cold Water Pipe," George E. Loup, Ed., *Proceedings of the 4th Annual Conference on Ocean Thermal Energy Conversion*, University of New Orleans, Mar. 22–24, 1977, pp. v-23-v-39.

M. C. Roco
Department of Mechanical Engineering,
University of Kentucky,
Lexington, KY 40506
Mem. ASME

C. A. Shook
Department of Chemical Engineering,
University of Saskatchewan,
Saskatchewan, S7N 0W0, Canada

Turbulent Flow of Incompressible Mixtures[1]

The spatial nonuniformities and the interactions between the components determine the flow behavior of multicomponent systems. A space/time averaging approach of the governing equations modeling these factors is presented in this paper. It is defined for a weighted averaging volume whose size is related to the local scale of turbulence. Numerical solutions for concentration and velocity distributions are obtained using integral finite volume techniques. The predictions are comapred with good results to multi-species particle slurry flows in pipelines.

Introduction

The hydraulic handling of bulk materials of broad size distribution (coal, limestone, etc.) is widely applied in mining, chemical and other industrial processes. Despite the large area of application, the known models do not complete satisfy either the scientific rigor or engineering needs for numerical predictions. Increases research activities have been oriented in this domain in the last few years.

This paper presents a model for the turbulent flow of multi-species particle suspensions, in which a new set of equations is derived using a space/time averaging approach. The model assumptions are valid for large particles and high concentrations (up to 70 percent of maximum packing concentration), when particle-particle interactions are important.

The temporal nonuniformities in single phase turbulent flows are shown in the mean flow equations using time averaging. The Reynolds stresses appear in this way in momentum equations and have predominant values compared to the viscous stresses. To express the spatial nonuniformities in multicomponent flows it is also necessary to average the governing equations by volume. As the time averaging yields terms showing new qualitative effects, so the space averaging is expected to reveal not only quantitative changes of the nonlinear terms but also some new qualitative aspects of the component interactions.

The formulation of the governing equations for heterogeneous flow has been done either by considering each phase separately with corresponding interaction terms, by assuming a continuum medium with averaged field quantitites, or by using volume averaging (see Soo, 1967; Whitaker, 1973; Hestroni, 1982). The local volume averaging procedure for multiphase systems may be performed in various ways related to the specific flow conditions (for porous media Slattery, 1967; for fluidized beds, Anderson and Jackson, 1967; for boiling, Vernier and Delhaye, 1968, etc.). In this paper we discuss an averaging approach specifically for multicomponent turbulent flow.

The spatial nonuniformities in multi-species particle flow are reflected in the random distributions of the flow components, as well as in particle cluster formation in shear suspension flows. The spatial nonuniformities strongly affect the non-linear terms in the equations of motion. To analyze the multicomponent flows, we suggest a weighted averaging for a local volume whose dimensions are related to the length scale of turbulence. The weighted averaging is appropriate since it is known that the spatial cross-correlations in turbulent flow decrease with the space interval. For steady-state turbulent flow the instantaneous point equations are averaged only over the weighted averaging volume. The computation of the component velocities and concentrations is performed using an appropriate integral finite volume technique. The results are compared with a large set of experimental results considering one to five species of particles (of size $d \leq 13$ mm) flowing with water in various pipes (rectangular, circular $D = 40$–495 mm).

In the space allowed by this paper we detail aspects related to the momentum equation and concentration calculation. The eddy-diffusivity used for concentration calculation was obtained from a transport equation (one-equation model).

Composed Averaged Equations

The local volume averaging for differential equations has to be performed in agreement with the averaging of the quantities used in the equations. A typical situation occurs when the temporal averaged measurement of the considered quantities is taken over a prescribed volume or surface. This is the case for the velocity measurements reported later in the paper. Another situation occurs when the time dependent flow is analyzed using the instantaneous spatial averages in the equations. In this case the averaging space is related to the flow conditions. Sometimes, the volume averaging may be considered to improve the continuity and differentiability of the variables. The spatial averaging has a supplementary meaning and computational significance when finite volume techniques are employed. All these situations are covered by the weighted average by volume proposed in the sections which follow.

Alternatively, to calculate the instantaneous point variables

---

[1] Paper presented at the 4th International Symposium on Turbulent Shear Flow, Organized by NSF/ONR/USAF/ASME, Karlsruhe, 1983, pp. 12.1–12.8.

Contributed by the Fluids Engineering Division for publication in the JOURNAL OF FLUIDS ENGINEERING. Manuscript received by the Fluids Engineering Division, October 11, 1983.

one must use the time dependent equations with a very fine grid compared to the length scale of turbulence and a small timestep. This approach has been tested only for single fluid flow in small domains and proved to be very expensive and thus without immediate practical interest.

Space/Time Averaging Approach. Let us consider a flowing mixture of N solid components in an incompressible fluid. The space/time average of a function f for the Kth component at a position $\mathbf{r}$ and time t is:

$$\bar{f}^K = \frac{1}{\Delta T}\int_{t-\Delta T/2}^{t+\Delta T/2} <\alpha(\mathbf{r},t)>_K \cdot <f(\mathbf{r},t)>^K \cdot dt \tag{1}$$

where:

$<\alpha(\mathbf{r},t)>_K$ = bulk space averaged concentration for the Kth component
$<f(\mathbf{r},t)>^K$ = intrinsic space average of f for the Kth component
ΔT = averaging time interval

The volume averaging for the Kth component is weighted by the Eulerian cross-correlation for velocities $R_K(\xi-\mathbf{r})$, which gives a measure of the influence of flow parameters at ξ on the flow parameters at $\mathbf{r}$ (Fig. 1):

$$R_K(\xi-\mathbf{r}) = \frac{\overline{V_K'(\mathbf{r})\cdot V_K'(\xi)}}{\sqrt{\overline{V_K'(\mathbf{r})^2}\cdot\overline{V_K'(\xi)^2}}} \tag{2}$$

where

$V_K'(\mathbf{r}), V_K'(\xi)$ = instantaneous fluctuating velocities of the Kth component at $\mathbf{r}$ and ξ, respectively.

If the same lump of fluid, or the same turbulent eddy, involves both points $\mathbf{r}$ and ξ, the $R_K(\xi - \mathbf{r}) = 1$. If $R_K(\xi - \mathbf{r}) = 0$ no interaction between the turbulence parameters at ξ and $\mathbf{r}$ occurs. It is well known that in turbulent flows the largest eddies may have dimensions close to the characteristic length of the flow domain. A global measure of the cross-correlations $R_K(\xi - \mathbf{r})$ is the mixing length Λ_K.

The intrinsic volume averaging of f about $\mathbf{r}$ is:

$$<f(\mathbf{r},t)>^K = \int_{\Delta v} f(\xi,t)\cdot K(\xi,t)\cdot R_K(\xi-\mathbf{r})\cdot dv \Big/ \int_{\Delta v} K(\xi,t)\cdot R_K(\xi-\mathbf{r})\cdot dv \tag{3}$$

where:

$f(\xi,t)$ = instantaneous local value of f
Δv = averaging volume, about $\mathbf{r}$ (Fig. 1(a))
ξ = position vector for an interior point in Δv
$K(\xi,t) = \begin{cases} 1 \text{ if component } K \text{ resides at } (\xi, t) \\ 0 \text{ otherwise} \end{cases}$
$R_K(\xi-\mathbf{r})$ = spatial cross-correlation, defined in (2)

The averaging volume should be taken as a domain large enough to contain large scale turbulent eddies. In usual situations only an ellipsoid with the main axes equal to the mixing lengths around $\mathbf{r}$ may be sufficient (at solid boundaries R_K is very small or approaches zero).

The bulk space average of concentration about $\mathbf{r}$ is:

$$<\alpha(\mathbf{r},t)>_K = \int_{\Delta v} K(\xi,t)\cdot R_K(\xi-\mathbf{r})\cdot dv \Big/ \int_{\Delta v} R_K(\xi-\mathbf{r})\cdot dv \tag{4}$$

The first integral is the weighted averaging volume over the Kth component, the second - over all the components.

By using this averaging approach (1) one can take into account the spatial non-uniformities which affect the flow behavior at a point, including cluster formation and macroturbulent structure. The volume averages (3) and (4) can be used if data on the spatial cross-correlation $R_K(\xi - \mathbf{r})$ and particle distributions $K(\xi, t)$ are available. Such data can be obtained using various experimental techniques (three dimensional camera, Graham et al., 1982; laser apparatus, Lee and Durst, 1982) or from analytical or numerical simulations. Since there are fewer data on volume integrals we present here a conversion from the weighted space integrals to weighted time integrals.

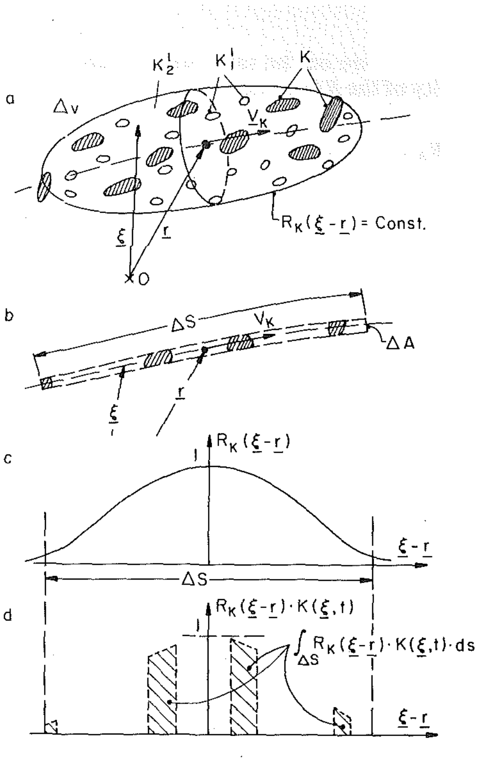

Fig. 1 Averaging volume (Δv)

From Volume Averaging to Time Averaging. There are two reasons to replace the space with time integrals: (1) it is easier to measure the time variations at a point (Eulerian description), (2) the mathematical schemes already used for time averaging are available.

In an isotropic turbulent flow about a position $\mathbf{r}$ the surfaces of equal $R_K(\xi - \mathbf{r})$ are spherical, and the averaging volume Δv may be taken as a sphere. When the turbulence has an anisotropic character the averaging volume should be an ellipsoid, bounded by a surface of constant cross-correlation (2). The presence of solid walls may produce an asymmetrical surface of constant $R_K(\xi - \mathbf{r})$. When the sheared flow has a predominant direction, so has the averaging volume. A simplified approach is to employ a volume defined by Λ_K, without weighting function R_K (Roco, 1983).

Let us consider the stream tube passing through $\mathbf{r}$, which should be along the largest semiaxis of the averaging ellipsoid. The initial integrals on Δr from (3) and (4) are replaced by integrals on stream tubes $\Delta v' = \Delta A \cdot \Delta s$ (Fig. 1(b)), assuming the same spatial nonuniformity occurs on both averaging volumes Δv, $\Delta v'$. Changing the variable $\Delta t = \Delta s/\bar{V}_K$ we obtain from (3):

$$<f(\mathbf{r},t)>^K = \int_{t-\Delta t/2}^{t+\Delta t/2} f(\mathbf{r},\tau)\cdot K(\mathbf{r},\tau)\cdot R_K(\tau-t)\cdot d\tau \Big/ \int_{t-\Delta t/2}^{t+\Delta t/2} K(\mathbf{r},\tau)\cdot R_K(\tau-t)\cdot d\tau \tag{5}$$

where: $\tau = |\xi-\mathbf{r}|/\bar{V}_K$

in which ξ and **r** are on the same stream tube, and $\bar{V}_K$ is the mean velocity of the Kth component;

$$R_K(\tau-t)=\frac{\overline{V'_K(t)\bullet V'_K(t-\tau)}}{\overline{V'_K(t)^2}} \tag{6}$$

is the Eulerian time correlation:

$$\int_{t-\Delta t/2}^{t+\Delta t/2} K(\mathbf{r},\tau)\bullet R_K(\tau-t)\bullet d\tau = Z_K\bullet <\alpha(\mathbf{r},t)>_K \tag{7}$$

in which Z_K is the Eulerian time scale for the Kth component.

The averaging formla (5) is specific for turbulent flow, when all $K = 1, N$ components are in motion. If at least one component is at rest ($V_K \rightarrow 0$) the variable change $\Delta v \rightarrow \Delta t$ is no longer recommended and the previously defined formula (3) should be used.

The interval of time Δt can be approximated by different formulae defining the time scale of turbulence, or by taking $\bar{V}_K$ equal to the mean velocity scale. This approximation is acceptable because the differences will be in domains where $R_K(\tau - t) \ll 1$. The averaging (5) can directly be applied determining Δt by iteration. It should be noted that formula (5) may be employed to define constitutive equations for typical flow situations, when all instantaneous and mean flow indices are either measured, or determined analytically or numerically by independent means.

Close to the wall, in the boundary layer, Δt takes finite values approaching zero in the laminar sublayer ($\Delta t = \Delta s/\bar{V}_K \sim \Lambda_K/\bar{V}_K$; the mixing length Λ_K approaches zero faster than $\bar{V}_K$; in the laminar sublayer $\Lambda_K = 0$ while $\bar{V}_K \neq 0$).

The time-space averaging operator (1) becomes with (5) a double time averaging operator:

$$\bar{f}^K=\frac{1}{\Delta T}\int_{t-\Delta T/2}^{t+\Delta T/2}\left[\frac{1}{Z_K}\int_{t-\Delta t/2}^{t+\Delta t/2} f(\mathbf{r},\tau)\bullet K(\mathbf{r},\tau)\bullet R_K(\tau-t)\bullet d\tau\right]\bullet dt \tag{8}$$

The inner integral represents the spatial integration converted to a time integration by relating space and time through velocity. The averaging time interval Δt (Δv, respectively) depends on the flow conditions, and in general can be taken as variable in the flow domain. It is assumed that the gradient of the averaging volume in space or time is small compared to its absolute value. The changes in Δt are mainly due to the component nonuniformities and may be important compared to the time (ΔT) change in the average. In the case of $K(\mathbf{r}, t) = 1$ for liquid the equation (8) becomes identical to that found in literature for one-phase turbulence.

A local instantaneous value differs from the mean value $\bar{f}^K$ by two fluctuating components: one reflecting the spatial nonuniformities $(f'_K)_t$, the second the time nonuniformities of the spatial average $(f'_K)_T$:

$$f'_K=f_K-\bar{f}^K=(f'_K)_t+(f'_K)_T \tag{9}$$

where: $(f'_K)_t=f_K-<f_K>^K$

$(f'_K)_T=<f_K>^K-\bar{f}^K$

Averaged Conservation Equations. The local instantaneous conservation equation can be written for each component K, as well as for the entire mixture, in a general form:

$$\frac{\partial}{\partial t}(\rho\,\psi)+\nabla\bullet(\rho\,\psi\,\mathbf{U})+\nabla\,\mathbf{J}-S=0 \tag{10}$$

where: ρ = density

U = velocity vector

ψ = specific quantity attached to mass

J = flux tensor

S = source term

By averaging for each component ($K = 1, N$) the conservation equations of mass, momentum and energy dissipation one obtains a new system of equations to determine mean velocity, concentration and turbulence index distributions. We rearranged the equations in such a way for solutions to be conveniently obtained by an iterative explicit scheme.

Let us consider *the momentum equation* in the **i** direction: ψ_K corresponds to the projection of the velocity vector, $\mathbf{J}_K$ to the shear stress tensor and S_K to the projection of the body force vector.

The space/time averaging process of the local instantaneous momentum equation in the **i** direction yields for the Kth component in steady-state regime without component generation (no attrition and no phase change) is:

$$\begin{aligned}\rho_K\frac{\partial}{\partial x_j}(\bar{\alpha}_K\bar{U}_{Ki}\bar{U}_{Kj}) &= \rho_K\bar{\alpha}_K\bar{b}_i-\frac{\partial}{\partial x_i}(\bar{\alpha}_K\bar{p}_K+\overline{\alpha'_Kp'_K})\\ &+\frac{\partial}{\partial x_j}(\bar{\alpha}_K\tau_{K\Sigma_{ji}}+\overline{\alpha'_K\tau'_{K\Sigma_{ji}}})-\rho_K\frac{\partial}{\partial x_j}[\overline{\alpha'_K(U_{Ki}U_{Kj})'}\\ &+\bar{\alpha}_K\overline{U'_{Ki}U'_{Kj}}]+\sum_{-K}\left[\frac{\mathbf{e}_i}{\Delta T}\int_{t-\Delta T/2}^{t+\Delta T/2}\frac{1}{Z_K}\bullet\sum_m\frac{\underline{\mathbf{T}}_{KK'}\bullet n_K}{\mathbf{U}_{KK'}\bullet n_K}\right.\\ &\left.\bullet R_K(\tau-t)\bullet dT\right]\end{aligned} \tag{11}$$

where:

i, j $= x, y, z$

$\bar{f}$ is a simplified notation of $\bar{f}^K$

f' = fluctuating part of f given in (9)

U'_{Ki}, U'_{Kj} = projections of the fluctuating velocity, in the **i** and **j** directions, respectively.

$\bar{b}_i$ = mass force in the **i** direction

$\tau_{K\Sigma_{ji}}$ = superficial stress for component K

$\Sigma_{-K}[\ldots]$ = projection in the **i** direction of the interactions with all other flow components $K' = 1, N_{-K}$, including viscous friction, collisions and Coulombic contacts between components.

$\mathbf{e}_i$ = unit vector in the **i** direction

Z_K = Eulerian time scale for the Kth component

m = denotes the number of an interface between K and other component K' passing through **r** during the interval t.

$\mathbf{U}_{KK'}$ = velocity vector of the interface point crossing **r**

$\underline{\mathbf{T}}_{KK'}$ = stress tensor between the Kth and K'th components

$\mathbf{n}_K$ = unit normal vector to component K

Assuming low correlations between α'_K and p'_K (i.e., $\overline{\alpha'_Kp'_K}$ neglected) the following terms in equations (11) have to be modelled:

$\bar{\tau}_{K\Sigma_{ji}}$, $\overline{\alpha'_K\tau'_{K\Sigma_{ji}}}$, $\overline{\alpha'_K(U_{Ki}U_{Kj})'}$, $\overline{U'_{Ki}U'_{Kj}}$, and interaction terms $\Sigma_{-K}[\ldots]$

Modeling may be achieved by using measurements of instantaneous quantities in the averaging volume, or mechanistic approaches or from dimensional analysis of local flow indices. To obtain engineering models for these terms we follow the steps: (1) find the physical interpretation, (2) identify the local dimensionless parameters (the ratios particle size/turbulence scale, gravitational force/hydrodynamical force, etc.) affecting the terms, and (3) propose constitutive equations based on the analysis at particle scale and comparison of the mean flow predictions with a large set of experiments.

We observe that the tensor $\underline{\mathbf{T}}_{KK'}$ in the interaction term $\Sigma_{-K}\ [\ldots]$ has components corresponding to $\bar{\tau}_{K\Sigma_{ji}}$, $\overline{\alpha'_K\tau'_{K\Sigma_{ji}}}$, $\overline{\alpha'(U_{Ki}U_{Kj})'}$; and $\overline{U'_{Ki}U'_{Kj}}$. It means that the same types of interactions occur between particles of the same species and particles of different species, i.e., similar models for both groups of terms may be employed. The physical interpretation of these terms is:

(1) $\tau_{K\Sigma_{ji}}$ - stress transmitted by Coulombic contacts between solid particles or by viscous effects when the flow component is a fluid. The Coulombic shear stress depends on the normal stress transmitted by particle contacts ($\tau_{K\Sigma_{jj}}$) and a friction coefficient ($\tan\beta$) independent of the rate of strain (Roco and Shook, 1983a):

$$\tau_{K\Sigma_{jj}} = \tau_{K\Sigma_{ji}} / \tan\beta \tag{12}$$

where $\tau_{K\Sigma_{jj}}$ can be estimated as a supported load stress. The viscous effects are taken in account by the drag force:

$$\frac{3}{4}\,\alpha_K\,\frac{\rho_L \bullet C_{DK}}{d_K}\,\frac{|V_L - V_K|\,(V_L - V_K)}{(1-\alpha_K)^{1.7}} \tag{13}$$

where:

α_K = concentration of a solid component

d_K = particle dimension

V_L, V_K = velocity of liquid and the Kth component, respectively

C_{DK} = drag coefficient depending on dimensions and shape of solid particles (component K) (Roco and Shook, 1983a). Published data on C_{DK} were reviewed by Ishii and Mishima, 1983.

(2) $\rho_K \overline{\alpha_K' (U_{Ki} U_{Kj})'}$ and $\overline{\alpha_K' \tau_{K\Sigma_{ji}}'}$ - stresses caused by elastic and plastic particle collisions, respectively. The global value of the repulsive normal stress ($\tau_{DS_{jj}}$) acting between sheared layers of suspensions due to collisions depends on the shear stress τ_{Sij} and a coefficient of dynamic friction by collisions ($\tan\theta$):

$$\tau_{DS_{jj}} = \rho_K \overline{\alpha_K' (U_{Kj} U_{Kj})'} + \overline{\alpha_K' \tau_{K\Sigma_{jj}}'} = \frac{\tau_{S_{ji}}}{\tan\theta} \tag{14}$$

where: $\tan\theta$ may be related to the local Froude number, taking values about $\tan\theta \approx .5$ (Roco and Shook, 1983b). By considering the momentum exchange between colliding particles in the averaging volume (Fig. 2) one can obtain the ratio between the shear and normal stress ($\tau_{S_{ji}}/\tau_{DS_{jj}} = \tan\theta$) as function of local hydrodynamic parameters and the restitution coefficient ($\epsilon_R = 1$ elastic collision; $\epsilon_R = 0$ plastic collision). The mechanistic model yields the following expression for uniform particles (Shen, 1983).:

$$\left|\frac{\tau_{S_{ji}}}{\tau_{DS_{jj}}}\right| = \tan\theta = \frac{\pi^2}{2} \bullet \left[\frac{(1+\alpha_{CI})(0.05+0.08\mu_F)\dfrac{3C_{DK}\rho_L}{2\lambda p_S} + \dfrac{(1+\epsilon_R^2)}{8} + \dfrac{\mu_F(1+\epsilon_R)}{2\pi} - \dfrac{\mu_F^2(1+\epsilon_R)^2}{8}}{\alpha_{CI}(1+\epsilon_R)}\right]^{1/2} \tag{15}$$

where: α_{CI} = linear concentration

μ_F = coefficient of kinetic friction

ϵ_R = coefficient of restitution

ρ_L = density of liquid

C_{DK} = drag coefficient for particle species K

By adopting averaged values of the coefficients for sand particles (with $\epsilon_R = .9$) one obtains the dynamic coefficient of friction between .5 and .6. The model includes the drag force. The same averaged value ($\tan\theta \simeq .5$) is obtained from the numerical analysis of the experimental data on the mean flow.

(3) $\rho_K \alpha_K \overline{U_{Ki}' U_{Kj}'}$ - turbulent inertial stress due to the random exchange of particles between neighboring layers. In our study two models for this term were used in parallel:

— eddy viscosity $\epsilon_{K_{ji}}$ model (Boussinesq)

$$-\overline{U_{Ki}' U_{Kj}'} = \epsilon_{K_{ji}} \frac{\partial \bar{U}_{Ki}}{\partial x_j} \tag{16}$$

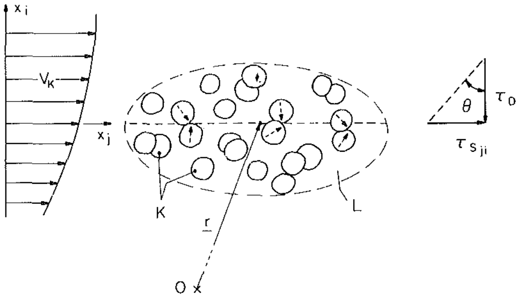

Fig. 2 Stresses between colliding particles: $\tau_{DS_{ii}}$ · dispersive stress, $\tau_{S_{ji}}$ · shear stress

— streamtube diffusion $\lambda_{K_{ji}}$ model (Roco, 1980)

$$-\overline{U_{Ki}' U_{Kj}'} = \frac{\partial}{\partial x_j}(\lambda_{K_{ji}} \bar{U}_{Ki}^2) \tag{17}$$

The shear stresses are expressed in this model in terms of partial derivatives of the mean flow kinetic energy multiplied by a turbulence index, denoted $\lambda_{K_{ji}}$. The $\lambda_{K_{ij}}$ tensor components depend on the boundary conditions and mean flow parameters.

The Boussinesq model was used in conjunction with the transport equation for the energy dissipation rate (Roco and Balakrishnan, 1982). The second model was applied for two-phase liquid solid particle flow using a specific distance from the pipe wall (Roco and Shook, 1981). In both approaches the mixture turbulence parameter is obtained by taking the sum of the contributions of all the flow components.

A detailed interpretation of the pressure terms in the averaged two-phase equations, (11), including the case of large separation velocities between phases, is given in [7].

The new set of equations resulting from the space/time averaging (8) of the conservation equations was rearranged for an iterative explicit scheme to calculate successively concentrations, velocities and turbulence parameter. The concentration equation is detailed further in this paper.

Concentration Equation. The equation for the Kth component is derived by subtracting from the momentum equation for the Kth component the equivalent momentum equation for a virtual mixture ($-K$) composed from all other components except K. The last equation is obtained by summing momentum equations for solid components $K' = 1, \ldots, K-1, K+1, \ldots N$ and for the carrying liquid, multiplying the intermediate results by $\bar{\alpha}_K/\bar{\alpha}_{-k}$ and space/time averaging (where $\bar{\alpha}_{-K} = 1 - \bar{\alpha}_K$). Neglecting $\alpha_K' p_K'$, the equation is:

$$\underbrace{\frac{\partial}{\partial x_j}\bar{\alpha}_K\left[\rho_K \bar{U}_{Ki}\bar{U}_{Kj} - \sum_{-K} \rho_{K'}\bar{\alpha}_{K'}\bar{U}_{K'i}\bar{U}_{K'j}/\bar{\alpha}_{-K}\right]}_{(A)}$$

$$\underbrace{+\sum_{-K}\left[\frac{\mathbf{e}_i}{\Delta T}\int_{t-\Delta T/2}^{t+\Delta T/2}\frac{1}{Z_K}\bullet\sum_m \frac{\underline{\mathbf{T}}_{KK'}\bullet\mathbf{n}_K}{\mathbf{U}_{KK'}\bullet\mathbf{n}_K}\bullet R_K(\tau-t)\right]/\bar{\alpha}_{-K}}_{(B)}$$

$$+\frac{d}{dt}\Big[\underbrace{\rho_K\overline{\alpha_K' U_{Ki}'}}_{(C1)} - \underbrace{\sum_{-K}\rho_{K'}\overline{\alpha_K' U_K'}/\bar{\alpha}_{-K}}_{(C2)}\Big]$$

$$\frac{\partial}{\partial x_j}\Big[\underbrace{\overline{\alpha'_K \tau'_{K\Sigma_{ji}}}}_{(D1)} - \underbrace{\sum_{-K} \overline{\alpha'_K \tau'_{K'\Sigma_{ji}}} \cdot \bar{\alpha}_K / \bar{\alpha}_{-K}}_{(D2)}\Big]$$

$$+ \frac{1-\delta_{it}}{\tan\theta} \cdot \frac{\partial}{\partial x_i}\Big(\underbrace{\tau_{K_{it}}}_{(E1)} - \underbrace{\sum_{-K} \tau_{K'_{it}} \cdot \bar{\alpha}_K / \bar{\alpha}_{-K}}_{(E2)}\Big)$$

$$+ \frac{\partial}{\partial x_i}\Big(\underbrace{\tau_{K\Sigma_{ii}}}_{(F1)} - \underbrace{\sum_{-K} \tau_{K'\Sigma_{ii}} \cdot \bar{\alpha}_K / \bar{\alpha}_{-K}}_{(F2)}\Big)$$

$$\underbrace{- \bar{\alpha}_K \cdot (\rho_K - \rho_{-K}) \cdot g = 0}_{(G)} \qquad (18)$$

where: Σ_{-K} denotes the sum over all components except K.

The "concentration equation" for a component K (18) can be interpreted as an equilibrium between elementary forces acting on the ensemble of particles K, under the influence of gravitation (G), relative acceleration (A), relative mean flow compared to other flow components (B), mixing effects due to turbulent fluctuating velocities of component $K(C1)$ and of the virtual mixture $-K$ ($C2$), dispersive stress from particle collisions in flowing suspensions ($D1$, $D2$ - plastic collisions; $E1$, $E2$ - elastic collisions) and Coulombic contacts between particles ($F1$, $F2$).

Let us consider the equation (18) for the cross-section of a circular pipe. In the absence of secondary currents the term (A) vanishes. The contributions of the interaction term between different species and K (B) may be combined with the effects of the interaction between the corresponding pairs of species due to the turbulent diffusion (term $C2$), dispersive stress (terms $D2$, and $E2$) and supported load (term $F2$). The models for the characteristic terms (12)-(17) are affected by the spatial nonuniformities in the averaging volume and especially by the ratio (particle dimension/length scale of turbulence). Extending the models for unidimensional case [10], [11] to the pipe cross-section flow, one obtains a simpler computational form of equation (18):

$$\frac{\bar{\epsilon}_K^2}{W_K^2} \cdot |\nabla \bar{\alpha}_K| \cdot \nabla \bar{\alpha}_K + \frac{\rho_K \bar{\alpha}_K}{(\rho_K - \rho_{-K}) \cdot g} \cdot \nabla \left(\frac{\tau_S - \tau_{SL}}{\tan\theta} + \sigma_{SL} \right) + \bar{\alpha}_K^2 \cdot \mathbf{j} = 0 \qquad (19)$$

where: K $= 1, 2, \ldots N$ (flow component)

α_K = mean concentration of component K

W_K = hindered settling velocity of particles K

ρ_K, ρ_{-K} = density of the component K and of the mixture containing all components except K, respectively

$\bar{\epsilon}_K$ = diffusion coefficient, depending on concentration of solid components

τ_S = shear stress between solid particles of component K and all solid components (acting in the normal direction to the pipe cross-section)

σ_{SL}, τ_{SL} = normal and shear stresses between solid particles of component K and all solid components in Coulombic contact (supported load)

$\mathbf{j}$ = vertical unit vector

$\tan\theta$ = dynamic coefficient of friction (component K).

The terms $\bar{\epsilon}_K$, τ_S, σ_{SL}, τ_{SL} and $\tan\theta$ are functions of solid concentration as discussed in [11], [12]. At low concentration and particles small compared to the mixing length, the first term in equation (19) is determined by the turbulent diffusion of the carrier fluid, and the second term expressing particle interactions is negligible. When particles of relatively large size are handled at concentrations over 10% by volume, the principal part of the diffusion term is determined by fluctuating solid velocities and the second term plays a major role.

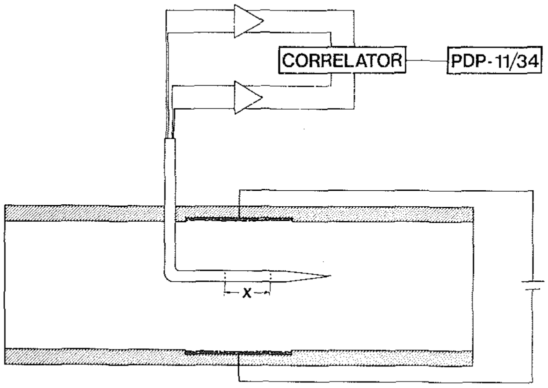

Fig. 3 Scheme for solid particle velocity probe

Algorithm for Velocities and Turbulence Parameter. The following calculation approaches were adopted in previous work:

(1) By summing the corresponding equation (11) in the same direction for all flow components one obtains the mixture momentum equation where the interaction terms between components are reciprocally cancelled (similar to Roco and Shook, 1983a). Together with the equations written for the relative velocity between each component and the mixture, the system of equations for mean velocities $\bar{V}_K$ can be solved. Compared to Soo's (1980), the equation has two additional terms due to the dispersive stress and Coulombic contacts between particles. Also, the mixture density in the convective term is weighted by the momentum flux and the space/time averaging for turbulent flow is applied in our approach.

(2) The transport equation for mixture eddy viscosity contains terms due to diffusion, generation, decay and acceleration (ϵ model, Roco and Balakrishnan, 1982). A coherent calculation approach is used for both eddy viscosity (used in the velocity calculation) and eddy-diffusivity (employed in the concentration equation).

(3) For the streamtube diffusion coefficient $\lambda_{K_{ij}}$ in equation (17) a computational scheme was proposed which superposes the effects of various flow components (λ model, Roco and Shook, 1981).

Experimental

The model has been tested with data obtained in closed loop laboratory systems, using circular and rectangular conduits. In addition to the conventional determinations of frictional headlosses (differential manometers) as a function of mean velocity (magnetic flux flowmeter) and slurry concentration (Cs 137 nuclear densimeter), the particle concentration distribution was obtained experimentally in all the tests. These employed either gamma ray absorption (chord-average concentrations) or a photographic technique (Scarlett and Grimley, 1974). In some of the studies, particle velocities were determined using the probe shown in Fig. 3. The amplitude of the cross-correlation between resistivity fluctuations at two pairs of electrodes, normalized with the autocorrelations, was determined a function of position (Brown and Shook, 1982).

For this last device, resistivity changes resulting from concentration fluctuations (α'_S) produce voltage fluctuations at sensor electrodes displaced in the applied potential field normal to the direction of mean flow. The transit time for the distance x is determined by cross correlation of the signals from the sensor electrode pairs. From this, a mean velocity

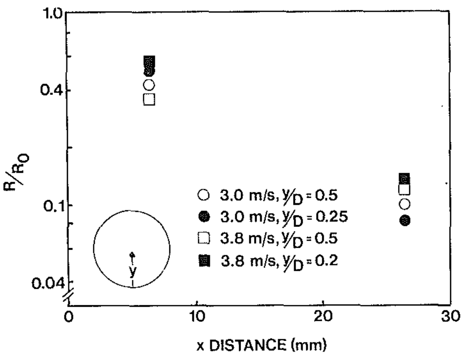

Fig. 4 Concentration fluctuation cross-correlation (R/R_0) versus distance between electrodes (x)

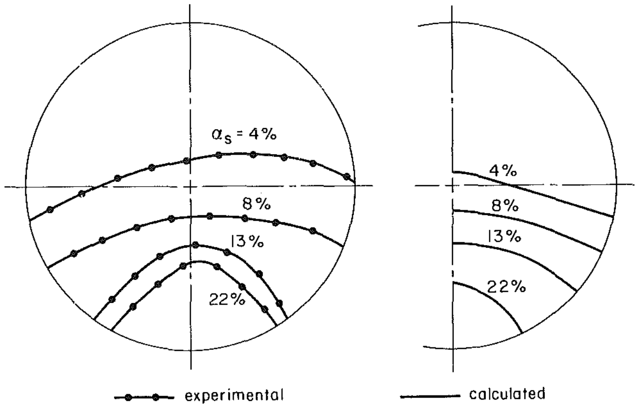

Fig. 5 Experimental (Scarlett and Grimley, 1974) and calculated concentration distribution of glass sphere .58 mm/water mixture flow (Run C2)

for the region defined by the sensor electrodes can be determined. For turbulent slurry flow, calibration studies showed particle retardation by the probe to be of the order of 3 percent of the local velocity provided conditions near deposition of particles at the bottom of the pipe were avoided. For a properly aligned probe, mean velocities varied little with the location or spacing x, provided a suitable displacement from the nose of the probe was maintained.

In addition to mean velocities, the probe has given at least a qualitative indication of the structure of the flow through comparison of autocorrelations and cross correlations of electrode signals. With a sands of d = 0.165 mm and sensor electrode displacements of the order of 1 mm, autocorrelations in pipelines of 50 and 500 mm I.D. indicate mixing lengths approximately proportional to pipe diameter.

With larger particles, of diameter greater than the sensor electrode displacement, the autocorrelations suggest that the electrodes respond to the passage of individual particles. For the finer particles, it is apparently clusters which produce the resistivity fluctuations to which the device responds. Such concentration fluctuations are always visually apparent at the pipe wall for slurries which display a concentration gradient within the pipe.

With increasing electrode pair separation distances (x values) the amplitude of the cross-correlation decays, presumably as a consequence of diffusion processes. Recent measurements of these amplitudes (R), normalized with the autocorrelations (R_0), are shown in Fig. 4 for a 0.165 mm sand in a 50 mm I.D. pipeline, at a mean concentration of 10 percent by volume. For a sand of similar size in a 500 mm pipeline the decay process was correspondingly slower, requiring 100 mm to produce the same relative decrease as that produced at $x = 10$ mm in a 50 mm pipeline.

Application for Two- and Multicomponent Flows

The general approach was applied for uniform particle slurry flow in pipes, as well as for multispecies particles mixtures. The main set of experiments used for tests is given in Table 1, for various materials: sand ($S = 2.65$), glass ($S = 2.7$) and coal ($S = 1.3$-1.7). The tests were performed at various flow conditions: pipe diameter between 40 mm and 495 mm, concentrations up to 40 percent by volume, particle diameters up to 13 mm and velocities up to three times the critical speed. Samples of experiments with sand and other solids in rectangular pipes were previously analyzed with positive results (Roco and Shook, 1983b).

The system of equations for concentrations, velocities and eddy-viscosity (or streamtube diffusion coefficient, respectively) was solved numerically using *Integral Finite Volume techniques*. The calculation domain is discretized and the variables are chosen at interior nodes. The integrals of the differential equations over a finite volume are transformed to surface integrals. The computation is performed using the interfaces between volumes to store and count the data. The analytical interpolation law is suitable for large convective terms. The algorithm can be applied in 2-D and 3-D problems (Roco and Balakrishnan, 1982).

The calculation model is hier used for uniform flow in linear sections of horizontal pipes. The volume averaging is reflected in the supplementary terms resulted from averaging and in their models. For modeling one can consider either the statistical analysis of the mixture flow characteristics using local instantaneous measurements, or dimensional analysis of the main local parameters in the averaging volume, or analytical and numerical simulations. For the first approach there is not yet available a complete set of data. Adopting the second approach, we found the significant local parameters to be the ratio between the gravitation and inertial forces (F_g/F_i, i.e., the modified Froude number $\mathrm{Fr}_* = \rho_L/\rho_M \cdot V_*^2/gd(S-1)$, where V_* is the friction velocity) and the relative dimension of solid particles compared to the averaging

Table 1 Experimental data in circular pipes used for model development

Run No.	Material	Specific density	Pipe diameter	Particle diameter	Average velocity	Average solid concentration
-	-	S(-)	D(mm)	d(mm)	V_M(m/s)	α_S(% by vol.)
A1-A20	sand	2.65	51.5,263, 495	.165	1.66-4.33	8.4-34.1
B1-B6		2.65	51.5	.48	1.66-3.44	6.3-29.6
C1-C5		2.65	50.7	.52	1.9 -4.0	11.4-24.7
D1-D2		2.65	263	13.0	3.2 -4.0	9.5-10.2
G1-G6	glass	2.7	40	.58	1.05-2.88	7.0-12.0
M1-M8	coal (multispecies particles)	1.31-1.73	158,495	0-6.5	1.68-3.16	≤45.4

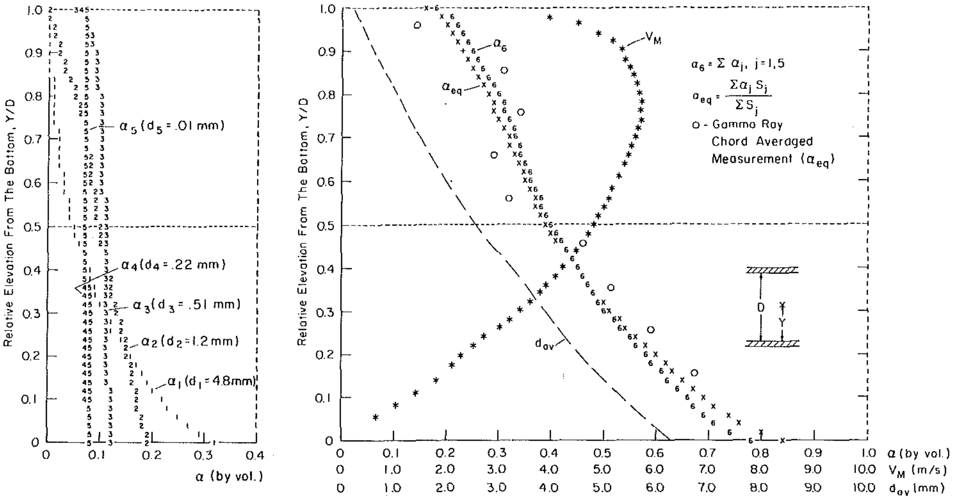

Fig. 6 Concentrations (α_1, α_2, . . . α_5), velocity (V_M) and averaged particle size (d_{av}) distributions of Kaiser coal/water mixture flow in the vertical mid-plane of a circular pipe D = 495 mm (Run M6)

volume when dimensions are given by the local scale of turbulence (d_K/Λ_K) (Roco and Shook, 1983a and 1983b; Roco, 1983). The local contributions of the dispersive and supported loads are strongly correlated to Fr_*, as it is suggested by the analysis at particle scale. The ratio d_K/Λ_K determines the predominant terms in equation (11), the relative values of the fluctuating components $(f_K')_T$ and $(f_K')_t$, and the ratio between eddy-viscosity and eddy-diffusivity.

The comparisons with experimental data show the ability of the calculation model to predict the velocity and concentration distributions in the pipe cross-section, as well as headlosses along the pipe. In Fig. 5 is illustrated the computed concentration distribution α_S in single species glass sphere (d = .58 mm)/water mixture flow compared to photographic measurements (Scarlett and Grimley, 1974). In this first test the ϵ model and Integral Finite Volume techniques were used.

Numerical predictions of concentration for multispecies coal/water slurry flowing in 495 mm pipe employing the λ model are given in Fig. 6(a) and (b). The mixture was modeled with five species of coal particles of dimensions d_1 = 4.8 mm, d_2 = 1.2 mm, d_3 = .51 mm, d_4 = .22 mm, d_5 = .01 mm of assumed specific densities S_1 = 1.7, S_2 = 1.43, S_3 = 1.23, S_4 = 1.23, S_5 = 1.23. The total coal concentration at an elevation Y over the pipe bottom (α_6) is compared to gamma-ray measurements (Saskatchewan Research Council, 1981).

Experimental and computed distributions of concentration (α_S) and velocity (V_S) for sand (.165 mm)/water mixture flow in 51.5 mm pipe are presented in Figs. 7 and 8. Measured and predicted headlosses (i) in a 50.7 mm pipe with flowing suspension of sand .52 mm are plotted versus average velocity (V_M) in Fig. 9. The comparisons (Figs. 5–8) show the numerical simulations predict with good approximation these sets of experimental data. The model overpredicts shear stresses at solid concentrations over 40 percent. This could be due to the neglection of turbulence damping in two-phase flows when concentrations approach the maximum packing concentration.

The particle velocity distribution determined by the proposed method has been employed to estimate the critical deposit velocity in slurry flow systems (Roco and Shook, 1984).

Some empirical coefficients are used in the model for the friction by Coulombic contact (tanβ) and particle collisions (tanθ), as well as in the ϵ transport equation or in the λ computational algorithm (Roco and Shook, 1983a; Roco and Balakrishnan, 1982). They do not alter for various flow conditions (D, V_M, α). The coefficients tanβ and tanθ depend on the particle material (i.e., the roughness of the particle surface, modulus of elasticity and coefficient of restitution in collisions). In our tests, tanβ varied between .3 and .35 (for sand = .35, fr coal $\simeq$ .32, for glass = .3). The angle β corresponds to the angle of inclination of a pipe without through flow at which a layer of immersed particles sedimented on the bottom begins to shear, sliding downwards. The coefficient tanθ can be estimated as function of the modified Froude number Fr_* (Roco and Shook, 1983b, Fig. 6), and takes values about tan$\theta \simeq .5$ (from .35 $\approx$ tanβ at

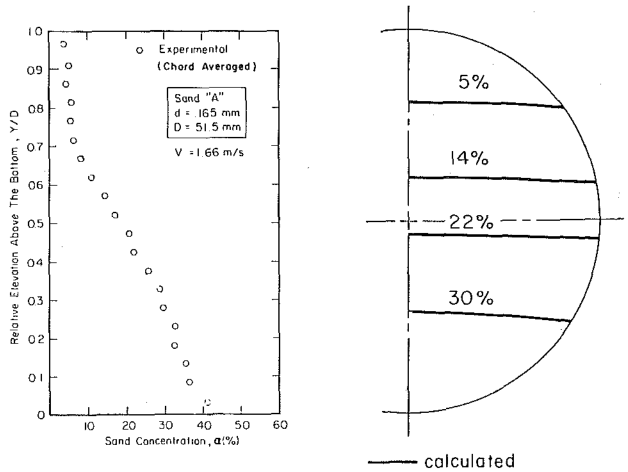

Fig. 7 Experimental and calculated concentration (α_S) distribution of sand .165 mm/water mixture flow in 51.5 mm pipe (Run A3)

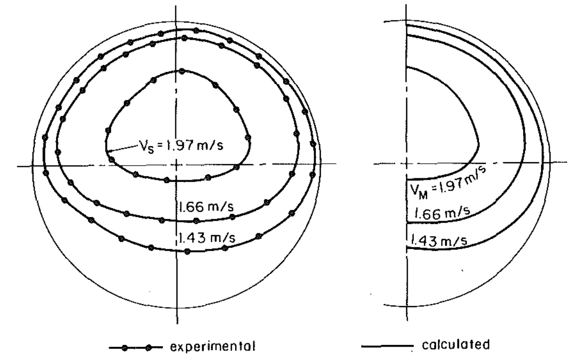

Fig. 8 Experimental and calculated velocity distribution of sand .165 mm/water mixture flow in 51.5 mm pipe (Run A3)

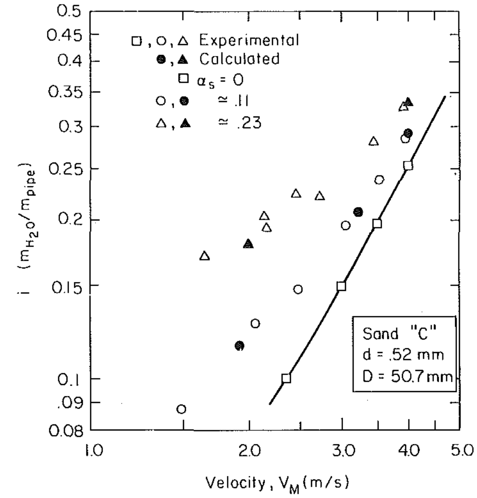

Fig. 9 Headlosses (i) versus sand .52 mm/water mixture velocity (V_M) (Runs C1-C5)

$Fr_* < 2$-3 up to .75 at larger Froude numbers $Fr_* \geq 14$). This estimation can be qualitatively explained by using stochastics analysis of particle collisions. The coefficients for the generation (k_G) and decay (k_D) terms in the eddy-viscosity (ϵ) transport equation are maintained constant ($k_G = .13$, $k_D = .8$), the same for single fluid and slurry flows in all flow situations. After the material coefficients were chosen for sand, coal and glass, we obtained good agreement between experiments and flow computations ($\alpha(x, y)$, $V_M(x, y)$, headlosses) when the pipe diameter, velocity and concentration were widely varied (Table 1).

The effect of the pipe roughness on mixture velocity profile strongly diminishes if the particle concentration overpasses 5-10 percent by volume.

The proposed general approach may be applied to steady and unsteady flows, and can be extended to other two- or multicomponent flow patterns.

Conclusions

1. The suggested space/time averaging of differential equations maintains a good amount of information about the turbulent flow phenomenon with high concentrations. It creates a framework for further studies in which the effects of the temporal and spatial fluctuations, ratio particle size/length scale of turbulence, dispersive and supported load stresses between solid particles can be analyzed.

2. The computational approach for multi-species particle turbulent flow contains some new components, which are specific for turbulent flow of incompressible mixtures with solid concentrations between 5 and 40 percent by volume. Integral Finite Volume techniques are employed to numerically solve the system of differential equations derived from the conservation laws. The terms due to particle interactions are predominants at high concentrations and large particles.

3. The tests performed with different solid materials for various flow parameters in pipes show a satisfactory agreement between predictions and experimental results. Design calculations can be made for any set of given parameters. The approach can be used to extrapolate data from laboratory to industrial situations.

Acknowledgments

The studies reported here were supported by the National Science Foundation Grant CPE 8205217 and Canadian NSERC A1037.

References

1 Anderson, T. B., and Jackson, R. A., "A Fluid-Mechanical Theory of Fluidized Beds," *Ind. Eng. Chem. Fund.*, Vol. 6, 1967, p. 527.

2 Brown, N. P., and Shook, C. A., "A Probe for Particle Velocity," *Proc. Hydrotransport 8*, BHRA-Fluid Engineering, Cranfield, U.K., Vol. 8, G1, 1982, p. 339.

3 Graham, A. L., Steele, R. D., and Bird, R. B., "Particle Clusters in Concentrated Suspensions," 54th Annual Meeting of the Society of Rheology, Evanston, Oct. 1982.

4 Ishii, M., and Mishima, K., "Study of Two-Fluid Model and Interfacial Area," Argonne National Laboratory Report, ANL-80-111, 1983.

5 Hestroni, G., *Handbook of Multiphase Flow*, McGraw-Hill, 1982.

6 Lee, S. L., and Durst, F., "On the Motion of Particles in Turbulent Duct Flows," *Int. J. Multiphase Flow*, Vol. 8, 1982, p. 125.

7 Prosperetti, A. and Jones, A. V., "Pressure Forces in Disperse Two-Phase Flow," *Int. J. Multiphase Flow*, Vol. 10, No. 4, 1984, p. 425.

8 Roco, M. C., "Ein Neues Rechnenmodell Zür Untersuchung der Turbulenzströmung," 3 Rohre-International, Vol. 19, Heft 6, 1980, p. 347.

9 Roco, M. C., "Space/Time Averaged Equations for Multicomponent Turbulent Flow," Cavitation and Multiphase Forum, Spring ASME Fluid Mechanics Meeting, Houston, June 1983, p. 92.

10 Roco, M. C., and Balakrishnan, B., "Multi-Dimensional Liquid-Solid Flow Analysis by Using an Integral Volume Approach," 54th Annual Meeting Society of Rheology, Evanston, paper D30, 1982 (also *J. of Rheology*, Vol. 29, 1985).

11 Roco, M. C., and Shook, C. A., "A Model for Turbulent Slurry Flow," ASME/ASCE Mechanics Conference, Boulder, Colo., 1981 (also *J. of Pipelines*, Vol. 4, 1984, p. 3).

12 Roco, M. C., and Shook, C. A., "Modeling Slurry Flow: The Effect of Particle Size," *Can. J. Chem. Eng.*, Vol. 61, No. 4, 1983a, p. 494.

13 Roco, M. C., and Shook, C. A., "Dispersive Stress in Shear Slurry Flow," 3rd Multi-Phase Flow and Heat Transfer Symposium, Elsevier, ed. T. N. Veziroglu, 1983b.

14 Roco, M. C., and Shook, C. A., "Critical Deposit Velocity in Slurry Flow," Cavitation and Multiphase Flow Forum (ed. J. W. Hoyt), FED-Vol. 9, 1984, p. 49.

15 Saskatchewan Research Council, "Coarse Coal in Water Slurries Pipeline Tests," SRC E-725-7-C-81, 1981.

16 Scarlett, B., and Grimley, A., "Particle Velocity and Concentration Profiles During Hydraulic Transport in a Circular Pipe," *Proc. Hydrotransport 3*, BHRA-Fluid Engineering, Cranfield, U.K., Vol. 3, paper D3, 1974, p. 23.

17 Shen, H. H., "Stresses in a Rapid Flow of Spherical Solid with Two Sizes," 20th Annual Meeting of SES, Newark, Delaware, 1983.

18 Shook, C. A., et al., "Flow of Coarse and Fine Sand Slurries in Pipelines," *J. of Pipelines*, Vol. 3, 1982, p. 13.

19 Soo, S. L., *Fluid Dynamics of Multiphase Systems*, Blaisdell, Mass., 1967.

20 Soo, S. L., "Equations of Multiphase Multidomain Mechanics," *Multiphase Transport*, Hemisphere, (Ed. Veziroglu), Vol. 1, 1980, p. 291.

21 Vernier, Ph., and Delhaye, J. H., "General Two-Phase Flow Equations Applied to the Thermodynamics of Boiling Water Nuclear Reactors," *Energie Primaire*, Vol. 4, No. 1-2, 1968, p. 5.

22 Wallis, G. B., *One-Dimensional Two-Phase Flow*, McGraw-Hill, New York, 1969, p. 182.

23 Whitaker, S., "The Transport Equations for Multiphase Systems," *Chem. Ing. Sci.*, Vol. 28, 1973, p. 139.

Cycle Resolved LDV Measurements in a Motored IC Engine

T-M. Liou[1]
Graduate Student.

D. A. Santavicca[2]
Research Engineer.

Department of Mechanical
and Aerospace Engineering,
Princeton University,
Princeton, NJ 08544

LDV measurements have been made in an IC engine motored at 1200 rpm. The data rates were sufficiently high to allow the bulk velocity to be characterized in individual cycles. The relative cyclic fluctuation of the bulk velocity was found to be as large as 200 percent. The turbulence intensity was calculated using both the velocity fluctuation with respect to the ensemble average velocity and the velocity fluctuation with respect to the cycle resolved bulk velocity. The former includes both the cyclic fluctuation of the bulk velocity and the turbulence, and therefore gave estimates of the ensemble averaged turbulence intensity which were from 50 to 100 percent greater than that obtained using the in-cycle fluctuation with respect to the bulk velocity. The relative cyclic fluctuation of the time averaged turbulence intensity, calculated over a 64-degree interval in each cycle, was found to be small, i.e., less than 20 percent. The high data rates also made it possible to determine the ensemble averaged temporal autocorrelation function from which the spectral energy distribution and the integral time scale were calculated.

Introduction

The velocity field in an internal combustion (IC) engine is turbulent and nonstationary. The turbulence is important because of its effect on the flame speed, and in turn the combustion rate [1]. The standard method of characterizing a nonstationary process is to use ensemble averaging [2], which for the case of an IC engine corresponds to taking the average of the quantity of interest at a particular crankangle recorded over many engine cycles. The turbulence can then be defined as the difference between the instantaneous velocity, herein referred to as the velocity, and the ensemble averaged velocity. In an IC engine however, this definition can result in erroneously high estimates of the turbulence intensity [3] due to the fact that the fluctuation with respect to the ensemble averaged velocity includes both the cyclic fluctuation of the bulk velocity and the turbulence. The only way to separate the cyclic fluctuation of the bulk velocity and the turbulence is to make velocity measurements at very high data rates such that the bulk velocity can be characterized in each engine cycle [4, 5]. Such measurements can be made with hot wire probes but hot wire measurements made in IC engines are subject to large uncertainties due to calibration problems, flow reversal and large relative turbulence intensities [6]. This paper presents laser Doppler velocimetry (LDV) measurements made in a motored IC engine at data rates which are high enough to allow characterization of the bulk velocity in each cycle. These measurements are the first cycle resolved LDV measurements made in an IC engine motored at practical engine speeds [7]. The data was analyzed using an ensemble averaged analysis, i.e. using the velocity fluctuation with respect to the ensemble averaged velocity, and a cycle resolved analysis, i.e., using the velocity fluctuation with respect to the bulk velocity in each cycle, and the results of the two analyses compared.

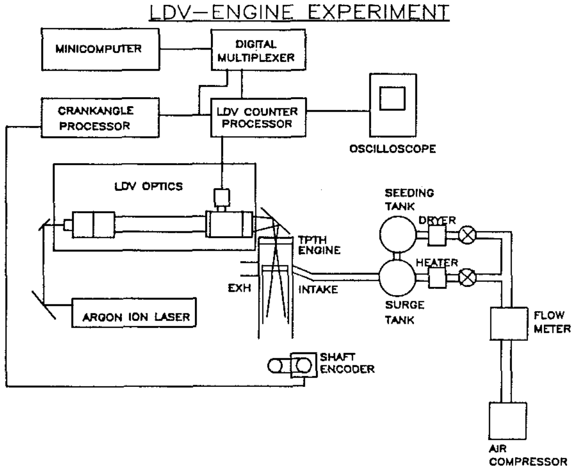

Fig. 1 Schematic diagram of laser Doppler velocimetry and engine experimental set-up

Engine-LDV Experiment

The engine and LDV experimental set-up is shown in schematic form in Fig. 1. The velocity measurements were made in one of the transparent-piston, transparent-head engines in the Engine Combustion Laboratory at Princeton

---

[1] Assistant Professor, Department of Power Mechanical Engineering, National Tsing Hua University.

[2] As of 8/1/84, Associate Professor, Department of Mechanical Engineering, Pennsylvania State University.

Contributed by the Fluids Engineering Division of THE AMERICAN SOCIETY OF MECHANICAL ENGINEERS and presented at the Symposium on Engineering Applications of Laser Velocimetry, Phoenix, Ariz., November 14-19, 1982. Manuscript received by the Fluids Engineering Division, April 6, 1983.

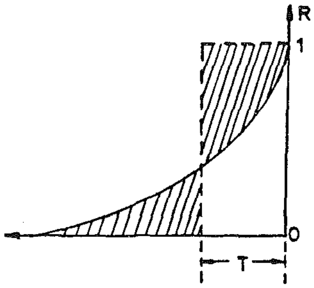

Fig. 2 Definition of integral time scale

University. The piston-cylinder assembly was mounted on a high speed, Waukesha CFR-48 crankcase and had an 8.26 cm diameter bore and an 11.43 cm stroke. Air intake and exhaust passed through ports in the cylinder wall as in a two-cycle engine. Optical access was through a flat quartz window covering the entire head of the combustion chamber. The piston was elongated, after the design of Bowditch [8], with a flat, transparent, quartz crown. The combustion chamber was open and "pancake" shaped with a compression ratio of 13.5. The intake ports were directed radially therefore there was no swirl. The timing of the exhaust and intake ports was ±113 degrees and ±126 degrees, respectively, where 0 degree was top dead center (TDC). The standard piston rings were replaced with teflon impregnated bronze rings, enabling the engine to be motored or fired without cylinder lubrication.

For the work presented in this paper the engine was motored at 1200 rpm. The intake air was supplied by an air compressor at a flow rate of 16.5 gm/s, corresponding to a volumetric efficiency of 100 percent. The intake manifold pressure and temperature were 124 kPa and 25° C, respectively. The exhaust manifold pressure was 99 kPa. A cyclone seeding chamber [9] was used to introduce seed particles into the intake air flow. The particles used in this study were phenolic microballoons supplied by Union Carbide. These are hollow phenolic spheres with a nominal geometric diameter of 40 microns and a corresponding aerodynamic diameter of 1 micron [10].

The LDV optics were set up in a dual beam, backscatter configuration. The probe volume dimensions were 0.42 mm by 0.08 mm. A Bragg cell was used to eliminate the directional ambiguity. This was essential because of the flow reversal which was expected in an engine with no swirl. The output of the photomultiplier was electronically downmixed to 10 MHz thereby improving the velocity resolution to approximately 10 cm/s. A counter type signal processor with 1 nsec resolution was used to process the Doppler signal. All of the LDV optics and electronics were manufactured by TSI. The laser source was a Lexel 95-2 argon ion laser operated single frequency at 514.5 nm. The output power was typically 800 mW.

The engine crankangle was monitored by an optical shaft encoder with one-half degree resolution. When a velocity measurement was validated by the counter processor, the crankangle was sampled and the crankangle-velocity data pair was transferred by a digital multiplexer at rates up to 30 kHz to a minicomputer for storage.

Tangential velocity measurements were made at one point located in the center of the clearance height, at half the chamber radius on the diameter separating the intake and exhaust ports. The measurements were made with one-half degree resolution over a sixty-four degree crankangle interval centered on TDC.

Ensemble Averaged Analysis

The data was analyzed using an ensemble averaged analysis and a cycle resolved analysis. In the ensemble averaged analysis the instantaneous velocity, U, is defined as the sum of the ensemble averaged velocity, U_{EA}, and the fluctuation, u_F

$$U(\theta,\Delta\theta,i)=U_{EA}(\theta,\Delta\theta)+u_F(\theta,\Delta\theta,i)$$

where θ is the crankangle, $\Delta\theta$ is a crankangle window about θ, and i is the ith cycle. Since the LDV measurements occur randomly in time, i.e., whenever a particle passes through the probe volume, it is necessary to assign the velocity measurements which are made within the window $\theta\pm\Delta\theta/2$ to the crankangle θ. The ensemble averaged velocity is defined as

$$U_{EA}(\theta,\Delta\theta)=\frac{1}{N_M(\theta)}\sum_{i=1}^{N_c}U(\theta,\Delta\theta,i)$$

and the ensemble averaged fluctuation intensity is defined as

$$u'_{F,EA}(\theta,\Delta\theta)=\left[\frac{1}{N_M(\theta)}\sum_{i=1}^{N_c}[u_F(\theta,\Delta\theta,i)^2]\right]^{1/2}$$

where N_c is the number of cycles and $N_M(\theta)$ is the total number of measurements at crankangle θ over N_c cycles.

In these and all other ensemble averaged quantities, whenever there was more than one measurement in a given crankangle window and cycle, only the first measurement was used.

Cycle Resolved Analysis

The cycle resolved analysis requires the calculation of the

Nomenclature

f = frequency
F = normalized one-dimensional power spectral density function
i = ith cycle
L = integral length scale
$N(i)$ = number of crankangles over which measurements were made in cycle i
N_c = number of cycles
$N_i(\theta)$ = number of measurements at crankangle θ in cycle i
$N_M(\theta)$ = total number of measurements at crankangle θ over N_c cycles
$N_M(i)$ = total number of measurements in cycle i over $N(i)$ degrees
R = Eulerian temporal autocorrelation coefficient
S = conversion factor between time and crankangle
T = integral time scale
u_F = instantaneous velocity fluctuation about ensemble averaged velocity, i.e., the fluctuation
u_T = instantaneous velocity fluctuation about bulk velocity, i.e., the turbulence
$u'_{F,EA}$ = ensemble averaged fluctuation intensity
$u'_{T,EA}$ = ensemble averaged turbulence intensity
$u'_{T,TA}$ = time averaged turbulence intensity
$u'_{T,TA,EA}$ = ensemble average of time averaged turbulence intensity
$u'_{T,TA,rms}$ = RMS fluctuation of time averaged turbulence intensity
U = instantaneous velocity
U_{EA} = ensemble averaged velocity
$\bar{U}$ = bulk velocity
$\bar{U}_{EA}$ = ensemble average of bulk velocity
$\bar{U}_{\mathrm{rms}}$ = RMS fluctuation of bulk velocity
$\Delta\theta$ = crankangle window about θ
θ = crankangle
Φ = phase angle

bulk velocity in each cycle. The bulk velocity, $\bar{U}$, is related to the velocity, U, as follows

$$U(\theta,\Delta\theta,i) = \bar{U}(\theta,\Delta\theta,i) + u_T(\theta,\Delta\theta,i)$$

where u_T is the instantaneous fluctuation about the bulk velocity, herein called the turbulence. Unlike the ensemble averaged velocity, the bulk velocity can vary from cycle to cycle.

There are several methods [11] which can be used to determine the bulk velocity in each cycle from the velocity versus crankangle data. These include time averaging over short time intervals, polynomial curve fitting and digital low pass filtering. All three methods in effect serve to low pass filter the data. The first approach has been used by Lancaster [4] on hot wire measurements in a motored IC engine where he calculated the time averaged velocity over a 45 degree window. This corresponds to an equivalent low pass filter cutoff frequency of 80 Hz at 1200 rpm. The second approach has been used by Rask [5] on LDV measurements in a motored IC engine. One disadvantage of this approach is that it is difficult to define an equivalent low pass filter cutoff frequency. This is important because one wants to separate the low frequency components, which define the bulk velocity, from the high frequency components, which define the turbulence, based on some characteristic time of the phenomenon of interest, in this case turbulent flame propagation in an IC engine. In this work, digital low pass filtering was used to determine the bulk velocity in each cycle. The low pass filter cutoff frequency was determined by the characteristics of the velocity field itself which allows for its variation with engine speed and spatial location.

The procedure used in this work for determining the bulk velocity can be described as follows. The sixty-four degree interval over which data was acquired in each cycle was divided into sixty-four one-degree windows. Only those cycles which have measurements in at least 40 of the 64 one-degree windows were selected. In each of these cycles, those windows with multiple measurements were averaged and those with no measurements were assigned values by linear interpolation, thereby obtaining a set of engine cycles with one measurement for each crankangle degree. Once the data was in this form the frequency spectrum of the velocity versus crankangle (time) data in each cycle was obtained using a fast Fourier transform.

The next step in the calculation of the bulk velocity was the selection of a cutoff frequency. The simplest non-stationary flow would be one with distinctly different time scales for the bulk and the turbulent motion. In this case, the frequency spectrum of the velocity versus time data would show a distinct grouping of low frequency components which could be attributed to the bulk motion and a distinct grouping of high frequency components which could be attributed to the turbulent motion. Therefore the selection of a cutoff frequency, above which lie the turbulent frequency components and below which lie the bulk motion frequency components, would be obvious. In the nonstationary flow of an IC engine however there is no obvious separation of the bulk motion and turbulent motion frequencies, therefore another method of selecting the cutoff frequency had to be found.

The cutoff frequency should be related to a characteristic time of the combustion process of interest. However, the structure of turbulent flames in general, and engine flames in particular, is poorly understood at present. Therefore the approach used was to take the maximum frequency in the frequency spectrum of the ensemble averaged velocity versus crankangle (time) data as the frequency which separates the bulk motion from the turbulent motion. Once the cut-off frequency was chosen, all frequency components above that frequency were set to zero and the inverse transform taken, yielding the desired bulk velocity. To avoid oscillations [12] in the resultant bulk velocity due to Gibbs phenomenon [12, 13], the frequency cut-off was not implanted with a step function but with a Fermi-Dirac function which is centered on the cut-off frequency and has a half-height width equal to 10 percent of the cutoff frequency [13, 14].

After the bulk velocity was determined for each engine cycle, the ensemble average of the bulk velocity, $\bar{U}_{EA}$, and of the rms fluctuation of the bulk velocity, $\bar{U}_{\text{rms}}$, were calculated.

$$\bar{U}_{EA}(\theta,\Delta\theta) = \frac{1}{N_c}\sum_{i=1}^{N_c} \bar{U}(\theta,\Delta\theta,i)$$

$$\bar{U}_{\text{rms}}(\theta,\Delta\theta) = \left[\frac{1}{N_c}\sum_{i=1}^{N_c}[\bar{U}(\theta,\Delta\theta,i) - \bar{U}_{EA}(\theta,\Delta\theta)]^2\right]^{1/2}$$

The ensemble averaged rms fluctuation of the bulk velocity is indicative of the magnitude of the cycle fluctuations in the bulk motion.

The next calculation in the cycle resolved analysis was of the ensemble averaged turbulence intensity, $u'_{T,EA}$,

$$u'_{T,EA}(\theta,\Delta\theta) = \left[\frac{1}{N_M(\theta)}\sum_{i=1}^{N_c} u_T(\theta,\Delta\theta,i)^2\right]^{1/2}$$

The ensemble averaged turbulence intensity is an average over many engine cycles and therefore does not give any indication of the cyclic variation of the turbulence intensity. This was obtained by first calculating the rms fluctuation of the turbulence over the 64 degree crankangle interval in each engine cycle. This gives the turbulence intensity in a single cycle averaged over the 64 degree interval, $u'_{T,TA}$, which is referred to as the time averaged turbulence intensity.

$$u'_{T,TA}(i) = \left[\frac{1}{N_M(i)}\sum_{j=1}^{N(i)} u_T(\theta,\Delta\theta,i)^2\right]^{1/2}$$

where $N(i)$ is the number of crankangles over which measurements were made in the ith cycle and $N_M(i)$ is the total number of measurements in the ith cycle.

The next calculation was of the ensemble average of the time averaged turbulence intensity, $u'_{T,TA,EA}$, and of the rms fluctuation of the time averaged turbulence intensity,

$$u'_{T,TA,EA} = \frac{1}{N_c}\sum_{i=1}^{N_c} u'_{T,TA}(i)$$

and,

$$u'_{T,TA,rms} = \left[\frac{1}{N_c}\sum_{i=1}^{N_c} \bar{u}'_{T,TA} - u'_{T,TA,EA}]^2\right]^{1/2}$$

The ensemble averaged rms fluctuation of the time averaged turbulence intensity is indicative of the magnitude of the cyclic fluctuations in the turbulence intensity.

Note that only the bulk velocity was determined from data which was averaged to one degree, which at 1200 rpm corresponds to a Nyquist frequency of 3.6 kHz. The ensemble averaged fluctuation intensity, the ensemble averaged turbulence intensity and the time averaged turbulence intensity calculations were all made using the original data, which was recorded with one-half degree resolution which corresponds to a Nyquist frequency of 7.2 kHz at 1200 rpm.

Spectral Analysis

In addition to providing a more accurate estimate of the turbulence intensity, i.e., one that is free of the contribution due to cycle variations in the bulk velocity, the cycle resolved measurements also allow one to calculate the turbulence autocorrelation coefficient from which the spectral power density function and the integral time scale can be determined. This has only been done in the past from IC engine measurements made using hot wire anemometry. The definitions of the autocorrelation coefficient, the spectral power density function, the integral time scale and the integral length scale are given next.

Autocorrelation Coefficient

For a nonstationary flow the Eulerian temporal autocorrelation coefficient is defined as

$$R(\Phi,\theta)=\frac{1}{N_c}\,\frac{\sum_{i=1}^{N_c} u(\Phi,i)\cdot u(\theta,i)}{u'_{EA}(\Phi)u'_{EA}(\theta)}$$

where θ is the crankangle, Φ is the phase angle with respect to θ, i is the ith cycle and N_c is the number of cycles. In the ensemble averaged analysis u is the fluctuation and u'_{EA} is the ensemble averaged fluctuation intensity. In the cycle resolved analysis u is the turbulence and u'_{EA} is the ensemble averaged turbulence intensity. Note that the autocorrelation coefficient is obtained by ensemble averaging, which is the standard method used for nonstationary flows, and that the frequency response is therefore related not to the measurement rate but to the window size used in the ensemble average. In this work a one-half degree window was used which corresponds to a maximum frequency response of 7.2 kHz at 1200 rpm.

Integral Time Scale

The definition of the integral time scale as proposed by G. I. Taylor [15] is the interval of time, T, which is equal to the area under the temporal autocorrelation curve and is a measure of the time the velocity is correlated with itself. Actually at least two integral time scales are required for the velocity to be uncorrelated [16]. Taylor's definition of the integral time scale is depicted in Fig. 2 for an exponentially decaying autocorrelation curve. In flows without mean motion the integral time scale provides a rough indication of the lifetime of the large eddies; however, in flows with mean motion the integral time scale only provides an indication of the eddy transit time.

Integral Length Scale

The integral length scale is obtained from the spatial autocorrelation curve in the same way that the integral time scale is obtained from the temporal autocorrelation curve [16]. The integral length scale, L, is related to the extent of coherent motion and is an indication of the size of the large eddies. It can also be thought of as a characteristic mixing length and is useful in computing turbulent diffusion coefficients [17, 18].

Length and time scales can be related using Taylor's hypothesis [19]. The conditions for which this is valid however are generally not satisfied by the flowfield in an IC engine. Nevertheless, because of the difficulty of making spatial correlation measurements in an IC engine, the only reported length scale measurements in an IC engine have been obtained from time scale measurements using Taylor's hypothesis [4, 20–23]. This is the approach that was used in this work as well.

1-D Power Spectral Density Function

The normalized one-dimensional power spectral density function, $F(\Phi,f)$, is defined by

$$F(\Phi,f)=\frac{4}{S}\int_{-\infty}^{\Phi}\left[R(\Phi,\theta)\cdot\cos\left(2\pi f\frac{\theta}{S}\right)\right]d\theta$$

and

$$\int_0^{\infty}F(\Phi,f)df=1$$

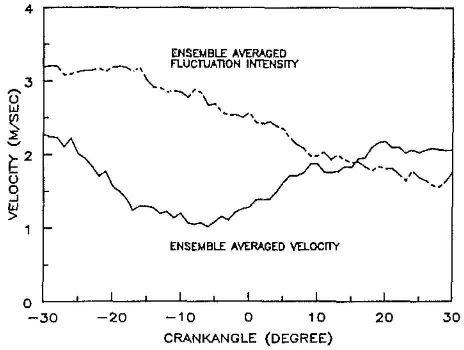

Fig. 3 Ensemble averaged velocity and fluctuation intensity versus crankangle. (Uncertainty in $U_{EA}=\pm3$ percent to ±13 percent, in $u'_{F,EA}=\pm3$ for 95 percent confidence level)

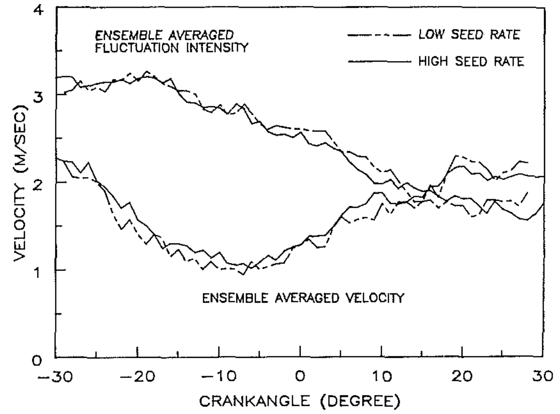

Fig. 4 The effect of seed concentration on ensemble averaged velocity and fluctuation intensity. (Uncertainty in $U_{EA}=\pm3$ to ±13 percent, in $u'_{F,EA}=\pm3$ for 95 percent confidence level)

where Φ is the phase angle, S is the conversion factor between time and crank angle, f is the frequency, θ is the crankangle, and R is the Eulerian autocorrelation coefficient. The energy spectrum of turbulence as defined by this equation shows how the turbulence energy is distributed among different frequencies or different eddy sizes, and is useful in understanding the production and dissipation of turbulent energy in a flow field.

Results and Discussion

Details of the measurement conditions were given in the section Engine-LDV Experiment. The measurements were made over 2494 consecutive engine cycles and there were from 40 to 110 measurements per cycle in the 64-degree measurement interval. The data rate was approximately 10 kHz. The error in the individual velocity realizations has been estimated to be less than 0.5 percent [24]. The main source of error in the reported results is statistical uncertainty in the ensemble averaged quantities due to the finite number of measurements. In the ensemble averaged analysis one degree crankangle windows were used with typically 2000 measurements per average. The statistical error in the ensemble averaged velocity varies from 3 to 13 percent, assuming uncorrelated, normally distributed measurements with a 95 percent confidence level [25]. Similarly, the statistical error in the ensemble averaged fluctuation intensity is 3 percent. In the cycle resolved analysis, measurements from 199 engine cycles were used to calculate the ensemble averaged turbulence intensity. The statistical uncertainty in this result is 11 percent.

The results of the ensemble averaged analysis are shown in

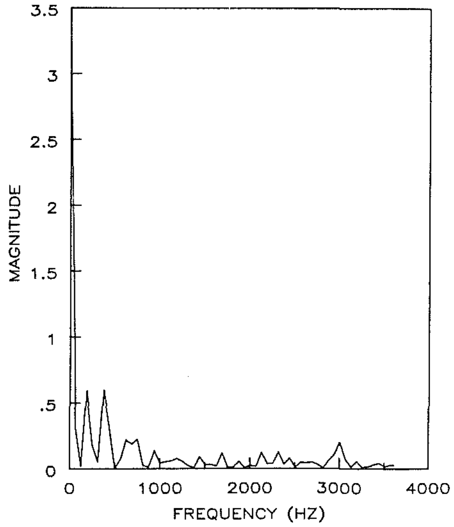

Fig. 5 Frequency spectrum of one-degree averaged and interpolated data for a typical cycle

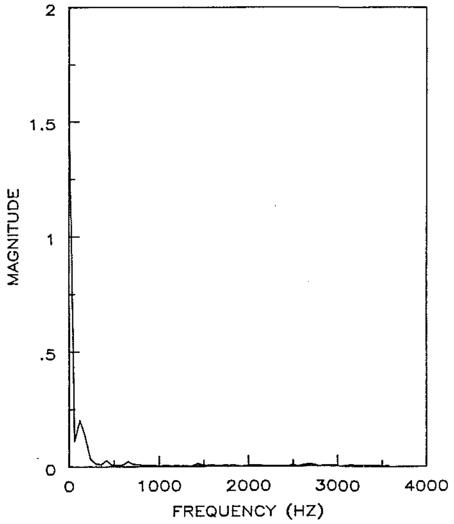

Fig. 6 Frequency spectrum of the ensemble averaged velocity

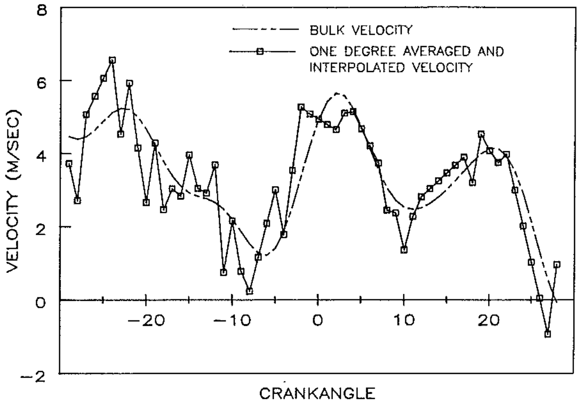

Fig. 7 Bulk velocity and one-degree averaged and interpolated data versus crankangle for a typical cycle

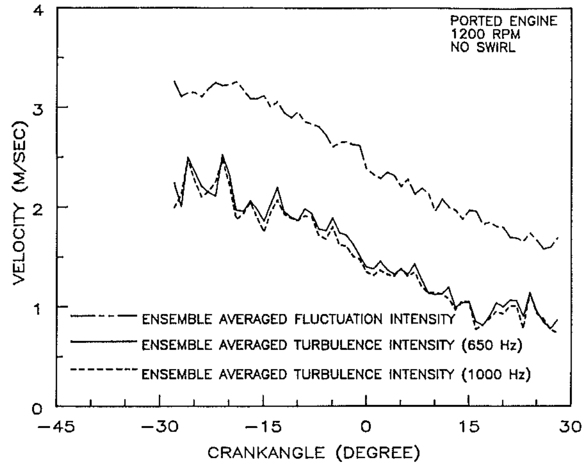

Fig. 8 Sensitivity of the ensemble averaged turbulence intensity to the cut-off frequency

Fig. 3. Approaching TDC the ensemble averaged velocity decreases but approximately 10 degrees before TDC it begins to increase and continues to do so beyond TDC. The ensemble averaged fluctuations decay approaching TDC and continue to do so beyond. Note that the magnitude of the fluctuation intensity is equal to or larger than the ensemble averaged velocity. Such large fluctuations are to be expected near TDC in an engine with no swirl or squish.

The cycle resolved analysis requires high data rates which in turn requires large seed concentrations. The seed concentrations needed for the cycle resolved measurements however did not affect the gas velocity. This is evidenced by Fig. 4 which shows the ensemble averaged velocity and fluctuation intensity for the high seed rate used in this work and for a seed rate which is reduced by a factor of 15.

The first step in the cycle resolved analysis was the calculation of the bulk velocity in each cycle. There were 199 engine cycles which had measurements in at least 40 of the 64 one-degree windows. These data were averaged and interpolated to obtain one velocity for each crankangle degree. The frequency spectrum of the one degree averaged and interpolated data for a typical cycle is shown in Fig. 5, where the absence of a clear separation of bulk velocity and turbulence frequencies is apparent. The frequency spectrum of the ensemble averaged velocity is shown in Fig. 6. From this result a cutoff frequency of 650 Hz was selected to separate the bulk motion from the turbulence. The resultant bulk velocity for one of the 199 engine cycles is shown in Fig. 7, along with the one degree averaged and interpolated data. The insensitivity of the ensemble averaged turbulence intensity to the cutoff frequency is shown in Fig. 8, where the results for cutoff frequencies of 650 Hz and 1000 Hz are given. The requirement that there be measurements in at least 40 of the 64 one-degree windows was based on the fact that the intervals over which there were no LDV measurements in these cycles was always less than 5 crankangle degrees. This corresponds to a Nyquist frequency of 720 Hz as compared to the 650 Hz maximum frequency of the bulk velocity.

The ensemble average and rms fluctuation of the bulk velocity over the 199 engine cycles are shown in Fig. 9. The relative fluctuation in the bulk velocity varies from 100 to 200 percent indicating very large cyclic fluctuations in the bulk motion. The ensemble averaged rms fluctuation of the bulk velocity and the ensemble averaged fluctuation intensity (Fig. 3) show similar behavior in that they both decay up to and past TDC; however, the ensemble averaged fluctuation intensity is larger since it includes the added contribution of the turbulence.

The ensemble averaged turbulence intensity over the 199 engine cycles is shown in Fig. 10 along with the ensemble averaged fluctuation intensity and the ensemble averaged RMS fluctuation of the bulk velocity. The ensemble averaged fluctuation intensity is from 50 to 100 percent larger than the ensemble averaged turbulence intensity. This large difference is due to the large cyclic fluctuations in the bulk velocity. Note that the difference between the square of the ensemble

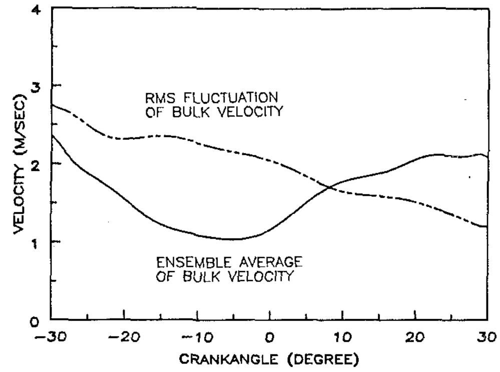

Fig. 9 Ensemble average and rms fluctuation of bulk velocity versus crankangle

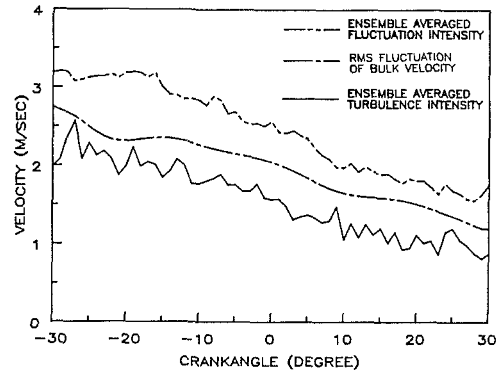

Fig. 10 A comparison of the ensemble averaged turbulence intensity, the ensemble averaged fluctuation intensity and the rms fluctuation of the bulk velocity

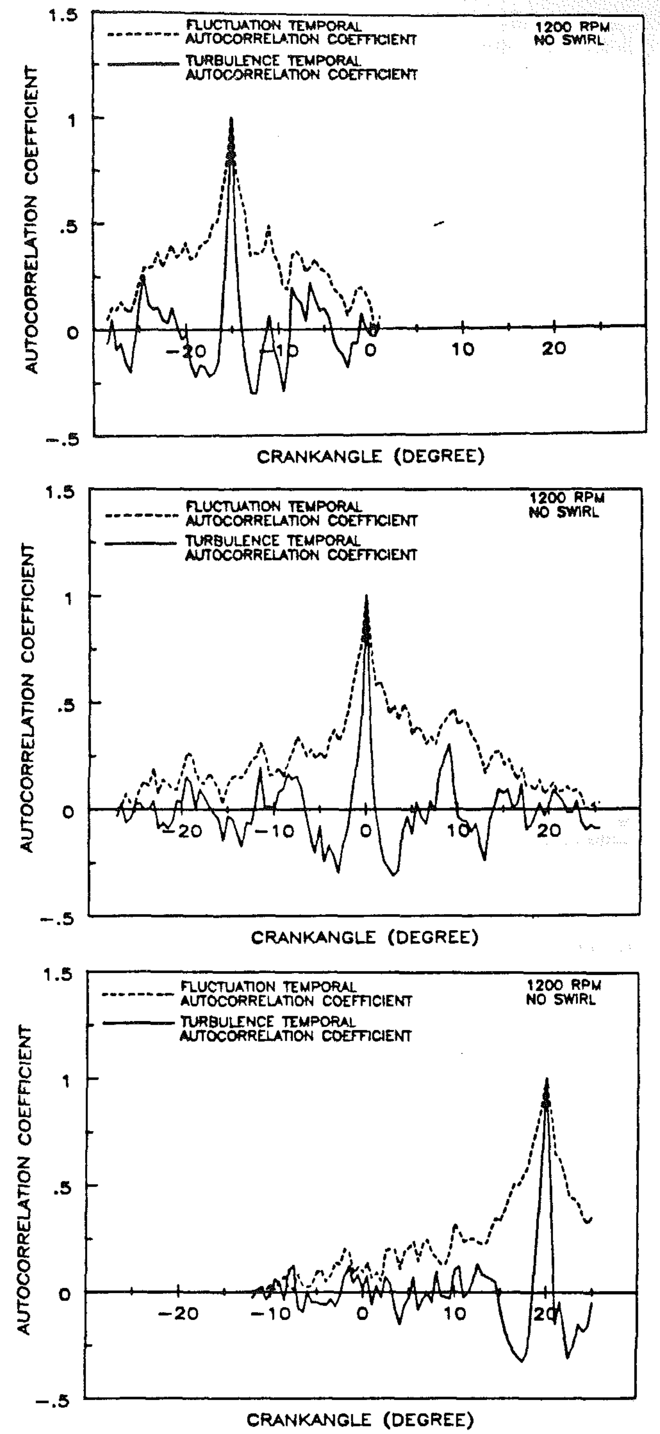

Fig. 11 Fluctuation and turbulence temporal autocorrelation coefficients at −15°, TDC and 20°

averaged fluctuation intensity and the square of the ensemble averaged rms fluctuation of the bulk velocity is approximately equal to the square of the ensemble averaged turbulence intensity. Also note that after eliminating the contribution of the cyclic fluctuations, the ensemble averaged turbulence intensity is still comparable to the ensemble averaged velocity (Fig. 3).

The next result is that of the time averaged turbulence intensity averaged over the 64 degree interval in each engine cycle. The ensemble average of the time averaged turbulence intensity over the 199 engine cycles is 1.75 m/s. The relative ensemble averaged rms fluctuation or cyclic fluctuation in the time averaged turbulence intensity is 20 percent, however approximately 10 percent of that is due to statistical uncertainty. Therefore the relative cyclic fluctuation in the time averaged turbulence intensity is less than 20 percent.

Additional measurements have been made in the same engine at other locations and engine speeds and the same trends have been observed [24, 26, 27].

The autocorrelation coefficient results are shown in Fig. 11, for both the ensemble averaged analysis and the cycle resolved analysis, at 15 degrees before TDC, TDC, and 20 degrees after TDC. The results of both analyses show an asymmetric shape which is a result of the non-stationary nature of the flowfield. Both analyses also show that the correlation time increases with crank angle, due to the fact that the low frequency (large-scale) motions become more profound during the relaxation of the turbulence [3]. In the ensemble averaged analysis the autocorrelation curves decay but generally stay positive which is similar to the behavior observed by others using hot-wire measurements and the same ensemble averaged analysis [22]. In the cycle resolved analysis however, the autocorrelation curves show an initial rapid decay followed by an oscillating behavior with a gradual decay in amplitude. Such oscillations in the autocorrelation coefficient have been observed both in an engine simulator [20] and in other flow fields [28, 29], and are perhaps related to large scale coherent structure in the flow.

The normalized one-dimensional power spectral density functions at TDC for both analyses are shown in Fig. 12. The main difference between the two results occurs at low frequency as one would have expected since the purpose of the cycle resolved analysis is the separation of the low frequency bulk motion components from the high frequency turbulence components. These are one-dimensional spectra whereas the flow field is three-dimensional, therefore part of the low

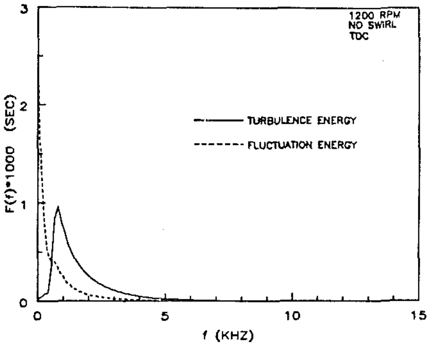

Fig. 12 Fluctuation and turbulence energy distribution versus frequency

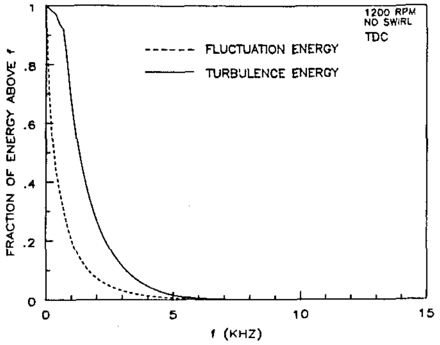

Fig. 13 The effect of cyclic fluctuations in the bulk velocity on the fractional energy distribution

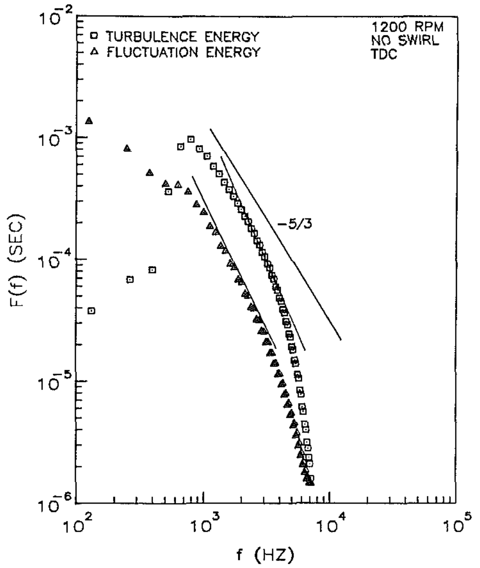

Fig. 14 Logarithmic fluctuation and turbulence energy distribution

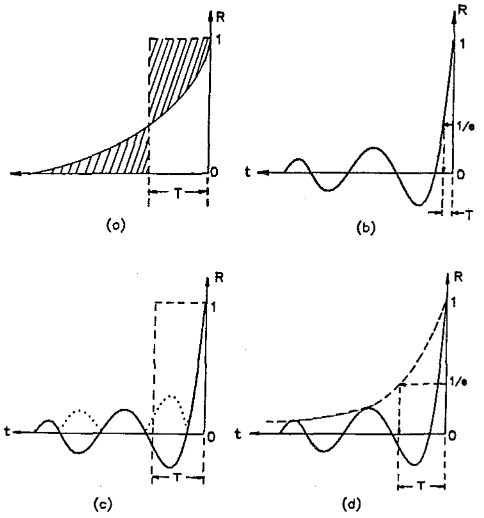

Fig. 15 Schematic diagrams of different definitions of the integral time scale

frequency content is due to aliasing effects [16]. By removing the low frequency bulk motion components the cycle resolved spectrum shows relatively more energy at higher frequencies. This is shown in Fig. 13 which is a plot of the fractional energy distribution versus frequency. Both analyses show that most of the turbulent energy is below 5 KHz which corresponds to a sampling frequency of 10 kHz whereas the 1/2 degree resolution encoder used in this work gave a 14.4 kHz sampling frequency at 1200 rpm. This is consistent with what has been found using a stationary analysis [21] of hot wire measurements made in valved engines motored at approximately the same rpm. At higher frequencies, however, the cycle resolved spectrum shows relatively more energy, i.e., the cycle resolved results show that 64 percent of the energy is above 1 KHz while the ensemble averaged result shows only 21 percent above 1 KHz.

It is also useful to look at the logarithmic energy spectrum which is shown in Fig. 14. Neither result achieves the $-5/3$ slope predicted by Kolmogorov's Law of the inertial subrange [30] which implies that the turbulence Reynolds number is less than 4000 [16]. For this 1200 rpm case the ensemble averaged analysis overestimates the turbulence Reynolds number which is consistent with the previous observation that the ensemble averaged analysis also overpredicted the turbulence intensity.

The standard definition of the integral time scale given earlier, i.e., the area under autocorrelation curve, (Fig. 15(*a*)), is obviously not applicable to the oscillating autocorrelations (Fig. 11) from the cycle resolved analysis. In this study three definitions of the integral time scale were used and compared. Several previous investigators [20, 23] have defined the integral time scale as the $1/e$ decay time of the autocorrelation coefficient as shown in Fig. 15(*b*). Another approach is to take the absolute value of the autocorrelation coefficient before integrating to determine the area, i.e., see Fig. 15(*c*). The third way is based on the decaying envelope of oscillating peaks as shown in Fig. 15(*d*). The results obtained for the ensemble average analysis and the cycle resolved analysis using these three different definitions are given in Fig. 16. All curves show that the integral time scale is increasing or constant with crankangle. This is consistent with the observation made before, i.e., the correlation time is increasing with crankangle near TDC. This increase is due to the low-frequency (large-scale) motions becoming more pronounced as the flow field relaxes [3].

Comparing the results of the two analyses, using the first definition (Fig. 15(*b*)), one finds that the ensemble averaged analysis overestimates the integral time scale by a factor of 3 to 8. Using the second (Fig. 15(*c*)) and third (Fig. 15(*d*)) definitions one obtains comparable results, with the cycle resolved analysis predicting an integral time scale less than that of ensemble averaged analysis by a factor of 1.5 to 3. The fact that the ensemble averaged analysis overestimates the integral time scale is due to the contribution of the low frequency cyclic variation of the bulk velocity.

Since Taylor's hypothesis is not valid in an IC engine running at practical speeds, due in part to the fact that the ensemble averaged turbulence intensity is of the same order as

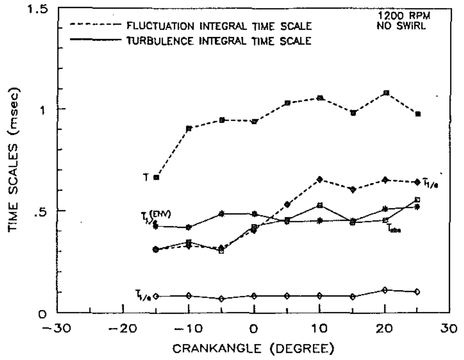

Fig. 16 Fluctuation and turbulence integral time scales versus crankangle

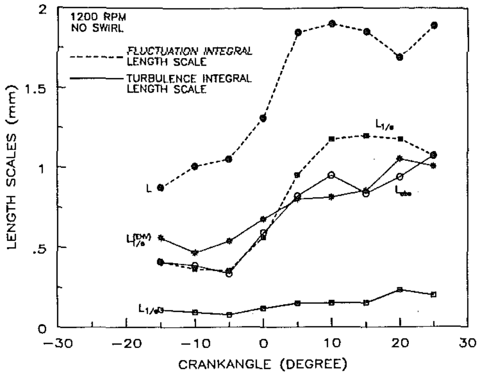

Fig. 17 Fluctuation and turbulence integral length scales versus crankangle

or even larger than the bulk velocity, the length scale should be obtained directly from spatial correlation measurements. However, since such measurements are very difficult, all researchers [4, 21–23] to date have used Taylor's hypothesis to obtain length scale measurements in engines.

Taylor's frozen turbulence hypothesis assumes that if the entire flow field is homogeneous and is translated with a constant bulk velocity, $\bar{U}$, and if $\bar{U} >> u'$, where u' is turbulence intensity, then the temporal and spatial scales of turbulence can be related by

$$L = \bar{U} \cdot T$$

The integral length scales obtained using Taylor's hypothesis are given in Fig. 17, where $\bar{U}$ was taken to be the ensemble averaged velocity.

Since the time scale only slightly increases with crank angle, the variation of Taylor's length scale with crankangle reflects the larger variations in the bulk velocity (see Fig. 3). That is, it first decreases with crankangle until around 10 deg before TDC, then it increases with crankangle.

The ensemble averaged analysis overestimates the length scales in the same way that it does the time scales, as one would expect given that they were obtained using Taylor's hypothesis.

Conclusions

LDV measurements have been made in a motored engine operated at practical engine speeds at data rates high enough to allow characterization of the bulk velocity in a single cycle. With no swirl, the cyclic fluctuations in the bulk velocity were found to be very large, i.e., comparable to the ensemble average of the bulk velocity. The cyclic fluctuations in the bulk velocity resulted in ensemble averaged fluctuation intensities which were 50 to 100 percent greater than the ensemble averaged turbulence intensity. From this result it is clear that cycle resolved measurements are important for the accurate characterization of the turbulence intensity in an IC engine. The cyclic fluctuations in the time averaged turbulence intensity were found to be less than 20 percent, therefore considerably smaller than the cyclic fluctuations in the bulk velocity.

A comparison between ensemble averaged and cycle resolved spectral analyses has been made. Both analyses showed that most of the turbulence energy is contained within 5 kHz for 1200 rpm. But the ensemble averaged analysis gives a low frequency bias in the energy spectrum due to the inclusion of cyclic variations of the bulk velocity in the nonstationary definition of engine turbulence. Both analyses show that near TDC the integral time scale increases with crankangle. However, the ensemble averaged analysis gives a higher estimate of the integral time scale than that of the cycle resolved analysis.

Acknowledgments

This work was carried out in the Engine Combustion Laboratory of the Mechanical and Aerospace Engineering Department at Princeton University. The authors are grateful to Professor F. V. Bracco who encouraged this work, to Messrs. T. O. Williams and S. McDougall for their assistance in writing the data acquisition and analysis software, and to Mr. J. Semler for his technical assistance with the construction of the transparent-piston, transparent-head engine. The support for this work was provided by DOE, NSF, Volkswagenwerk, General Motors, and Fiat.

References

1 Lancaster, D. R., Krieger, R. B., Sorenson, S. C., and Hull, W. L., "Effects of Turbulence on Spark-Ignition Engine Combustion," SAE Paper No. 760160, 1976.

2 Bendat, J. S., and Piersol, A. G., *Random Data: Analysis and Measurement Procedures*, Wiley-Interscience, 1971, p. 351.

3 Reynolds, W. C., "Modeling of Fluid Motions in Engines—An Introductory Overview," in *Combustion Modeling in Reciprocating Engines*, edited by J. N. Mattavi and C. A. Amann, Plenum Press, 1980.

4 Lancaster, D. R., "Effects of Engine Variables on Turbulence in a Spark-Ignition Engine," SAE Paper No. 760159, 1976.

5 Rask, R. B., "Comparison of Window, Smooth-Ensemble and Cycle-by-Cycle Data Reduction Techniques for Laser-Doppler Anemometer Measurement of In-Cylinder Velocity," in *Fluid Mechanics of Combustion Systems* edited by T. Morel, R. P. Lohmann and J. M. Rackley, New York, American Society of Mechanical Engineers, 1981.

6 Witze, P. O., "A Critical Comparison of Hot-Wire Anemometry and Laser Doppler Velocimetry for I. C. Engine Applications," SAE Paper No. 800132, 1980.

7 The cycle resolved measurements reported in reference [4] were made at 300 RPM.

8 Bowditch, F. W., "A New Tool for Combustion Research: A Quartz Piston Engine," SAE Paper No. 150B, Mar. 1960.

9 Glass, M., and Kennedy, I., "An Improved Seeding Method for High Temperature Laser Doppler Velocimetry," *Comb. and Flame*, Vol. 29, No. 3, 1977.

10 Agarwal, J. K., and Fingerson, L. M., "Evaluation of Various Particles for Their Suitability as Seeds in Laser Velocimetry," in *Laser Velocimetry and Particle Sizing*, edited by H. D. Thompson and W. H. Stevenson, Hemisphere Publishing Co., 1979.

11 Bendat, J. S., and Piersol, A. G., *Random Data: Analysis and Measurement Procedures*, Wiley-Interscience, 1971, p. 353.

12 Brigham, E. O., *The Fast Fourier Transform*, Prentice-Hall, 1974, p. 140.

13 Bendat, J. S., and Piersol, A. G., *Random Data: Analysis and Measurement Procedures*, p. 296.

14 Ormsby, J. F. A., "Design of Numerical Filters with Applications to Missile Data Processing," *J. Assoc. Computing Machinery*, Vol. 8, No. 3, July 1961, p. 440.

15 Taylor, G. I., "Diffusion by Continuous Movement," "Proceedings of the London Mathematical Society, Sr. 2, 20, 1921, pp. 196–211.

16 Tennekes, H., and Lumley, J. L., *A First Course in Turbulence*, MIT Press, Cambridge, 1972.

17 Hinze, J. O., *Turbulence*, McGraw-Hill, New York, 1959.

18 Launder, B. E., and Spalding, D. B., *Lectures in Mathematical Models of Turbulence*, Academic Press, 1972.

19 Taylor, G. I., "The Spectrum of Turbulence," *Proc. Roy. Soc. of London*, A151, 1935.

20 Tsuge, M., Kido, H., Kato, K., and Nomiyama, Y., "Decay of Turbulence in a Closed Vessel," *Bulletin of the JSME*, Vol. 17, 1956.

21 Dent, J. C., and Salama, N. S., "The Measurement of Turbulence Characteristics in an Internal Combustion Engine Cylinder," SAE Paper No. 750886, 1975.

22 Witze, P. O., "Measurements of the Spatial Distribution and Engine Speed Dependence of Turbulence Air Motion in an IC Engine," SAE Paper No. 770220, 1977.

23 Wakisaka, T., Hamamoto, Y., Ohigashi, S., and Hashimoto, M., "Measurement of Air Swirl and Its Turbulence Characteristics in the Cylinder of an Internal Combustion Engine," Paper No. C91/79, I. Mech. E., 1979.

24 Liou, T.-M., "Laser Doppler Velocimetry Measurements in Valved and Ported Engines," Ph.D. thesis, Department of Mechanical and Aerospace Engineering, Report No. 1602-T, May 1983.

25 Burington, R. S., and May, D. C., *Handbook of Probability and Statistics*, McGraw-Hill, 1970.

26 Liou, T.-M., Santavicca, D. A., and Bracco, F. V., "Turbulence Measurements in a Ported IC Engine," Int'l. Symposium on Applications of Laser-Doppler Anemometry to Fluid Mechanics, Lisbon, Portugal, July 1982.

27 Liou, T-M., and Santavicca, D. A., "Cycle Resolved Turbulence Measurements in a Ported Engine with and without Swirl," SAE Paper No. 830419, 1983.

28 Loader, A. J., and Thew, M. T., "Analysis and Characteristics of Turbulence in a Confined Swirling Flow Studied with a LDA," *Proceedings of the LDA-Symposium*, Copenhagen, 1975.

29 Dandekar, K. V., and Gouldin, F. C., "Temperature and Velocity Measurements in a Premixed Turbulent Flames," *AIAA Journal*, Vol. 20, No. 5, May 1981.

30 Kolmogorov, A. N., *Compt. Und Acad. Sci. URSS*, Vol. 30, 1941, p. 301.

J. F. Thompson

C. W. Mastin

Department of Aerospace Engineering,
Department of Mathematics,
Mississippi State University,
Mississippi State, MS 39762

Order of Difference Expressions in Curvilinear Coordinate Systems

The order of finite difference representations on general curvilinear coordinate systems is considered in some detail. It is shown that the uniform grid order is formally preserved on the nonuniform, nonorthogonal grid in the sense of the error behavior with an increase in the number of points. However, the coefficients in the series expansion may become quite large for some point distributions. Several specific distributions are evaluated.

Introduction

Numerically generated, boundary-conforming curvilinear coordinate systems have now become common in the numerical solution of partial differential equations, allowing very general codes to be constructed which are applicable to regions with arbitrarily-shaped boundaries. Surveys have been given in [1 and 2], and a source book with both basic exposition and state-of-the-art developments, [3], has recently become available.

Difference representations on curvilinear coordinate systems are constructed by first transforming derivatives with respect to cartesian coordinates into expressions involving derivatives with respect to the curvilinear coordinate and derivatives of the cartesian coordinates with respect to the curvilinear (the metric coefficients). The derivatives with respect to the curvilinear coordinates are then replaced with difference expressions on the uniform grid in the transformed region.

Considerable attention is appropriately now being focussed on evaluation of the truncation error of difference expressions on these curvilinear systems, but some misunderstandings have arisen regarding the identification of the true order of these expressions. The "order" of a diffrence representation refers to the exponential rate of decrease of the truncation error with the point spacing. On a uniform grid this concerns simply the behavior of the error with a decrease in the point spacing. With a nonuniform point distribution, there is some ambiguity in the interpretation of order, in that the minimum spacing may be decreased either by increasing the number of points in the field or by changing the distribution of a fixed number of points. Both of these could, of course, be done simultaneously, or the points could even be moved randomly, but to be meaningful the order of a difference representation must relate to the error behavior as the point spacing is decreased according to some pattern. This is a moot point with uniform spacing, but two senses of order on a nonuniform grid emerge: the behavior of the error as (1) the number of points in the field is increased while maintaining the same relative point distribution over the field, or (2) the point distribution over the field is changed so as to reduce the minimum spacing with a fixed number of points in the field.

On curvilinear coordinate systems, then, the definition of order of a difference representation is integrally tied to point distribution functions. The order is determined by the error behavior as the spacing varies with the points fixed in a certain distribution, either by increasing the number of points or by changing a parameter in the distribution, not simply by consideration of the points used in the difference expression as being unrelated to each other. This point is essentially what is noted by Hoffman in [4]. Actually global order is meaningful only in the first sense, since as the minimum spacing is reduced with a fixed number of points in the field, the spacing somewhere else must certainly increase. This second sense of order on a nonuniform grid then is relevant only locally in regions where the spacing does in fact decrease as the point distribution is changed.

The question of order with nonuniform spacing has recently been considered by Vinokur [5], Hoffman [4], and by Thompson [2]. Other studies of error on curvilinear coordinate systems have been reported in [6-7]. The present discussion attempts to clarify this question.

Order on Nonuniform Spacing

A general one-dimensional point distribution function can be written in the form

$$x(\xi)=g\left(\frac{\xi}{N}\right)\quad(0\le\xi\le N)\tag{1}$$

In the following analysis, x will be considered to vary from 0 to 1. Any other range of x can be constructed simply by multiplying the distribution functions given here by an appropriate constant. With this form for the distribution function, the effects of increasing the number of points in a discretization of the field can be seen explicitly by defining the values of ξ at the points to be successive integers from 0 to N. In this form, $N+1$ is then the number of points in the discretization, so that the dependence of the error expressions on the number of points in the field will be displayed explicitly by N. This form removes the confusion that can arise in interpretation of analyses based on a fixed ξ interval (0, 1) where variation of the number of points is represented by

---

Contributed by the Fluids Engineering Division and presented at the Fluids Engineering Conference, Houston, Texas, June 1983. Manuscript received by the Fluids Engineering Division, August 9, 1983.

variations of the interval $\Delta\xi$. The form of the distribution function, i.e., the relative concentration of points in certain areas while the total number of points in the field is fixed, is varied by changing parameters in the function.

The transformation of the first derivative is given by

$$f_x = \frac{f_\xi}{x_\xi} \tag{2}$$

if f_ξ is approximated by the second-order central difference expression we have, since $\Delta\xi = 1$ here,

$$f_\xi = 1/2(f_{i+1} - f_{i-1}) + T_\xi \tag{3}$$

where T_ξ is the truncation error of this difference expression, and $i \pm 1$ indicates points adjacent to the central point, i.e., indicates increments in ξ. A Taylor series expansion in ξ yields

$$T_\xi = f_\xi - 1/2 \sum_{n=0}^{\infty} \frac{1}{n!} f_{(n)} + 1/2 \sum_{n=0}^{\infty} \frac{(-1)^n}{n!} f_{(n)}$$

where $f_{(n)}$ represents the nth ξ-derivative of f. The $n = 0$ and $n = 1$ terms lead to cancellations, so that T_ξ can be written

$$T_\xi = -\sum_{n=1}^{\infty} \frac{1}{(2n+1)!} f_{(2n+1)} \tag{4}$$

Using (3), the difference expression for f_x on this point distribution is

$$f_x = \frac{1}{2x_\xi}(f_{i+1} - f_{i-1}) + T_x \tag{5}$$

where now $T_x = (1/x_\xi)\ T_\xi$ is the truncation error in this difference represetation of f_x. From (4) we have then

$$T_x = -\frac{1}{x_\xi} \sum_{n=1}^{\infty} \frac{1}{(2n+1)!} f_{(2n+1)} \tag{6}$$

Here the metric coefficient, x_ξ, is considered to be evaluated analytically, and hence has no error. (The case of numerical evaluation of the metric coefficients is considered in a later section.)

Now the series in (6) cannot be truncated without further consideration since the ξ-derivatives, $f_{(2n+1)}$, are dependent on the point distribution. Thus if the point distribution is changed, either through the addition of more points or through a change in the form of the distribution function, these derivatives will change. Since the terms of the series do not contain a power of some quantity less than unity, there is no indication that the successive terms become progressively smaller.

It is thus not meaningful to give the truncation error in terms of ξ-derivatives of f. Rather, it is necessary to transform these ξ-derivatives to x-derivatives, which, of course, are not dependent on the point distribution. The first ξ-derivative follows from (2):

$$f_\xi = x_\xi f_x \tag{7}$$

Now f_ξ, and the higher derivatives, depends on ξ explicitly through the ξ-derivatives of the metric derivatives, e.g., x_ξ, and implicitly through the x-dependence of f. Thus

$$\frac{d(f_\xi)}{d\xi} = \left(\frac{\partial(f_\xi)}{\partial\xi}\right)_x + \left(\frac{\partial(f_\xi)}{\partial x}\right)_\xi x_\xi \tag{8}$$

or, in operator form

$$\frac{d}{d\xi} = \frac{\partial}{\partial\xi} + x_\xi \frac{\partial}{\partial x} \tag{9}$$

For example,

$$\begin{aligned} f_{\xi\xi} &= \left(\frac{\partial}{\partial\xi} + x_\xi \frac{\partial}{\partial x}\right) f_\xi = \left(\frac{\partial}{\partial\xi} + x_\xi \frac{\partial}{\partial x}\right)(x_\xi f_x) \\ &= x_{\xi\xi} f_x + x_\xi^2 f_{xx} \end{aligned}$$

In general, then

$$f_{(n)} = \frac{d^n f}{d\xi^n} = \left(\frac{\partial}{\partial\xi} + x_\xi \frac{\partial}{\partial x}\right)^n f \tag{10}$$

Note here that since f has no explicit ξ-dependence, we have

$$\left(\frac{\partial}{\partial\xi} + x_\xi \frac{\partial}{\partial x}\right) f = x_\xi f_x = f_\xi$$

as expected.

The truncation error in f_x can then be written, using (10) in (6), as

$$T_x = -\frac{1}{x_\xi} \sum_{n=1}^{\infty} \frac{1}{(2n+1)!} \left(\frac{\partial}{\partial\xi} + x_\xi \frac{\partial}{\partial x}\right)^{2n+1} f \tag{11}$$

Note that the binomial theroem cannot be used to expand the power of the derivative operator here since $(\partial/\partial\xi)$ and $x_\xi\ (\partial/\partial x)$ do not commute, i.e.,

$$\left(\frac{\partial}{\partial\xi}\right)\left(x_\xi \frac{\partial}{\partial x}\right) = x_{\xi\xi} \frac{\partial}{\partial x} + x_\xi \frac{\partial^2}{\partial\xi\partial x}$$

while

$$\left(x_\xi \frac{\partial}{\partial x}\right)\left(\frac{\partial}{\partial\xi}\right) = x_\xi \frac{\partial^2}{\partial\xi\partial x}$$

Thus all permutations of the operator products of degree $2n+1$ will occur in the expansion of the $2n+1$ power of the derivative operator. For example, with $2n+1 = 3$, the following eight operator products will occur:

$$\left(\frac{\partial}{\partial\xi}\right)^3, \left(\frac{\partial}{\partial\xi}\right)^2 \left(x_\xi \frac{\partial}{\partial x}\right), \left(\frac{\partial}{\partial\xi}\right)\left(x_\xi \frac{\partial}{\partial x}\right)^2, \left(x_\xi \frac{\partial}{\partial x}\right)^3,$$

$$\left(\frac{\partial}{\partial\xi}\right)\left(x_\xi \frac{\partial}{\partial x}\right)\left(\frac{\partial}{\partial\xi}\right), \left(x_\xi \frac{\partial}{\partial x}\right)\left(\frac{\partial}{\partial\xi}\right)\left(x_\xi \frac{\partial}{\partial x}\right),$$

$$\left(x_\xi \frac{\partial}{\partial x}\right)\left(\frac{\partial}{\partial\xi}\right)^2, \left(x_\xi \frac{\partial}{\partial x}\right)^2 \left(\frac{\partial}{\partial\xi}\right)$$

But since f has no explicit ξ-dependence, all of these operator products having a ξ on the extreme right will make no contribution. Therefore, of the above eight-products for the $2n+1$ power term, only four need to be considered:

$$\left(\frac{\partial}{\partial\xi}\right)^2 \left(x_\xi \frac{\partial}{\partial x}\right), \left(\frac{\partial}{\partial\xi}\right)\left(x_\xi \frac{\partial}{\partial x}\right)^2, \left(x_\xi \frac{\partial}{\partial x}\right)^3,$$

$$\left(x_\xi \frac{\partial}{\partial x}\right)\left(\frac{\partial}{\partial\xi}\right)\left(x_\xi \frac{\partial}{\partial x}\right)$$

Also since there is no explicit ξ-dependence in f, the following relations apply:

$$\left[\left(x_\xi \frac{\partial}{\partial x}\right)^m\right] f = x_\xi^m \frac{d^m f}{dx^m}$$

$$\left[\left(\frac{\partial}{\partial\xi}\right)^m \left(x_\xi \frac{\partial}{\partial x}\right)\right] f = x_{(m+1)} \frac{df}{dx}$$

where $x_{(m+1)}$ indicates the $m+1$ ξ-derivative of x. Also

$$\left[\left(\frac{\partial}{\partial\xi}\right)^l \left(x_\xi \frac{\partial}{\partial x}\right)^m\right] f = \left(\frac{\partial}{\partial\xi}\right)^l \left(x_\xi^m \frac{d^m f}{dx^m}\right) = \frac{d^l(x_\xi^m)}{d\xi^l} \frac{d^m f}{dx^m}$$

and,

$$\begin{aligned} &\left[\left(x_\xi \frac{\partial}{\partial x}\right)^l \left(\frac{\partial}{\partial\xi}\right)^m \left(x_\xi \frac{\partial}{\partial x}\right)^n\right] f \\ &= \left(x_\xi \frac{\partial}{\partial x}\right)^l \left[\frac{d^m(x^n)}{d\xi^m} \frac{d^n f}{dx^n}\right] \\ &= x_\xi^l \frac{d^m(x_\xi^n)}{d\xi^m} \frac{d^{l+n} f}{dx^{l+n}} \end{aligned}$$

Other combinations appearing can be inferred from these.

From these relations it follows that $((\partial/\partial x)+x_\xi\,(\partial/\partial x))^p$ will expand to the sum of products of ξ-derivatives of x, in each of which product the total number of ξ-differentiations is p. All possible combinations of ξ-derivatives appear in these products:

$p=1$ x_ξ

$p=2$ $x_\xi^2, x_{\xi\xi}$

$p=3$ $x_\xi^3, x_{\xi\xi}x_\xi, x_{\xi\xi\xi}$

$p=4$ $x_\xi^4, x_{\xi\xi\xi}x_\xi, {x_{\xi\xi}}^2, x_{\xi\xi}{x_\xi}^2, x_{\xi\xi\xi\xi}$

$p=5$ $x_\xi^5, x_{\xi\xi\xi\xi}x_\xi, x_{\xi\xi\xi}x_{\xi\xi}, x_{\xi\xi\xi}{x_\xi}^2, {x_{\xi\xi}}^2x_\xi, x_{\xi\xi}{x_\xi}^3,$
$x_{\xi\xi\xi\xi\xi}$

The n-term of the series in (11) then is of the form

$$\frac{1}{(2n+1)!}\sum_{m=1}^{2n+1} C_m\frac{d^mf}{dx^m}\prod_{i=1}^{2n+1} x_{(i)}^{a_{im}}\,(m=1,2,\;.\;.\;.\;2n+1) \tag{12}$$

where the a_{im} are non-negative integers on the interval $(0, 2n+1)$ such that

$$\sum_{i=1}^{2n+1} i\,a_{im}=2n+1(m=1,2,\;.\;.\;.\;2n+1) \tag{13}$$

Also

$$a_{i,1}=\delta_{i,2n+1}, a_{i,2n+1}=(2n+1)\delta_{i,1}$$

Neither the exponents, a_{im}, nor the numerical coefficients, C_m, depend on the point distribution. The first and last of the C_m coefficients are unity: $C_1=C_{2n+1}=1$. In (12), $x_{(i)}$ is the i^{th} ξ-derivative of x. As an example of (12), for $n=1$ we have the term

$$\frac{1}{3!}\left(\frac{\partial}{\partial\xi}+x_\xi\frac{\partial}{\partial x}\right)^3 f$$

which expands to

$$\frac{1}{6}\,(x_{\xi\xi\xi}f_x+3x_\xi x_{\xi\xi}f_{xx}+x_\xi^3f_{xxx})$$

Here $m=1, 2, 3$, and $C_1=C_3=1$, $C_2=3$, and $a_{13}=3$, $a_{12}=a_{22}=a_{31}=1$, with all the other a_{im} being zero. In the general case, as in this example, the $2n+1$ products that are summed to construct the n-term of the series will each contain $2n+1$ ξ-differentiations.

Order With Fixed Distribution Function. Now from the form of the distribution function (1), it is clear that

$$x_{(i)}=\frac{D_i}{N^i} \tag{14}$$

where the coefficient D_i does depend on the point distribution function of (1), but not on the number of points, N. Therefore, in (12),

$$\prod_{i=1}^{2n+1} x_{(i)}^{a_{im}}=\prod_{i=1}^{2n+1}\left(\frac{D_i}{N^i}\right)^{a_{im}}=\frac{\prod\limits_{i=1}^{2n+1}D_i^{a_{im}}}{\sum\limits_{i=1}^{2n+1} i\,a_{im}}=\frac{\prod\limits_{i=1}^{2n+1}D_i^{a_{im}}}{N^{2n+1}}$$

by (14). The truncation error in the difference expression for f_x then is

$$T_x=-\sum_{n=1}^{\infty}\frac{1}{(2n+1)!N^{2n}}\sum_{m=1}^{2n+1}A_{mn}\frac{d^mf}{dx^m} \tag{15}$$

where the coefficients, A_{mn}, given by

$$A_{mn}=\frac{C_m}{D_1}\prod_{i=1}^{2n+1}D_i^{a_{im}} \tag{16}$$

depend on the distribution function, but not on the number of points. The series (15) is thus a power series in the inverse of the number of points in the field. It therefore is possible to truncate the series as the number of points in the field, N, increases, with the result

$$T_x=-\frac{1}{6N^2}\sum_{m=1}^{3}A_{m1}\frac{d^mf}{dx^m} \tag{17}$$

where, from (16),

$$A_{m1}=\frac{C_m}{D_1}\prod_{i=1}^{3}D_i^{a_{im}}\,(m=1,2,3)$$

and, as noted above,

$$C_1=C_3=1, C_2=3, a_{13}=3, a_{12}=a_{22}=a_{31}=1$$

and all other a_{im} are zero. Thus

$$A_{11}=\frac{D_3}{D_1}, A_{21}=D_2, A_{31}=D_1^2$$

The truncation error of the difference expression (5) can then be written, using (14), as

$$T_x=-\frac{1}{6}\frac{x_{\xi\xi\xi}}{x_\xi}f_x-\frac{1}{2}x_{\xi\xi}f_{xx}-\frac{1}{6}x_\xi^2f_{xxx} \tag{18}$$

The first two terms arise from the nonuniform spacing, while the last term is the familiar term occurring with uniform spacing as well.

From (17) it is clear that the difference represenation (5) is second-order *regardless of the form of the point distribution function* in the sense that the truncation error goes to zero as $1/N^2$ as the number or points increases. This means that the error will be quartered when the number of points is doubled in the same distribution function. Thus all difference representations maintain their order on a nonuniform grid with any distribution of points in the formal sense of the truncation error decreasing as the number of points is increased while maintaining the same relative point distribution over the field.

The critical point here is that the same relative point distribution, i.e., the same distribution function is used as the number of points in the field is increased. If this is the case, then the error will be decreased by a factor that is a power of the inverse of the number of points in the field as their number is increased. Random additions of points will, however, not maintain order. This point has also been noted by Hoffman in [4]. In a practical vein this means that a solution made with twice the number of points as another solution will exhibit one-fourth of the error (for second-order representations in the transformed plane) when the two solutions use the same point distribution function. However if the number of points is doubled without maintaining the same relative distribution the error reduction will not be as great as one-fourth.

From the standpoint of formal order in this sense, then, there is no need for concern over the form of the point distribution. However, formal order in this sense relates only to the behavior of the truncation error as the number of points is increased, and the coefficients A_{mn} in the series (15) may become large as the parameters in the distribution are altered to reduce the minimum spacing with a given number of points in the field. Thus, although the error will be reduced by the same order for all point distributions as the number of points is increased, certain distributions will have smaller error than others with a given number of points in the field, since the coefficients in the series, A_{mn}, while independent of the number of points, are dependent on the distribution function.

Since the numerical coefficients, C_m, in (16) do not depend on the distribution function, the quantities of concern for the n-term of the series (15) are

$$\frac{A_{mn}}{C_m} \equiv \frac{1}{D_1} \prod_{i=1}^{2n+1} D_i^{a_{im}} \, (m=1,2, \ldots ,2n+1)$$

$$= \frac{1}{Nx_\xi} \prod_{i=1}^{2n+1} N^{ia_{im}} x_{(i)}{}^{a_{im}}$$

$$= (Nx_\xi) \sum_{i=1}^{2n+1} a_{im} - 1 \prod_{i=1}^{2n+1} \left(\frac{N^{i-1} x_{(i)}}{x_\xi} \right)^{a_{im}} \tag{19}$$

Now at least one a_{im} must be greater than or equal to unity for each m, and therefore the exponent of Nx_ξ in the above expression is not negative. Since the $a_{im}d$ do not depend on the distribution function, we are lead by (19) to compared distribution functions on the basis of behavior of the following quantities as the minimum value of x_ξ on the field goes to zero with fixed N:

$$Nx_\xi \quad \text{and} \quad \frac{N^{i-1} x_{(i)}}{x_\xi} \; (i=1,2, \ldots , 2n+1) \tag{20}$$

Now for uniform spacing we have $D_i = 0$ for $i \geq 2$, and then by (16), all A_{mn} are zero except $A_{2n+1,n}$, which is given by

$$A_{2n+1,n} = \frac{C_{2n+1}}{D_1} D_1{}^{a_{1,2n+1}} = D_1{}^{2n}$$

Thus the contribution to the truncation error that remains with uniform spacing arises from the $m = 2n+1$ term of (15). The ratio of the coefficients A_{mn} to the coefficient $A_{2n+1,n}$, corresponding to the uniform spacing error, is then, from (16) and (14).

$$\frac{A_{mn}}{A_{2n+1,n}} = \frac{C_m}{C_{2n+1}} \frac{\prod_{i=1}^{2n+1} D_i^{a_{im}}}{\prod_{i=1}^{2n+1} D_i^{a_{i,2n+1}}}$$

$$= \frac{C_m}{D_1{}^{2n+1}} \prod_{i=1}^{2n+1} D_i^{a_{im}} = C_m \prod_{i=2}^{2n+1} \left(\frac{x_{(i)}}{x_\xi^i} \right)^{a_{im}} \tag{21}$$

Note that this ratio is the ratio of the coefficient of $d^m f/dx^m$ to that of f_x in the n-term, i.e., the $(1/N)^{2n+1}$ term, of the series (15) for the truncation error. The ratios of the terms arising from the nonuniform spacing to that from the spacing itself in the n-term of the truncation error expansion (15) as a power series in the inverse of number of points are then

$$\frac{A_{mn}}{A_{2n+1,n}} \frac{\dfrac{d^m f}{dx^m}}{\dfrac{d^{2n+1} f}{dx^{2n+1}}} = C_m \frac{\dfrac{d^m f}{dx^m}}{\dfrac{d^{2n+1} f}{dx^{2n+1}}} \prod_{i=2}^{2n+1} \left(\frac{x_{(i)}}{x_\xi^i} \right)^{a_{im}} \tag{22}$$

Order With Fixed Number of Points. The above considerations have been concerned with order in the formal sense of the truncation error being reduced by a factor equal to a power of N as the number of points in the field is increased, while maintaining the same relative point distribution. It has been shown that all point distributions maintain formal order in this sense, but that some distributions may be superior to others with a given total number of points in the field. Also, comparisons, may be made on the basis of the magnitude of the series coefficients, ultimately through the quantities given in (20). All this was based on a series expansion of the error in ascending inverse powers of the number of points in the field, N.

An alternate sense of order for point distributions is based on expansion of the truncation error in a series in ascending powers of the spacing, x_ξ. This can be developed from the series given above as (15), but with D_i from (14) substituted in the expression for A_{mn} given by (15):

$$A_{mn} = \frac{C_m}{D_1} \prod_{i=1}^{2n+1} (N^i x_{(i)})^{a_{im}}$$

$$= \frac{C_m}{D_1} \prod_{i=1}^{2n+1} \left[\left(\frac{D_1}{x_\xi} \right)^i x_{(i)} \right]^{a_{im}}$$

But, by (13),

$$\prod_{i=1}^{2n+1} D_1{}^{ia_{im}} = D_1{}^{\sum_{i=1}^{2n+1} ia_{im}} = D_1{}^{2n+1}$$

so that

$$A_{mn} = C_m D_1^{2n} \prod_{i=1}^{2n+1} \left(\frac{x_{(i)}}{x_\xi^i} \right)^{a_{im}}$$

$$= C_m (Nx_\xi)^{2n} \prod_{i=1}^{2n+1} \left(\frac{x_{(i)}}{x_\xi^i} \right)^{a_{im}} \tag{23}$$

Then the series (15) becomes

$$T_x = - \sum_{n=1}^{\infty} \frac{(x_\xi)^{2n}}{(2n+1)!} \sum_{m=1}^{2n+1} B_{mn} \frac{d^m f}{dx^m} \tag{24}$$

where

$$B_{mn} = C_m \prod_{i=1}^{2n+1} \left(\frac{x_{(i)}}{x_\xi^i} \right)^{a_{im}} \tag{25}$$

Recall that the numerical coefficients, C_m, and the exponents, a_{im}, do not depend on the distribution function. However, in contrast to the series of (15), the coefficients, B_{mn}, may be dependent on the variation of the spacing, x_ξ, with a fixed number of points. The series here is therefore not a power series in x_ξ, and cannot be truncated unless the coefficients, B_{mn}, are bounded as the spacing goes to zero with a fixed number of points. A sufficient condition for this is that the quantities involved in the ratio of the coefficients to that arising with uniform spacing, i.e., (22),

$$\frac{x_{(i)}}{x_\xi^i} \quad (i=1,2, \ldots ,\infty) \tag{26}$$

be bounded as x_ξ goes to zero with fixed N. Where this is the case, the order of the difference representation is maintained with the non-uniform point distribution in the sense that the truncation error is reduced by a factor equal to a power of the spacing as the spacing is decreased with a fixed number of points in the field.

In the specific distribution functions to be considered below, it will be seen that it is possible for the quantities of (20) to be larger than those of (26), but for most functions the reverse is true. The difference between these two approaches to order should be kept clear. The first approach concerns the behavior of the truncation error as the number of points in the field increases with a fixed relative distribution of points. The series here is a power series in the inverse of the number of points in the field, and formal order is maintained for all point distributions. The coefficients in the series may, however, become large for some distribution functions as the minimum spacing decreases for any given number of points.

Table 1 Coefficients at minimum spacing

FUNCTION	NS	$(L_N^{(2)})_0$	$(L_N^{(3)})_0$	$(L_S^{(2)})_0$	$(L_S^{(3)})_0$
Exponential: $\frac{e^{\alpha\bar{\xi}} - 1}{e^{\alpha} - 1}$	$\frac{\alpha}{e^{\alpha} - 1}$	α	α^2	$e^{\alpha} - 1$	$(e^{\alpha} - 1)^2$
Hyperbolic Tangent : $1 - \frac{\tanh \alpha(1 - \bar{\xi})}{\tanh \alpha}$	$\frac{2\alpha}{\sinh 2\alpha}$	$2\alpha \tanh \alpha$	$2\alpha^2(3\tanh^2\alpha - 1)$	$2\sinh^2\alpha$	$\frac{1}{2}(3\tanh^2\alpha - 1)\sinh^2 2\alpha$
Hyperbolic Sine : $\frac{\sinh \alpha\bar{\xi}}{\sinh \alpha}$	$\frac{\alpha}{\sinh \alpha}$	0	α^2	0	$\sinh^2\alpha$
Error Function : $1 - \frac{\mathrm{erf}\ \alpha(1 - \bar{\xi})}{\mathrm{erf}\ \alpha}$	$\frac{2}{\sqrt{\pi}} \frac{\alpha e^{-\alpha^2}}{\mathrm{erf}\ \alpha}$	$2\alpha^2$	$2\alpha^2(2\alpha^2 - 1)$	$\sqrt{\pi}\ \alpha e^{\alpha^2} \mathrm{erf}\alpha$	$\frac{\pi}{2}(2\alpha^2 - 1)(e^{\alpha^2} \mathrm{erf}\alpha)^2$
Tangent : $\frac{\tan \alpha\bar{\xi}}{\tan \alpha}$ $(0 \leq \alpha \leq \frac{\pi}{2})$	$\frac{\alpha}{\tan \alpha}$	0	$2\alpha^2$	0	$2\tan^2\alpha$
Arctangent : $1 - \frac{\tan^{-1}\alpha(1 - \bar{\xi})}{\tan^{-1}\alpha}$	$\frac{\alpha}{(1 + \alpha^2)\tan^{-1}\alpha}$	$\frac{2\alpha^2}{1 + \alpha^2}$	$\frac{2\alpha^2(3\alpha^2 - 1)}{(1 + \alpha^2)^2}$	$2\alpha \tan^{-1}\alpha$	$2(3\alpha^2 - 1)(\tan^{-1}\alpha)^2$
Sine : $1 - \frac{\sin \alpha(1 - \bar{\xi})}{\sin \alpha}$ $(0 \leq \alpha \leq \frac{\pi}{2})$	$\frac{\alpha}{\tan \alpha}$	$\alpha \tan \alpha$	α^2	$\tan^2\alpha$	$-\tan^2\alpha$
Log : $1 - \frac{\ln[1 + \alpha(1 - \bar{\xi})]}{\ln(1 + \alpha)}$	$\frac{\alpha}{(1 + \alpha)\ln(1 + \alpha)}$	$\frac{\alpha}{1 + \alpha}$	$\frac{2\alpha^2}{(1 + \alpha)^2}$	$\ln(1 + \alpha)$	$2[\ln(1 + \alpha)]^2$
Inverse Hyperbolic Tangent : $\frac{\tanh^{-1}\alpha\bar{\xi}}{\tanh^{-1}\alpha}$ $(0 \leq \alpha \leq 1)$	$\frac{\alpha}{\tanh^{-1}\alpha}$	0	$2\alpha^2$	0	$2(\tanh^{-1}\alpha)^2$
Quadratic : $\alpha\bar{\xi} + (1 - \alpha)\bar{\xi}^2$ $(0 \leq \alpha \leq 1)$	α	$\frac{2(1 - \alpha)}{\alpha}$	0	$\frac{2(1 - \alpha)}{\alpha^2}$	0

Table 2 Maximum coefficients

	$(L_N^{(2)})_{max}$	$(L_N^{(3)})_{max}$	$(L_S^{(2)})_{max}$	$(L_S^{(3)})_{max}$
Exponential:	same (uniform)	same (uniform)	same $(\bar{\xi} = 0)$	same $(\bar{\xi} = 0)$
Hyperbolic Tangent :	same $(\bar{\xi} = 0)$	same $(\bar{\xi} = 0)$	same $(\bar{\xi} = 0)$	same $(\bar{\xi} = 0)$
Hyperbolic Sine :	$\alpha \tanh \alpha$ $(\bar{\xi} = 1)$	same (uniform)	$\frac{1}{2} \sinh \alpha$ $(\sinh \alpha\bar{\xi} = 1)$	same $(\bar{\xi} = 0)$
Error Function :	same $(\bar{\xi} = 0)$	same $(\bar{\xi} = 0)$	same $(\bar{\xi} = 0)$	same $(\bar{\xi} = 0)$
Tangent :	$2\alpha \tan\alpha$ $(\bar{\xi} = 1)$	$2\alpha^2(3\tan^2\alpha + 1)$	$\tan \alpha$ $(\bar{\xi} = \frac{\pi}{4\alpha})$	$\frac{9}{4} \tan^2\alpha$ $(\tan \alpha\bar{\xi} = \frac{1}{\sqrt{3}})$
Arctangent :	$\frac{\sqrt{3}}{2} \alpha$ $(\bar{\xi} = 1 + \frac{1}{\sqrt{3}\ \alpha})$	$\frac{9}{8} \alpha^2$ $(\bar{\xi} = 1 + \frac{\sqrt{5}}{3} \frac{1}{\alpha})$	same	same
Sine :	same $(\bar{\xi} = 0)$	same (uniform)	same $(\bar{\xi} = 0)$	same $(\bar{\xi} = 0)$
Log :	α $(\bar{\xi} = 1)$	$2\alpha^2$ $(\bar{\xi} = 1)$	same (uniform)	same (uniform)
Inverse Hyperbolic Tangent :	$\frac{2\alpha^2}{1 - \alpha^2}$ $(\bar{\xi} = 1)$	$\frac{2\alpha^2(3\alpha^2 + 1)}{(1 - \alpha^2)^2}$ $(\bar{\xi} = 1)$	$2\alpha \tanh^{-1}\alpha$ $(\bar{\xi} = 1)$	$2(3\alpha^2 + 1)(\tanh^{-1}\alpha)^2$ $(\bar{\xi} = 1)$
Quadratic :	same $(\bar{\xi} = 0)$	same $(\bar{\xi} = 0)$	same $(\bar{\xi} = 0)$	same $(\bar{\xi} = 0)$

NOTE: 'Same' indicates maximum value is same as value at $\bar{\xi} = 0$.

Table 3 Coefficients as minimum spacing approaches zero

	$(L_N^{(2)})_0$	$(L_N^{(3)})_0$	$(L_S^{(2)})_0$	$(L_S^{(3)})_0$	$(L_N^{(2)})_{max}$	$(L_N^{(3)})_{max}$	$(L_S^{(2)})_{max}$	$(L_S^{(3)})_{max}$
Exponential:	$\ell n \frac{1}{NS}$	$(\ell n \frac{1}{NS})^2$	$\frac{1}{NS}$	$(\frac{1}{NS})^2$	same	same	same	same
Hyperbolic Tangent :	$\ell n \frac{1}{NS}$	$(\ell n \frac{1}{NS})^2$	$\frac{1}{NS}$	$(\frac{1}{NS})^2$	same	same	same	same
Hyperbolic Sine :	0	$(\ell n \frac{1}{NS})^2$	0	$(\frac{1}{NS})^2$	$\ell n \frac{1}{NS}$	same	$(\ell n \frac{1}{N})^2$	same
Error Function :	$2\ell n(\frac{1}{NS})$	$4(\ell n \frac{1}{NS})^2$	$\frac{\sqrt{\pi}}{2} \frac{1}{NS}$	$\frac{\pi}{4} (\frac{1}{NS})^2$	same	same	same	same
Tangent :	0	$\frac{\pi^2}{2}$	0	$\frac{\pi^2}{2} (\frac{1}{NS})^2$	$\frac{\pi^2}{2} \frac{1}{NS}$	$\frac{3\pi^4}{8} (\frac{1}{NS})^2$	$\frac{\pi}{2} \frac{1}{NS}$	$\frac{9\pi^2}{16} (\frac{1}{NS})^2$
Arctangent :	2	6	$\frac{2}{NS}$	$6(\frac{1}{NS})^2$	$\frac{\sqrt{3}}{\pi} \frac{1}{NS}$	$\frac{9}{2\pi^2} (\frac{1}{NS})^2$	same	same
Sine :	$\frac{\pi^2}{4} \frac{1}{NS}$	$\frac{\pi^2}{4}$	$\frac{\pi^2}{4} (\frac{1}{NS})^2$	$-\frac{\pi^2}{4} (\frac{1}{NS})^2$	same	same	same	same
Log :	1	2	$\frac{1}{NS}$	$2(\frac{1}{NS})^2$	$e^{\frac{1}{NS}}$	$2(e^{\frac{1}{NS}})^2$	same	same
Inverse Hyperbolic Tangent :	0	$2(1 - NS)$	0	$2(\tanh^{-1}\alpha)^2$	$\frac{2}{NS}$	$8(\frac{1}{NS})^2$	$\frac{2}{NS}$	$8(\frac{1}{NS})^2$
Quadratic:	$\frac{2}{NS}$	0	$2(\frac{1}{NS})^2$	0	same	same	same	same

NOTE: 'same' indicates maximum value is same as value at $\xi = 0$.

Evaluation of particular distribution functions in this approach is based on the quantities of (20). The other approach concerns the behavior of the error as the minimum spacing decreases with a fixed number of points in the field. Distribution functions satisfying the conditions (26) maintain order in this second sense and can be compared on the basis of these quantities. This second sense of order is thus more stringent. The conditions of (26) seem to be unattainable, however,

Conditions equivalent to those given in (20) for comparison of distribution functions were also obtained by Vinokur in [5] from consideration of appropriate length scales in regions of large gradients. (In that analysis the transformed variable, ξ, is normalized to the interval (0, 1) so the number of points in the field does not appear explicitly. The correct interpretation of the results of [5] with the present form of distrifunction is the conditions of (20) and not as given in [2] where the N^{i-1} factor was omitted.)

Evaluation of Distribution Functions

As an example of the application of the measures of order discussed above, ten distribution functions were analysed with specified spacing at $\xi = 0$. The functions and the coefficients discussed above are listed in Tables 1-3, using the following notation:

$$L_N^{(i)} \equiv N^{i-1} \frac{x_{(i)}}{x_\xi} \quad L_S^{(i)} \equiv \frac{x_{(i)}}{x_\xi^i} \quad S \equiv (x_\xi)_0$$

$$\bar{\xi} \equiv \frac{\xi}{N}$$

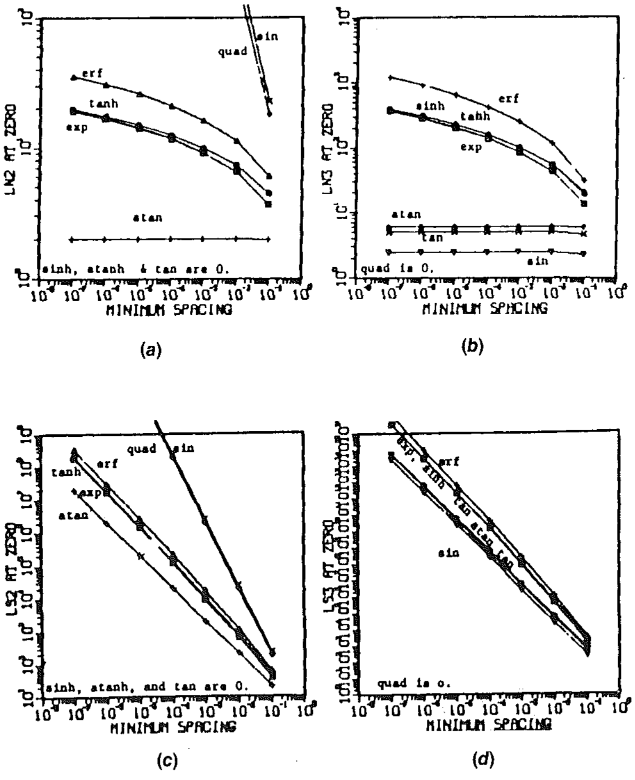

(a) (b)

(c) (d)

Fig. 1 $L_N^{(i)}$ and $L_S^{(i)}$ $\xi (i = 2, 3)$ at point of minimum spacing ($\xi = 0$)

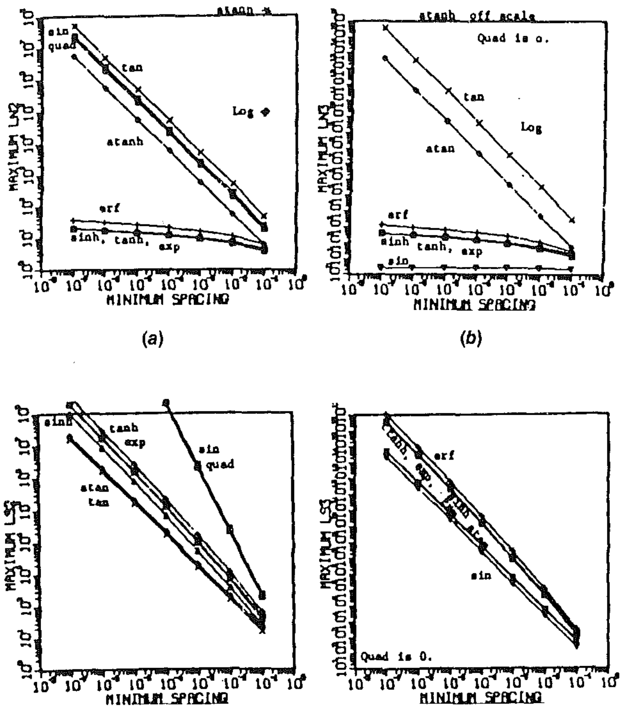

(a) (b)

(c) (d)

Fig. 2 Maximum values of $L_N^{(i)}$ and $L_S^{(i)}$ (i = 2, 3)

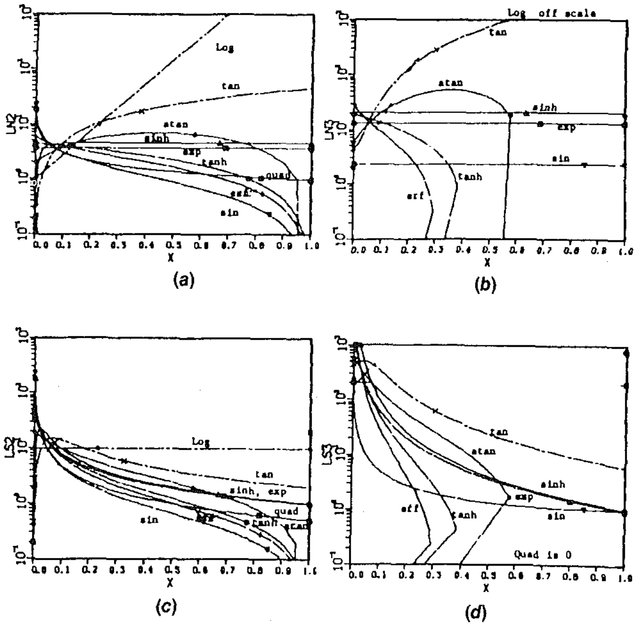

(a) (b)

(c) (d)

Fig. 3 Variations of $L_N^{(i)}$ and $L_S^{(i)}$ over the field for minimum spacing of 10^{-3}

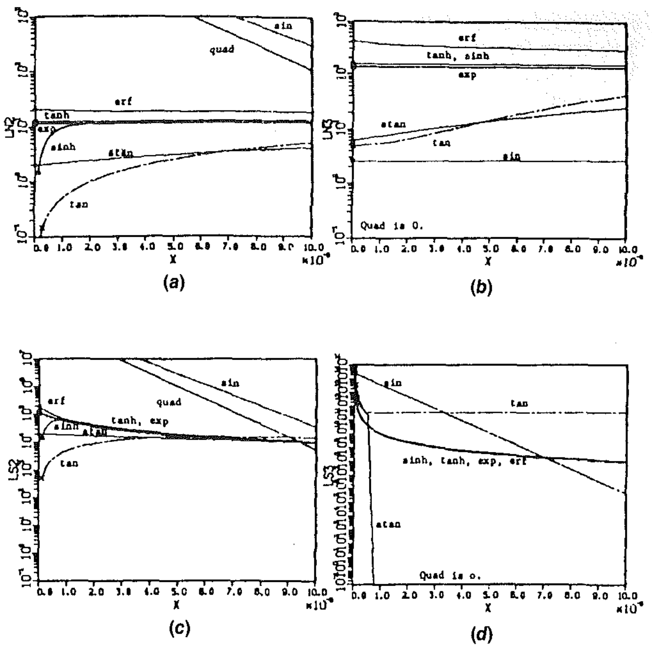

(a) (b)

(c) (d)

Fig. 4 Variation of $L_N^{(i)}$ and $L_S^{(i)}$ (i = 2, 3) near point minimum spacing (ξ = 0) for a minimum spacing of 10^{-6}

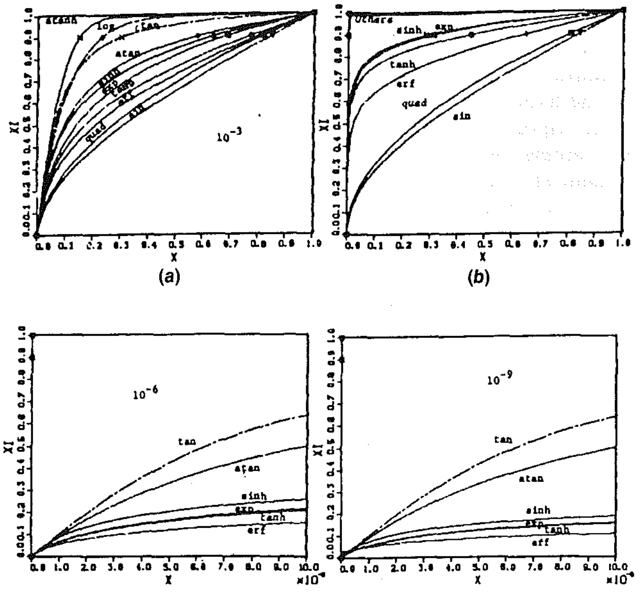

(a) (b)

(c) (d)

Fig. 5 Point distribution

with the subscripts 0 and N indicating evaluation at $\xi = 0$ and N, respectively. The table both the values of the coefficients, L_N and L_S, at the points of minimum spacing, i.e., $\xi = 0$, and the maximum values, together with the location of the maximum. The relation of these coefficients to the produce NS as the minimum spacing S, approaches zero is also given. Plots of the coefficients at $\xi = 0$ and the maximum values of the coefficients against the minimum spacing are given in Figs. 1 and 2. The variation of the coefficients over the field is shown in Figs. 3 and 4. The first of these shows the entire field for a minimum spacing of 10^{-3}, while the second gives detail of the region near the minimum spacing ($\xi = 0$) for a minimum spacing of 10^{-6}. The behavior of the coefficients is qualitatively the same for different values of the minimum spacing. Finally, Fig. 5 shows the variation of ξ with x, i.e., the point distribution, the entire field being shown for minimum spacings of 10^{-3} and 10^{-6}, while detail of the region near the minimum spacing ($\xi = 0$) is shown for minimum spacings of 10^{-6} and 10^{-9}. Here the ordinate, ξ, can also be interpreted as the fraction of the total number of points that fall between $x = 0$ and the local value of x.

From Fig. 5(*b*) it is clear that, of the functions considered here, only the exponential, the hyperbolic sine, the hyperbolic tangent, and the error function are suitable as point distribution functions with very small minimum spacing. The quadratic and sine functions do not actually achieve the specified spacing of 10^{-6}, and the rest of the functions concentrate essentially all of the points at the left boundary. The error function gives the smoothest coverage of the field. The hyperbolic tangent is next in this regard, while the exponential and hyperbolic sine give about the same distributions in most of the field. Of the four suitable functions the hyperbolic sine concentrates more points near the minimum spacing, i.e., the left boundary. This function also gives the most nearly uniform point distribution in the region of high concentration, since the second derivative, and hence $L_N^{(2)}$ and $L_S^{(2)}$, vanishes at $\xi = 0$. This vanishing second derivative also occurs with the tangent and arctangent, but these functions concentrate too many of the points near the left boundary.

The plots of the coefficients over the field, Figs. 3 and 4, show $L_N^{(2)}$ for the hyperbolic sine rising rapidly from zero to quickly level off just above the uniform value for the exponential. The hyperbolic tangent, by contrast, falls from a value close to that at which the hyperbolic sine levels off. The error function starts a bit higher than the hyperbolic tangent but falls faster. All four of these functions give essentially uniform values of the coefficient $L_N^{(2)}$ in the region extending 100 times the minimum spacing from the left boundary, cf. Fig. 4(*a*), except for the initial rise from zero that occurs for the hyperbolic sine in the region extending 10 times the minimum spacing from the boundary. The value that occurs for the error function is about twice that for the others. Outside this boundary layer region near the left boundary, the hyperbolic tangent and the error function drop off to zero, while the exponential and hyperbolic sine remain uniform. Thus the hyperbolic sine has the best behavior very near the minimum spacing, while the error function, followed closely by the hyperbolic tangent, behaves best outside the boundary layer region. The error function is, however, a bit higher than the others within the boundary layer. Note that the exponential, although a suitable distribution function, maintains the uniform value near that from which the hyperbolic tangent drops off, and therefore the exponential is never as good as the hyperbolic tangent in regard to the coefficient $L_N^{(2)}$. The trends for $L_N^{(3)}$ are essentially the same as for $L_N^{(2)}$, except that now the value for the hyperbolic sine is uniform, so that this function has no advantage in regard to $L_N^{(3)}$.

For the coefficient $L_S^{(2)}$, all four functions give very nearly the same values within the boundary layer, except for the rapid initial rise from zero that occurs for the hyperbolic sine and a slightly larger initial value occurring for the error function. Outside the boundary layer the values for the error function and the hyperbolic tangent drop off to zero, the drop being a bit faster for the error function, while the values for the exponential and hyperbolic sine drop off together to a nonzero value. Again the behavior of $L_S^{(3)}$ is qualitatively the same.

It thus appears that the following conclusions can be reached on the basis of these coefficients:

(1) The exponential is not as good as the hyperbolic tangent and therefore should not be used.

(2) The hyperbolic sine is the best function in the lower part of the boundary layer. Otherwise this function is not as good as the hyperbolic tangent.

(3) The error function and the hyperbolic tangent are the best functions outside the boundary layer. Between these two the hyperbolic tangent is the better within the boundary layer, while the error function is the better outside.

(4) The logarithm, sine, tangent, arctangent, inverse hyperbolic tangent, quadratic, and also the inverse hyperbolic sine (not included in Table 1 or the figures) are not suitable.

Figures 1 and 2 show that the variations of both $L_N^{(i)}$ and $L_S^{(i)}$ with the minimum spacing are essentially the same for all four of the suitable functions (except that $L_N^{(2)}$ and $L_S^{(2)}$ at $\xi = 0$ remain zero for the hyperbolid sine). These figures also show that consideration of the vlaues at $\xi = 0$ only would be deceptive, leading incorrectly to preference for the tangent and arctangent, both of which are shown by the other figures to be unsuitable. Finally, Fig. 2 shows that the four suitable functions do in fact preserve order in the sense of variation of truncation error as the number of points in the field increases, since $L_N^{(i)}$ has only small variation with the minimum spacing. The same cannot be said, however, for order in the sense of variation of the error as the minimum spacing decreases with a fixed number of points. In fact, Figs. 2(*c*) and (*d*) show that the logarithmic slope of $L_S^{(i)}$ is near -1 for these functions, and hence the order is strictly only first in this sense (since the $L_S^{(i)}$ are the coefficients of the x_ξ^2 term in the error expansion).

Vinokur [5] considered all of the functions included here, except the exponential, logarithm, and quadratic, and also considered the arcsine, which was found to be unsuitable. As noted above, the anlaysis of that reference is based on the quantities $L_N^{(i)}$. Vinokur also shows how to use a basic distribution function, with specified slope x_ξ at one boundary, to construct a distribution function that allows the slope to be specified at both boundaries. Forms that allow the slope to be specified at an interior point are also given.

Although, as has been shown, all distribution functions maintain order in the formal sense with nonuniform spacing as the number of points in the field is increased. The results obtained for these particular distribution functions show that considerable error can arise with nonuniform spacing in actual applications. Recall that the ratio of the coefficients from the nonuniform spacing in the series (15) to the coefficient arising from spacing itself is given by (22), which with the definitions of $L_S^{(i)}$ gives the following bound for this ratio:

$$\frac{A_{mn}}{A_{2n+1,n}}\;\frac{\dfrac{d^m f}{dx^m}}{\dfrac{d^{2n+1}f}{dx^{2n+1}}} \le C_m\;\frac{\dfrac{d^m f}{dx^m}}{\dfrac{d^{2n+1}f}{dx^{2n+1}}}\;\prod_{i=2}^{2n+1}\,(L_S^{(i)})^{a_{im}} \qquad (27)$$

The $n=1$ term then yields, for the coefficients involved in the leading term of the series (15):

$$\frac{A_{13}}{A_{31}}\;\frac{f_x}{f_{xxx}} = L_S^{(3)}\;\frac{f_x}{f_{xxx}},\quad \frac{A_{23}}{A_{31}}\;\frac{f_{xx}}{f_{xxx}} = 3L_S^{(2)}\;\frac{f_{xx}}{f_{xxx}} \qquad (28)$$

Now a typical case involving a boundary layer might have 100 points with a minimum spacing of 10^{-6} relative to a maximum field extent of unity. Thus $N = 10^2$, $S = 10^{-6}$, and $NS = 10^{-4}$. Then for

$$L_S^{(i)} \cong \left(\frac{1}{NS}\right)^{i-1}$$

as for the best of the functions considered, we have

$$L_S^{(2)} = 10^4, L_S^{(3)} = 10^8$$

and then the ratios of the error from the nonuniform spacing to that which arises from the spacing itself are, approximately

$$10^8\,\frac{f_x}{f_{xxx}} \quad \text{and} \quad 10^4\,\frac{f_x}{f_{xxx}}$$

Since the error term from the spacing here is $S^2 f_{xxx} = 10^{-12} f_{xxx}$, the error terms due to the nonuniform spacing are

$$10^{-4} f_x \quad \text{and} \quad 10^{-8} f_{xx}$$

as compared with $10^{-12} f_{xxx}$ due to the spacing. Now for the same number of points with uniform spacing we would have a spacing of 10^{-2} and an error of $10^{-4} f_{xxx}$. Thus the error due to the nonuniform spacing in this case is well below what would occur on a uniform grid with the same number of points, except for the f_x term. (It will be shown below that this term can be eliminated from the truncation error by evaluating the coordinate derivatives numerically rather than analytically.)

This example shows that the contributions to the error from the nonuniform spacing are significant and must be considered. While the contribution form the spacing itself decreases with the spacing, the contributions from the nonuniform spacing increase as the spacing decreases for very small spacings.

Effect of Numerical Metric Coefficients

All of the above considerations have assumed that the derivatives of x with respect to ξ are evaluated exactly. If the coordinate derivative, x_ξ, in the difference expression (5) is evaluated numerically by the same central difference expression used for f we have, in place of (5):

$$f_x = \frac{f_{i+1} - f_{i-1}}{x_{i+1} - x_{i-1}} + T_x' \tag{29}$$

With x expanded in Taylor series we have

$$x_{i+1} - x_{i-1} = 2x_\xi + 2 \sum_{n=1}^{\infty} \frac{x_{(2n+1)}}{(2n+1)!} \tag{30}$$

Using this and (5) in (29) we then have

$$f_x = \frac{f_x - T_x}{1 + \dfrac{1}{x_\xi} \displaystyle\sum_{n=1}^{\infty} \frac{x_{(2n+1)}}{(2n+1)!}} + T_x' \tag{31}$$

Now the f_x term of T_x corresponds to $m = 1$ in (15):

$$-\sum_{n=1}^{\infty} \frac{A_{1n}}{(2n+1)!N^{2n}}$$

and by (16),

$$A_{1n} = \frac{C_1}{D_1} \sum_{i=1}^{2n+1} D_i^{a_{i1}}$$

But $C_1 = 1$ and $a_{i1} = \delta_{i,2n+1}$, as given above, so that, using (14),

$$A_{1n} = \frac{D_{2n+1}}{D_1} = \frac{N^{2n} x_{(2n+1)}}{x_\xi}$$

Then the coefficient of f_x in T_x is

$$-\frac{1}{x_\xi} \sum_{n=1}^{\infty} \frac{x_{(2n+1)}}{(2n+1)!}$$

and, for use in (31), we have

$$f_x - T_x = f_x \left(1 + \frac{1}{x_\xi} \sum_{n=1}^{\infty} \frac{x_{(2n+1)}}{(2n+1)!}\right) + \sum_{n=1}^{\infty} \frac{1}{(2n+1)!N^{2n}} \sum_{m=2}^{2n+1} A_{mn} \frac{d^m f}{dx^m}$$

But the coefficient of f_x on the right here is exactly the denominator in (31), so that, using (14) in this denominator, we have the following expression for the truncation error in the difference representation (29):

$$T_x' = -\frac{\displaystyle\sum_{n=1}^{\infty} \frac{1}{(2n+1)!N^{2n}} \sum_{m=2}^{2n+1} A_{mn} \frac{d^m f}{dx^m}}{1 + \dfrac{1}{D_1} \displaystyle\sum_{n=1}^{\infty} \frac{D_{2n+1}}{(2n+1)!N^{2n}}} \tag{32}$$

The lead term of the error then is

$$T_x' = -\frac{1}{6N^2} \sum_{m=2}^{3} A_{m1} \frac{d^m f}{dx^m}$$

which is the same as (17), except that the lower limit of m is 2 in the present case. This can finally be written as

$$T_x' = -\frac{1}{2} x_{\xi\xi} f_{xx} - \frac{1}{6} x_\xi^2 f_{xxx} \tag{33}$$

Thus the use of numerical evaluation of the coordinate derivative, rather than exact analytical evaluation, eliminates the f_x term from the truncation error. Since this term is the most troublesome part of the error, being dependent on the derivative being represented, it is clear that numerical evaluation of the metric coefficients *by the same difference representation used for the function* whose derivative is being represented is preferable to exact analytical evaluation. It should be understood that there is not incentive, per se, for accuracy in the metric coefficients, since the object is simply to represent a discrete solution accurately, not to represent the solution on some particular coordinate system. The only reason for using any function at all to define the point distribution is to ensure a smooth distribution. There is no reason that the representations of the coordinate derivatives have to be accurate representatives of the analytical derivatives of that particular distribution function.

Two-Dimensions. The two-dimensional transformation of the first derivative is given by

$$f_x = \frac{1}{J}(y_\eta f_\xi - y_\xi f_\eta) \tag{34}$$

where the Jacobian of the transformation is

$$J = x_\xi y_\eta - x_\eta y_\xi$$

With two-point central difference representations for all derivatives, we have

$$f_x = \frac{\delta_\eta y \delta_\xi f - \delta_\xi y \delta_\eta f}{\delta_\xi x \delta_\eta y - \delta_\eta x \delta_\xi y} + T_x \tag{35}$$

where

$$\delta_\xi f \equiv f_{i+1,j} - f_{i-1,j} \qquad \delta_\eta f \equiv f_{i,j+1} - f_{i,j-1}$$

and T_x is the truncation error. After expansion of all quantities in Taylor series about the central point and considerable algebraic manipulation, we have for the leading term of the truncation error

$$\begin{aligned} T_x = {} & \frac{1}{2J}(y_\xi x_\eta x_{\eta\eta} - x_\xi y_\eta x_{\xi\xi}) f_{xx} \\ & + \frac{1}{2J}(y_\xi y_\eta)(y_{\eta\eta} - y_{\xi\xi}) f_{yy} \\ & + \frac{1}{2J}[y_\xi y_\eta (x_{\eta\eta} - x_{\xi\xi}) + x_\eta y_\xi y_{\eta\eta} - x_\xi y_\eta y_{\xi\xi}] f_{xy} \\ & + \text{second-order terms in the spacing} \end{aligned} \tag{36}$$

where the coordinate derivatives are understood to represent central differences expressions, e.g.,

$$x_\xi = \frac{1}{2}(x_{i+1,j} - x_{i-1,j}), x_\eta = \frac{1}{2}(x_{i,j+1} - x_{i,j-1})$$

$$x_{\xi\xi} = x_{i+1,j} - 2x_{ij} + x_{i-1,j}$$

$$x_{\eta\eta} = x_{i,j+1} - 2x_{ij} + x_{i,j-1}$$

These contributions to the truncation error arise from the nonuniform spacing. The familiar terms proportional to a power of the spacing occur in addition to these terms as noted.

Sufficient conditions can be stated for maintaining the order of the difference representations. First of all, as in the one-dimensional case, the ratios

$$\frac{x_{\xi\xi}}{x_\xi^2}, \frac{y_{\xi\xi}}{y_\xi^2}, \frac{x_{\eta\eta}}{x_\eta^2}, \frac{y_{\eta\eta}}{y_\eta^2}$$

must be bounded as x_ξ, x_η, y_ξ, y_η approach zero. A second condition must be imposed which limits the rate at which the Jacobian approaches zero. This condition can be met by simply requiring that $\cot\theta$ remain bounded, where θ is the angle between the ξ and η coordinate lines. The fact that this bound on the nonorthogonality imposes the correct lower bound on the Jacobian follows from the fact that

$$|\cot\theta| \leq M \tag{37}$$

implies

$$J^2 \geq \frac{1}{M^2+1}\left[x_\xi^2 x_\eta^2 + x_\xi^2 y_\eta^2 + x_\eta^2 y_\xi^2 + y_\xi^2 y_\eta^2\right].$$

With these conditions on the ratios of second to first derivatives, and the limit on the nonrothogonality satisfied, the order of the first derivative approximations is maintained in the sense that the contributions to the truncation error arising from the nonuniform spacing will be second-order terms in the grid spacing.

The truncation error terms for second derivatives that are introduced when using a curvilinear coordinate system are very lengthy and involve both second and third derivatives of the function f. However, it can be shown the same sufficient conditions, together with the condition that

$$\frac{x_{\xi\eta}}{x_\xi x_\eta} \quad \text{and} \quad \frac{y_{\xi\eta}}{y_\xi y_\eta}$$

remain bounded, will insure that the order of the difference representations is maintained.

It was noted above that a limit on the nonorthogonality, imposed by (37), is reuired for maintaining the order of difference representations. The degree to which nonorthogonality effects truncation error can be stated more precisely. The truncation error for a first derivative f_x can be written

$$T_x = \frac{1}{J}\left(y_\eta T_\xi - y_\xi T_\eta\right)$$

where T_ξ and T_η are the truncation errors for the difference expressions f_ξ and f_η. Now all coordinate derivatives can be expressed using direction cosines of the angles of inclination, ϕ_ξ and ϕ_η of the ξ and η coordinate lines. After some simplification, the truncation error has the form

$$T_x = \frac{1}{\sin(\phi_\eta - \phi_\xi)}\left(\sin\phi_\eta \cos\phi_\xi \frac{T_\xi}{x_\xi} - \sin\phi_\xi \cos\phi_\eta \frac{T_\eta}{x_\eta}\right) \tag{38}$$

Therefore the truncation error, in general, varies inversely with the sine of the angle between the coordinate lines. Note that there is also a dependence on the direction of the coordinate lines. To further clarify the effect of nonorthogonality, the following example is included. For simplicity, only the truncation error terms arising from nonuniform spacing are considered.

The contribution from nonorthogonality can be isolated by considering the case of skewed parallel lines with $x_\eta = x_{\eta\eta} = x_{\xi\eta} = y_{\xi\xi} = y_{\xi\eta} = 0$

Here (36) reduces to

$$T_x = -\frac{1}{2} x_{\xi\xi} f_{xx} + \frac{1}{2}\left(\frac{y_\xi}{x_\xi}\right) y_{\eta\eta} f_{yy} - \frac{1}{2}\left(\frac{y_\xi}{x_\xi}\right) x_{\xi\xi} f_{xy}$$

Since $\cot\theta = (y_\xi / x_\xi)$, this may be written

$$T_x = -\frac{1}{2} x_{\xi\xi} f_{xx} + \frac{1}{2}\left(y_{\eta\eta} f_{yy} - x_{\xi\xi} f_{xy}\right)\cot\theta \tag{39}$$

The first term occurs even on an orthogonal system and corresponds to the first term in (33). The last two terms arise from the departure from orthogonality. For $\theta \leq 45$ deg, these terms are no greater than those from the nonuniform spacing. Reasonable departure from orhtogonality is therefore of little concern when the rate-of-change of grid spacing is reasonable. Large departure from orthogonality may be more of a problem at boundaries, where one-sided difference expressions are needed. Therefore, grids should probably be made as nearly orthogonal at the boundries as is practical. Note that the contribution from nonorthogonality vanishes on a skewed uniform grid.

References

1 Thompson, J. F., Warsi, Z. U. A., and Mastin, C. W., "Boundary-Fitted Coordinate Systems for Numerical Solution of Partial Differential Equations—A Review," *Journal of Computational Physics*, Vol. 47, 1982, pp. 1-108.

2 Thompson, J. F., "A Survey of Grid Generation Techniques in Computational Fluid Dynamics," AIAA-83-0447, AIAA 21st Aerospace Sciences Meeting, Reno (1982).

3 Thompson, J. F., ed., *Numerical Grid Generation*, North-Holland, 1982.

4 Hoffman, J. D., "Relationship between the Truncation Errors of Centered Finite-Difference Approximation on Uniform and Nonuniform Meshes," *Journal of Computational Physics*, Vol. 46, 1982, pp. 469-474.

5 Vinokur, Marcel, "On One-Dimensional Stretch-functions for Finite-Difference Calculations," NASA CR 3313, Ames Research Center, 1980.

6 Mastin, C. W., "Error Induced by Coordinate Systems," in *Numerical Grid Generation*, J. F. Thompson, (ed.) North Holland, 1982.

7 Mastin, C. W., and Thompson, J. F., "Adaptive Grids Generated by Elliptic Systems," AIAA Paper No. 83-0451, AIAA 21st Aerospace Sciences Meeting, Reno, Nevada, January 1983.

R. P. Taylor
Assistant Professor.
Mem. ASME

H. W. Coleman
Professor.
Mem. ASME

B. K. Hodge
Professor.
Mem. ASME

Mechanical and Nuclear
Engineering Department,
Mississippi State University,
Mississippi State, MS 39762

Prediction of Turbulent Rough-Wall Skin Friction Using a Discrete Element Approach

A discrete element model for turbulent flow over rough surfaces has been derived from basic principles. This formulation includes surface roughness form drag and blockage effects as a constituent part of the partial differential equations and does not rely on a single-length-scale concept such as equivalent sandgrain roughness. The roughness model includes the necessary empirical information on the interaction between three-dimensional roughness elements and the flow in a general way which does not require experimental data on each specific surface. This empirical input was determined using data from well-accepted experiments. Predictions using the model are compared with additional data for fully-developed and boundary layer flows. The predictions are shown to compare equally well with both transitionally rough and fully rough turbulent flows without modification of the roughness model.

Introduction

Skin friction can be significantly larger for turbulent flow over a rough surface as compared with an equivalent turbulent flow over a smooth surface. Many systems of engineering interest, such as re-entry vehicles, missiles, aircraft, ships, turbines, heat exchangers, piping networks and atmospheric flows, have surfaces which are often rough in the aerodynamic sense. Therefore, there is significant interest in accurate predictive models for turbulent flows over rough surfaces.

In turbulent flow analysis, use of time-averaged equations leads to the necessity of formulating a turbulence model with empirical input to achieve closure. A similar situation exists in analysis of flow over rough surfaces. Unless the equations can be solved on a grid which is fine enough to resolve the surface roughness geometry, a roughness model with empirical input is necessary.

There are two general approaches which have been used in formulating the required roughness models—the classic equivalent sandgrain roughness approach and the discrete element approach. Both of these are discussed in detail by the authors in reference [1]. A brief summary is presented below.

Equivalent Sandgrain Roughness Approach. Schlichting [2] first proposed the equivalent sandgrain roughness (k_s) concept and experimentally determined k_s for a variety of rough surfaces. He defined k_s as the size of sandgrain in Nikuradse's [3] pipe flow experiment which would give the same skin friction as that observed on a particular rough surface. One problem in using this approach is determining k_s for a specific surface of interest when no skin friction data are available for that surface. Dvorak [4], Simpson [5] and Dirling [6] all presented correlations which essentially allowed k_s to be determined based on various geometric characteristics of the roughness elements on the surface. These correlations suffer from two basic problems: (1) they do not correlate the available data well, and (2) they rely primarily on Schilchting's experimental results. The authors [7] have shown that, due to erroneous assumptions in data reduction, Schlichting's results for skin friction are high by amounts ranging up to 73 percent and his results for k_s are high by 26 to 555 percent. In addition, the idea that the effects of all surface roughnesses can be modeled using a single length scale (k_s) has not been successful in application [1].

The equivalent sandgrain roughness concept has been used in predictive modeling through algebraic correlations, integral methods, and differential (finite difference) methods. Typical of the differential methods are those of Healzer [8], Cebeci and Chang [9], and Ligrani [10].

Discrete Element Approach. In the discrete element approach, the effects of a collection of individual roughness elements on the flow are generally considered by including a form drag term in the momentum equation and accounting for the blockage effect of the roughness elements on the flow.

In the same paper [2] in which Schlichting introduced the equivalent sandgrain roughness approach, he proposed that the flow resistance of a rough surface be divided into two components—that due to the form drag on the roughness elements and that due to the viscous shear on the smooth surface area between the roughness elements. He used these ideas in a brief, simple analysis of some of his experimental data, but evidently carried the idea no further. Later, Liepmann and Goddard [11] took this viewpont, as did Lewis [12]. Adams and Hodge [13] used a form drag term coupled with a turbulence model which depended on k_s, while Lin and Bywater [14] included both roughness element form drag and

---

Contributed by the Fluids Engineering Division of THE AMERICAN SOCIETY OF MECHANICAL ENGINEERS and presented at the Fluids Engineering Conference, Albuquerque, N. Mex., June 24–26, 1985. Manuscript received by the Fluids Engineering Division, May 9, 1984. Paper No. 85-FE-2.

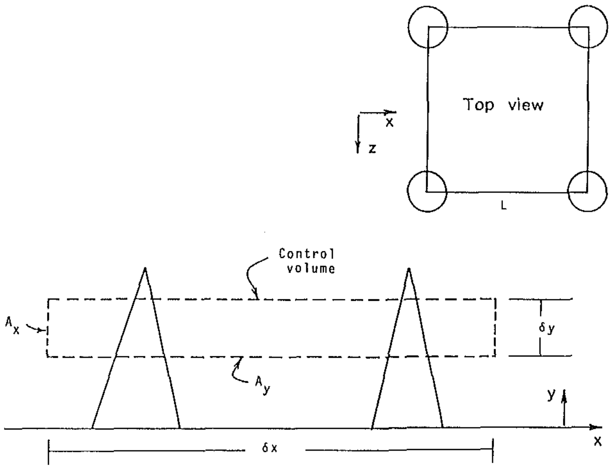

Fig. 1 Control volume for flow over a rough surface

blockage effects combined with turbulence models which depended on k_s.

Finson and his co-workers [15, 16, 17] presented results using a discrete element approach coupled with a turbulence model which contained no sandgrain roughness dependence. The earliest work [15] did not include the blockage phenomenon. The later works [16, 17] included both blockage and form drag effects. In their approach, the blockage factors were applied somewhat inconsistently in the equations, with blockage factors considered functions of y in some terms and not in others. An incorrect formulation of the blockage in yz planes was used, with the maximum blockage rather than an x-direction averaged blockage appearing in the model.

Christoph and Pletcher [18] and Christoph [19] used Finson's discrete element model, but included additional roughness effects in a mixing length turbulence model. The equation used for determining skin friction coefficient contained blockage effects in a manner inconsistent with the usage in the differential equations. That is, the expression for C_f which would be obtained by integrating the differential equation across the boundary layer is not consistent with the equation actually used to determine C_f.

In the discrete element approaches discussed above [13-19], the roughness models were formulated by adding terms to equations and multiplying various terms in the equations by factors determined in an ad hoc manner. In addition, the calibration of the roughness element form drag model was based primarily on Schlichting's skin friction data [2] as originally reported, which has been shown [7] to be high by amounts ranging up to 73 percent.

The Discrete Element Roughness Model

The discrete element model presented in this article is formulated for roughness elements with three-dimensional shapes (as opposed to transverse ribs, for example) for which the element cross-section can be approximated as circular at every height, y. The physical effects of roughness on the flow field are modeled by considering the blockage effect of the roughness elements and the drag forces which the roughness elements exert on the fluid. In the following, attention is restricted to roughness elements of uniform shape and spacing. Formulations for the case of general three-dimensional elements of random shape, height and spacing are presented in the Appendix.

Derivation of the Differential Equations. The differential equations including roughness effects are derived by applying the basic conservation statements for mass and momentum to a control volume (CV) such as that shown in Fig. 1. This CV is shown with an exaggerated length, δx, in the primary flow direction as an aid in correctly formulating the roughness effects. The CV includes all the fluid in the volume and, as shown, is penetrated by solid roughness elements.

Basic to this approach is the idea that the two-dimensional, time-averaged turbulent boundary layer equations can be applied in the flow region below the crests of the roughness elements. Therefore, the flow variables must be viewed as having been averaged over the transverse (z) direction and averaged in the longitudinal (x) direction over an appropriate x distance.

The physical effects of the roughness elements on the flow field are modeled by considering the flow blockage and by postulating that the total force of the elements on the flow can be incorporated as a drag force. As is evident in Fig. 1, the areas available for mass and momentum transport in the yz-plane (A_x) and the xz-plane (A_y) are decreased by the presence of the roughness elements. The areas on which shear stresses and pressures act are decreased in the same manner. This blockage effect is included using blockage factors β_x and β_y, which are defined as the fraction of the area open for flow through the yz and xz planes, respectively. Note that in the most general case the blockage factors are functions of x and y.

Nomenclature

A_p = projected area of a roughness element segment
A_x = area in yz-plane open to flow; Fig. 1
A_y = area in xz-plane open to flow; Fig. 1
C_D = roughess element drag coefficient defined in equation (1)
C_f = skin friction coefficient defined in equation (7)
d = local roughness element diameter
F_D = local drag force due to a roughness element
k = roughness element height
k_s = equivalent sandgrain roughness
l = roughness element spacing in z-direction; Fig. 1
l_m = Prandtl mixing length
L = roughness element spacing in x-direction; Fig. 1
P = pressure
Re = Reynolds number
R_τ = shear stress ratio; equation (14)
u = velocity component in x-direction
U = time mean value of u
u' = turbulent fluctuating value of u
u^* = friction velocity; $\sqrt{\tau_T/\rho}$
U_e = boundary layer edge velocity
U_∞ = free stream velocity
v = velocity component in y-direction
V = time mean value of v
v' = turbulent fluctuating value of v
x = streamwise coordinate; Fig. 1
y = coordinate normal to surface; Fig. 1
y^+ = nondimensional y; yu^*/ν
z = transverse coordinate; Fig. 1
β_x = blockage factor for yz-surface
β_y = blockage factor for xz-surface
δ = boundary layer thickness
δx = control volume dimension; Fig. 1
δy = control volume dimension; Fig. 1
μ = dynamic viscosity of fluid
ν = kimematic viscosity of fluid
ρ = density of fluid
τ = shear stress
τ_r = apparent surface shear stress due to roughness
τ_s = shear stress on smooth portion of surface
τ_T = total apparent surface shear stress; $\tau_r + \tau_s$

The drag force F_D is most conveniently handled by using a drag coefficient defined by

$$C_D = \frac{F_D}{\frac{1}{2}\rho u^2 A_p} \tag{1}$$

where A_p is the projected area of the slice of a roughness element penetrating the CV. Thus the drag force on the CV due to portion of a single element penetrating the CV is

$$F_D = \frac{1}{2}\rho u^2(y) C_D d(y)\,\delta y \tag{2}$$

The number of roughness elements per unit area of the xz plane is $1/(lL)$.

Using the above ideas, applying the conservation of mass and momentum statements to the CV in Fig. 1 and incorporating the boundary layer assumptions, the continuity and momentum equations for a steady (Reynolds-averaged), two-dimensional turbulent boundary layer are

$$\frac{\partial}{\partial x}(\rho\beta_x U) + \frac{\partial}{\partial y}(\rho\beta_y V) = 0 \tag{3}$$

and

$$\begin{aligned}\beta_x\rho U\frac{\partial U}{\partial x} + \beta_y\rho V\frac{\partial U}{\partial y} = &-\frac{\partial}{\partial x}(\beta_x P) \\ &+ \frac{\partial}{\partial y}\left[\beta_y\left(\mu\frac{\partial U}{\partial y} - \overline{\rho u'v'}\right)\right] \\ &- \frac{1}{2}\rho C_D d(y)\frac{U^2}{Ll}\left(1 + \frac{\overline{u'^2}}{U^2}\right)\end{aligned} \tag{4}$$

Examination of equation (4) shows that empirical models for $-\overline{\rho u'v'}$, $\overline{u'^2}$ and C_D are necessary for closure.

The parameters β_x, β_y and $d(y)$ are determined solely from the roughness element geometry and require no empirical input. For uniform arrays the cross-sectional diameter, $d(y)$, is the same for all of the elements at a given y-location. Determination of $d(y)$ is then simply a matter of considering the geometry of a single element. It can be seen by inspection of Fig. 1 that β_y is given by

$$\beta_y = 1 - \frac{\pi d^2}{4Ll} \tag{5}$$

On initial inspection, β_x appears to be $(1 - d/l)$. In fact, this has been the conclusion of other workers [15-19]. However, this is the maximum blockage. A better formulation is obtained by taking an average of the yz-plane blockage over a length corresponding to a multiple of the average x-direction roughness spacing. This average gives [1]

$$\beta_x = 1 - \frac{\pi d^2}{4Ll} \tag{6}$$

It is thus seen that $\beta_x = \beta_y$, which holds for any array of elements with circular cross-sections.

The boundary conditions for the discrete element approach for rough wall flows are identical to those for smooth wall flows. This is an advantage over typical equivalent sandgrain roughness approaches, in which attempts to interface k_s-based models with finite difference methods result in an ill-defined boundary condition [9]. The wall location ($y = 0$) is the smooth surface on which the roughness elements occur. (An exception to this is the case of spherical roughness elements packed in the most dense array. This special case is discussed in a following section.) At $y = 0$, all velocities go to zero, and as $y \to \infty$, $U \to U_\infty$.

The "wall shear stress" is defined as the sum of the shear and drag forces on the wall in the mean flow direction divided by the plan area of the wall. The corresponding skin friction coefficient is then

$$C_f = \frac{(\beta_y)_w \mu \left.\frac{\partial U}{\partial y}\right|_w + \frac{1}{2}\frac{1}{Ll}\int_0^\infty (\rho d C_D U^2)\,dy}{\frac{1}{2}\rho_\infty U^2{}_\infty} \tag{7}$$

Solution of the Equations. In order to solve equations (3) and (4), turbulence models for $-\overline{\rho u'v'}$ and $\overline{u'^2}$ and a roughness model for C_D are required. After consideration of the data base available for calibration of the roughness model and typical magnitudes of the turbulence intensity factor in the drag force term, the authors elected to include the $[1 + (\overline{u'^2}/U^2)]$ factor in the drag coefficient, C_D. Once such models were formulated in this study, the equations were transformed using a modified Illingsworth transformation. The transformed equations were then solved using an iterative, marching, implicit finite difference technique. Details of this procedure are presented in reference [1].

The Prandtl mixing length model with van Driest damping was used for closure. It is given by

$$-\overline{\rho u'v'} = \rho l_m{}^2\left(\frac{\partial U}{\partial y}\right)\left|\frac{\partial U}{\partial y}\right| \tag{8}$$

where

$$l_m = 0.40y[1 - \exp(-y^+/26)];\quad l_m < 0.09\delta \tag{9}$$

$$l_m = 0.09\delta \text{ otherwise.} \tag{10}$$

This model was not modified to include roughness effects since the physical effects of the roughness on the flow are included explicitly in the differential equations. In addition, both Pimenta [20] and Coleman [21] showed that, nondimensionally, the Reynolds stress distribution in turbulent boundary layers is the same for both smooth and rough surfaces.

The present authors, as did Lin and Bywater [14], have chosen to formulate the C_D model as a function of the local element Reynolds number

$$\text{Re}_d = u(y)d(y)/\nu \tag{11}$$

which includes roughness element size and shape information through $d(y)$. Some workers [15-19] have assumed a constant C_D value of 0.5 or 0.6, but this has never given satisfactory agreement with the data for the various shapes of roughness elements (spherical, spherical segment and conical) reported in the comprehensive experiment of Schlichting [2].

The data sets chosen for calibration of the model were the corrected [7] data of Schlichting [2] for surfaces with roughness elements of spherical, spherical segment and conical shapes and at various spacings. As discussed in reference [1], various functions $C_D(\text{Re}_d)$ were tested and compared with all of the Schlichting data mentioned above except for the case with spherical roughness elements packed in the most dense array. The general shape of the drag coefficient versus Reynolds number curves for flow past transverse cylinders was used as a starting point. The model which gave the best overall agreement between calculations and data was found to be

$$\begin{aligned}\log C_D &= -0.125\log(\text{Re}_d) + 0.375 && \text{Re}_d < 6\times10^4 \\ C_D &= 0.6 && \text{Re}_d \geq 6\times10^4\end{aligned} \tag{12}$$

This model is shown in Fig. 2.

The C_D model has been verified by comparisons with data for roughness element Reynolds numbers up to Re_d = 25,000. Equation (12) and Fig. 2 show an indicated

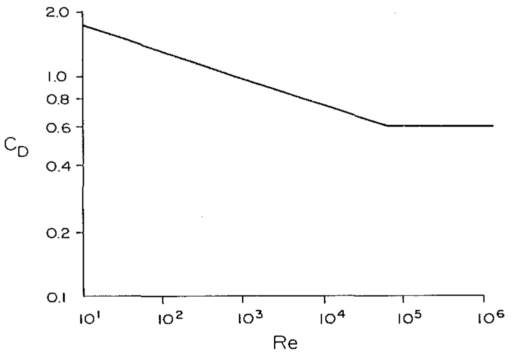

Fig. 2 Roughness element drag coefficient model

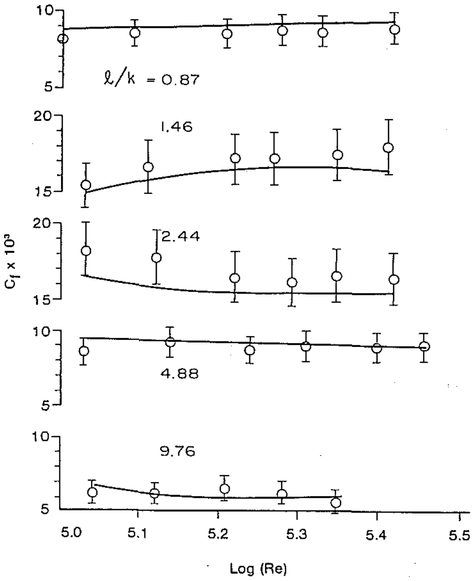

Fig. 3 Comparison of calculations with corrected skin friction data of Schlichting for spherical roughness elements (fully developed channel flow)

(proposed) relationship for Reynolds numbers greater than this value.

For the surface composed of spheres packed in the most dense array, special treatment is necessary. The flow evidently "sees" an apparent wall location well above the plane of the equators of the spheres due to the almost total flow blockage below this plane. The C_D model above was used in calculations with various assumed wall ($y = 0$) locations. After comparing these calculations with the experimental data, it was determined that the most appropriate wall location for the case of spheres in the most dense array is 0.2 D below the crests of the spheres, where D is the sphere diameter.

Comparison of Predictions with Experimental Data

Comparison of calculations using the discrete element model with Schlichting's corrected data (which were used to calibrate the model) are shown in Figs. 3, 4 and 5 for the surfaces with spherical elements of 0.41 cm diameter, spherical segment elements and conical elements, respectively. Schlichting's experiment utilized fully developed channel flow, but no average velocities were reported. The reference velocities used in C_f and Re are the reported maximum velocity values in the channel, and the reference length used in Re is the channel height. The uncertainty bands in Figs. 3, 4, and 5 represent ± 10 percent about the corrected data.

The discrete element method has been used for prediction of additional turbulent flows over rough surfaces for which

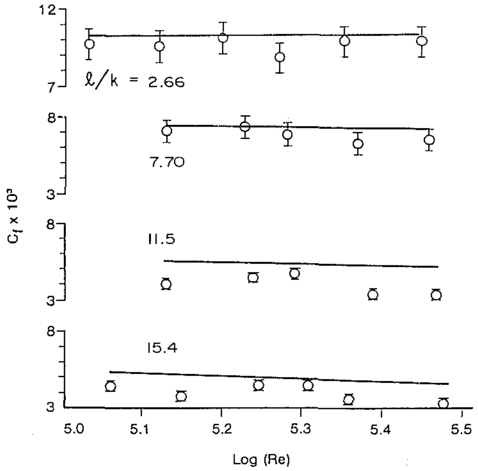

Fig. 4 Comparison of calculations with corrected skin friction data of Schlichting for spherical segment roughness elements (fully developed channel flow)

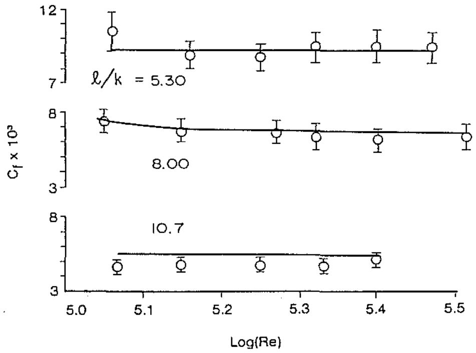

Fig. 5 Comparison of calculations with corrected skin friction data of Schlichting for conical segment roughness elements (fully developed channel flow)

experimental data are available. It should be emphasized that the discrete element model as described previously has remained invariant for all subsequent calculations. No empirical information is used for any specific rough surface—only the geometrical description of the roughness is input for "new" surfaces with three-dimensional type roughness.

Fully Developed Flows. Chen [22] reported detailed turbulence and skin friction measurements for fully developed air flow through a 0.19 meter diameter pipe roughened with hemispheres. He investigated three roughness densities—l/k = 18.5, 10.7, and 6.4, where k is the maximum roughness element height. Chen stated that the first two cases (l/k = 18.5 and 10.7) were in the transitionally rough regime and the third (l/k = 6.4) was "nearly" in the fully rough regime. One of the more interesting parts of Chen's work was the segregation of the two components of the apparent wall shear stress: (1) that due to the viscous shear (τ_s) on the smooth surface between the roughness elements, and (2) that due to the form drag on the roughness elements. Chen obtained the form drag term by measuring the force on a single element using a force balance. The portion due to the smooth surface was determined by subtracting the roughness element drag component from the total wall shear stress (τ_T), which was determined from pressure drop measurements.

The discrete element model was solved in the appropriate internal circular coordinates and the resulting predictions were compared with Chen's data. Figure 6 shows the comparisons for the skin friction coefficient and the ratio of the smooth wall component to the total shear stress. The comparisons indicate very good agreement. The comparison of

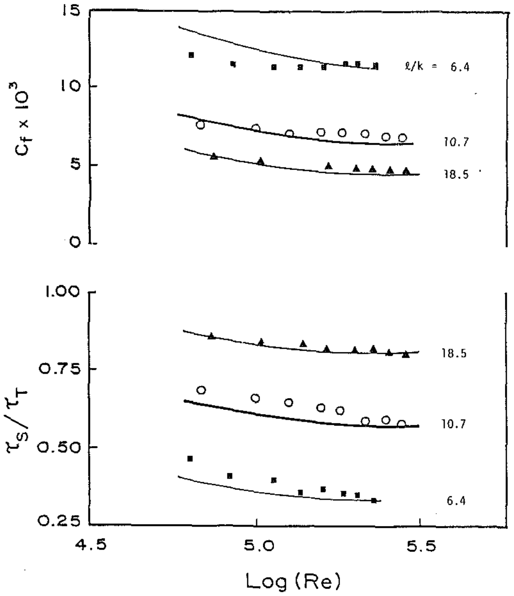

Fig. 6 Comparison of predictions with the skin friction data of Chen—hemispherical roughess elements in fully developed pipe flow

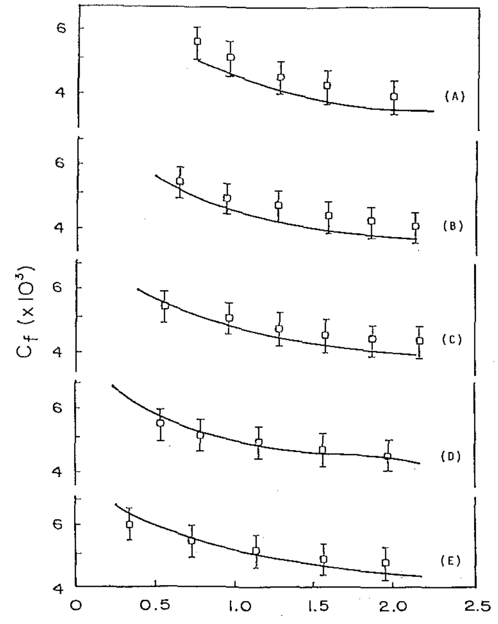

Fig 7 Comparison of predictions with zero pressure gradient Stanford skin friction data: (*a*) Healzer, U_∞ = 9.8 m/s; (*b*) Pimenta, U_∞ = 15.8 m/s, (*c*) Pimenta, U_∞ = 27 m/s; (*d*) Healzer, U_∞ = 58 m/s; (*e*) Healzer, U_∞ = 74 m/s. ((*a*) and (*b*), transitionally rough; (*c*), (*d*), and (*e*), fully rough).

the relative contribution of viscous shear forces between the elements and the drag on the elements are of particular interest. One of the major advantages of the discrete element model is that these two forces and their interactions are accounted for in the model. Inspection of Fig. 6 reveals good agreement between the predictions and data for τ_S/τ_T. The maximum disagreement is about 12 percent, and the preponderance of the points agree within 5 percent. This agreement indicates that the present discrete element model correctly incorporates much of the physics of the interaction between the roughness elements and the flow.

Boundary Layer Flows. The most detailed data sets for boundary layer flows over a well-defined rough surface are those [8, 20, 21] from the research program at Stanford University. Boundary layer profiles and skin friction coefficients were reported for turbulent boundary layer air flows over a flat plate constructed of 1.27 mm diameter spherical roughness elements packed in the most dense array. Healzer [8] and Pimenta [20] investigated zero pressure gradient flows, and comparisons of discrete element model predictions and data for five cases (two transitionally rough and three fully rough) are shown in Fig. 7. Examination of these comparisons shows that the agreement is excellent, with the predictions in each case being within the reported ±10 percent data uncertainty.

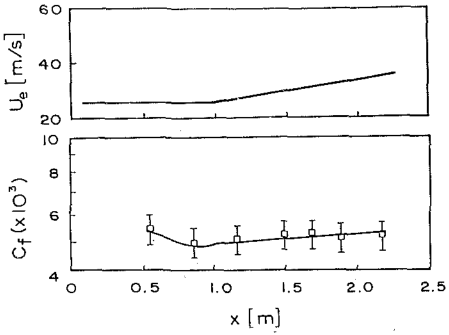

Fig. 8 Comparison of predictions with mild favorable pressure gradient skin friction data of Coleman

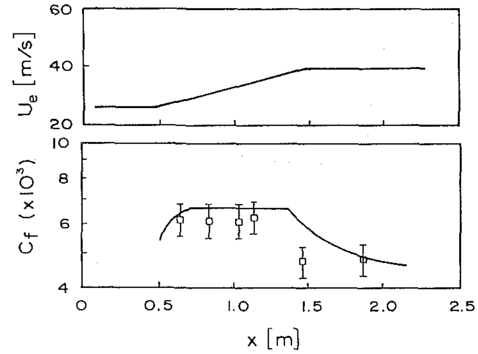

Fig. 9 Comparison of predictions with strong favorable pressure gradient skin friction data of Coleman

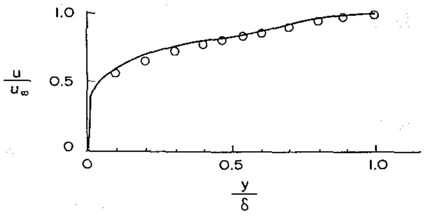

Fig. 10 Comparison of predicted and measured velocity profile data of Pimenta (U_∞ = 27 m/s)

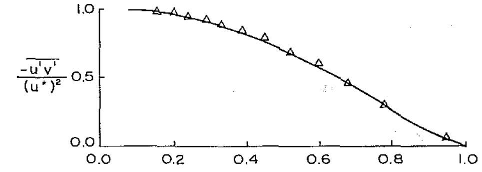

Fig. 11 Comparison of predicted and measured Reynolds shear stress profile data of Pimenta (U_∞ = 27 m/s)

Coleman [21] reported data for fully rough flows with favorable pressure gradients imposed. Shown in Figs. 8 and 9 are the freestream velocity variations and the comparisons of predictions and skin friction coefficient data for two cases. Inspection of the figures shows that the agreement is almost everywhere within the ±10 percent data uncertainty. The one data point at approximately 1.5 m in Fig. 9 which is in substantial disagreement is in the relaxation zone. The boundary layer does not respond instantaneously to changes in boundary conditions, but takes some x-distance to adjust. The turbulence model used did not account for this relaxation phenomenon.

Finally, Figs. 10 and 11 show comparison of predictions and data for the velocity and Reynolds stress profiles, respectively, for one of Pimenta's fully rough cases. The agreement seen in both figures is excellent. The agreement in the Reynolds stress profile is of particular interest, as it reinforces the idea that the smooth wall turbulence model does not need modification if the interactions between the flow and the roughness elements are correctly included in the discrete element approach.

Remarks on Predictions. As seen in the comparisons with Chen's data and the Stanford data, the discrete element method applies equally well for both transitionally rough and fully rough flows. No modifications to the model are made to distinguish the transitionally rough regime or fully rough regime. This is in marked contrast to roughness models based on the equivalent sandgrain roughness approach, for which separate models for the two regimes are used. This point supports the argument that the discrete element approach incorporates more of the basic physics of the interaction between the fluid and the roughness elements than does the equivalent sandgrain roughness approach.

In the past, the delimitation of the boundaries between the smooth, transitionally rough and fully rough regimes has been based on the magnitude of the roughness Reynolds number

$$\mathrm{Re}_{k_s} = u^* k_s / \nu \tag{13}$$

In the present model, the k_s concept has been abandoned. Some new delimiter is therefore required. A reasonable candidate is

$$R_\tau = \tau_r / \tau_T, \tag{14}$$

the ratio of the apparent wall shear stress due to the form drag of the roughness elements to the total apparent wall shear stress. Currently a lack of data from well-defined rough surfaces in the transitionally rough regime prevents a definitive determination of proper R_τ values to delimit the three flow regimes. Based on the available data, it is proposed that

$R_\tau < 0.05 - 0.10$, aerodynamically smooth
$0.05 - 0.10 < R_\tau < 0.080 - 0.90$, transitionally rough
$R_\tau > 0.80 - 0.090$, fully rough.

Acknowledgments

This work was supported by the U. S. Air Force Armament Laboratory, Contract F08635-82-K-0062. The authors wish to thank Lt. Bruce Haupt and Drs. Lawrence Lijewski and Donald Daniel for their support and encouragement.

References

1 Taylor, R. P., Coleman, H. W., and Hodge, B. K., "A Discrete Element Prediction Approach for Turbulent Flow Over Rough Surfaces," Report TFD-84-1, Mech. and Nuc. Eng. Dept., Mississippi State Univ., Feb. 1984.

2 Schlichting, H., "Experimentelle Untersuchungen zum Rauhigkeitsproblem," *Ingenieur-Archiv*, Vol. VII, No. 1, 1936, pp. 1-34. (Also "Experimental Investigation of the Problem of Surface Roughness," NACA TM 823).

3 Nikuradse, J., "Stromungsgesetze in Rauhen Rohren," *VDI-Forchungsheft 361*, 1933. (Also "Laws of Flow in Rough Pipes," NACA TM-1292).

4 Dvorak, F. A., "Calculation of Turbulent Boundary Layers on Rough Surfaces in Pressure Gradient," *AIAA Journal*, Vol. 7, 1969, pp. 1752-1759.

5 Simpson, R. L., " A Generalized Correlation of Roughness Density Effects on the Turbulent Boundary Layer," *AIAA Journal*, Vol. 11, 1973, pp. 242-244.

6 Dirling, R. B., "A Method for Computing Roughwall Heat Transfer Rates on Reentry Nosetips," AIAA Paper 73-763, 1973.

7 Coleman, H. W., Hodge, B. K., and Taylor, R. P., "A Re-Evaluation of Schlichting's Surface Roughness Experiment," ASME JOURNAL OF FLUIDS ENGINEERING, Vol. 106, 1984, pp. 60-65.

8 Healzer, J. M., "The Turbulent Boundary Layer on a Rough Porous Plate: Experimental Heat Transfer with Uniform Blowing," Ph.D. thesis, Mech. Eng. Dept., Stanford University, 1974. (Also Report HMT-18).

9 Cebeci, T., and Chang, K. C., "Calculation of Incompressible Rough-Wall Boundary-Layer Flows," *AIAA Journal*, Vol. 16, 1978, pp. 730-735.

10 Ligrani, P. M., "The Thermal and Hydrodynamic Behavior of Thick, Rough-Wall, Turbulent Boundary Layers," Ph.D. thesis, Dept. of Mech. Eng., Stanford University, 1979. (Also Report HMT-29).

11 Liepmann, H. W., and Goddard, F. E., "Note on the Mach Number Effect Upon the Skin Friction of Rough Surfaces," *J. Aeronautical Sci.*, Vol. 24, 1957, p. 784.

12 Lewis, M. J., "An Elementary Analysis for Predicting the Momentum and Heat Transfer Characteristics of a Hydraulically Rough Surface," ASME *Journal of Heat Transfer*, Vol. 97, 1975, pp. 249-254.

13 Adams, J. C., and Hodge, B. K., "The Calculation of Compressible, Transitional, Turbulent and Relaminarizational Boundary Layers Over Smooth and Rough Surfaces Using an Extended Mixing Length Hypothesis," AIAA Paper 77-682, 1977.

14 Lin, T. C., and Bywater, R. J., "The Evaluation of Selected Turbulence Models for High-Speed Rough-Wall Boundary Layer Calculations," AIAA Paper 80-0132, 1980.

15 Finson, M. L., and Wu, P. K. S., "Analysis of Rough Wall Turbulent Heating with Application to Blunted Flight Vehicles," AIAA Paper 79-008, 1979.

16 Finson, M. L., and Clark, A. S., "The Effect of Surface Roughness Character on Turbulent Reentry Heating," AIAA Paper 80-1459, 1980.

17 Finson, M. L., "A Model for Rough Wall Turbulent Heating and Skin Friction," AIAA Paper 82-0199, 1982.

18 Christoph, G. H., and Pletcher, R. H., "Prediction of Rough-Wall Skin Friction and Heat Transfer," *AIAA Journal*, Vol. 21, No. 4, 1983, pp. 509-515.

19 Christoph, G. H., "Skin Friction and Heat Transfer for Combined Roughness and Mass Addition," in *Laminar Turbulent Boundary Layers*, ASME Publication, FED-Vol. 11, 1984.

20 Pimenta, M. M., "The Turbulent Boundary Layer: An Experimental Study of the Transport of Momentum and Heat with the Effect of Roughness," Ph.D. thesis, Dept. Mech. Eng., Stanford University, 1975. (Also Report HMT-21).

21 Coleman, H. W., "Momentum and Energy Transport in the Accelerated Fully Rough Turbulent Boundary Layer," Ph.D. thesis, Dept. Mech. Eng., Stanford University, 1976. (Also Report HMT-24).

22 Chen, C. K., "Characteristics of Turbulent Flow Resistance in Pipes Roughened with Hemispheres," Ph.D. thesis, Washington State University, 1971.

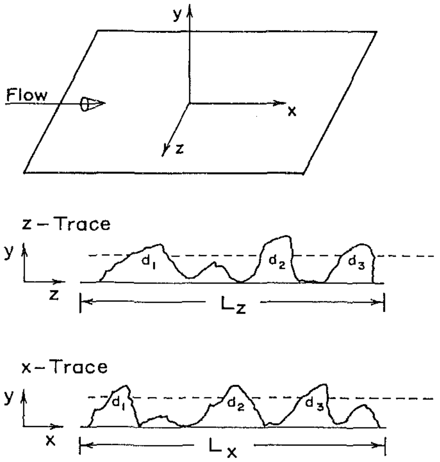

Fig. 12 Schematic diagram and coordinate system for a general rough surface

APPENDIX

Formulation of the Discrete Element Approach for Random Three-Dimensional Roughness

Consider the case of three-dimensional (as opposed to rib-type) roughness elements of random shape, height and spacing. The profiles of such surfaces are usually obtained by taking profilometer traces such as those shown schematically in Fig. 12. In the formulation presented below, the element cross-sections in xz-planes are approximated as circular with diameters d_i. The z-trace is used to establish the element diameters as a function of y, and the x-trace is used to establish the density of the elements on the surface.

The total xz area occupied by the elements in the neighborhood of the z-trace is

$$A_{\text{tot}} = \frac{\pi}{4} \sum_{i=1}^{N_z(y)} d_i^2(y) \tag{15}$$

where $N_z(y)$ is the number of elements in the z-trace at a y-level. To obtain the blockage factor β_y, the plan area associated with the z-trace must be determined. The z-dimension for this plan area is L_z, and an appropriate x-dimension is the average x-spacing of the elements, $L_x/N_x(0)$, where $N_x(0)$ is the number of elements at the level $y = 0$. The xz blockage is then

$$\beta_y = 1 - \frac{\pi N_x(0)}{4 L_x L_z} \sum_{i=1}^{N_z(y)} d_i^2(y) \tag{16}$$

For an average yz plane the area occupied by the elements is $d_{\text{ave}}\delta y$ where the averaging process is carried out in the x-direction. With a similar development to the one which produced equation (6), d_{ave} is

$$d_{\text{ave}} = \frac{\pi N_x(0)}{4 L_x} \sum_{i=1}^{N_z(y)} d_i^2(y) \tag{17}$$

The associated yz plan area is $L_z \delta y$ giving for the yz blockage

$$\beta_x = 1 - \frac{d_{\text{ave}}\delta y}{L_z \delta y} = 1 - \frac{\pi N_x(0)}{4 L_x L_z} \sum_{i=1}^{N_z(y)} d_i^2(y) \tag{18}$$

The form drag term for general roughness is evaluated in a manner similar to that for uniform arrays with L replaced by $L_x/N_x(0)$ and l replaced by L_z to give as the final term in equation (4)

$$-\frac{\rho U^2 N_x(0)}{2 L_x L_z} \sum_{i=1}^{N_z(y)} C_{D,i} d_i(y)$$

where the turbulence intensity factor has been absorbed into $C_{D,i}$.

For uniform arrays of identical elements, the above equations reduce to those previously presented. In this formulation no attempt has been made to correct for the bias in profilometer traces. This bias arises because the trace has a vanishing probability of passing through the peaks of the roughness elements. Thus, the indicated heights and diameters are always on the low side of the true values.

ERRATA

J. R. Koseff and R. L. Street, "The Lid-Driven Cavity Flow: A Synthesis of Qualitative and Quantitative Observations," **Journal of Fluids Engineering**, Vol. 106, Dec. 1984, pp. 390–398.

The corrected version of Fig. 13(*a*) in the paper by J. R. Koseff and R. L. Street is printed below.

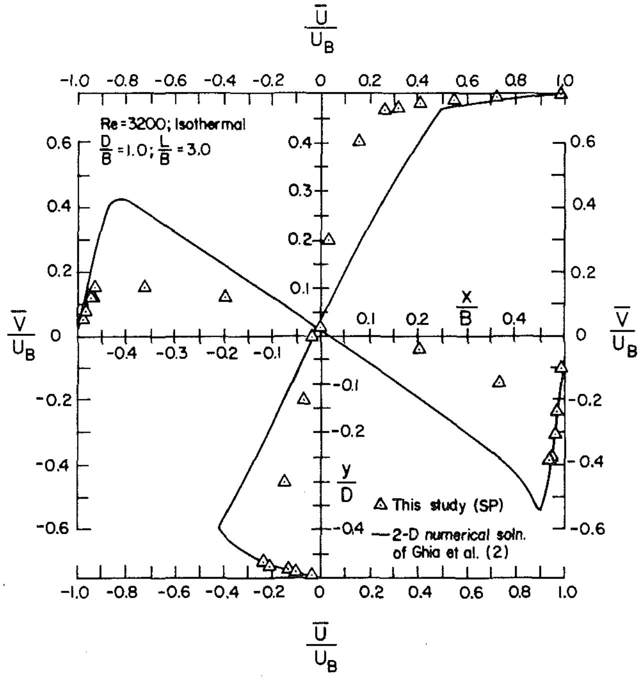

Fig. 13(*a*) Experimental data versus numerical simulation for normalized mean velocity profiles at symmetry plane for Re = 3200

The Instability of a Round Jet Surrounded by an Annular Shear Layer

R. Anderson
Solar Energy Research Institute,
Golden, CO 80401

A. Bejan
Department of Mechanical Engineering and
Materials Science
Duke University,
Durham, N.C. 27706

A linear stability analysis of the large-scale structure of a round jet surrounded by an annular shear layer is presented. The study is limited to the developing region near the jet nozzle in the limit $Re \rightarrow \infty$. The radial dependence of the amplitudes of growing disturbances are examined in order to illustrate the extent to which the disturbances penetrate into the jet and its surroundings. The region influenced by a disturbance is found to be directly proportional to the wavelength of the disturbance. Disturbance measurements made on the jet centerline tend to select for long wavelength disturbances, while measurements made in the shear layer tend to select for short wavelength disturbances. When the shear layer thickness is small compared with the jet radius, the wavelength of the most amplified disturbance scales with the shear layer thickness. As the shear layer thickness increases, this scaling quickly breaks down. This change in scaling appears to be responsible for the transition between the "ripples" which occur near the jet nozzle and the "puffs" which are observed further downstream. Amplified disturbances exhibit a phase lag across the shear layer, which may account for the spade-like structures evident in flow visualizations of turbulent jets.

1 Introduction

In a number of recent studies, the theory of hydrodynamic stability has been applied to the developing region of high-speed fluid jets. The developing region occurs in the first 6-8 diameters nearest the jet nozzle and consists of a potential core with constant velocity surrounded by an annular shear layer. Study of the developing region of turbulent jets has been motivated by the practical problem of controlling aerodynamic jet noise as well as fundamental interest in the problem of transition from laminar to turbulent flow.

Experimental studies have shown that large-scale eddies play an important role in determining the transport properties of turbulent shear layers. For example, Brown and Roshko [1] and Winant and Browand [2] have shown that turbulent mixing occurs primarily through a process of engulfment by large-scale eddies rather than by molecular diffusion. Reynolds [3], Bradshaw, Ferris and Johnson [4] and Mollø-Christensen [5] were among the first to demonstrate the existence of large-scale, coherent structures in the developing region of turbulent jets. Subsequently, Crow and Champagne [6] used a loudspeaker to generate a wave train on a turbulent jet and found that the phase velocity of the waves could be described by applying the linear theory of temporally growing instabilities to a "top hat" velocity profile. Michalke [7] considered spatially growing disturbances using a hyperbolic tangent velocity profile and also found good agreement with the experimental measurements made by Crow and Champagne. Chan [8] and Mattingly and Chang [9] found reasonable agreement between theory and experiment by modeling their jet velocity profiles with error functions and Gaussian distributions, respectively. Even though one would expect linear stability theory to be strictly valid only for the case of laminar flow, the papers cited above indicate that linear theory also provides a reasonable approximation to the behavior of large-scale eddies. It appears that the large-scale eddies respond primarily to the mean velocity profile at each cross section and are only slightly affected by local velocity fluctuations. For a comprehensive overview of shear layer instability the reader is referred to a recent review by Maslowe [10].

The objective of this paper is to use a simple stability model to identify some of the *global* properties of large-scale eddies. Previous studies have tended to make detailed comparisons between experimental and theoretical values of the phase speeds, growth rates and amplitudes of flow disturbances without attempting to isolate the general patterns which are characteristic of large-scale eddies. In this paper we will examine the radial dependence of the amplitudes of growing disturbances in order to illustrate their ability to penetrate into the interior of the jet and into its surroundings.

For the purposes of the following discussion we will limit our analyis to the onset of instability waves near the jet nozzle. This region is of major interest from an engineering standpoint because its properties are easily influenced by the experimenter or designer. The stability analysis is developed in detail in the following section. In Section 3 we use the results of the stability analysis to examine how disturbances scale as a function of shear layer thickness. Finally, Section 4

Contributed by the Fluids Engineering Division for publication in the JOURNAL OF FLUIDS ENGINEERING. Manuscript received by the Fluids Engineering Division, August 3, 1983.

is devoted to a detailed examination of the radial dependence of the amplitudes of disturbance quantities.

2 Instability Model and Analysis

In the present study the mean velocity profile for a developing jet will be divided into three regions: the outer flow, the shear layer, and the potential core. The transition between the central potential core of the jet and the cylindrical shear layer surrounding the jet occurs at $r=a-t$, where a and t are the local jet radius and shear layer thickness. The velocity at the center of the jet is U_j and the jet exits into a coflowing stream with the velocity U_0. The jet and its surroundings are assumed to be composed of equal density fluids at constant temperature.

It is assumed that the flow is incompressible and inviscid ($\mathrm{Re}\rightarrow\infty$), and that the growth of the shear layer is small enough over one wavelength that the flow can be considered to be locally parallel. By defining the jet velocity to consist of the parallel mean flow plus a small amplitude fluctuating component it can be shown (Batchelor and Gill [11]) that the Navier-Stokes equations reduce to the form

$$\frac{\partial \mathbf{u}}{\partial t}+\mathbf{U}\cdot\frac{\partial \mathbf{u}}{\partial x}+u_r\frac{\partial \mathbf{U}}{\partial r}=-\frac{1}{\rho}\nabla p \tag{1}$$

$$\nabla\cdot\mathbf{u}=0 \tag{2}$$

where $\mathbf{u}=(u_r,\ u_\theta,\ u_z)$ is the infinitesimal perturbation of the locally parallel jet velocity profile $\mathbf{U}=(0,\ 0,\ U_z\ (r))$, and p is the pressure perturbation. Second order terms involving perturbation quantities have been ignored. We assume that the pressure and velocity perturbation have the form

$$(u_r,u_\theta,u_z,p)=R\{(iR,\theta,Z,P)e^{in\theta+ikz-i\omega\tau}\} \tag{3}$$

thus, when $n=0$, the perturbations are axisymmetric and are of the "varicose" type, and when $n=1$, the waves are helical. The present study will be limited to consideration of these first two modes since Mattingly and Chang [9] have shown that these modes dominate the higher order modes. By substituting (3) into (1) and (2) and simplifying, it is possible to find the following differential equations for the radial amplitude

$$(U-c)\frac{d}{dr}\left\{\frac{r}{(n^2+k^2r^2)}\frac{d}{dr}(rR)\right\}$$
$$-(U-c)R=rR\frac{d}{dr}\left\{\frac{r}{(n^2+k^2r^2)}\frac{dU}{dr}\right\} \tag{4}$$

where the quantity $c=\omega/k=c_r+ic_i$ which appears in (4) is the complex velocity of the disturbance wave. The boundary conditions which R must satisfy are

$$R(\infty)\rightarrow 0 \tag{5}$$

$$R(0)\ \text{bounded, continuous} \tag{6}$$

Since the use of linear theory is most appropriate for flows with small rates of amplification (and thus small amplitudes) we will limit our discussion to cases where the velocity difference $\lambda=(U_j-U_0)/(U_j+U_0)$ and amplification rate are small. Monkewitz and Huerre [12] have shown that temporal and spatial representations are equivalent in the limit of small λ and can be related to one another via the group velocity of the disturbance waves (Gaster [13]). We can therefore assume for the purpose of the present study that k is purely real and that the disturbance waves grow exponentially in time. The real part of c determines the phase velocity of the disturbance wave and the imaginary part determines its temporal growth rate. For a discussion of the differences between spatial and temporal descriptions of laminar mixing layers where the group velocity transformation is not valid, the reader is referred to analytical and experimental work done by Michalke [14] and Freymuth [15].

In view of the preceeding assumptions, the results of our analysis will be strictly valid only in regions near the jet nozzle where the disturbance waves have small amplitudes. However, this linear region is also the region of most interest from an engineering standpoint because it is the region which is most easily influenced if one wishes to exert some degree of control over the flow. In this regard we note that Liepmann, Brown and Nosenchuck [16] and Liepmann and Nosenchuck [17] have recently demonstrated the ability to partially cancel instability waves in a laminar boundary layer by introducing a small amplitude disturbance which is out of phase with the initial instability.

Lopez and Kurzweg [18] demonstrated the existence of a class of flows for which equation (4) reduces to a particularly simple form. By choosing the mean flow defined by

$$U_1 = U_j,\qquad 0\le r\le x \tag{7}$$

$$U_2 = U_0+\frac{(U_j-U_0)\left[n^2\ln(r/a)-\frac{(ka)^2}{2}\left(1-\left(\frac{r}{a}\right)^2\right]}{\left[n^2\ln\left(\frac{x}{a}\right)-\frac{(ka)^2}{2}\left(1-\left(\frac{x}{a}\right)^2\right)\right]},\qquad x\le r\le a \tag{8}$$

$$U_3 = U_0,\qquad a\le r\le\infty \tag{9}$$

the right-hand side of equation (4) disappears and the solution for R can be expressed in terms of a modified Bessel function of order n. The subscripts in (7)–(9) and in all subsequent equations refer to the different regions of the jet. The quantity x is the thickness of the potential core of the jet

$$x=a-t. \tag{10}$$

We propose to use the stability model defined by equations (1)–(9) to determine: (1) the length-scales which are characteristic of amplified disturbances, and (2) the radial variations in amplitude and phase exhibited by the large-scale eddies. For values of $t/a\le 0.6$, the velocity profile defined by equations (7)–(9) closely resembles the mean velocity in the first 3–6 diameters of the real turbulent jets studied by Crow and Champagne [6] and Moore [19]. The velocity profile is

Nomenclature

A,B,C,D = integration constants
D_V = radial velocity disturbance amplitude ratio
D_P = pressure disturbance amplitude ratio
E = defined in equation (17)
P = amplitude of pressure perturbation
R = radial velocity perturbation amplitude
U = mean velocity
U_j = jet velocity at nozzle exit
U_0 = velocity of coflowing stream
Z = amplitude of axial velocity perturbation
a = local radius of jet
c = complex velocity
$\tilde{c}$ = defined in equation (23)
f = frequency
k = wavenumber
r = radial coordinate
t = local thickness of shear layer
$\mathbf{u}$ = velocity perturbation
x = thickness of potential core
z = axial coordinate
Φ = amplitude of azimuthal velocity perturbation
γ = tilt angle
θ = azimuthal coordinate
λ = velocity ratio
τ = time

Subscripts

1 = potential core
2 = shear layer
3 = external flow

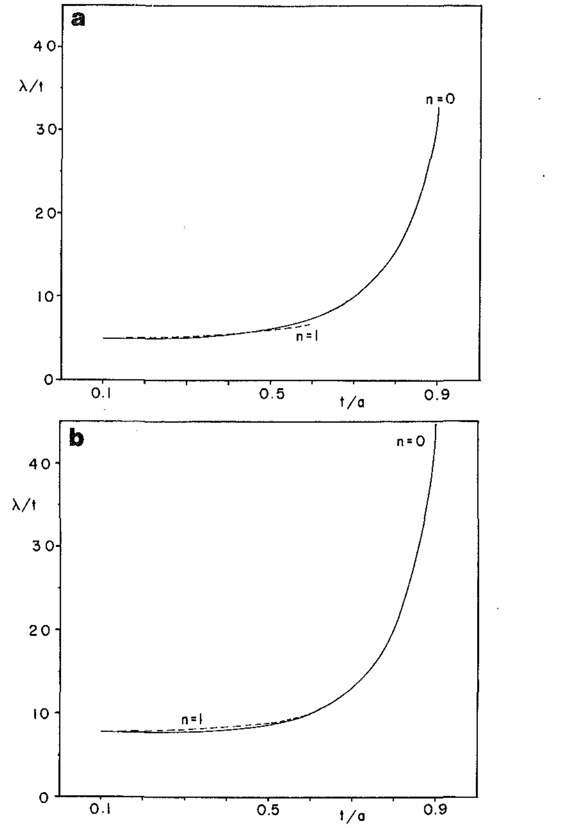

Fig. 1 Neutral, (*a*), and most unstable wavelength, (*b*), as a function of shear layer thickness

quadratic in r and independent of k when $n=0$. As t/a approaches zero the velocity profiles become trapezoidal and the discrepancy between the $n=0$ and $n=1$ modes disappear. When $t/a>0.6$, the differences between the $n=0$ and $n=1$ velocity profiles are so large that comparisons of the stability results for the two modes are no longer valid. Therefore, the $n=1$ mode is not considered in the present study when $t/a>0.6$.

3 Scaling of Amplified Disturbances

Substituting the velocity profile defined by (7)-(9) into (4) and applying the boundary conditions expressed in (5) and (6) leads to the solution

$$R_1 = kAI_n'(kr), \quad 0\le r\le x \tag{11}$$

$$R_2 = k[BI_n'(kr)+CK_n'(kr)], \quad x\le r\le a \tag{12}$$

$$R_3 = kDK_n'(kr), \quad a\le r\le \infty \tag{13}$$

$$\frac{P_1}{\rho} = k(U_1-c)AI_n(kr), \quad 0\le r\le x \tag{14}$$

$$\frac{P_2}{\rho} = k(U_2-c)[BI_n(kr)+CK_n(kr)]-krER_2(U_j-U_0), \quad x\le r\le a \tag{15}$$

$$\frac{P_3}{\rho} = k(U_3-c)DK_n(kr), \quad a\le r\le \infty \tag{16}$$

$$E = \frac{1}{\left[n^2\ln\left(\frac{x}{a}\right)-\frac{(ka)^2}{2}\left(1-\left(\frac{x}{a}\right)^2\right)\right]} \tag{17}$$

In this solution, I_n and K_n are modified Bessel functions of the first and second kind and the primes indicate differentiation with respect to the arguments of the Bessel functions. The constants A, B, C, and D are determined by requiring the radial velocity and pressure to be continuous at $r=x$ and $r=a$. By eliminating A and D in favor of B and C, we obtain the homogeneous system

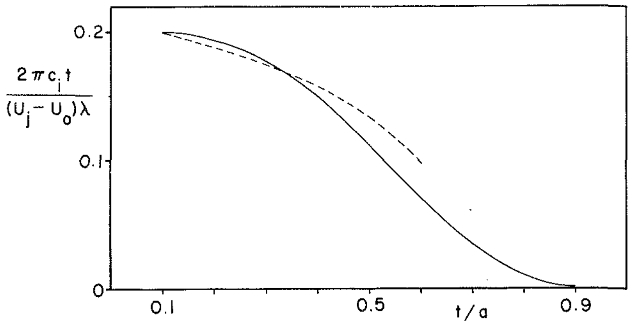

Fig. 2 Relative magnitude of the most unstable growth rate as a function of shear layer thickness

$$\begin{bmatrix} m_{11} & m_{12} \\ m_{21} & m_{22} \end{bmatrix} \begin{bmatrix} B \\ C \end{bmatrix} = 0 \tag{18}$$

where

$$m_{11} = I_n'(kx)I_n'(kx) \tag{19}$$

$$m_{12} = I_n'(kx)K_n'(kx)-\frac{(1-\bar{c})}{(kx)^2E} \tag{20}$$

$$m_{21} = K_n'(ka)I_n'(ka)-\frac{\bar{c}}{(ka)^2E} \tag{21}$$

$$m_{22} = K_n'(ka)K_n'(ka) \tag{22}$$

$$\bar{c}=\frac{c-U_0}{(U_j-U_0)} \tag{23}$$

The desired equation for the eigenvalue c is the condition

$$\text{Det}\begin{bmatrix} m_{11} & m_{12} \\ m_{21} & m_{22} \end{bmatrix} = 0 \tag{24}$$

The neutral wavelength and the wavelength with maximum amplification are plotted as functions of the shear layer thickness in Fig. 1. It can be seen that for $t/a\le 0.5$, both the neutral wavelength ($c_i=0$) and the wavelength with maximum growth scale with the shear layer thickness and have the limiting values $\lambda/t\approx 5$, and $\lambda/t\approx 8$, respectively, as $t/a\to 0$. As t/a increases above 0.5 this scaling quickly breaks down. In the limit of a thin shear layer the jet's curvature becomes less important (i.e., the shear layer is approximately two-dimensional), and the limiting values reported above compare well with the results of a two-dimensional study done by Michalke [14], who found that the ratio λ/t for the neutral and for the most amplified modes is 6.28 and 7.79, respectively.

The drastic change in scaling behavior as t/a increases above 0.5 may explain why Crow and Champagne [6] interpreted the surface ripples they observed close to the jet nozzle to be a separate phenomenon from the puffs they observed to occur farther downstream. The "puffs" correspond to the response of a jet with a *thick* shear layer while the "ripples" correspond to the response of a jet with a *very thin shear layer*. These ripples and puffs appear as two different phenomena because their respective instabilities are characterized by different length scales.

The magnitudes of the growth rates for the axisymmetric mode ($n=0$) and the first helical mode ($n=1$) are compared in Fig. 2. For small values of t/a the axisymmetric mode is slightly more unstable than the helical mode. As t/a increases beyond 0.3, the first helical mode dominates. These results confirm the conclusions reached by Lopez and Kurzweg [18], although they limited their analysis to the three values $t/a=0.09$, $t/a=0.33$, and $t/a=0.72$. Michalke and Hermann [20] report a similar behavior of the growth rates of the first two modes on a jet with a hyperbolic tangent velocity profile.

4 Radial Dependence of Disturbance Amplitudes

In addition to the stability results reported in the preceeding section it is also desirable to extract information concerning the spatial structure of the velocity and pressure perturbations postulated in (3). To do this we nondimensionalize the disturbance amplitudes R and P by dividing by their respective values at the edge of the shear layer, $r=a$. The *radial velocity disturbance amplitude ratio* D_V and *pressure disturbance amplitude ratio* D_P calculated by this method are

$$D_{V_1} = \frac{A}{D}\frac{I_n'(kr)}{K_n'(ka)}, \quad 0 \le r \le x \tag{25}$$

$$D_{V_2} = \frac{1}{K_n'(ka)}\left[\frac{B}{D}I_n'(kr) + \frac{C}{D}K_n'(kr)\right], \quad x \le r \le a \tag{26}$$

$$D_{V_3} = \frac{K_n'(kr)}{K_n'(ka)}, \quad a \le r \le \infty \tag{27}$$

and,

$$D_{P_1} = -\frac{(1-\bar{c})}{\bar{c}}\left[\frac{A}{D}\frac{I_n(kr)}{K_n(ka)}\right., \quad 0 \le r \le x \tag{28}$$

$$D_{P_2} = -\frac{(\bar{U}-\bar{c})}{\bar{c}}\left[\frac{B}{D}\frac{I_n(kr)}{K_n(ka)} + \frac{C}{D}\frac{K_n(kr)}{K_n(ka)}\right] + \frac{krE}{\bar{c}}\left[\frac{B}{D}\frac{I_n'(kr)}{K_n(ka)} + \frac{C}{D}\frac{K_n'(kr)}{K_n(ka)}\right], \quad x \le r \le a \tag{29}$$

$$D_{P_3} = \frac{K_n(kr)}{K_n(ka)}, \quad 0 \le r \le \infty \tag{30}$$

where

$$\bar{U} = \frac{U_2 - U_0}{U_j - U_0} \tag{31}$$

The subscripts of D_V and D_P refer to the three regions defined in equations (7)-(9).

Both D_V and D_P depend upon the quantities A/D, B/D, and C/D. These quantities can be evaluated by applying the pressure and radial velocity continuity conditions at $r=x$ and $r=a$, and are

$$\frac{A}{D} = \frac{\left[1 - \frac{(ka)^2E}{\bar{c}}\right]I_n'(ka)K_n'(ka)}{\frac{(kx)^2E}{(1-\bar{c})}I_n'(kx)I_n'(kx)} \tag{32}$$

$$\frac{B}{D} = \frac{(ka)^2E}{\bar{c}}K_n'(ka)K_n'(ka) \tag{33}$$

$$\frac{C}{D} = 1 - \frac{(ka)^2}{\bar{c}}EK_n'(ka)I_n'(ka) \tag{34}$$

It should be noted that the disturbance amplitudes are in general complex quantities and, therefore, the disturbance amplitude ratios contain both relative phase and relative amplitude information. Thus, the D_V, D_P ratios can be expressed as

$$D_{V,P} = |D_{V,P}|e^{i\phi_{V,P}} \tag{35}$$

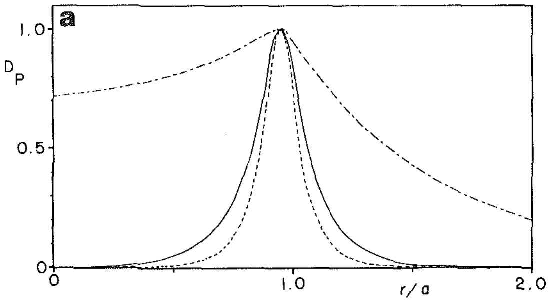

Fig. 3(*a*) The pressure disturbance amplitude ratio, D_P, as a function of wavelength. $t/a = 0.1$ and $n=0$. "______" = most unstable case ($\lambda/t = 7.88$). "_ _ _ _ _ _" = neutral case ($\lambda/t = 4.93$). "___ • ___" = slightly unstable case ($\lambda/t = 50$).

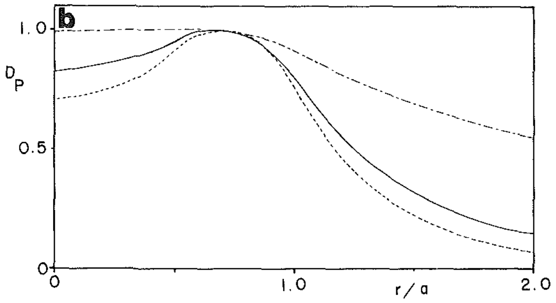

Fig. 3(*b*) The pressure disturbance amplitude ratio, D_P, as a function of wavelength. $t/a = 0.5$ and $n=0$. "______" = most unstable case ($\lambda/t = 8.64$). "_ _ _ _ _ _" = neutral case ($\lambda/t = 6.06$). "___ • ___" = slightly unstable case ($\lambda/t = 50$).

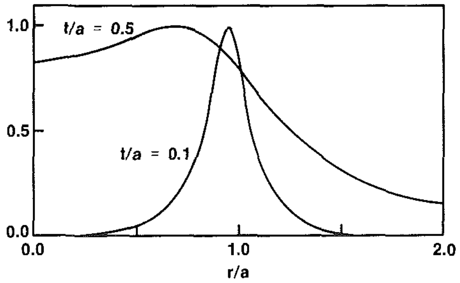

Fig. 4 The pressure disturbance amplitude ratio, D_P, as a function of shear layer thickness. Most amplified mode. $n=0$.

where ϕ is the phase shift of the wave at any radial position r relative to the disturbance with the disturbance with the same wavelength at the edge of the jet, $r=a$.

4.1 Wavelength Dependence.

In Figs. 3(*a*) and Fig. 3(*b*) the pressure disturbance amplitude ratio D_P is plotted for two different values of the shear layer thickness, $t=0.1a$ and $t=0.5a$. In these and all subsequent figures discussed in this section, results are reported for the axisymmetric mode only ($n=0$). The $n=0$ mode is the most amplified mode near the jet nozzle. The behavior of the first helical mode was found to be qualitatively the same as far as the phenomena discussed below are concerned. Figure 3(*a*) shows that the disturbance reaches its peak inside the shear layer when the shear layer is thin. The region affected by the disturbance grows and penetrates into the potential core and into the surroundings of the jet with increasing disturbance wavelength. As the shear layer thickens (Fig. 3(*b*)), the location of the disturbance peak shifts slightly inward and the peak is considerably less distinct. A comparison of the most amplified modes for $t/a=0.1$ and $t/a=0.5$ is shown in Fig. 4.

Figures 3 and 4 demonstrate that: (1) the depth of disturbance penetration inside and outside the jet is directly proportional to the wavelength of the disturbance, and (2) the depth of disturbance penetration for waves with constant

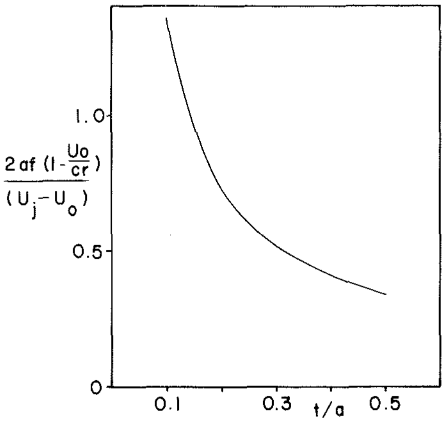

Fig. 5 The Strouhal number dependence of the most unstable wavelength

relative rates of amplification is directly proportional to the local thickness of the shear layer. These two conclusions shed light on the physics behind the $\lambda \sim t$ scaling shown by the instability curves discussed in Section 3. Disturbances lead to instability when they can penetrate through the shear layer, thus effecting the transfer of energy from the jet to the ambient. The scaling of the penetration distance with wavelength of the disturbance can be clearly seen in experimental measurements reported by Freymuth for the case of a laminar shear layer (see reference [15], Fig. 19).

The behavior shown in Figs. 3 and 4 can also explain pressure measurements made by Chan (1974). Chan found the Strouhal number (fD/U_{exit}) associated with maximum growth on the jet centerline to be 0.35 while the Strouhal number with maximum growth in the shear layer had the value $\text{St} = 0.5$. Strouhal number results from the present analysis are shown in Fig. 5. The frequency, f, was calculated by using the relation

$$f = \frac{c_r}{\lambda} \tag{36}$$

As the shear layer thickness increases in Fig. 5, the Strouhal number of the most amplified mode decreases. However, from Fig. 5 we know that the amplification rate also drops rapidly with increasing shear layer thickness. Therefore the most amplified disturbance in the shear layer will tend to occur near the nozzle and have a large Strouhal number. On the other hand, measurements made at the center of the jet tend to select disturbances made by thicker shear layers occurring farther from the jet nozzle and yielding smaller Strouhal numbers, because highly amplified disturbances made by thin shear layers do not "penetrate" into the center of the jet (Fig. 4). Crighton and Gaster [21] and Plasko [22] have calculated the gain in pressure amplitude with axial distance on the centerline and in the center of the shear layer, respectively. Their results agree with the measurements made by Chan [8] and with the selection process described above. This selection process is fundamentally different from the purely axial-dependent selection process which occurs in the fully developed region of a laminar jet [23].

4.2 Phase Variations. As emphasized in the introduction to this section, the disturbance amplitude ratios contain relative phase as well as relative amplitude information. This phase information is displayed in Figs. 6 and 7. The total phase shift that occurs across the shear layer is shown as a function of wavelength in Fig. 6. The total phase shift is zero at the neutral wavelength and increases rapidly as the maximum growth wavelength is approached. Beyond the maximum growth wavelength the D_V phase shift increases slowly while the D_P phase shift decreases. A phase shift is required in order for a wave to be unstable, but beyond a certain point, further increases in phase shift cause the wave to regain stability.

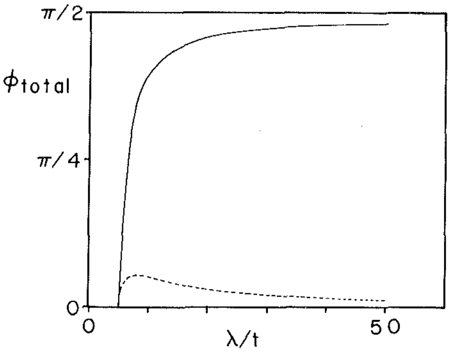

Fig. 6 Total phase shift across the shear layer, as a function of wavelength. "______" = D_V. "_ _ _ _ _ _" = D_P. $t/a = 0.1$.

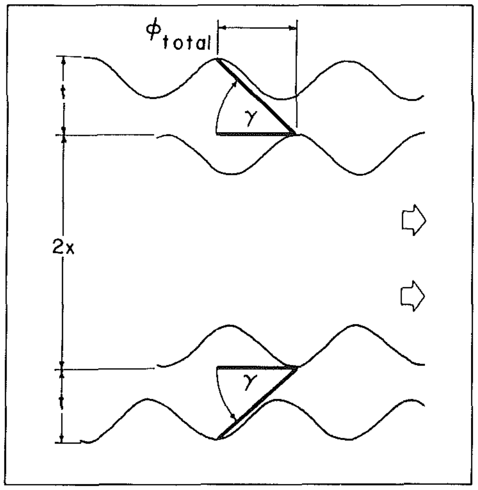

Fig. 7 Tilt angle due to phase shift in radial disturbance velocity

A schematic of the radial velocity disturbance waves located at the inner and outer edges of the shear layer is shown in Fig. 7. The wave on the outside of the jet lags behind the wave on the inside of the shear layer by the phase angle ϕ_{total}. The tilt angle γ, Fig. 7, can be expressed as

$$\gamma = \tan^{-1}\left(\frac{t}{\left[\dfrac{\phi_{\text{total}}}{2\pi}\right]\lambda}\right) \tag{37}$$

Since the peak in the radial disturbance velocity is associated with the radial exchange of fluid between jet and ambient, it is tempting to draw comparisons between the tilt angle γ and published Schlieren photographs of turbulent jets. Although there is no direct basis for comparing the results of the present linear theory to finite amplitude waves, the similarity between Fig. 7 and photographs of the jet nozzle region which appear in [6] is evident; the tilt angle is visualized by several distinct spade-like puffs which propagate downstream.

5 Conclusions

In this study we focused on the instability and large-scale structure of the near nozzle region of a round jet at high Reynolds numbers. The mean velocity profile of the jet was assumed to be a curvilinear trapezoid. This assumed profile approximates the mean profile in the developing region of a round jet. The stability analysis demonstrated that the wavelength of the most amplified disturbance scales with the shear layer thickness when the shear layer thickness is small compared with the jet radius. This scaling quickly breaks down as the shear layer thickness approaches the jet radius. Based on the above proportionality between disturbance wavelength and shear layer thickness, it was argued that the "ripples" and "puffs" observed in turbulent jets are separate manifestations of the same instability phenomenon.

The radial dependence of the amplitudes of growing disturbances was examined in order to illustrate the extent to which a disturbance penetrates into the jet and its surroundings. It was found that the short wavelength modes which are amplified near the jet nozzle do not disturb the center of the jet, but that long wavelengths amplified farther downstream do. On the basis of these findings it was argued that disturbance measurements made on the centerline of the jet tend to select for long wavelength disturbances while measurements made in the shear layer tend to select for short wavelength disturbances. This selection model agrees with measurements made by Chan [8]. Finally, it was found that amplified disturbances exhibit a phase lag across the shear layer which may account for the spade-like structures evident in flow visualizations of turbulent jets.

References

1 Brown, G. L., and Roshko, A., "On Density Effects and Large Structure in Turbulent Mixing Layers," *J. Fluid Mech.*, Vol. 64, 1974, pp. 775-816.

2 Winant, C. D., and Browand, F. K., "Vortex Pairing: The Mechanism of Turbulent Mixing-Layer Growth at Moderate Reynolds Numbers," *J. Fluid Mech.*, Vol. 63, 237-255. Vol. 63, 1974, pp. 237.

3 Reynolds, A. J., "Observations of a Liquid into Liquid Jet," *J. Fluid Mech.*, Vol. 14, 522-567. Vol. 14, 1962, pp. 522-567.

4 Bradshaw, P., Ferris, D. H., and Johnson, R. F., "Turbulence in the Noise-Producing Region of a Circular Jet," *J. Fluid Mech.*, Vol. 19, 1964, pp. 591-624.

5 Mollø-Christensen, E., "Jet Noise and Shear Flow Instability seen from an Experimenter's Viewpoint," ASME *Journal of Applied Mechanics*, Vol. 34, 1967, pp. 1-7.

6 Crow, S. C., and Champagne, F. H., "Orderly Structure in Jet Turbulence," *J. Fluid Mech.*, Vol. 48, 547-591. Vol. 48, 1971, pp. 547-591.

7 Michalke, A., "Instabilität eines runden Freistrahls unter Bërucksichtigung des Einflusses der Strahlgrenzschichtdicke," *Z. Flugwis*, Vol. 19, 1971, pp. 319-328.

8 Chan, Y. Y., "Spatial Waves in Turbulent Jets," *Phys. Fluids.*, Vol. 17, 1974, pp. 46-53.

9 Mattingly, G. E., and Chang, C. C., "Unstable Waves on an Axisymmetric Jet Column," *J. Fluid Mech.*, Vol. 65, 1974, pp. 541-560.

10 Maslowe, S. A., "Shear Flow Instabilities and Transition," in *Hydrodynamic Instabilities and the Transition to Turbulence*, edited by H. L. Swinney and J. P. Gollub, Springer-Verlag, Berlin, *1981*.

11 Batchelor, G. K., and Gill, A. E., "Analysis of the Stability of Axisymmetric Jets," *J. Fluid Mech.*, Vol. 14, 1962, pp. 529-551.

12 Monkewitz, P. A., and Huerre, P., "Influence of the Velocity Ratio on the Spatial Instability of Mixing Layers," *Phys. Fluids.*, Vol. 25, 1982, pp. 1137-1143.

13 Gaster, M., "A Note on the Relation Between Temporally-Increasing and Spatially-Increasing Disturbances in Hydrodynamic Stability," *J. Fluid Mech.*, Vol. 14, 1962, pp. 222-224.

14 Michalke, A., "On Spatially Growing Disturbances in an Inviscid Shear Layer," *J. Fluid Mech.*, Vol. 23, 1965, pp. 521-544.

15 Freymuth, P., "On Transition in a Separated Laminar Boundary Layer," *J. Fluid Mech.*, Vol. 25, 1966, pp. 683-704.

16 Liepmann, H. W., Brown, G. L., and Nosenchuck, D. M., "Control of Laminar-Instability Waves Using a New Technique," *J. Fluid Mech.*, Vol. 118, 1982, pp. 187-200.

17 Liepmann, H. W., and Nosenchuck, D. M., "Active Control of Laminar-Turbulent Transition," *J. Fluid Mech.*, Vol. 118, 1982, pp. 201-204.

18 Lopez, J. L. and Kurzweg, U. H., "Amplification of Helical Disturbances in a Round Jet," *Phys. Fluids.*, Vol. 20, 1977, pp. 860-861.

19 Moore, C. H., "The Role of Shear-Layer Instability Waves in Jet Exhaust Noise," *J. Fluid Mech.*, Vol. 80, 1977, pp. 321-367.

20 Michalke, A., and Hermann, G., "On the Inviscid Instability of a Circular Jet with External Flow," *J. Fluid Mech.*, Vol. 114, 1982, pp. 343-359.

21 Crighton, D. G., and Gaster, M., "Stability of Slowly Diverging Jet Flow," *J. Fluid Mech.*, Vol. 77, 1976, pp. 397-413.

22 Plasko, R., "Helical Instabilities of Slowly Divergent Jets," *J. Fluid Mech.*, Vol. 92, 1979, pp. 209-215.

23 Mollendorf, J. C., and Gebhart, B., "An Experimental and Numerical Study of the Viscous Stability of a Round Laminar Vertical Jet with and without Thermal Bouyancy for Symmetric and Asymmetric Disturbances," *Journal of Fluids Mechanics*, Vol. 61, 1973, pp. 367-399.

B. R. Ramaprian
Professor and Research Engineer.
Department of Mechanical Engineering and
Iowa Institute of Hydraulic Research,
University of Iowa,
Iowa City, Iowa 52242
Mem. ASME

M. S. Chandrasekhara*
Post Doctoral Fellow,
Joint Institute for Aeronautics
and Accoustics,
Stanford University,
Stanford, Calif. 94305
Assoc. Mem. ASME

LDA Measurements in Plane Turbulent Jets

Measurements on the mean and most of the significant turbulent properties of plane isothermal and heated (but essentially "nonbouyant") jets are reported. The velocity measurements were made using two-component, frequency-shifted Laser Doppler Anemometry (LDA) and the temperature measurements were made using fast-response resistance thermometry. A simple but effective technique was developed for obtaining accurate velocity measurements from the LDA in a nonisothermal environment. These measurements, some of which are the first of their kind, provide an independent data base with which to compare existing hot-wire data on jets. The LDA measurements indicate lower turbulence intensities and lower turbulent fluxes compared to the hot-wire data.

Introduction

The plane turbulent jet has been studied by several researchers partly because of its practical applications and more because of the relative simplicity and universality of its asymptotic state. It provides a very good test case in the development of turbulence models. Some of the more detailed studies on plane isothermal jets are listed as references [1-9], while a larger list can be found in Kotsovinos [10] and Goldschmidt and Young [11]. Two-dimensional turbulent heated jets in which the heat does not introduce significant buoyancy effects but plays only a passive role have also been studied by several investigators [10, 12-15].

Turbulence measurements have been made in many of the above studies on isothermal as well as heated jets. All these measurements with one exception, namely those of Kotsovinos [10, 12], have been made using hot-wire anemometry. This technique presents several difficulties when used for measurements in jets, even under isothermal conditions. The most important of these is the presence of very large relative turbulence intensities, which introduce errors due to nonlinearity and large changes in instantaneous flow orientation. Additional difficulties arise in heated jet studies, where simultaneous velocity and temperature measurements are to be made using multiple sensors. These include calibration drifts, sensitivity of velocity sensors to temperature and vice verse and probe interference. Considerable effort has been made in many of the studies cited above to overcome these difficulties. However, the absence of data obtained using an alternate technique has so far been a great disadvantage. The experiments of Kotsovinos [10] on two-dimensional jets seem to be the only ones where Laser Doppler Anemometry (LDA) was used for velocity measurements. However, the single component LDA used in these experiments could only provide the mean velocity $\bar{U}$ and the rms turbulence intensity u'. The experiments reported in the present paper provide a set of detailed data on most of the significant mean and turbulent properties of plane jets, obtained using LDA. Both isothermal and heated jets have been studied with emphasis on the fully developed (asymptotic) region of the flow. These data can, therefore, be used as a different and independent data base for comparison with the hot-wire data on the one side and the asymptotic theory on the other. In addition, the present study has addressed some important issues such as nonconservation of momentum flux and decay rate of the centerline velocity in the jet.

Experimental Details

The Apparatus and Instrumentation. The present experiments were conducted in a free-surface hydraulic flume. The flume is 450 mm wide, 750 mm deep and 6750 mm long. It is possible to maintain a constant rate of flow of water in the flume at any desired depth by adjusting a tilting gate at the downstream end of the flume. However, in the present experiments, the flume was used primarily as a large reservoir. The jet originates from a nozzle assembly located near the bottom of the flume. The details of this assembly are shown in Fig. 1. The assembly is made of plexiglas and is essentially a rectangular box 300 mm long, 450 mm wide and 75 mm deep. Hot or cold water enters the box through two vertical pipes terminating in a perforated horizontal tube. It is then passed through a 50 mm thick layer of nylon net, which removes the large eddies in the flow. The water then flows through a length of calming section, followed by a smooth contraction of 15:1 area rtaio. The contraction also turns the flow by 90 degrees. A 25 mm long straight passage, straightens the flow which eventually issues from the surface as a vertical jet, through a rectangular slot 5 mm in width and 250 mm in span. Preliminary flow visualization studies using dye injection indicated that the flow through the nozzle was very nearly vertical. Two false side-walls of plexiglas spaced 250 mm apart were used to limit the span of the jet. The side walls not only made it easier to use the laser anemometer, but also helped in maintaining the two dimensionality of the flow.

The flow rate through the nozzle was measured using a calibrated orifice meter. This flow rate was maintained

---

Contributed by the Fluids Engineering Division of THE AMERICAN SOCIETY OF MECHANICAL ENGINEERS and presented at the Fluids Engineering Conference, Albuquerque, N. Mex., June 24-26, 1985. Manuscript received by the Fluids Engineering Division, March 28, 1983. Paper No. 85-FE-9.

*Presently: Applications Engineer, TSI, Inc., St. Paul, MN 55164

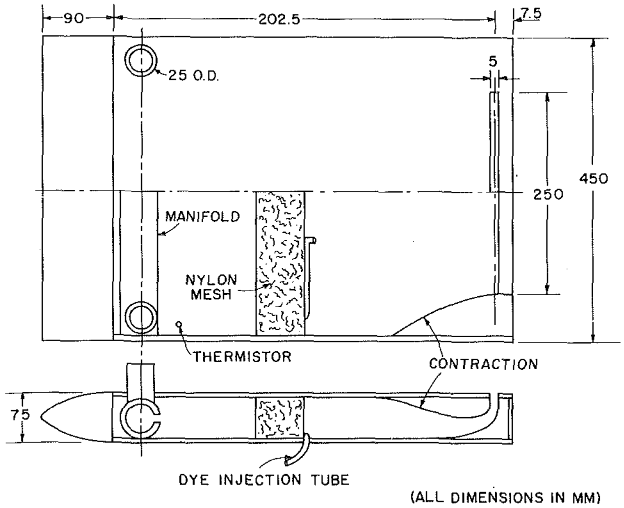

Fig. 1 Details of the nozzle assembly

constant to within 1 percent of the desired value during the entire experiment and was used to calculate the nominal exit velocity, U_j of the jet. The jet exit temperature T_j and the ambient temperature T_a were measured using thermistors from which the nominal exit temperature excess ΔT_j was obtained. Velocities in the jet were measured using a TSI two-component frequency-shifted, LDA. The LDA was used in the forward-scatter, three-beam mode using polarization to separate the two components of the velocity (System 9100-9). Two analog frequency trackers were used for validating and processing the Doppler frequency shift. The optical arrangement and processing procedure used allowed one to obtain simultaneously the two components U and V of the instantaneous velocity in the flow. It was not possible to obtain the W componet of the velocity with the present optical system. Details of the LDA instrumentation are described in [16]. The entire LDA optics was mounted on a three-dimensional traverse which could be positioned to an accuracy of 0.025 mm. Instantaneous temperature excess ΔT in the jet was measured using the well-known "cold-film" resistance thermometry. However, since commercially available temperature "anemometers" were found to be unsuitable for use in water, a special instrument consisting of two DISA hot-film probes (55R11), a differential bridge circuit and a DC-coupled precision preamplifier was built for this purpose. It was verified that even at a probe current of 5 mA, there was no detectable sensitivity of the instrument to velocity. One of the two probes was placed in the ambient as the reference probe. The other probe was mounted on the LDA traverse and was located about 1 mm downstream of the focal volume of the LDA. This separation is substantially smaller than the integral length scale of turbulence and is not expected to have introduced any significant errors into the measurements reported in this study. The estimated frequency response of the cold-film probe is about 65 Hz which is considered more than adequate for the present studies.

A high-speed data-acquisition system consisting of a HP-1000 minicomputer and a Preston analog-to-digital converter (ADC) was used in the experiments for acquiring and processing the instantaneous outputs of the two channels of the LDA and of the temperature system. The data were low pass filtered at 50 Hz before being sampled. The sampling rate was 20 per second and the record length was 128 s. These sampling conditions (selected after several trials) gave acceptable statistical stability in evaluating correlations upto the third order.

Special Problems and Techniques. Measurements with LDA pose certain problems when dealing with flows involving temperature fluctuations. Also, because of the constant injection of hot water into the system and the long duration of the experiments, contamination of the ambient fluid with heat was a problem. These two problems were handled in the manner described below.

Refractive Index Fluctation. The presence of temperature fluctuations in the heated jet resulted in refractive index fluctuations. These caused the laser beams to wander, consequently making it virtually impossible for them to focus at a given point in the flow. The result was a frequent loss of signal. In fact, even when the signal was present, it could be contaminated with the effect of refractive index fluctuations. This is because the oscillations of the focal volume (carrying the fringes with it) would be interpreted by the receiving optics and signal processor as turbulent fluctuations of velocity. This problem would increase in severity with the increase in the length of the path through the fluid that the beams have to travel before intersecting at the focal volume. After several trials, a suitable technique was found to overcome this difficulty to a large extent. The technique was very simple and consisted of isolating the beams from the fluid over a large part of their path. This was done by using three thin tubes (straws), of 3 mm diameter and 75 mm in length, through which the beams were made to pass before crossing one another at the focal volume. The tubes were suspended in the flow from a special fixture mounted on the LDA traverse. The tubes were filled with cold water and the laser-end of each tube was closed with a Wratten gelatin filter #81B to prevent convection currents through them. The open ends of the tubes were about 25 mm from the probe volume. This intrusion into

Nomenclature

b = half-width
C_1, C_2 = constants associated with the decay of $\bar{U}_m$
D = jet width at exit
D_s = length scale $(D-2\theta)$
K_1, K_2 = constants associated with the growth of b
M = kinematic momentum flux
P = pressure
Pr = Prandtl number
q^2 = $(u^2+v^2+w^2)$
T = temperature
ΔT = temperature excess $(T-T_a)$
t = temperature fluctuation
U = streamwise velocity
U_s = velocity scale defined by equation (2)
u = streamwise turbulent velocity
V = cross-stream velocity
v = turbulent cross-stream velocity
w = turbulent spanwise velocity
x = streamwise direction
y = cross-stream direction
ϵ = eddy viscosity
ϵ_t = eddy thermal diffusivity
ϵ_1 = rate of dissipation of turbulent energy
η = nondimensional cross-stream coordinate y/b
ρ = density
θ = momentum thickness of boundary layer on nozzle wall

Subscripts

a = ambient
e = edge of jet
m = centerline of jet
max = maximum value
o = jet exit
t = pertaining to temperature
u = pertaining to velocity
overbar = time average
prime = rms value

Table 1 Axial development of plane nonbuoyant jets

Investigators	M_∞/M_0 (Reported)	K_{1u}	C_{1u} Reported (based on U_j)	C_{1u} recomputed (based on U_s)	K_{1t}	C_{1t}
Bicknell (from [10])	1.45	0.115	0.112	0.162	0.17	
Bradbury [1]	0.96	0.109	0.160	0.154		
Davies, Keffer, and Baines [14]		0.109	0.149		0.155	0.255
Goldschmidt [11]	0.80	0.099	0.207	0.166		
Gutmark and Wygnanski [3]	0.89	0.110	0.165	0.147		
Heskestad [4]	0.63	0.110	0.27	0.170		
Hussain and Clark [17] (expt. N-50)	1.55	0.118	0.123	0.190		
Jenkins and Goldschmidt [15]					0.130 average	
Knystautas [5]	0.88	0.106	0.18	0.158		
Kotsovinos [10] Experiment P-7	0.87	0.087	0.17	0.148		
Kotsovinos [10] Experiment PLVT-2	0.77	0.109	0.214	0.165	.167	0.20
Miller and Comings [6]	0.83	0.072	0.181	0.150		
Reichardt [7]					0.170	
Vander Hegge [9] Zijnen	0.89	0.095	0.162	0.144	0.141	0.25
Present Study	1.55	0.112	0.093	0.168	0.167	0.194

Table 2 Asymptotic turbulence structure of plane isothermal jets*

Investigators	$u'_{\text{C.L.}}$	$u'_{\max}$	$v'_{\text{C.L.}}$	$v'_{\max}$	$\overline{uv}_{\max}$	ϵ_m
Bradbury [1]	0.210	0.255	0.240	0.240	0.026	0.036
Davies et al. [14]	0.190	0.220	–	–	–	–
Everitt (strong jet) from [2]	0.195	0.224	0.195	0.195	0.020	–
Gutmark and Wygnanski [3]	0.275	0.310	0.205	0.205	0.024	0.0336
Heskestad [4]	0.265	0.290	0.184	0.184	0.020	0.028
Kotsovinos [10] Experiment P-7B	0.220	0.290	–	–	–	–
Miller and Comings [6]	0.245	0.265	0.241	0.241	0.025	–
Reichardt [7]	–	–	–	–	0.025	0.035
Robins (from [2])	0.224	0.237	0.212	0.212	0.020	–
Van der Hegge Zijnen [9]	0.180	–	0.170	–	–	–
Present Study	0.200	0.230	0.170	0.180	0.02	0.028

*All the properties are normalized using $\bar{U}_m$ and b_u. C.L. refers to the centerline.

the flow, through normally not desirable was, however, accepted in this case as no better alternative was available. To examine whether the presence of these tubes altered the basic flow, measurements were made with and without the tubes in the case of isothermal/non-buoyant jets. Results obtained for the cold (isothermal) jet without tubes were compared with those obtained using the tubes in a heated, but non-buoyant jet. In the latter case, the tubes *had* to be used in order that measurements could be made. The comparisons showed no measurable differences even in the Reynolds stress distributions justifying thereby, the use of the tubes in the present studies.

Even with this technique, it was not possible to track the signal close to the jet exit, owing to high temperature gradients there. Hence, the heated jet studies were limited to distances beyond 20 slot widths from the nozzle. Because of possible effects of free surface of the flume, measurements were not made beyond 60 slot widths (corresponding to about 60 slot widths below the free surface).

Contamination of the Ambient. In the heated jet experiment, since hot water was being steadily injected into the system, there arose a need for keeping the flume clean and free of contamination. This was accomplished by withdrawing the warm fluid from the top layers in the flume. To make up for this, sufficient quantity of cold water was continuously introduced at a point far away (about 2 meters) from the jet. The rates of water addition and withdrawal of water could be controlled by valves. The correct valve settings were arrived at by a process of trial and error. It was confirmed from cold jet measurements performed with and without the suction/refill arrangement, that the arrangement had no measurable effect on the jet behavior, over a reasonably wide range of suction/refill rates. The experiments typically lasted several hours, (12–15) at a time. So, despite the above arrangement, there was still some contamination caused, perhaps by molecular diffusion alone. This was partially eliminated by maintaining a very small cross flow velocity, say 1-2 mm/s in the flume. This served to flush the system continuously of hot water. But, this also caused a slight bending of the jet. The maximum inclination of the axis of the jet to the vertical was less than 3 degrees, It is reasonable to assume that this small inclination does not cause any dynamic effects on the jet. The small geometric effect produced, such as asymmetry was corrected by an appropriate rotation/displacement of the co-ordinate system. Details of the correction procedure are given in [16].

Experimental Procedure. Two experiments were performed- one on an isothermal jet [designated as experiment MSC1] and the other on a slightly heated jet [designated as experiment MSC2]. The effects of buoyancy can be considered to be negligible in the heated jet. In both the experiments, the nominal jet exit velocity was 30 cm/s. The nominal exit temperature excess in the "nonbuoyant"-jet experiment was 5°C. A check for two-dimensionality of the flow was made in the isothermal-jet experiment by obtaining distributions of mean and turbulent properties across the jet at several spanwise positions at the axial location $x/D = 40$. These measurements showed that the flow was acceptably two-dimensional over the middle third of the span. For example, the centerline values of $\bar{U}$ and $\overline{uv}$ did not vary by more than 10 percent over the mid 35 percent of the span. The details of these measurements as well as other precautions

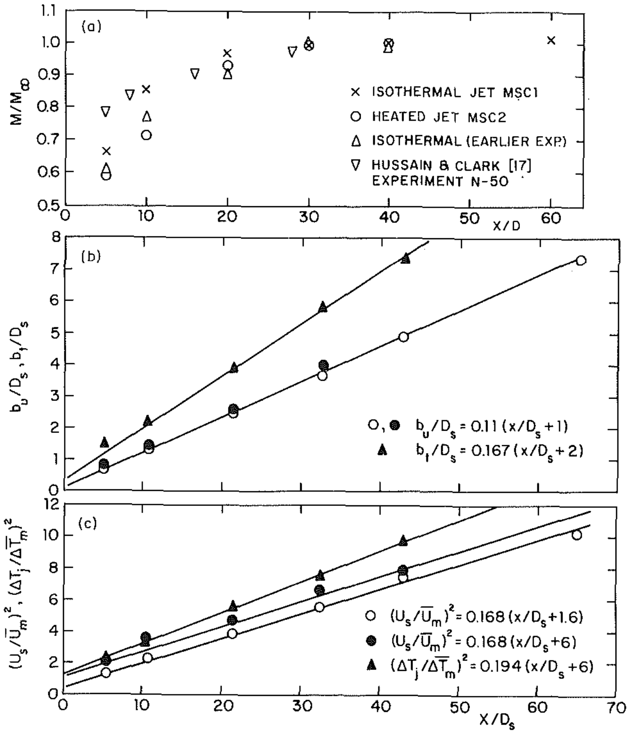

Fig. 2 Kinematic momentum flux, spread and decay of jets MSC1 and MSC2 [open symbols denote jet MSC1 and filled symbols denote jet MSC2 in (b) and (c)]

taken to insure accuracy of measurement are described in [16] and will not be elaborated here. The following are the estimated experimental uncertainties. $\bar{U}$: ± 2.5 mm/s, $\bar{V}$: 1.5 mm/s, ΔT: ± 0.2°C, u', v', t': 5 percent, $\overline{uv}$, $\overline{ut}$, $\overline{vt}$: 10 percent $\overline{u^2v}$, $\overline{v^3}$: 15 percent.

Results and Discusison

Since, the isothermal jet and the heated jet gave similar results for the mean and turbulent properties related to momentum transport, detailed results will generally be presented only for the isothermal jet. Only the results for the last measurement station in the heated jet will be given in these cases for comparison. The mean and turbulent properties associated with heat transfer will be presented for the heated jet. The present data on the significant flow properties of the *asymptotic jet* will be compared with the data reported by earlier investigators. These comparisons are summarized in Tables 1 and 2.

Kinematic Momentum Flux. The kinematic momentum flux across a plane normal to the jet axis is usually defined by

$$M = \int_{-\infty}^{\infty} U^2 dy = \int_{-\infty}^{\infty} (\bar{U}^2 + u'^2) dy \tag{1}$$

and has often been assumed to be a conserved quantity. However, a survey of the literature indicates that this is not what measurements have revealed. Table 1 shows the momentum measured at the last station in the many plane-jet experiments reported in the literature. It is seen that many researchers have measured a decrease in M with axial distance. Kotsovinos [10] attempted to provide an explanation for this decrease in momentum from an induced-flow approach. However, early experiments by Bicknell, (reported in Kotsovinos, [10]) and the more recent experiments of Hussain and Clark [17] showed an increase in M with x. In the latter investigation, the asymptotic momentum flux M_∞ was anywhere between 1.2 M_0 to 1.55 M_0 depending on the initial conditions.

Figure 2(*a*) shows the results from the two present experiments. It is seen that the jet momentum increases from a minimum value near the slot exit to a value about 1.5 times larger at $x/D = 30$ beyond which it remains constant. (The exact value of the momentum flux at the jet exit could not be measured because of instrumentation difficulties.) This constant value can be regarded as the asymptotic momentum M_∞ of the jet. In fact, all the other values shown in Fig. 2(*a*) have been normalized using M_∞ as the scale. Also plotted in Fig. 2(*a*) is the result from an other isothermal-jet experiment performed by the authors. In this case, the nozzle did not have a straightening portion (see Fig. 1) as in the present case and the jet issued immediately after the contraction. It can be seen that the same trend in the evolution of M is observed in this case also. The results of one typical experiment (experiment *N*-50) by Hussain and Clark [17] are also shown in the figure. The present experiments are seen to corroborate their results. Hussain and Clark attributed the momentum increase to the presence of negative pressure in the interior of the jet, supported by the turbulent fluctuations in the cross-stream velocity component. It can be shown from the momentum equation that even small pressure changes can account for significant changes in momentum flux. In fact pressure distributions in the jet have been measured by Hussain and Clark [17], by Miller and Comings [6] and Bradbury [1]. These pressure measurements show negative pressures within the jet and qualitatively support the theory of [17]. However, quantitative verification is possible only if accurate pressure measurements can be made in the near field. But, as pointed out in [17], such measurements are very difficult to make because of the strong turbulence in this region. In the present studies, pressure measurements were not made.

Velocity and Length Scales for the Jet. In view of the above discussion concerning the nonconservation of momentum in the near field of the jet, it is necessary to define appropriate velocity and length scales that characterize the far-field behavior of the jet. Such definitions are also required because many of the jets do not have a top-hat (uniform) profile at the nozzle exit due to the boundary-layer growth on the nozzle walls. Thus, exit centerline velocity as used often in the literature is, in particular, not the appropriate scaling velocity for the jet. In fact, there is a wide variation in the values quoted by different investigators for the rate of decay of the centerline velocity [see Table 1] and this is partly due to the choice of the centerline velocity at the jet exit as the scaling velocity.

We now define a velocity scale U_s for the jet as

$$U_s = \sqrt{\frac{M_\infty}{(D - 2\theta)}} \tag{2}$$

where θ is the momentum thickness of the boundary layer at the nozzle walls at the jet exit. If no measurements in the nozzle can be made, the best guessed value for the given flow conditions can be used to compute θ. In the present case, the nozzle boundary-layer characteristics were not measured, so the displacement and momentum thickness at the exit were estimated assuming laminar flow in the nozzle.

The asymptotic plane jet has no preferred reference length scale and hence any convenient length can be used to normalize axial distances. Here, the use of the length scale D_s, defined by

$$D_s = (D - 2\theta) \tag{3}$$

is recommended. In many experiments $2\theta << D$ and it would be adequate to regard $D_s \simeq D$. It is emphasized that none of the asymptotic growth/decay rates quoted later in this paper depends on the choice of the reference length scale.

Growth Rate. Figure 2(*b*) presents the growth of the width of the velocity and temperature profiles with distance. The jet width is usually measured in terms of its half width b_u (or b_t) which is the distance from the axis to the point where the velocity (or temperature excess) is half the value at the centerline. The data presented for the two jets MSC1 and MSC2 indicate that the asymptotic growth for the half width b_u, can be represented by the linear expression

$$\frac{b_u}{D_s} = K_{1u}[x/D_s + K_{2u}] \tag{4}$$

with an average value of $K_{1u} = 0.110$ and $K_{2u} = 1.0$ for both the jets.

It should be noted that the length scale used here is D_s and not D, the slot width. The growth rate K_{1u} is not affected by the choice of the length scale. The virtual origin, however, is affected. The measured growth rate K_{1u} is in general agreement with those of others as can be seen from Table 1.

It is seen from Fig. 2(*b*) that the growth of the half width b_t of the temperature profile (in the jet MSC2) with x is also linear. However, its rate of growth, K_{1t} is about 0.167 which is larger than that of b_u. Table 1 shows that the result $K_{1t} > K_{1u}$ is in general agreement with the observation of others. However, the numerical value of K_{1u} seems to vary from experiment to experiment depending on the experimental conditions. The present value is in agreement with the experiments of [10] which were performed under approximately similar conditions to the present experiment.

Decay of Centerline Velocity and Temperature Excess. The decay of the maximum velocity in the two jets is shown in Fig. 2(*c*). The decay is seen to be according to the law

$$\left(\frac{U_s}{U_m}\right)^2 = C_{1u}\left[\frac{x}{D_s} + C_{2u}\right] \tag{5}$$

with an average value of 0.168 for C_{1u} for both the jets. C_{2u}, however, is different (as expected because of the difference in the exit conditions) for the two jets. A survey of the literature on plane-jet experiments shows [see Table 1] that the constant C_{1u} (based on $U_s = U_j$) varies widely (from 0.112 to 0.27). The reasons for this variation, as already stated, are non-conservation of momentum, and (possibly) nonuniform velocity profiles at the exit, apart from, of course, experimental errors. It is important to note that experiments in which momentum increased in the nearfield as well as those in which momentum decreased are included in Table 1. It can be seen that the lowest values of C_{1u} correspond to experiments ([10], [17] and present study) in which momentum flux increases in the near field. The values of C_{1u} will be modified if we use the scaling velocity U_s as defined by equation (2), instead of the exit centerline velocity U_j, used by the investigators. The values of the decay constant C_{1u}, recomputed in this manner, are also shown in Table 1. In each case, the momentum M_∞ for obtaining U_s was the asymptotic momentum (momentum at the last measuring station) quoted by the investigators. It is seen that this procedure reduces the scatter in the measured decay constant to the range 0.147–0.190. The scatter that persists even after this correction is applied, should be attributed to uncertainties in the measurements with hot wires/total head tubes and also to insufficient flow development. It can be easily shown (see [16]) that if the velocity distribution in the asymptotic jet is Gaussian and if $K_{1u} = 0.110$, the value of C_{1u} has to be 0.166. The present experimental results are thus self-consistent.

Figure 2(*c*) also shows the variation (in the jet MSC2) of the centerline temperature excess ΔT, plotted in the usual coordinates. It is seen that the decay of ΔT with x can be represented by

$$\left(\frac{\Delta T_j}{\Delta T_m}\right)^2 = C_{1t}\left(\frac{x}{D} + C_{2t}\right) \tag{6}$$

with $C_{1t} \approx 0.194$. This value of C_{1t} agrees with that measured in the experiment of [10], quoted in Table 2. However, Van der Hegge Zijnen [9] and Davies, Keffer, and Baines [14] found $C_{1t} \approx 0.25$. The variation in the development rates of heated jets in different experiments is presumably due to effects of buoyancy becoming significant in the downstream regions of the jet. The values of K_{1t} and C_{1t} are very sensitive to buoyancy effects as has been shown in [10, 12]. The present experiments were performed under conditions of negligible buoyancy, as confirmed from estimating the local Richardson number [16].

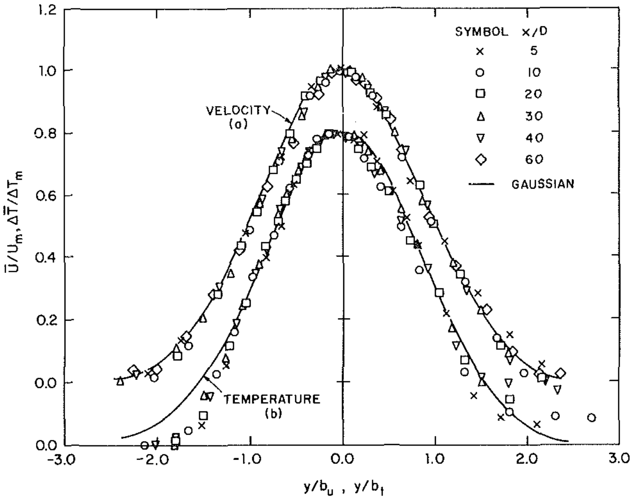

Fig. 3 Distributions of longitudinal mean velocity and mean excess temperature

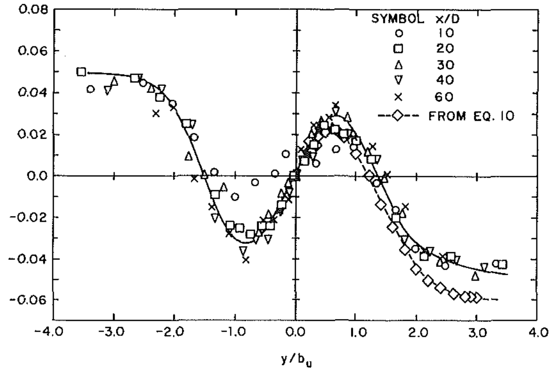

Fig. 4 Distributions of lateral mean velocity

Distributions of $\bar U$, $\bar V$ and $\Delta \bar T$. The distribution of $\bar U$, $\bar V$, and $\Delta \bar T$ across the jet is shown in Figs. 3 and 4 for several axial locations. The axial distances henceforth are referred to in terms of x/D rather than x/D_s for ease of reference. The velocity profiles (in Fig. 3(*a*)) at different stations have been normalized by $\bar U_m$ and b_u. It is seen that the profiles exhibit self-similarity (without any significant scatter) for $x/D > 10$. Slight negative velocities are seen near the edges. This result is believed to be correct, because of the ability of the LDA system used to measure low and negative velocities. The self-similar velocity profile is seen to be described well everywhere except near the edges, by the Gaussian curve

$$\frac{\bar U}{\bar U_m} = \exp(-A\eta_u^2) \tag{7}$$

with

$$A = \ln 0.5$$

The temperature profiles shown in Fig. 3(*b*) are normalized by $\Delta \bar T_m$ and b_t. These profiles also show self-similarity beyond $x/D = 10$ and can also be approximately represented by a Gaussian distribution. The slight asymmetry and nonzero

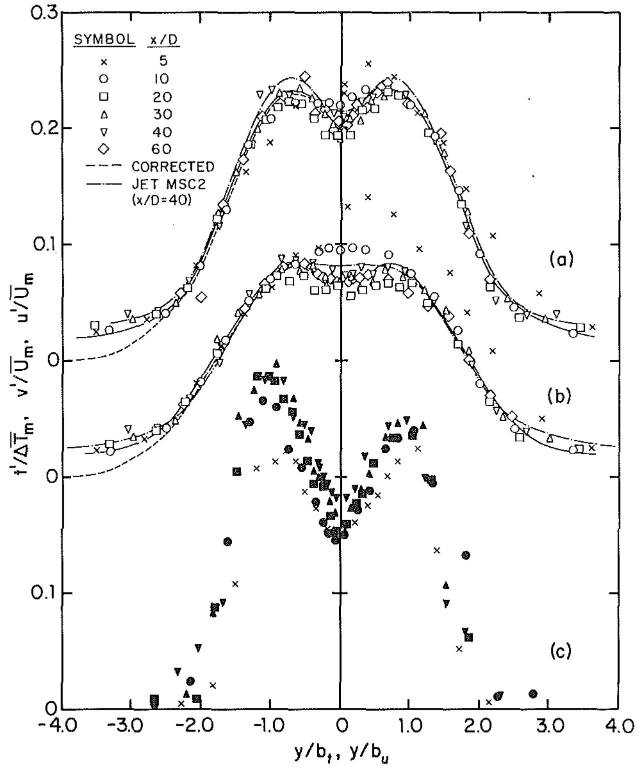

Fig. 5 Distributions of rms turbulent intensities (open symbols denote jet MSC1 and filled symbols denote jet MSC2)

values seen at the right edge of the jet are due to asymmetric contamination of the ambient by the jet fluid.

Cross-Stream Velocity. A direct measurement of the cross-stream mean velocity (albeit with some uncertainty) and hence the rate of entrainment by the jet was possible because of the use of the two-component, frequency-shifted LDA. The distribution of $\bar{V}$ for the isothermal jet is presented in Fig. 4 after normalizing by $\bar{U}_m$. As already mentioned, the profiles have been corrected for inclination of the jet to the vertical by a simple coordinate rotation (described in [16]). This inclination was found to be less than 3 degrees and hence was assumed to have no effect on the flow dynamics. The correction forces the value of $\bar{V}$ to go to zero on the axis but does not significantly alter the edge values. The results presented in Fig. 4 indicate self-similarity and a fair degree of symmetry. It should be noted that the actual velocity $\bar{V}$ is of the order of only a few millimeters per second and even at these low values, the scatter observed in the data is not very large. In this and the other following figures the solid line is a mean line drawn (by eyeball judgement) through the self-similar data corresponding to the downstream locations. From the figures, an average value for the entrainment coefficient, $\alpha = 2\bar{V}_e/\bar{U}_m$ is obtained as 0.090.

The velocity $\bar{V}$ can also be calculated from the measured distribution of $\bar{U}$, using the continuity equation, as follows

$$\bar{V} = -\int_0^y \frac{\partial \bar{U}}{\partial x}dy \tag{8}$$

Assuming the self-similar distribution of equation (7), the above equation can be integrated to yield

$$\frac{\bar{V}}{\bar{U}_m} = 1/2\sqrt{\pi/A}\,\mathrm{erf}(\eta_u\sqrt{A})\left[\frac{1}{\bar{U}_m}\frac{d\bar{U}_m}{dx}b_u + \frac{db_u}{dx}\right] + \frac{db_u}{dx}\eta_u\exp(-A\eta_u{}^2) \tag{9}$$

Assuming asymptotic growth and decay for b_u and $\bar{U}_m$, respectively, one finally gets

$$\frac{\bar{V}}{\bar{U}_m} = [-1/4\sqrt{\pi/A}\,\mathrm{erf}(\eta_u\sqrt{A}) + \eta_u\exp(-A\eta_u{}^2)]\frac{db_u}{dx} \tag{10}$$

The values computed from equation (10) using the measured value of db_u/dx $(=K_{1u})$, have also been plotted in Fig. 4. There is generally good agreement between the calculated and measured values of $\bar{V}$ in the central part of the jet, but in the outer parts of the jet, there is some disagreement. The edge value of $\bar{V}_e/\bar{U}_m$ obtained from the continuity equation is 0.059, while the measured value is about 0.045. This discrepancy is very likely due to errors in measurement of the velocity of the order of a few mm/sec in a region of low turbulence (and hence of low scattering particle density). It can also be due, in part, to the invalidity of the assumptions concerning the asymptotic jet such as the Gaussian distribution of velocity $\bar{U}$.

Distributions of Turbulence Intensities; u', v', and t'. Figure 5 shows the distributions of rms turbulence intensities u' and v' for the isothermal jet and the rms temperature fluctuation t' for the heated jet at the stations surveyed. The turbulent velocity data for the station $x/D = 40$ in the heated jet are also shown for comparison. The velocity data exhibit good symmetry. These profiles become self-similar beyond $x/D = 20$, while the mean velocity distributions were seen to become self-similar a little earlier. The dotted lines shown in the figures correspond to the distirbutions corrected (approximately) for noise in the LDA system (see [16] for details). A comparison of some of the significant turbulence properties of the asymptotic isothermal jet, as measured by LDA in the present experiments, with the hot-wire data reported in the literature is presented in Table 2. The value of $u'/\bar{U}_m$ at the centerline is about 0.20 to 0.21, in the present experiments, which is in agreement with Bradbury's [1] "strong" jet. The peak intensity is 0.23 and occurs at around $\eta_u = 0.71$. These values can be compared with the hot-wire data shown in Table 2, which vary over a very wide range; from 0.2 to 0.27 at the centerline and 0.22 to 0.29 for the maximum value. It is seen that the present measurements are in reasonable agreement with the LDA data for Run P-7B of Kotsovinos [10], in respect of the centerline intensity but not maximum intensity.

The profiles of v'/U_m at the downstream locations are symemtric with a slight but distinct dip near the centerline. This dip can be expected to be a feature of the asymptotic profile, since it is consistent with the fact that the production of turbulent energy is maximum away from the centerline. The dip is not, however, present in the near field. This is also consistent with the limited data available on static pressure distributions across the jet in the near field [6, 17]. As already mentioned, these data indicate negative mean static pressures in the mixing reigon of a jet, with the peak negative pressure occuring on the centerline. These measurements have also shown that the pressure distribution across the jet becomes more and more uniform with the increase in the axial distance. It can be seen from Table 2 that the earlier hot-wire data do not indicate any dip in the downstream v'-profiles $(v'_m = v'_{\max})$. It is again seen that there is disagreement among the different hot-wire data with regard to the intensities of v' in the jet. The present LDA measurements indicate a value of about 0.18 for the maximum intensity and 0.17 at the axis. These are generally lower than the hot-wire data reported by others except Heskestad [4].

The temperature data for jet MSC2 show some asymmetry. This is due to the effect of contamination as already mentioned. It is also seen that the turbulent temperature fluctuations continue to evolve more slowly than the velocity fluctuations and that they have not attained complete self-similarity even at $x/D = 40$, especially in the central part of the jet. The present results are in good agreement with the earlier measurements of [10] in similar flows. The strong dip

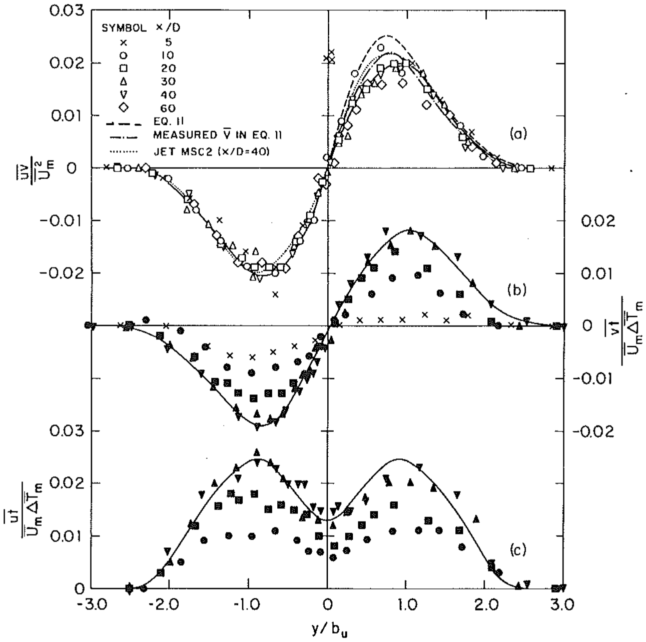

Fig. 6 Distributions of Reynolds shear stress and turbulent heat fluxes (open symbols denote jet MSC1 and filled symbols denote jet MSC2)

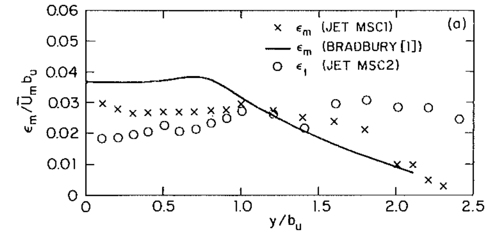

Fig. 7(*a*) Distributions of eddy momentum and thermal diffusivities

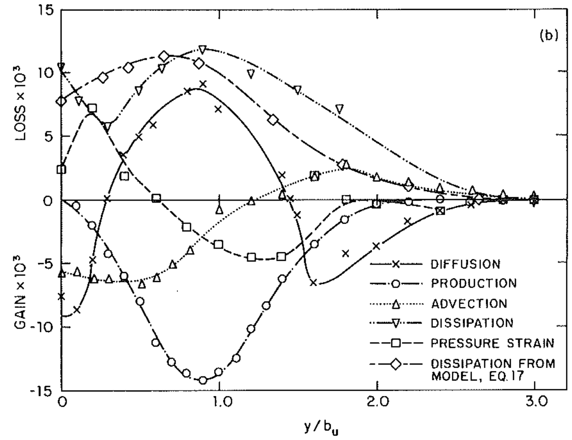

Fig. 7(*b*) Turbulent kinetic energy balance

in the intensity near the centerline is characteristic of nonbuoyant heated jets in which thermal mixing is produced essentially by the hydrodynamic mixing in the mixing layer.

Turbulent Transport Fluxes $\overline{uv}$, $\overline{vt}$, $\overline{ut}$. The shear stress data normalized, as usual, using $\bar U_m{}^2$ and b_u, are shown in Fig. 6(*a*). The distributions show very good similarity, with little scatter for $x/D > 10$. The maximum value is about 0.02 and occurs at around $\eta_u \simeq 0.9$ to 1.0. Reference to Table 2 shows that this value is in agreement with the data of Everitt (reported in [2]) and Heskestad [4], but is lower when compared with the rest of the hot-wire, data by about 15-25 percent. It is also possible to calculate the distribution of uv, by integrating the momentum equation across the jet. The resulting integral momentum equation, after the incorporation of the asymptotic growth and decay relations reduces to

$$\frac{\overline{uv}}{\bar U_m{}^2} = -\left(\frac{\bar U}{\bar U_m}\right)\left(\frac{\bar V}{\bar U_m}\right) + \left(\frac{db_u}{dx}\right)\left(\frac{\bar U}{\bar U_m}\right)^2 \eta_u \qquad (11)$$

The shear stress distribution can then be obtained by substituting $\bar V$ from equation (10) and db_u/dx from equation (4). The result is shown by the broken line in Fig. 6(*a*). There is some disagreement between the calculated and measured values in the central part of the jet but the agreement is good in the outer parts. The lower values of shear stress measured are consistent with the lower rms intensities measured. It is also significant that if, instead of using the theoretical value of $\bar V$ from equation (10), the *measured* value is used in equation (11), the calculated shear stress agrees fairly well with the measurement. This is also shown in Fig. 6(*a*). The measurements are thus internally consistent. The results for $x/D = 40$ obtained from the heated jet experiments are also shown in Fig. 6(*a*). The agreement between the isothermal and heated-jet experiments is an indication of the success of the technique used for overcoming the problem posed by the refractive index fluctuations.

The distributions of the turbulent heat fluxes in the cross stream direction, ($\overline{vt}$) and in the axial direction, ($\overline{ut}$) are shown in Figs. 6(*b*) and 6(*c*), respectively. A very definite evolving trend is noticeable in both the cases upto $x/D = 30$. Beyond this distance, the profiles show near-self-similarity. The peak value of $\overline{vt}/(\Delta T_m U_m)$ is about 0.018 in magnitude which is slightly lower than the value measured for $(|\overline{uv}|_{max}/\bar U^2)$. Note that if the transport mechanisms for momentum and heat were identical, these values should be the same. The axial turbulent flux $[\overline{ut}/(\bar U_m \Delta \bar T_m)]$ has a maximum value of about 0.024. The axial heat transport due to turbulence [which can be obtained from the area under the $\overline{ut}$ curve in Fig. 6(*b*)] has been calculated to be 4 percent of the heat transport due to mean convection. This should be compared with the value of 6 percent reported by Kotsovinos [10].

The eddy diffusivities for the transport of mass and momentum can be obtained from the usual definitions

$$-\overline{uv} = \epsilon_m \partial \bar U/\partial y \qquad (12)$$

and

$$-\overline{vt} = \epsilon_t \partial(\Delta \bar T)/\partial y \qquad (13)$$

Using the fitted Gaussian distributions for $\bar U$ and $\Delta \bar T$ and the smoothed distributions (shown by full lines in Fig. 6) for $\overline{uv}$ and $\overline{vt}$, the distributions of ϵ_m and ϵ_t in the asymptotic jet were obtained. The results are shown in Fig. 7(*a*). It is seen that ϵ_m is fairly constant over a large part of the jet MSC1 with the average value for the nondimensional quantity $(\epsilon_m/\bar U_m b_u)$ being about 0.028. This is generally lower than the values obtained from hot-wire measurements, again as seen from Table 2. For example, the value obtained by Bradbury is 0.036. His data, shown in Fig. 7(*a*), however, indicate constant viscosity over a much smaller part of the jet than indicated by the present measurements. The present heat-flux data indicate a value of about 0.025 for the nondimensional eddy thermal diffusivity $(\epsilon_t/\bar U_m b_t)$. It is seen from Fig. 7(*a*) that ϵ_t is also fairly constant across the jet. The present data, thus, support the assumption of constant turbulent Prandtl number across the asymptotic heated "nonbuoyant" jet. An average value for the turbulent Prandtl number is obtained as

$$P_{r_t} = \frac{\epsilon_m}{\epsilon_t} = \frac{\epsilon_m/\bar U_m b_u}{\epsilon_t/\bar U_m b_t}\,\frac{b_u}{b_t} \approx 0.74 \qquad (14)$$

Turbulent Energy Balance. Using $\bar U_m$ and b_u as the normalizing velocity and length scales, the turbulent kinetic energy equation for an isothermal jet can be written as

$$\frac{b_u}{\bar{U}_m{}^3}\,\frac{\bar{U}}{2}\,\frac{\partial\overline{q^2}}{\partial x}+\frac{b_u}{\bar{U}_m{}^3}\,\frac{\bar{V}}{2}\,\frac{\partial\overline{q^2}}{\partial y}=-\frac{\overline{uv}}{\bar{U}_m{}^2}\,\frac{\partial(\bar{U}/\bar{U}_m)}{\partial\eta}$$
$$-\frac{\partial}{\partial\eta}\,\frac{(\overline{q^2v}/2+\overline{pv}/\rho)}{\bar{U}_m{}^3}-\frac{\epsilon_1 b_u}{\bar{U}_m{}^3} \tag{15}$$

Some of the terms in the above equation were measured directly. The others were estimated indirectly from other measurements making certain assumptions. The pressure-strain term could be estimated only as the closing term in the energy balance. Since the w-component of the turbulent velocity was not measured, the following usual assumptions (see [16]) were made for $\overline{q^2}$ and $\overline{q^2v}$ as

$$\begin{aligned}\overline{q^2}&=3/2(\overline{u^2}+\overline{v^2})\\ \overline{q^2v}&=3/2[\overline{q^2v}+\overline{v^3}]\end{aligned} \tag{16}$$

All the terms on the right hand side of equation (16) were measured. The dissipation rate ϵ_1 was not measured directly, but was estimated indirectly from the measured spectra of u'^2, in the manner suggested by Lawn [18].

The various energy balance terms of equation (15) are shown plotted in Fig. 7(*b*). The distributions appear to be qualitatively similar to the hot-wire results obtained by others but the terms were found to be generally smaller than the hot-wire data. Quantitative differences are of the order of 10–30 percent. The turbulent production term is maximum near the maximum shear stress point. Its value of 0.014 from the present measurements, was found to be slightly lower than that of others, (for example, 0.017 of [1]) excepting Heskstad [4]. This is, of course, due to the lower shear stress measured in the present experiments. From Fig. 7(*b*), it is seen that there is a net diffusion of turbulent energy into the central part ($0 < \eta < 0.3$) as well as into the outer part ($\eta \geq 1.4$) from the region $0.3 \leq \eta \leq 1.4$ where most of the turbulent energy is produced. The diffusion curve integrates very nearly to zero (the area under this curve is only 2.8 percent of the total production), indicating that the estimation of this term is reasonably satisfactory. The distribution of the dissipation rate exhibits a peak away from the center, similar to the profile of the turbulent kinetic energy. This distribution is consistent with the dissipation rate model usually used in the computation of turbulent flows namely

$$\epsilon_1=C_D(\overline{q^2})^{3/2}/L_D \tag{17}$$

where L_D is the dissipation length scale. In fact, the values of ϵ_1 were calculated in the present case, using the standard assumptions for C_D and L_D (see [16]), and the results were found to agree reasonably well with the distribution shown. This can be seen from Fig. 7(*b*). Most reported measurements of ϵ_1, however, show a much higher and fairly constant value near the central part of the jet. For example, Bradbury's [1] experiments indicate a maximum value of about 0.018 for $\epsilon_1/\bar{U}_m b_u^3$ compared to the present value of about 0.012.

The pressure-strain term obtained by difference is fairly large. If this result is correct it shows that this term plays a significant role in transporting energy from the central part ($\eta < 0.6$) to the outer part ($\eta > 0.6$) of the jet. It would then be important to model this term correctly in numerical calculations of the plane jet.

Conclusions

1 The present experiments have provided a very useful set of LDA data on the asymptotic properties of plane isothermal and heated jets. The special technique used in this study has made it possible to use LDA in a nonisothermal environment. The results obtained are self-consistent and repeatable.

2 The mean properties of the asymptotic jet agree with existing information on these flows. The turbulent velocities and fluxes however, as measured by the LDA, are lower than the values usually reported from hot-wire measurements, and the theoretical values obtained from the assumption of Gaussian velocity distribution. Further study is needed to understand the reason for these differences.

3 The apparent scatter in the reported asymptotic decay rates of the centerline velocity can be reduced by scaling the results with the asymptotic jet momentum rather than with the exit velocity.

Acknowledgment

This work was supported by the National Science Foundation under grant numbers ENG-77-22756 and CME-80-06797. This support is gratefully acknowledged.

References

1 Bradbury, L. J. S., "The Structure of a Self-Preserving Turbulent Plane Jet," *J. Fluid Mech.*, Vol. 23, 1965, p. 31.

2 Everitt, K. W., and Robins, A. G., "The Development and Structure of Plane Jets," *J. Fluid Mech.*, Vol. 88, 1965, p. 563.

3 Gutmark, E., and Wygnanski, J., "The Planar Turbulent Jet," *J. Fluid Mech.*, Vol. 73, 1976, p. 465.

4 Heskestad, G., "Hot Wire Measurements in a Plane Turbulent Jet," ASME *Journal of App. Mech.*, Vol. 32, 1965, p. 721.

5 Knystautas, R., "The Turbulent Jet from a Series of Holes in Line," *Aero Quart.*, Vol. 15, 1964, p. 1.

6 Miller, D. R., and Comings, E. W., "Static Pressure Distribution in a Free Turbulent Jet," *J. Fluid Mech.*, Vol. 3, 1957, p. 1.

7 Reichardt, H., "Gesetzmaβigkeiten der Freien Turbulenz," *VDI Forschung sheft*, 1942, p. 414.

8 Sato, H., "The Stability and Transition of a Two-Dimensional Jet," *J. Fluid Mech.*, Vol. 7, 1960, p. 53.

9 Van der Hegge Zijnen, B. G., "Measurements of the Velocity Distribution in a Plane Turbulent Jet of Air," *Appl. Sci. Res.*, Vol. 7, 1957, p. 256.

10 Kotsovinos, N. E., "A Study of the Entrainment and Turbulence in a Plane Buoyant Jet," W. M. Keck Laboratory of Hydraulics and Water Resources, Rep. No. KH-R-32, California Inst. of Technology, 1975.

11 Goldschmidt, V. W., and Young, M. F., "Energy Spectrum and Turbulent Scales in a Plane Air Jet," *Proceedings of the 4th Biennial Symposium on Turbulence in Liquids*, Rolla-Missouri, 1975, p. 39.

12 Kotsovinos, N. E., and List, E. J., "Plane Turbulent Buoyant Jets. Part I: Integral Properties," *J. Fluid Mech.*, Vol. 81, 1977, p. 25.

13 Bashir, J., and Uberoi, M. S., "Experiments on Turbulent Structure and Heat Transfer in a Two-Dimensional Jet," *Phys. Fluids*, Vol. 18, 1975, p. 405.

14 Davies, A. E., Keffer, J. F., and Baines, W. D., "Spread of a Heated Plane Turbulent Jet," *Phys. Fluids*, Vol. 18, 1975, p. 770.

15 Jenkins, P. E., and Goldschmidt, V. W., "Mean Temperature and Velocity in a Plane Turbulent Jet," ASME JOURNAL OF FLUIDS ENGINEERING, 1973, p. 581.

16 Chandrasekhara, M. S., "Study of Vertical Plane Turbulent Jets and Plumes," Ph.D. thesis, 1983, The University of Iowa.

17 Hussain, A. K. M. F. and Clark, A. R., "Upstream Influence on the Near Field of a Plane Turbulent Jet," *Phys. Fluids*, Vol. 20, 1977, p. 1416.

18 Lawn, C. J., "The Determination of the Rate of Dissipation in Turbulent Pipe Flow," *J. Fluid Mech.*, Vol. 48, 1971, p. 477.

R. L. Bass
Department Director.
Mem. ASME

E. B. Bowles, Jr.
Senior Research Engineer.
Assoc. Mem. ASME

Department of Mechanical Sciences,
Southwest Research Institute,
San Antonio, Texas 78284

R. W. Trudell

J. Navickas

J. C. Peck

McDonnell Douglas
Astronautics Company,
Huntington Beach, Calif.

N. Yoshimura

S. Endo

Tsu Research Laboratory,
Nippon Kokan K. K. Tsu, Japan

B. F. M. Pots
Koninklijke-Shell/
Laboratorium, Amsterdam,
Amsterdam, Netherlands
(Shell Research B.V.)

Modeling Criteria for Scaled LNG Sloshing Experiments

This paper presents an overview of the current state-of-the-art in scale modeling of liquefied natural gas sloshing in ship tanks. The numerous potentially significant scaling parameters are discussed in detail and laboratory test data illustrating the effects of the important scaling parameters are presented. In view of current knowledge, an indication of appropriate scaling criteria is presented and recommendations for additional research efforts are outlined.

Introduction

Background. Potentially damaging loads can result from sloshing liquids in partially filled (slack) cargo tanks. This has been realized by the marine industry for years, and with the advent of the supertanker and large liquefied natural gas (LNG) ships, sloshing loads have been of even greater concern. In the case of LNG ships, certain operational constraints call for the transport of liquid in slack tanks, and, in addition, the absence of tank internals results in no damping of the liquid motions. Typical operational fill levels are 95 to 97 percent because of boil-off, and liquid dynamic loads can be significant even in these fully loaded conditions. Also, as ship tanks have grown in size, the probability of resonant sloshing has increased since resonant sloshing periods and ship motions more closely match. In view of this, a concentrated activity has been undertaken by various worldwide laboratories to establish sloshing loads in LNG cargo tanks. Experimental programs have been conducted using instrumented scale-model tanks. These test programs have covered many different ship tank geometries, excitation amplitudes and frequencies, and liquid fill depths. A comprehensive review of these studies is provided by Bass, et al. [1].

Historically, scale model experiments were conducted since large amplitude sloshing was not amenable to the analytical

---

Contributed by the Fluids Engineering Division of THE AMERICAN SOCIETY OF MECHANICAL ENGINEERS and presented at the ASME Applied Mechanics, Bioengineering, and Fluids Engineering Conference, San Antonio, Texas, June 1983 at the Symposium on Rapid Fluid Transients in Fluid-Structure Interactions. Manuscript received by the Fluids Engineering Division, November 8, 1983.

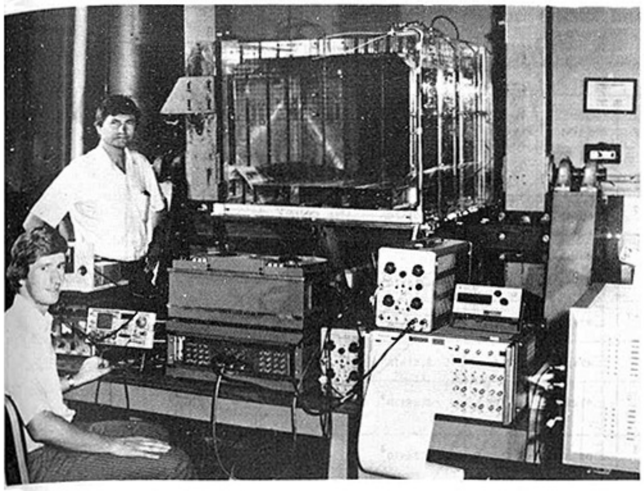

Fig. 1 Prismatic model tank lab setup with associated instrumentation

prediction of tank wall impact pressures. However, in the past few years significant progress has been made by Navickas et al. [2] through the use of two-dimensional numerical solutions based on Marker-and-Cell techniques which can include both viscous and compressibility effects. Even with these analytical advances, the numerical solutions are limited in their utility and scale model experiments are still used extensively to establish sloshing loads. The numerical solutions have allowed an assessment of the effects of fluid and structural properties on sloshing pressures and, as such, have provided additional insight into scaling considerations.

Objectives. The proper reproduction in model scale of the dominant phenomena which affect impact pressures in a full scale tank of 50,000 cubic meters carrying LNG is not trivial. In fact, the proper scaling criteria has been the subject of considerable discussion and debate among the sloshing community [1]. The objectives of this paper are to: (1) provide a comprehensive overview of the factors affecting the scaling of sloshing loads for a liquid transported at its vapor pressure, and (2) to present recent experimental data that provide important new information pertaining to slosh scaling.

Although the results in this paper are pointed at LNG, they can be generalized to the scaling of any liquid sloshing at its vapor pressure.

Model Experiments

Typical Model Test Configuration. The majority of scale model tests have investigated LNG tanks with a prismatic geometry. The top and bottom corners of the prismatic tanks are chamfered and little or no internal structure is present. This is representative of the full scale tanks. A smaller number of tests have been conducted on spherical tanks. The principal tank dimension has been on the order of one meter or less, resulting in a geometric scale factor ranging from about 1/30th to 1/50th scale. Figure 1 shows a typical scale model prismatic tank and associated instrumentation in the laboratory.

Several liquids have been used in model testing to simulate LNG. The choice of liquid usually depends on the particular physical or thermodynamic phenomena being modeled. Past experiments have studied such effects as liquid viscosity, liquid and ullage gas compressibility, and ullage vapor condensation. Some of the more common model liquids and their physical properties are included in Table 1. However, for cost and convenience, the majority of the model tests performed to date have used water for the test liquid. In recent years, several test programs have used scaled ullage pressures to improve the simulation.

Another important aspect of the scale model testing is the excitation motion of the model tank. Most model testing has been performed using one-degree-of-freedom systems; meaning the tank undergoes a single translational or rotational motion. The motion can represent surge, sway, or heave in the translational mode or pitch, roll, or yaw in the rotational mode. It is generally accepted that sway and heave are the dominant translational motions and pitch and roll are the dominant rotational motions. Recently, some multi-degree-of-freedom simulations have been conducted to evaluate coupling effects that may be present with multi-

Nomenclature

A = area
a = acceleration
C = speed of sound
c = specific heat
C' = effective speed of sound in a liquid with entrained vapor bubbles
E = bulk modulus
F = external force(s)
g = acceleration of gravity
H = tank height
h = static liquid filling height or enthalpy
K = nondimensional parameter or spring constant
k = real effects constant in compressible liquid impact pressure equations
LNG = liquefied natural gas
M = mass
m = gas-liquid volume fraction
P = dynamic pressure
R = distance from the center of a slosh wave impact area to the nearest liquid free surface where pressure relief occurs
T = time
t = temperature
V = velocity
$\not{V}$ = volume
x = translational tank excitation amplitude or coordinate vector
Z = acoustic impedence
α = ratio of acoustic impedences of two different materials
γ = ratio of specific heats (isentropic exponent)
Δ = incremental change
λ = ratio of model scale characteristic tank length to the full scale characteristic tank length
μ = dynamic viscosity
ν = kinematic viscosity
ρ = density
σ = surface tension
τ = slosh pressure impact duration
ϕ = rotational excitation amplitude of a ship tank
l = characteristic tank dimension (usually tank length in the direction of slosh wave motion)

Subscripts

C = Cauchy number
Con = condensation number
fg = evaporation
G = gas
L = liquid
m = model scale
n = percent exceedance pressure level (where n is between 0 and 100 percent)
o = stagnation condition or volumetric fraction
P = pressure
p = prototype or full scale
Re = Reynolds number
s = surface
sat = saturation
u = ullage
v = vapor or vapor pressure
w = wall

Table 1 Properties of full-scale and model scale liquids with dimensionless groups [7]

Model Liquids at 25°C (unless noted otherwise)

Liquid	Tank Length ℓ (m)	Density ρ_L (kg/m^3)	Dynamic Viscosity μ_L (kg/m-s)	Kinematic Viscosity ν_L (m^2/s)	Bulk Modulus E_L (kPa)	Vapor Pressure P_v (kPa)	R_e $\frac{\rho_L g^{1/2} \ell^{3/2}}{\mu_L}$	K_c^{-1} $\frac{\rho_L g \ell}{E_L}$
LNG	30	474	0.000118	2.5×10^{-7}	1.63×10^{7}	101	2.05×10^{9}	8.55×10^{-6}
CH_2Cl_2 40°C	1.0	1340	0.00037	2.87×10^{-7}	(Assumed) 1.87×10^{7}	101	1.13×10^{7}	7.02×10^{-7}
CH_2Cl_2	1.0	1340	0.00042	3.15×10^{-7}	1.87×10^{7}	46	9.99×10^{6}	7.02×10^{-7}
H_2O	1.0	1000	0.000893	8.93×10^{-7}	2.43×10^{7}	2.3	3.51×10^{6}	4.03×10^{-7}
60% Glycerin 40% H_2O	1.0	1150	0.00882	7.68×10^{-6}	2.97×10^{7}	<100	4.08×10^{5}	3.79×10^{-7}
Hydraulic Oil	1.0	880	0.065	7.4×10^{-5}	2.09×10^{7}	<100	4.24×10^{4}	4.13×10^{-7}
86% Glycerin 14% H_2O	1.0	1230	0.091	7.4×10^{-5}	5.07×10^{7}	<100	4.23×10^{4}	2.38×10^{-7}
Glycerin	1.0	1260	0.954	7.57×10^{-4}	5.44×10^{7}	<100	4.13×10^{3}	2.27×10^{-7}

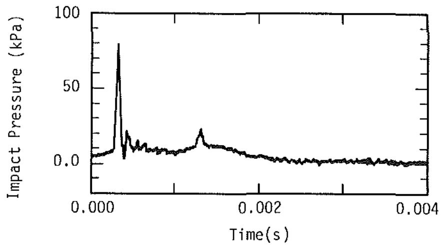

Fig. 2 Typical impact pressure time history

degree-of-freedom excitations and to simulate ship motion in several important degrees-of-freedom. Some of these studies have used complete six-degree-of-freedom motion simulation. The amplitudes of the motions usually are less than one-tenth (peak to peak) of the principle tank length for translational motions and less than 0.3 radians (peak to peak) for rotational motions.

The excitation may be either harmonic or random. Harmonic simulations are usually conducted at the frequency that will cause resonant liquid sloshing in the tank. This condition causes the largest wave amplitudes and the highest impact pressures on the tank boundaries. Random simulations, based on predicted tank (ship) motions, more accurately simulate in-service conditions. Random simulations have become more prevalent in recent years.

Past studies have shown that liquid filling levels between about 5 and 98 percent can generate significant liquid impact forces on the tank boundaries. The most recent studies have concentrated on predominant operational filling levels above 90 percent where liquid impact loading of the tank top is likely to occur. Since the tank top is the weakest part of the tank, an accurate definition of the sloshing-induced dynamic loading on the tank top is important to the designer.

Typical Data Recorded. The most prevalent data recorded during model tests are impact pressures (on the tank walls) generated by the sloshing of the liquid cargo. Other measured parameters include liquid impact velocities (which also indicate the magnitude of the impact loads) and the total forces and moments acting on the tank. The most important measurement to setting tank design load criteria is the local slosh-induced impact pressure on the tank wall. A typical pressure-time history for a slosh impact from a model test is shown in Fig. 2. Both the pressure magnitude and duration are of importance for design considerations.

Typical Data Presentation. Measured pressure data from previous experiments is presented in a nondimensional format by the following impact pressure coefficient:

$$K_p = \frac{P}{\rho_L g l} \tag{1}$$

Most investigators also include a nondimensional tank excitation amplitude in equation 1 as follows:

$$K_p = \frac{P}{\rho_L g l \phi} \tag{2}$$

Where ϕ is the rotational excitation amplitude. For translational motion, ϕ is replaced by x/l where x is the excitation amplitude. A similar nondimensionalized force coefficient is used if forces are being evaluated.

Due to the random nature of the sloshing phenomena in a ship tank, large variations in the impact pressure magnitude and duration occur from cycle to cycle, even with harmonic excitation. Consequently, a large number of cycles of test data are required to provide an accurate indication of the worst-case pressures that can be expected during the service life of a ship tank. Over the years, researchers have used a number of different methods to present long-term pressure data. Some have measured pressures for a given number of resonant (worst-case) sloshing cycles and presented the maximum and average pressures measured during the test. The total number of resonant slosh cycles for these types of tests range from several hundred to several thousand.

Another data presentation method uses exceedance level pressure values. With this format, a random or harmonic motion test is conducted and all impact pressures are measured and recorded. Then, various exceedance pressure levels are presented for the test results. For example, a 10 percent exceedance level pressure (P_{10}) is greater in magnitude than the lowest 90 percent of the pressure spikes measured during the test.

The current state-of-the-art uses the short-term scale-model pressure data as the basis for predicting long-term pressures. Usually, the test data are analyzed with an appropriate statistical model and then long-term statistical predictions are generated. The long-term pressure data are presented in exceedance level form. For design purposes, the 1 to 10 percent exceedance values are generally used.

Scaling Complexities

Phenomena. Model studies to date [1] have utilized

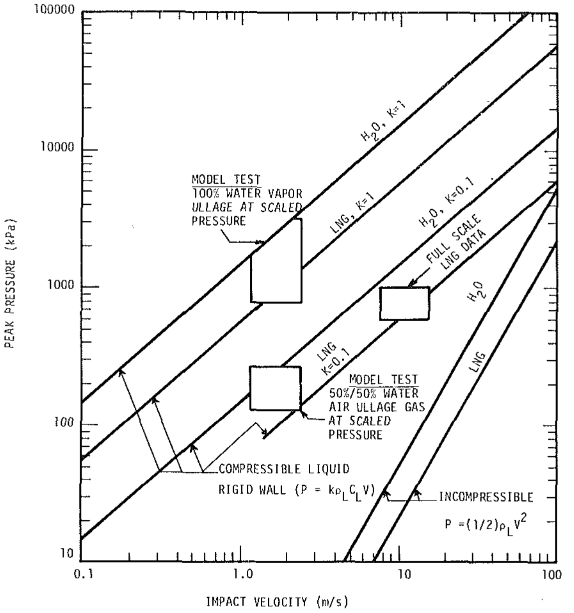

Fig. 3 **Estimated impact pressure/velocity relationships from almost-full prismatic tank slosh tests and analyses**

Froude and Euler (incompressible) scaling to predict full-scale loads where no allowance for real fluid effects is considered. Depending on the cargo to be carried, some of these fluid properties could be important. For example, LNG is transported at its vapor pressure, and, therefore, thermodynamic (vapor condensation) effects could be important. Also, LNG has a low viscosity compared with water, and model tests using water could produce nonconservative predictions of full-scale loads if the model tests were overdamped. Also, compressibility of the impacting liquid/vapor is important in scaling sloshing pressures.

For geometric similitude between model (m) and full scale (p), Froude and Euler scaling yields the following scaling criteria:

λ = model length/full-scale length (scale factor)

$$V_m = V_p \lambda^{1/2} \text{ (velocity)} \tag{3}$$

$$T_m = T_p \lambda^{1/2} \text{ (time)} \tag{4}$$

$$a_m = a_p \text{ (acceleration)} \tag{5}$$

$$P_m = P_p (\rho_{L_m}/\rho_{L_p})(\lambda) \text{ (static and dynamic pressure in liquid)} \tag{6}$$

With Froude scaling, the gross liquid surface shape at any instant in time (in the sloshing cycle) will be geometrically simulated if liquid inertia and gravity forces are dominant as they will be for large amplitude sloshing. The velocities of the model waves will be smaller ($V_p \lambda^{1/2}$) but the model time between velocity changes will be faster by $\Delta T_m = \Delta T_p \lambda^{1/2}$.

The liquid impact pressure on the tank will be established by

1. the surface shape, velocity and density of the approaching liquid;
2. the elasticity (compressibility) of the cushioning entrapped gas which is affected by ullage gas pressure and composition;
3. the compressibility of the liquid, which includes bubbles and entrapped gases;
4. a change of state of entrapped gas under increasing pressure (condensation; that is, thermodynamic effects), and
5. the structural properties of the wall.

The impact velocity is dependent on Items 1, 2, and 3. The gross surface shape and wave velocity are maintained similar by Froude scaling; however, out-of-scale viscous, surface tension or thermodynamic related forces can alter the local shape and bubble content, thus affecting Items 1, 3, and 4. The ullage pressure and gas composition will affect Items 2, 3, and 4 because pure vapor in the ullage space changes the release rate of the liquid from the tank ceiling.

For sloshing with a gas above the liquid, the compressibility of the liquid/gas impact is important if trapped ullage gas cushions the impact, as might occur in the tank top corners at near-full sloshing. To provide the correct elasticity of the ullage gas in model scale [3] requires ullage pressure, P_u, to scale as

$$P_{u_m}/P_{u_p} = (\rho_{L_m}/\rho_{L_p})\lambda \tag{7}$$

which means that ullage pressures scale the same as static and dynamic liquid pressures. For model tests conducted with atmospheric ullage pressure simulating full-scale sloshing wtih atmospheric ullage pressures, the model gas is too stiff; thus, pressures measured in model scale could be lower than if the correct ullage pressure (gas stiffness) were used.

For correct impact pressure scaling when liquid compressibilty is considered

$$P = k\rho_L C_L V \tag{8}$$

where k accounts for real effects such as surface characteristics and entrapped gas bubbles. The factor k can be a maximum of 1.0 but typically is on the order of 0.1 [4]. If Froude scaling sets wave velocity, then

$$P_p/P_m = (\rho_{L_p}/\rho_{L_m})(C_{L_p}/C_{L_m})(1/\sqrt{\lambda}) \tag{9}$$

for $k_m = k_p$. This implies that all forces which affect the surface shape (which has a significant effect on k) are correctly modeled. In nearly all previous model testing, Froude scaling was used for velocity and incompressible pressure scaling and no ullage pressure scaling was attempted; thus

$$P_p/P_m = (\rho_{L_p}/\rho_{L_m})(1/\lambda) \tag{10}$$

If P_u or thermodynamic effects are not important, the scale factor is conservative by $1/\lambda$ compared with $1/\lambda^{1/2}$ (assuming $C_{L_m} = C_{L_p}$). The assumption that $C_{L_m} = C_{L_p}$ implies that the bulk modulus of elasticity for each liquid is known.

Typical Results. The pressure-time histories of recorded model pressures have the characteristic short duration pressure spike (see Fig. 2) which is indicative of a loading controlled by compressible phenomena. An evaluation of the peak pressure levels and wave velocities in model scale provide additional insight regarding compressible versus incompressible scaling.

A recent set of consistent experimental and theoretical data also indicates that the dominant phenomena in ceiling impacts are compressible in nature. This is illustrated in Fig. 3, where equation (8) has been plotted for $k = 1$ and 0.1 along with the relevant $(1/2)\,\rho_L V^2$ pressure. Also shown on this diagram are the approximate ranges of upper-bound experimental data. The model scale pressures are the three highest measured in recent tests conducted by the authors which used scaled ullage pressure and simulated the full-scale LNG ship damage experience reported in [5]. The full-scale pressures were estimated from the damage thresholds found in [5] and similar tests. The impact velocities were calculated using the slosh code presented in [2].

First, looking at the Fig. 3 model test data with 100 percent-water-vapor ullage gas, one sees that pressures in the range of the ideal $\rho_L C_L V$ pressures (i.e., $k = 1.0$) with rigid walls were obtained. These data represent a fundamentally traceable reference point in the physics of sloshing. However, these pressure are obviously too high to be scalable to the full scale, even using the compressible scaling law. Furthermore, since they lie vastly in excess of any reasonable value for

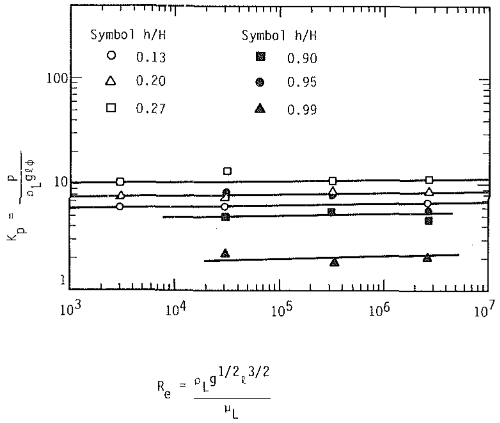

Fig. 4 Effect of liquid viscosity on measured impact pressures at resonance [7] and [8]

$P/((1/2)\rho_L V^2)$, they do not arise from incompressible liquid behavior.

Second, looking at the Fig. 3 model test data with 50 percent water vapor and 50 percent air as the ullage gas, one sees that the impact pressures are reduced dramatically. Nevertheless, the pressures are still far in excess of possible incompressible pressures, so the compressible behavior applies, with a k of about 0.1 arising from ullage gas cushioning. From this, one can also say that the pure water vapor ullage condensed so easily that it acted as nearly a perfect vacuum.

Third, looking at the Fig. 3 full-scale data; one sees that they are also consistent with a k of about 0.1. The full-scale pressures shown have a higher k because they correspond to a larger exposure time and thus represent somewhat rarer statistical occurrences, but this is compensated for, at least partly by the tendency for k to be lower with the more flexible walls of the full-scale tank. These data are inconsistent with incompressible liquid behavior. Finally, the full-scale data corroborate theoretical expectations that pure water vapor at scaled ullage pressure condenses much more readily than LNG vapor at atmospheric pressure.

The data on Fig. 3 form a consistent set for the almost full tank case when viewed as arising from compressible liquid behavior, and cannot be explained in terms of incompressible liquid behavior. The compressible behavior represented by equation (9) is recommended as the appropriate scaling law for this case consistent with model tests conducted at scaled ullage pressure. No parallel experiments exist for the 20–30 percent fill ratio case.

Dimensional Analysis. Considering the various parameters which could affect the scaling of impact pressures leads to

$$\frac{P}{\rho_L V^2} = f\Big[\frac{V^2}{gl}, \frac{\rho_L V l}{\mu_L}, \frac{P_u}{\rho_L V^2}, \frac{E_L}{\rho_L V^2}, \frac{P_u - P_v}{\rho_L V^2},$$

$$\frac{\rho_G}{\rho_L}, m_o, \frac{\rho_L V^2 l}{\sigma_L}, \frac{\rho_L c_L (t_w - t_{\text{sat}})}{\rho_v h_{\text{fg}}}, \qquad (11)$$

$$\text{wall properties, geometry}\Big]$$

or to

$$\frac{P}{\rho_L g l} = f'\Big[\overset{①}{\frac{\rho_L g^{1/2} l^{3/2}}{\mu_L}}, \overset{②}{\frac{P_u}{\rho g l}}, \overset{③}{\frac{E_L}{\rho g l}}, \overset{④}{\frac{P_u - P_v}{\rho_L g l}},$$

$$\overset{⑤}{\frac{\rho_G}{\rho_L}}, \overset{⑥}{m_o}, \overset{⑦}{\frac{\rho_L g l^2}{\sigma_L}}, \overset{⑧}{\frac{\rho_L c_L (t_w - t_{\text{sat}})}{\rho_v h_{\text{fg}}}}, \qquad (12)$$

$$\overset{⑨}{\text{wall properties}}, \overset{⑩}{\text{geometry}}\Big]$$

where Froude scaling is included in the appropriate terms in equation (12).

The first term in equation (12) accounts for viscous effects, the second term for ullage gas compressibility, the third term, the well-known Cauchy number, for liquid compressibility, the fourth term reproduces boiling liquid effects, the seventh term, surface tension effects, and the eighth term, liquid thermodynamic properties and the coupled effect of temperature and pressure. The seventh term has been shown, on the basis of theoretical considerations [6], to be unimportant as the surface tension forces are trivial compared to other forces which are dominant in the gross sloshing motions. Terms 2, 3, 4, 5, 6, and 8 relate to both compressibility and thermodynamic effects. Term 5 requires that the liquid-to-gas density ratio in the model be equivalent to the prototype, and term 6 requires that the gas-liquid volume fraction, m_o, be simulated.

It is obviously impossible to maintain similitude for all the terms in equation (12). Therefore, as is usually the case in scale model studies, some compromise must be made. In previous studies, geometrically similar, rigid wall models were used and only Froude and Euler scaling was considered important, i.e., $f' =$ constant. However, it was recognized that the compressibility and thermodynamic effects were potentially important but Froude/Euler scaling was used to eliminate the complexities of compressibility/thermodynamic scaling. This was justified on the basis of conservatism (scaling by $1/\lambda$ instead of $1/\sqrt{\lambda}$) and assuming that by not scaling ullage pressure this conservation would not be offset. Because of practical limitations in ship tank design, this conservatism may be unwarranted. As a result, research has continued to provide information on the LNG scaling effects discussed above. The important results of this research are discussed in the following.

Scaling Considerations

Viscous Effects. The Froude modified Reynolds number, $\text{Re} = \rho_L g^{1/2} l^{3/2}/\mu_L$, for LNG in a full scale tank is $\sim 2 \times 10^9$. For water in model scale, $\text{Re} = \sim 3.5 \times 10^6$ which implies that out-of-scale viscous damping could cause an improper reduction in measured model pressures. To evaluate viscous effects, scale model sloshing experiments have been conducted [7] by varying Re over a range from 4.1×10^3 to 1.1×10^7 by using six different model test liquids. Impact pressures were recorded for resonant, large amplitude harmonic liquid sloshing at tank filling levels ranging from 13 to 27 percent. Figure 4, which shows the results of these experiments, indicates that impact pressures are essentially constant over the Re range investigated. These results imply that for large amplitude sloshing, viscous forces are of secondary importance.

Additional viscous effects tests have been conducted [8] at high fill levels (above 90 percent) since it was postulated that viscous damping might be more dominant at high fill levels because of greater surface contact between the slosh waves and the tank top and end walls. The results in Fig. 4, for fill levels ≥ 90 percent also show that viscous damping has an insignificant effect on measured pressures over the Re range investigated.

Although these data are for $\text{Re} < 2 \times 10^9$, representative of full scale, the range covered by the model tests (4×10^3 to

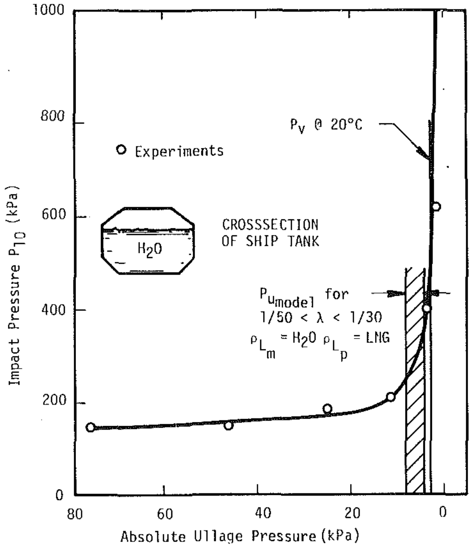

Fig. 5 Impact pressure versus ullage pressure [9]

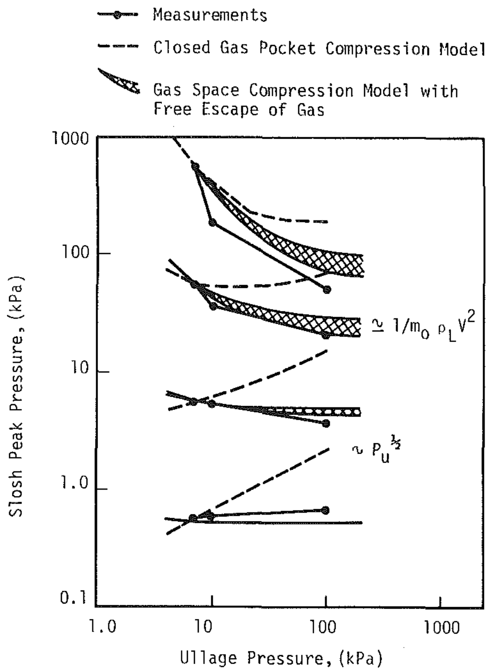

Fig. 6 Slosh peak pressure versus ullage pressure

1×10^7) is considered sufficient to show that viscous scaling need not be reproduced in model testing. The pressures presented in Fig. 4 are average values for 25 to 200 cycles for $0.13 \leq h/H \leq 0.27$ and 200 cycles for $h/H \geq 0.90$ of resonant sloshing in the fundamental mode. Also, all the data were obtained with air at atmospheric pressure in the ullage space. More recent studies [1] have shown the need to obtain at least 200 cycles of resonant sloshing pressure data to provide an accurate measure of the average impact pressure. Also, the need to scale ullage pressure for a more exact modeling of compressibility phenomena has been established. However, in spite of the limitations of other studies [7, 8], it is believed that the results adequately show that viscous effects are secondary in the scaling of large amplitude nonlinear sloshing impact pressures.

When low amplitude (linear) sloshing occurs, viscous effects become much more important as the viscous forces become larger compared to inertial forces. Results in [3] show that for excitation amplitudes of $x/l < 0.01$, viscous forces must be considered in scaling. However, these conditions are not of interest in determining worst-case tank impact loads.

Liquid Compressibility Effects. The effects of liquid compressibility on scale model impact pressure magnitudes were also investigated in [7], for atmospheric ullage pressure. Two model liquids providing Cauchy numbers of 1.99×10^{-7} and 3.46×10^{-7} and with equivalent $Re = 3.2 \times 10^4$ were utilized. The bulk modulus for these two liquids is 5.07×10^7 and 2.07×10^7 kPa, respectively. As for the viscous scaling tests, 25 to 100 cycles of impact pressures were recorded during resonant sloshing at filling levels of 15 and 20 percent. No significant differences in the average impact pressures were recorded for the two values of $E_L/\rho_L gl$. The results of these tests show that the liquid compressibility did not have a significant effect on the measured impact pressure when the tests were conducted with air in the ullage space at a pressure of ~100 kPa. No attempt has been made to determine the compressibility effects of the impacting liquid at scaled ullage pressures and high filling levels where one expects compressibility to be more important.

Ullage Space Compressibility Effects. Experiments have been conducted [9] at reduced ullage pressure that show significant increases in impact pressures at low pressures when compared with atmospheric pressure results. The results in Fig. 5 show that reducing ullage pressure has little effect on impact pressures until rather low pressures are reached, which are near to the vapor pressure. In this region ($P_u < 7$ kPa absolute pressure), a significant increase in impact pressure is recorded. Also noted in Fig. 5 is the range of scaled ullage pressures for a model of 1/50th to 1/30th scale using water. This range is in the region of the curve where impact pressure increases significantly with a small decrease in the absolute ullage pressure. It is not clear from these results if ullage cmopressibility or ullage gas condensation (thermodynamic effects) is the cause of the drastic pressure rise. Therefore, at the scale of most model tests (typically $\lambda = 1/50$ to $1/30$), the ullage pressure could be a significant factor and must be addressed in any scaling treatment. Since the compressibility of the ullage space (adiabatic and without regard to saturation) is simply $(\gamma P_o)^{-1}$, the static pressure in the ullage space determines its compressibility. It has been shown [3] that the forces due to ullage space compressibility do not have the correct relationship to the forces from static and dynamic pressure unless the ullage pressure is properly scaled by:

$$\left(\frac{\gamma_m}{\gamma_p}\right)\left(\frac{P_{u_m}}{P_{u_p}}\right)=\left(\frac{\rho_{L_m}}{\rho_{L_p}}\right)\lambda \qquad (13)$$

A good approximation to the interaction of the ullage gas and liquid in large amplitude sloshing is obtained by assuming the ullage gas to be compressible but without mass and the liquid to have mass but be incompressible. This system was modeled in [3] as lumped springs and masses; the gas pockets and bubbles being the springs and the liquid being the masses. Admittedly, the properties of this system vary with time quite rapidly when compared with sloshing periods, but may be reasonably stationary during the impact period. A second difficulty is that it may not be possible to actually determine these properties for a computed solution. But an explicit solution is not actually necessary; instead, one can invoke the assumption of similitude between model and full scale.

Gas Cushioning. To evaluate potential gas cushioning effects in liquid sloshing, two different theoretical models for slosh impacts have been developed and analyzed by the authors. The first is a closed gas pocket compression model, the second an open gas space compression model with free escape of gas from between the slosh wave and tank wall. The latter model is similar to that of Verhagen [10]. For both models, the pressure at the slosh impact is considered compressible in nature ($P = \rho_L C'_L V$) having a duration of the

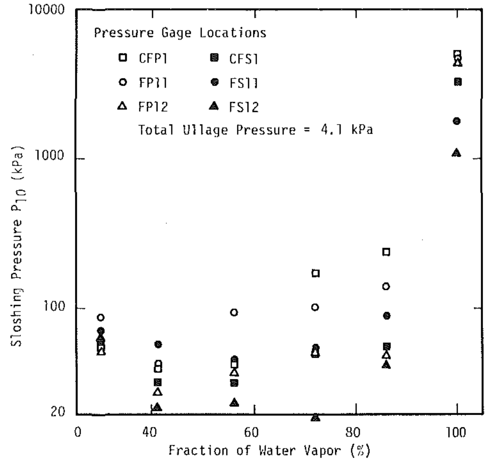

Fig. 7 Effect of ullage gas composition on measured P_{10} at P_u = constant

order of $\tau = R/C'_L$ where C'_L is the effective liquid sound speed incorporating gas cushioning and R is the distance from the impact center to the closest free surface where pressure relief occurs. After impact, the liquid starts to flow and the pressure tails off to a level on the order of $\rho_L V^2$. In the limit of low ullage pressure (vacuum), the limiting shock pressure $\rho_L C_L V$ is found. For closed gas pocket compression the dimensionless number $C'_L/(gl)^{1/2}$ depends on the Froude scaled ullage pressure $K_{P_u} = P_u/\rho_L gl$. Cauchy number $= K_C{}^{-1} = \rho_L gl/E_L$, gas liquid volume fraction m_o, and coefficient for isentropic gas compression γ. For the case of open gas space compression, the ratio of gas and liquid density ρ_G/ρ_L enters as an extra parameter. Comparing a water/air configuration at room temperature in a small scale model tank (1/30) with a full-scale LNG cargo tank, the closed gas pocket compression model shows that, using Froude-scaled slosh and ullage pressures, small-scale tests will overestimate slosh pressures as a result of improper liquid compressibility scaling (Cauchy), i.e., water in a small tank is too stiff. For open gas space compression, even larger discrepancies may occur (over a factor of ten) due to an additional high gas density in the prototype compared to a small scale tank at low ullage pressure. An equivalent statement is to say that for about the same gas sound speeds in prototype and model, due to the larger dimensions, escape of the gas is slower in the prototype, giving a better cushioning.

In Fig. 6, results from model tests with prismatic tanks (1/29) in harmonic motion are presented. These results show the effect of ullage pressure. The four sets of data represent four statistical groupings of model pressure measurements. Comparisons are shown with the above mentioned theoretical models for each grouping. As has been demonstrated earlier in Fig. 5, slosh pressures are very sensitive to the ullage pressure, in particular high slosh pressures at low ullage pressure. The sensitivity to ullage pressure is greatest for the highest pressure grouping ($P > 10$ kPa). At $P < 10$ kPa, little effect of ullage pressure is noted. Since the higher impact pressures will be more sensitive to factors affecting compressibility, the greater effect of ullage pressure on impact pressure at the higher impact pressure levels is expected. The experiment suggests that open gas space compression is more relevant for slosh impacts than closed gas pocket compression. Consequently, for correct simulation, small-scale experiments require simultaneous scaling of both ullage pressure and ullage density, which is complicated and would require a low temperature or heavy gas in the model. Failing this, a theoretical correction for lack of simulation should be applied to the results.

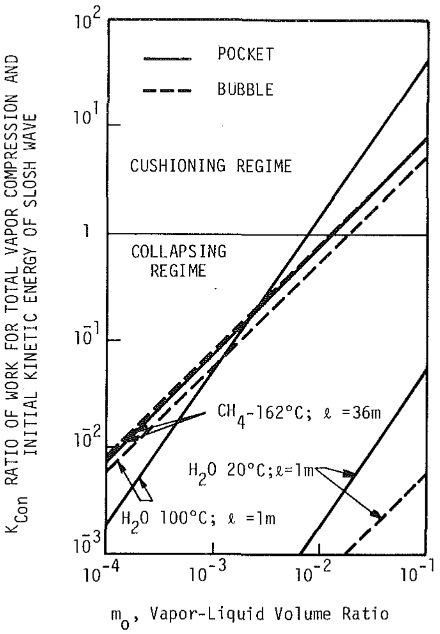

Fig. 8 Ratio of work for total vapor compression and initial kinetic energy of slosh wave as a function of vapor-liquid volume ratio for H_2O in model tank (20 and 100°C) and CH_4 in full-scale tank

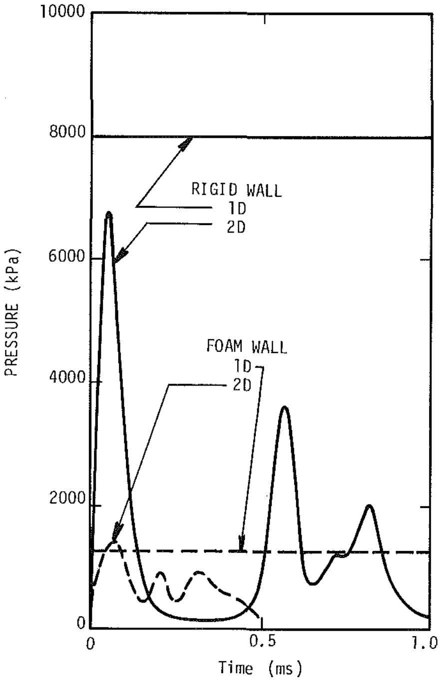

Fig. 9 Comparison of LNG impact pressures for rigid and foam walls

Ullage Vapor Condensation Effects. In a full-scale LNG tank, the ullage space is filled with mainly condensable methane vapor instead of non-condensable gas. If the vapor condenses during sloshing impacts, the effects of gas cushioning will be substantially diminished. The occurrence of vapor condensation is governed by changes in both temperature and pressure of the vapor. During a sloshing impact, the coupled effects of the rate of heat transfer between the vapor and liquid and the overpressurization of the vapor control the rate of vapor condensation.

Recently, the effects of such condensation have been studied at the model scale using scaled ullage pressure and heated water so that the vapor pressure of the water can be made equal to the ullage pressure and then the ullage space is filled with pure (saturated) water vapor. It was already shown in Fig. 3 that this results in a large increase in sloshing pressure. The effect of increasing the water vapor fraction in the ullage, while maintaining constant ullage pressure, is shown in Fig. 7. There is a gradual increase in pressure as the water vapor fraction is increased above 40 percent, but an order of magnitude increase for pure (100 percent) water vapor. This is a clear indication that rapid condensation is occurring under impact for model-scale conditions.

In the full-scale case, such rapid condensation is less likely to occur because the heat of condensation is much greater (due mainly to the much higher density of cryogenic LNG vapor). The heat cannot be transferred fast enough into the liquid to allow rapid condensation to occur and the cushioning will be similar to a non-condensable gas. Bass, et al. [8] showed that for LNG bubbles of a meter or so in diameter, the heat transfer time scale is orders of magnitude longer than the uncushioned collapse time scale. This shows that uncushioned collapse cannot occur.

Another approach to quantifying vapor condensation effects is to assume the vapor bubbles take the form of one-dimensional pockets and spherical bubbles. By introducing a dimensionless number, K_{Con}, which is the ratio between the work for full pocket or bubble compression and the initial kinetic energy of the slosh wave, one finds that for $K_{\mathrm{Con}} > 1$, cushioning is expected, whereas $K_{\mathrm{Con}} < 1$ indicates collapsing vapor. In Fig. 8 results of calculations are shown, where K_{Con} is given as a function of the vapor-liquid volume fraction at the start of compression. Three different configurations are compared: Methane/LNG (CH_4) at full scale (characteristic tank dimension of 36 meters), and water (H_2O) in model scale (characteristic tank dimension of one meter) at 20°C and at 100°C. It is clear that the configuration water/saturated-water-vapor at room temperature or somewhat elevated temperature in a small-scale tank is in the collapsing regime, whereas LNG in a prototype is in the cushioning regime for vapor-liquid volume ratios above about 1 percent. Although one has to be careful in deriving quantitative information from Fig. 8, more extended calculations with a computer code showed exactly the same trend.

One also sees that water at 100°C can be even less likely to collapse than the full-scale LNG case. This explains why model tests with boiling water at atmospheric pressure [3] have not shown condensation collapse.

In conclusion, in LNG sloshing research, no experiment should be carried out using water/saturated-water-vapor at room temperature or somewhat elevated temperature. On the other hand, water vapor at 100°C is in the cushioning regime, but the ullage pressure is too high to allow for correct Froude-scaled ullage pressure.

Wall Flexibility Effects. For high-pressure impacts governed by liquid compressibility, the flexibility of the tank wall is as important as the compressibility of the liquid. Walls made from foam insulation can be treated as a uniform elastic medium with an acoustic impedance $Z_W = \rho_w C_w$, which is usually less than the impedance of the liquid, $Z_L = \rho_L C_L$. For one-dimensional impact, flexibility reduces the impact pressure by the factor $\alpha/(1+\alpha)$ where $\alpha = Z_w/Z_L$. Since α is much less than one for foam walls, the pressure reduction is substantial. Results of two-dimensional impact calculations for curved surface (1 meter radius) LNG impact onto rigid and foam walls at 10 m/s velocity, using the PISCES Eulerian-Lagrangean finite-difference computer program [11], are shown in Fig. 9. These results confirm the general pressure levels predicted by the one-dimensional formulas, and also show that the curvature of the LNG leads to the submillisecond impact durations observed in practice, but not predictable from one-dimensional theory.

For built-up walls, the fluid-structural interaction can be very complicated. The model scaling of wall properties is probably too complex to be realistic. However, full scale pressures predicted from rigid wall model tests can be reduced through analytical considerations if an accurate mathematical modeling of wall structural response is available.

Conclusions

The discussions presented in this paper address the complexities and criteria for impact pressure scaling for large amplitude sloshing of a liquid transported at its vapor pressure. The use of a rigid wall, geometrically similar model tank driven either harmonically or with simulated ship motions in one or more degrees-of-freedom will allow a definition of worst-case wall impact pressures for design purposes. Factors which affect the simulation are:

- Froude scaling is required to reproduce the gross wave motions in model scale and is used to scale times and velocities to full scale.
- Viscous and surface tension forces need not be scaled as they are of secondary importance.
- The nature of the impact pressure (pressure-time history) indicates that the pressure as a function of time is controlled by compressible phenomena.
- The correct scaling of the dominant compressible phenomena requires simulating both ullage gas and liquid thermodynamic conditions. Based on analytical considerations and experimental results, the ullage pressures should be Froude scaled but a saturated vapor condition in the ullage should be avoided in simulating full scale LNG conditions.
- Scale model experiments are greatly simplified if compressible phenomena are not simulated and incompressible Froude/Euler scaling is used to predict impact pressures. This non-exact approach results in a conservative prediction of full scale pressures.
- The scaling of compressibility effects requires a more complicated simulation in model testing but should result in a more realistic prediction of full scale pressures. However, this requirement means that the dominant full scale compressible phenomena must be correctly reproduced in model scale. Also, sufficient cycles of sloshing pressure data must be obtained to accurately establish long-term operational worst-case pressures for design purposes. While this requirement is also true for incompressible scaling, the less conservative compressible pressure scaling emphasizes this need.

While the results presented in this paper indicate that significant knowledge in LNG slosh scaling has been gained in recent years, continued efforts are required to further the understanding of this subject. It is recommended that:

- Additional laboratory studies be conducted to more thoroughly investigate the effects of ullage gas pressure, density and composition on the scaling of impact pressures. These studies should be guided by the analytical considerations enumerated in this paper.
- Additional efforts should be undertaken to provide better methodology for predicting long-term worst-case, full-scale pressures from limited cycle laboratory data. As part of this effort, the minimum number of laboratory sloshing cycles should be established and the appropriateness of scaling impact momentum per unit area ($P\tau$) rather than P or τ alone should be investigated.
- Most importantly, full-scale pressures should be recorded simultaneously with ship motions on an LNG ship. This data in combination with mnodel simulation data should be used to evaluate the scaling considerations covered herein.

Uncertainty Analysis. The uncertainties of experimental measurements presented in this paper have been computed using the method of Kline and McClintock [12]. With this method, if R is the result of certain independent variables x_1, $x_2, \ldots, x_n$ and Δx_i is the uncertainty of a measured variable x_i, then the uncertainty of the result, ΔR, is given by:

$$\Delta R = \left[\sum_{i=1}^{n} \left(\frac{\partial R}{\partial x_i} \Delta x_i \right)^2 \right]^{1/2} \tag{14}$$

For the measured sloshing pressures presented in Figs. 3, 6, and 8, the uncertainty of measured pressures on the order of 100 kPa is ±0.83 percent while the uncertainty of pressures on the order of 1000 kPa is ±0.10 percent. For the ullage pressure shown on Fig. 6, the uncertainty for a pressure on the order of 10 kPa is ±0.70 percent while the uncertainty of a pressure on the order of 100 kPa is ±1.25 percent. Finally, the uncertainty of the measurement of the fraction of water vapor presented on Fig. 7 is ±2.5 percent.

Odds on the measured pressures are estimated at 20:1. Odds on the water vapor fractions are 10:1.

Acknowledgments

The authors of this paper wish to express their appreciation to their respective organizations for supporting this work and allowing its publication. Special thanks are also extended to the El Paso Marine Company for its continued support of LNG sloshing research from which a part of this paper is produced.

Also, special thanks are extended to Mrs. Dorothy Endicott and Mrs. Adeline Raeke who typed this manuscript and to Mr. Victor Hernandez for his skillful artwork on the figures.

References

1 Bass, R. L., Bowles, E. B., and Cox, P. A., "Liquid Dynamic Loads in LNG Cargo Tanks," Paper No. 3, Annual Meeting of the Society of Naval Architects and Marine Engineers, New York, N.Y., Nov. 13-15, 1980.

2 Navickas, J., Peck, J. C., Bass, R. L., Bowles, E. B., Yoshimura, N., and Endo, S., "Sloshing of Fluids at High-Fill Levels in Closed Tanks," *Proceedings*, ASME Winter Annual Meeting Symposium, Washington, D.C., Nov. 1981, pp. 191-198.

3 Olsen, H. A., and Hysing, T., "A Study of Dynamic Loads Caused by Liquid Sloshing in LNG Tanks," Report No. 74-276-C, Maritime Administration, Det norske Veritas, Dec. 1974.

4 Gerlach, C. R., "Investigation of Water Impact of Blunt Rigid Bodies—Real Fluid Effects," Contract No. N00014-67-C-0213, SwRI Project No. 02-2036, Technical Report No. 1, Dec. 29, 1967.

5 Nagamoto, R., Hagiwara, K., Fushimi, A., Kawamura, A., Mori, M., Kajita, E., Miyanari, T., Hori, T., Murata, S., and Tateishi, M., "On the Sloshing Force of Rectangular Tank Type LNG Carriers," Sixth International Conference on Liquified Natural Gas, Kyoto, Japan, Apr. 7-10, 1980.

6 Bass, R. L., "Liquid Impact Loads in LNG Carriers," Technical Report No. 1, El Paso Natural Gas Co., Southwest Research Institute, San Antonio, Texas, Aug. 1972.

7 Bass, R. L., and Ransleben, G. E., Jr., "Scaling Criteria for Large Amplitude Sloshing in LNG Ship Cargo Tanks," Technical Report No. 2 for Methane Tanker Service Co., Southwest Research Institute, San Antonio, Texas, Oct. 1974.

8 Bass, R. L., Dodge, F. T., and Bowles, E. B., Jr., "Evaluation of Scaling Criteria for Scale Model Sloshing Simulations of El Paso Marine Company's 125,000 Cubic Meter LNG Ship Tanks," El Paso Marine Company, Southwest Research Institute, San Antonio, Texas, 1979.

9 Olsen, H., "Local Impact Pressures in Basically Prismatic Tanks (OBO/-LNG)," Paper No. 10, Seminar on Liquid Sloshing, Det norske Veritas, Oslo, Norway, May 20-21, 1976.

10 Verhagen, J. H. G., "The Impact of a Flat Plate on a Water Surface," *Jour. of Ship Research*, Dec. 1967, p. 211.

11 *PISCES 2DELK User's Manual*, Physics International Co., San Leandro, Calif., May 1, 1980.

12 Kline, S. J., and McClintock, F. A., "The Description of Uncertainties in Single Sample Experiments," *Mechanical Engineering*, Jan. 1953, p. 3.

Y. Matsumoto
Associate Professor,
Department of Mechanical Engineering,
University of Tokyo,
Bunkyo-ku, Tokyo, 113 Japan

A. E. Beylich
Professor,
Stosswellenlabor,
Technische Hochschule Aachen,
Templergraben 55, 5100 Aachen,
Fed. Rep. of Germany

Influence of Homogeneous Condensation Inside a Small Gas Bubble on Its Pressure Response

The response of a small gas bubble to an ambient pressure reduction is investigated theoretically. Numerical results show that the temperature inside the bubble decreases due to adiabatic expansion at the first stage, then it recovers almost to the surrounding liquid temperature because of latent heat release caused by mist formation inside the bubble. Consequently, the bubble behaves apparently isothermally. The relation between the initial bubble radius and the critical pressure for cavitation inception to stepwise ambient pressure reduction becomes close to the relation under the assumption of isothermal change in the gas mixture inside the bubble.

1 Introduction

It has been understood that small air bubbles in water play an important role in cavitation inception. Also the pressure response of a bubble to the change of the ambient pressure field has been studied. For example, Sato and Shima [1] and Lin [2] have calculated the response of a small bubble to a stepwise ambient pressure reduction. A small bubble explodes when the ambient pressure is reduced below the critical value. Cramer [3] has reported the response of bubble in a oscillatory pressure field. Recently, Prosperetti [4] has surveyed the bubble dynamics.

Fujikawa and Akamatsu [5] and Tomita and Shima [6] have considered a nonequilibrium condensation on the bubble wall during its collapse. It has been calculated that a pure vapor bubble can rebound by thermodynamical nonequilibrium effects and the accommodation factor has a large influence on the maximum shock pressure radiated from the rebounded bubble. Although a considerable amount of research on bubble dynamics has been carried out, the behavior of the vapor and noncondensable gas mixture inside the bubble is still not clear. Many researchers have treated it only as a polytropic change.

The gas mixture inside the bubble seems to expand adiabatically when the bubble grows due to an ambient pressure reduction. On the other hand, Fujikawa and Akamatsu [7] have observed that a small hydrogen bubble grows isothermally after a stepwise ambient pressure reduction in an experiment using a hydro-shock tube. This phenomenon cannot be explained by the evaportion and heat transfer from the bubble wall. In this paper, the phenomena are explained as follows: First, a small gas bubble expands adiabatically, and the temperature inside the bubble decreases rapidly. Then, due to mist formation inside the bubble by homogeneous condensation, the temperature recovers almost to the initial one. Consequently, the bubble grows almost isothermally.

The following phenomena are taken into consideration when the governing equations are formulated: (i) nonequilibrium heat and mass transfer by evaporation and condensation on the bubble wall, (ii) formation of condensed droplets by homogeneous nucleation inside the bubble and the deposition of the droplets onto the bubble wall. Several typical conditions and the numerical results are shown in diagrams.

2 Assumptions and Governing Equations

2.1 Assumptions. The following assumptions are used to formulate the governing equations of the problem.

1) The bubble and the surrounding liquid move spherically and symmetrically.
2) The pressure, temperature and concentration inside the bubble are assumed as uniform except for a thin boundary layer near the bubble wall.
3) The inside boundary layer is thin enough compared with the bubble radius.
4) Vapor and noncondensable gas obey a perfect gas law.
5) Movement of the bubble wall by condensation or evaporation on the wall is assumed to be very small and therefore ignored.
6) The noncondensable gas obeys Henry's law.
7) Coalescence and fragmentation of droplets are neglected.
8) Slip between the droplet and the gas mixture is assumed to be small and ignored.

2.2 Governing Equations.

Equation of Motion of the Bubble. Using the approximate theory of Gilmore [8] based on the Kirkwood-Bethe assumption [9], the equation of bubble motion in a compressible liquid is written as

$$R\left(1-\frac{\dot{R}}{c}\right)\ddot{R}+\frac{3}{2}\left(1-\frac{\dot{R}}{3c}\right)\dot{R}^2-\left(1+\frac{\dot{R}}{c}\right)H$$

Contributed by the Fluids Engineering Division for publication in the JOURNAL OF FLUIDS DIVISION. Manuscript received by the Fluids Engineering Division, June 8, 1983.

$$-\frac{R}{c}\dot{H}\left(1-\frac{\dot{R}}{c}\right)=0 \qquad (1)$$

The enthalpy H and the speed of sound c at the double wall are written as

$$H=\int_{p_\infty}^{p_{(R)}}\frac{dp}{\rho_l}=\frac{n}{n-1}\,\frac{A^{1/n}}{\rho_{l0}}\left\{(p_{(R)}+B)^{\frac{n-1}{n}}-(p_\infty+B)^{\frac{n-1}{n}}\right\} \qquad (2)$$

and

$$c=\{c_0^2+(n-1)H\}^{1/2} \qquad (3)$$

where the equation of state of water is

$$p=A(\rho_l/\rho_{l0})^n-B \qquad (4)$$

and the pressure at the bubble wall $p(R)$ is

$$p_{(R)}=p_v+p_g-\frac{2\sigma}{R}-4\mu_l\frac{\dot{R}}{R} \qquad (5)$$

The constants c, A, B and n are estimated as follows for water (at 20°C): $c=1482$ m/s, $A=303.9$ MPa (3000 atm), $B=304.0$ MPa (3001 atm) and $n=7$.

Equations of Heat and Mass Transfer in the Liquid. If the compressibility of liquid has not much influence on the heat and mass transfer, the energy equation of the liquid and the diffusion equation of the dissolved gas component are written as

$$\frac{\partial T}{\partial t}+\frac{R^2}{r^2}\dot{R}\frac{\partial T}{\partial r}=\frac{\lambda_l}{\rho_l c_l}\left(\frac{\partial^2 T}{\partial r^2}+\frac{2}{r}\frac{\partial T}{\partial r}\right) \qquad (6)$$

and

$$\frac{\partial C}{\partial t}+\frac{R^2}{r^2}\dot{R}\frac{\partial C}{\partial r}=D_d\left(\frac{\partial^2 C}{\partial r^2}+\frac{2}{r}\frac{\partial C}{\partial r}\right) \qquad (7)$$

Equation of Conservation of Energy Inside the Bubble. For the conservation of energy inside the bubble, the first law of thermodynamics can be used as

$$\sum\frac{dE}{dt}+p_m\frac{dV}{dt}+\int_V\nabla\cdot q_i dV-\int_S(h\dot{m})_i dS=0 \qquad (8)$$

where the first term is the internal energy change, the second is the work, the third is the heat input through the bubble wall and the fourth is the enthalpy input through the wall. Since $\partial E/\partial v=0$ in a perfect gas, the first term can be written as

$$\sum\frac{dE}{dt}=(c_{vg}M_g+c_{vv}M_v+c_lM_c)\frac{dT_m}{dt}+e_g\frac{dM_g}{dt}+e_v\frac{dM_v}{dt}+e_l\frac{dM_c}{dt} \qquad (9)$$

where $M_g=4/3\pi R^3\rho_g$, $M_v=4/3\pi R^3\rho_v$ and M_c is the mass of condensed droplets. The third term of equation (8) can be rewritten as

$$\int_V\nabla\cdot q_i dV=-S\cdot\lambda_m\frac{\partial T_m}{\partial r}\bigg|_{r=R} \qquad (10)$$

where the partial differential value of T_m is available only in the neighborhood of the bubble wall. When h_i denotes the enthalpy at the wall, the fourth term of equation (8) can be written as

$$\int_S(h\dot{m})_i dS=h_{gi}\frac{dM_g}{dt}+h_{vi}\left\{\frac{dM_v}{dt}+\left(\frac{dM_c}{dt}\right)_e\right\}+h_{li}\left(\frac{dM_c}{dt}\right)_d \qquad (11)$$

where $(dM_c/dt)_e$ is the change of mass of the condensed droplets due to the evaporation and condensation, $(dM_c/dt)_d$ is the change due to the deposition onto the bubble wall and $dM_v/dt+(dM_c/dt)_e$ is the amount of evaporation or condensation on the bubble wall per unit time, $S\dot{m}_v$. On the other hand the specific internal energy e can be written as

$$e_g=h_g-\mathbf{R}_gT_m,e_v=h_v-\mathbf{R}_vT_m,e_l\approx h_l=h_v-L \qquad (12)$$

Using the above equations and the relations for perfect gas, $p_g=\rho_g\mathbf{R}_gT_g$ and $p_v=\rho_v\mathbf{R}_vT_v$, then

$$(c_{vg}M_g+c_{vv}M_v+c_lM_c)\frac{dT_m}{dt}-\frac{p_gM_g}{\rho_g^2}\frac{d\rho_g}{dt}-\frac{p_vM_v}{\rho_v^2}\frac{d\rho_v}{dt}-L\left(\frac{dM_c}{dt}\right)_e$$
$$-S\lambda_m\frac{\partial T_m}{\partial r}\bigg|_{r=R}+\Delta h_g\frac{dM_g}{dt}+\Delta h_v\left\{\frac{dM_v}{dt}+\left(\frac{dM_c}{dt}\right)_e\right\}+\Delta h_l\left(\frac{dM_c}{dt}\right)_d=0 \qquad (13)$$

where $\Delta h_g=h_g-h_{gi}=c_{vg}(T_m-T_i)$ and so on. The third term of equation (8) can be simplified using the following assumptions: When the bubble is growing, i.e., the gas mixture flow is directed toward the center at the bubble wall, the temperature gradient $\partial T_m/\partial r|_{r=R}$ at the wall is small enough compared with other terms of equations (8) and (23). On the other hand, when the bubble is shrinking, i.e., the gas mixture is flowing toward the bubble wall, the temperature gradient is steep and the heat flux by the temperature gradient is balanced with the enthalpy flux by the flow.

Nomenclature

C = dissolved gas content
D = diffusion coefficient
E = internal energy
H = enthalpy
I = number of droplets inside the bubble
J = nucleation rate
L = latent heat
M = mass inside the bubble
R = radius of the bubble
$\mathbf{R}$ = gas constant
S = surface area of the bubble
T = temperature
V = volume of the bubble
a = ratio of mesh distances
c = speed of sound, specific heat
e = specific internal energy
h = specific enthalpy
k = Boltzmann's constant
m = mass of a molecule
$\dot{m}$ = mass flux
n = polytropic exponent
q = heat flux
r = coordinate
r_* = critical radius of condensed droplet
r_d = radius of condensed droplet
t = time
u = velocity
v = specific volume
α = Henry's constant
α_M = mass accommodation factor
λ = heat conductivity
μ = viscosity
ρ = density
σ = surface tension
τ = dimensionless time, equation (25)
c = condensed droplet
d = dissolved gas
g = noncondensable gas
i = interface, initial condition
l = liquid
m = mixture
v = vapor
Δ = small amount
∞ = at infinity
o = saturated condition
• = time differential calculus

Equations of Condensation by Homogeneous Nucleation Inside the Bubble. It is assumed that the nucleation rate is given by the so-called classical theory [10] as

$$J=\left(\frac{2\sigma m}{\pi}\right)^{1/2}\frac{1}{\rho_l}\left(\frac{p_v}{kT_m}\right)^2\exp\left(-\frac{4\pi r_*^2\sigma}{3kT_m}\right) \tag{14}$$

where

$$r_*=\frac{2\sigma}{\rho_l\mathbf{R}_v T_m\ln(p_v/p_o)} \tag{15}$$

is the critical droplet radius, and p_0 is the saturated vapor pressure at temperature T_m inside the bubble. It is well known that surface tension on a curved surface is different from the one on a flat surface. Kawata and Mori [11] have reported that the experimental nucleation rate agrees with the theoretical value obtained by the classical theory using reduced surface tension. In this calculation, the reduction by curvature is estimated to be 30 percent. If the size of the condensed droplet is very small, the growing rate of condensed droplet is controlled by the molecular collisions, and if in addition a noncondensable gas is present, then it is reasonable to assume that the droplet temperature is the same as the surrounding one. Therefore, the equation for the growth of the droplets [12] is written as

$$\frac{dr_d}{dt}=\frac{\alpha_M(p_v-p_s)}{\rho_l\sqrt{2\pi\mathbf{R}_v T_m}} \tag{16}$$

where p_s is the vapor pressure at the surface of a droplet with radius r_d and is written as

$$p_s=p_0\exp\left(\frac{2\sigma}{\rho_l\mathbf{R}_v T_m r_d}\right) \tag{17}$$

The number of droplets formed inside the bubble during a certain time step j, I_j, is $J_j \bullet 4/3\pi R^3\Delta t$. When the bubble is shrinking, the droplets inside the bubble deposit onto the bubble wall, since they are transported by the net vapor flux induced by the condensation at the wall. If the droplets have no slip with the gas mixture, the number of droplets at the time step N, ${}^{N}I_j$, has the following relation to the number of droplets at the time step $N-1$, ${}^{N-1}I_j$.

$${}^{N}I_j=\left(1+3\frac{{}^{N-1}u_m\bullet\Delta t}{{}^{N-1}R}\right){}^{N-1}I_j \tag{18}$$

where u_m is the relative velocity of the gas mixture to the bubble wall caused by the condensation of the vapor and the dissolution of the noncondensable gas. If the volume occupied by the droplets is sufficiently small, the velocity u_m can be written as

$$u_m=\frac{\dot{m}_v+\dot{m}_g}{\rho_{vi}+\rho_{gi}} \tag{19}$$

When u_m is positive, equation (18) changes into ${}^{N}I_j={}^{N-1}I_j$.

From the above, the total condensed mass inside the bubble, M_c, is written as

$$M_c=\sum_{j=1}^{N}\frac{4}{3}\pi\,\rho_l\bullet{}^{N}r_{dj}^{\,3}\bullet{}^{N}I_j \tag{20}$$

where ${}^{N}r_{dj}$ is radius of the droplet at the time step N whose nucleus was formed at the time step j.

Boundary Conditions on the Bubble Wall and Initial Condition. The mass flux by the phase change on the bubble wall is written as follows, if the temperature discontinuity at the wall is not essential [13]:

$$\dot{m}_v=\frac{2\alpha_M}{2-\alpha_M}\frac{p_i-p_v}{\sqrt{2\pi\mathbf{R}_v T_i}} \tag{21}$$

where α_M is the mass accommodation factor and p_i is written as

$$p_i=p_o(T_i)\exp\left(\frac{-2\sigma}{\rho_l\mathbf{R}_v T_i R}\right) \tag{22}$$

The heat balance on the bubble wall is expressed as

$$\lambda_l\frac{\partial T}{\partial r}\bigg|_{r=R}-L\dot{m}_v-\lambda_m\frac{\partial T_m}{\partial r}\bigg|_{r=R}=0 \tag{23}$$

The relation between the dissolved gas content and the amount of noncondensable gas inside the bubble is written as

$$\frac{dM_g}{dt}=S\dot{m}_g=4\pi R^2 D_d\frac{\partial C}{\partial r}\bigg|_{r=R} \tag{24}$$

and the relation $C_i = \alpha p_g$ is available from Henry's law.

The numerical calculation is started from the following initial conditions: The bubble is at rest and the enthalpy at the bubble wall H and $\dot{H}$ are zero. The dissolved gas content in the liquid is uniform except at the bubble wall. The dissolved gas content at the bubble wall, C_i, obeys Henry's law and has the value αp_g.

2.3 Method of Numerical Calculation. If the term dH/dt of equation (1) is expressed by a backward difference formula, the bubble radius R at the time step $N+1$ can be solved by a Runge-Kutta method using the values of ${}^{N}R$, ${}^{N}\dot{R}$, ${}^{N}H$ and ${}^{N}\dot{H} = ({}^{N}H-{}^{N-1}H)/\Delta t$. In order to calculate equations (6) and (7) with sufficient accuracy, the origin of the coordinate is moved to the bubble surface and non-isodistance meshes are used, i.e., the $(n+1)$st mesh distance has the relation $dr_{n+1} = a\bullet dr_n$ $(a>1)$ with the nth mesh distance. An explicit finite difference scheme is used to calculate the values of the variables at time step $N+1$ from the values at time step N. The values inside the bubbles (temperature, pressure, concentrations) are calculated from equation (13) and the amount of condensed mass inside the bubble is calculated from equation (20). The temperature of interface at the time step $N+1$, ${}^{N+1}T_i$, is estimated to satisfy equations (21) and (23). The temperature dependence of the properties of the liquid and gases are considered in this calculation.

3 Calculated Results and Discussion

3.1 Pressure Response of a Small Gas Bubble. The response of a small gas bubble to a stepwise ambient pressure reduction from 100 kPa to the vapor pressure is calculated.

Influence of the Change of State of the Vapor and Non-Condensable Gas Mixture Inside the Bubble. Two imaginary reference cases, where the gas mixture inside the bubble changes isothermally and no condensation occurs inside the bubble, are shown in order to be compared with the main results. Figure 1 shows the case in which the gas mixture is assumed to change isothermally. The initial bubble radius is 10 μm and the initial temperature is 20°C. The abscissa is the dimensionless time being defined as

$$\tau=t/R_i\bullet\sqrt{(p_{\infty i}-p_v)/\rho_l} \tag{25}$$

The temperature inside the bubble is assumed to be equal to the temperature at the interface. The rate of evaporation and condensation is calculated by equation (21) and the mass accommodation factor is assumed as 0.3. The temperature at the interface maintains almost the initial temperature. In this case, the temperature fluctuation is only ±0.2 K. Namely, the heat transfer has little influence on these phenomena. When the ambient pressure decreases to the vapor pressure, the bubble starts to grow rapidly and oscillates around the new equilibrium radius. The vapor pressure inside the bubble is almost constant but the noncondensable gas pressure inside the bubble fluctuates with the oscillation of the bubble. The amount of the noncondensable gas inside the bubble increases by the diffusion through the bubble wall but the increasing rate is very small.

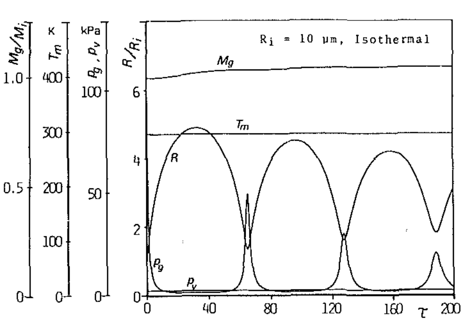

Fig. 1 The time history of the bubble radius R and the quantities inside the bubble T_m, p_g, p_v, M_g for the case where the gas mixture inside the bubble changes isothermally. The initial bubble radius is 10 μm.

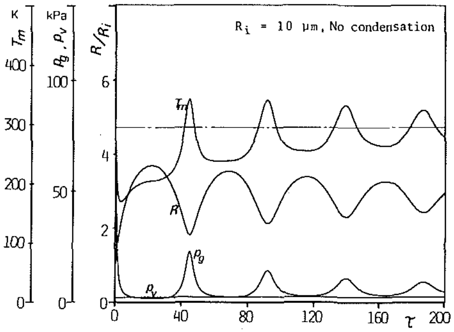

Fig. 2 The time history of the bubble radius R and the quantities inside the bubble T_m, p_g, p_v, for the case where the homogeneous condensation does not occur inside the bubble. The initial bubble radius is 10 μm.

Figure 2 shows the case in which no condensation by homogeneous nucleation is assumed to occur inside the bubble. The gas mixture changes nearly adiabatically (in fact it does not change completely adiabatically due to the enthalpy transport through the wall) and the temperature inside the bubble decreases to 168 K. When the bubble begins to shrink, the mixture is compressed, the temperature rises up and oscillates around the initial value shown by a dash-dotted line in the figure. This is because the enthalpy is transported by the evaporation and condensation on the bubble wall when the temperature inside the bubble is lower than the surrounding temperature. The motion is very different from the isothermal case shown in Fig. 1. The oscillation period is shorter and the maximum bubble radius is much smaller. It is understood that the bubble motion is influenced strongly by the change of state of the gas mixture inside the bubble.

Influence of Mass Accommodation Factor. The calculated results in which the homogeneous condensation inside the bubble is considered are shown in the following figures. Figure 3 shows the case where the mass accommodation factor α_M is 1.0. The bubble motion becomes very similar to the isothermal case according to the following process: The temperature inside the bubble, T_m, decreases rapidly with the bubble growth to a certain point, then it recovers to the surrounding liquid temperature due to the latent heat release caused by homogeneous condensation inside the bubble. When the bubble begins to shrink, the gas mixture inside the bubble is compressed and the temperature tends to increase. However it stays almost constant due to the evaporation of the condensed droplets. At the last stage of the shrinking, the droplets disappear from the inside by the evaporation and the deposition onto the bubble wall. After the condensed mass, M_c, becomes zero, the gas mixture is compressed adiabatically and the temperature increases up to 418 K when the bubble radius reaches its minimum.

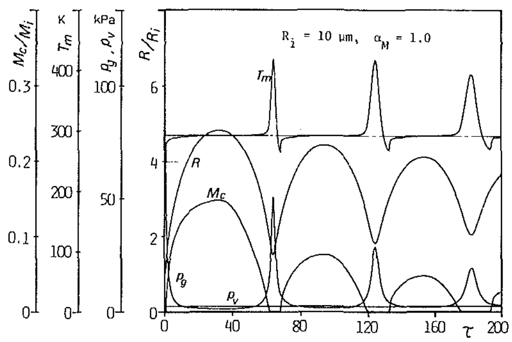

Fig. 3 The time history of the bubble radius R and the quantities inside the bubble T_m, p_g, p_v, M_c for the case with homogeneous condensation inside the bubble. The mass accommodation factor is 1.0. The initial bubble radius is 10 μm.

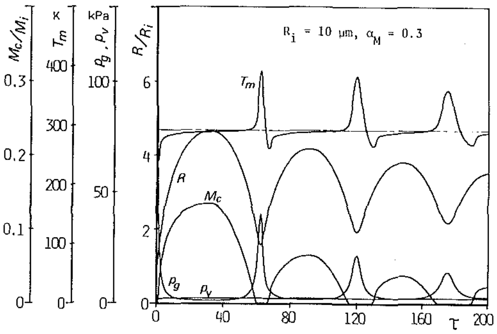

Fig. 4 The time history of the bubble radius R and the quantities inside the bubble T_m, p_g, p_v, M_c for the case with homogeneous condensation inside the bubble. The mass accommodation factor is 0.3. The initial bubble radius is 10 μm.

The second cycle starts from this high temperature condition and a similar process is observed. The condensed mass at this cycle is much smaller than at the first one. The reasons are explained as follows: The condensed droplets formed in the first cycle increase the enthalpy of the gas mixture but many of them deposit onto the bubble wall without the absorption of enthalpy by the evaporation. By these phenomena, the enthalpy has been transported into the bubble through the wall during the oscillation of the bubble. After several oscillations of the bubble, no condensed droplet forms inside the bubble.

Recently, Tanaka et al. have studied mass accommodation factors intensively and reported that $\alpha_M = 0.45$ [14] $-$ 0.2 [15]. The calculated results with $\alpha_M = 0.3$ is shown in Fig. 4. The tendency of the results is similar to the results with $\alpha_M =$ 1.0 although the thermodynamic nonequilibrium effects in the phenomena become larger. Namely, the maximum radius of the bubble becomes smaller than in the former case because of the slower recovery and the lower mean value of the temperature inside the bubble. Moreover, a larger damping of the bubble oscillation is observed.

Influence of Initial Bubble Radius. The period of the bubble oscillation, i.e., the characteristic time of the bubble dynamics, depends on the equilibrium radius at the ambient pressure. However, the characteristic time of the thermodynamic nonequilibrium, especially that of the condensation and evaporation inside the bubble is independent of the bubble radius. Here, two calculated results for the initial radii of 5μm and 20 μm are shown in Figs. 5 and 6. In the case of 5 μm, the temperature inside the bubble decreases more rapidly being accompanied by faster expansion, and the temperature gets lower than in the case of 10 μm, because the condensation cannot catch up with the expansion of the gas mixture inside the bubble. In the case of 20 μm, the recovery

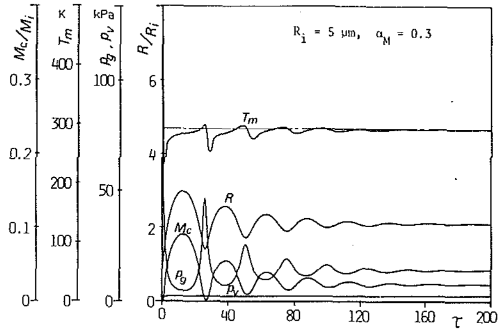

Fig. 5 The time history of the bubble radius R and the quantities inside the bubble T_m, p_g, p_v, M_c for the case with homogeneous condensation inside the bubble. The mass accommodation factor is 0.3. The initial bubble radius is 5 μm.

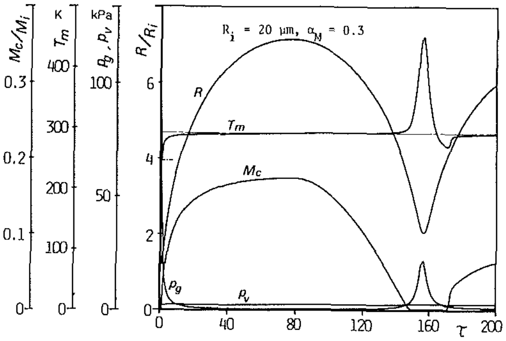

Fig. 6 The time history of the bubble radius R and the quantities inside the bubble T_m, p_g, p_v, M_c for the case with homogeneous condensation inside the bubble. The mass accommodation factor is 0.3. The initial bubble radius is 20 μm.

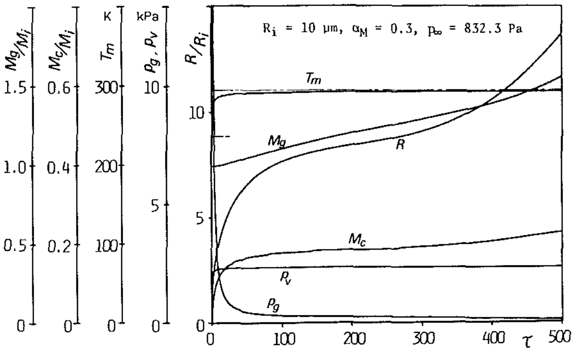

Fig. 7 The time history of the bubble radius R and the quantities inside the bubble T_m, p_g, p_v, M_g, M_c for the case where the ambient pressure is reduced to lower than the critical one. The mass accommodation factor is 0.3. The initial bubble radius is 10 μm.

of the inside temperature by the homogeneous condensation is faster than in the case of 10 μm, because the expansion speed of the gas mixture is not so fast and the inside temperature does not decrease so rapidly. The dispersion of the droplets from the inside during the shrinking is fast and the temperature inside the bubble becomes higher when the bubble rebounds. However, the temperature inside the bubble is closer to the surrounding temperature than in the case of 10 μm throughout the period of the oscillation. Thus, the larger the bubble radius, the more isothermal is the response of the bubble to a certain pressure change.

3.2 Critical Pressure for Cavitation Inception. The relation between the initial bubble radius and the critical pressure due to a stepwise ambient pressure reduction is calculated. The critical pressure is defined as the ambient pressure below which the bubble grows continuously.

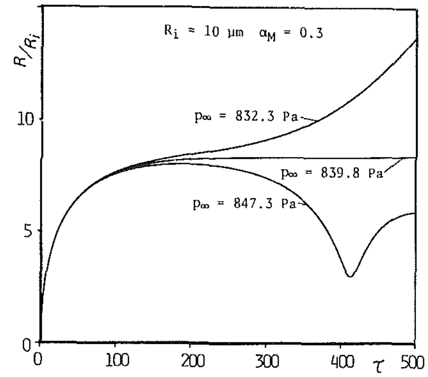

Fig. 8 The time history of the bubble radius R for the cases where the surrounding pressures are reduced to lower, critical and higher ones. The mass accommodation factor is 0.3. The initial bubble radius is 10 μm.

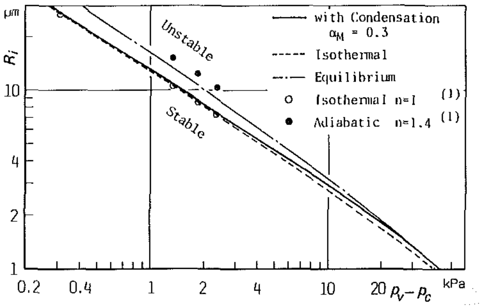

Fig. 9 The relations between the initial bubble radius R_i and the critical pressure p_c for the cavitation inception due to a stepwise ambient pressure reduction

The bubble motion is calculated and shown in Fig. 7, where the ambient pressure is reduced to 832.3 Pa which is slightly lower than the critical pressure under the following conditions: the initial radius is 10 μm, the surrounding temperature is 20°C, the initial ambient pressure is 101.3 kPa, the surrounding dissolved gas content is 25 ppm and the mass accommodation factor is 0.3. As mentioned in the previous section, the bubble grows almost isothermally because of the homogeneous condensation inside the bubble. The mass of the condensed droplets, M_c, increases with the growth of the bubble. E.g. the condensed mass is 2.4 percent of the mass of the vapor inside the bubble at $\tau = 200$ when the bubble motion has an inflection point. The mass of the noncondensable gas inside the bubble also increases with the bubble growth. The amount becomes 1.22 times of the initial amount at $\tau = 200$ and 1.57 times at $\tau = 500$. A relatively large amount of noncondensable gas diffuses into the bubble when the bubble explodes, but the noncondensable gas does not diffuse back to the liquid when the bubble collapses [16]. Therefore, the gas diffusing into the bubble plays an important role during the bubble collapse.

Three cases are shown in Fig. 8, where the ambient pressures are reduced to a pressure slightly lower than the critical pressure, to the critical pressure and to a slightly higher pressure, respectively. In the case of the nearly critical pressure of 839.8 Pa, the bubble radius continues to grow till about $\tau = 300$, and then it takes a constant value. Strictly speaking, the bubble motion has a maximal value (R/R_i = 8.272) at $\tau = 299.8$ and it has the minimal value ($R/R_i = 8.265$) at $\tau = 386.4$. Thereafter, the radius continues to grow and it gets to $R/R_i = 8.341$ at $\tau = 500$. The diffusion of the noncondensable gas into the bubble becomes important when the bubble is exposed to the low pressure for a longer time. In the case of $p_\infty = 847.3$ Pa, a remarkable rebound of the bubble motion is observed. The motion is qualitatively the same as the one mentioned in the previous section.

The relations between the initial bubble radius and the critical pressure are shown in Fig. 9, which are calculated under the same condition as in Fig. 7, except for the bubble radius. The solid line shows the relations where the homogeneous condensation is considered. The relation becomes close to the one where the isothermal change is assumed in the gas mixture (dash-dotted line in Fig. 9) when the initial bubble radius is larger than 8 μm. Especially, the above mentioned tendency is remarkable in the large radius region. However, in the small bubble radius region, the relation shifts off from the isothermal case toward the relation where a dynamic and thermodynamic equilibrium is assumed [16]. For reference, the relation where the isothermal change is assumed for the noncondensable gas inside the bubble [1] is shown by open circles and the relation where the adiabatical change is assumed [1] is shown by full circles.

4 Conclusion

Theoretical research has been done on the response of a small gas bubble to ambient pressure reduction which is important for cavitation inception. The equations for the bubble dynamics are formulated with special attention to the behavior of the gas mixture inside the bubble. Some characteristic cases are calculated numerically and the following conclusions are obtained:

1) A small gas bubble expands adiabatically at the first stage of growing, but then homogeneous condensation occurs inside the bubble and the inside temperature recovers almost to the surrounding temperature. Therefore, the bubble behaves apparently isothermally.

2) The bubble motion including the homogeneous condensation is influenced by the mass accommodation factor.

3) The oscillation period of the bubble is longer when the equilibrium bubble radius is larger. In this case, the temperature inside the bubble stays more contant and it behaves more isothermally.

4) When the initial bubble radius is relatively large ($R_i >$ 8 μm), the relation between the initial bubble radius and the critical pressure for cavitation inception due to stepwise pressure reduction becomes comparable to the relation under the assumption of the isothermal change in the gas mixture inside the bubble.

Acknowledgment

The main part of this work has been performed at the Stosswellenlabor, Technische Hochschule Aachen. The authors would like to thank the Alexander-von-Humboldt Foundation for the financial support for one of the authors to stay at the TH Aachen.

References

1 Sato, Y., and Shima, A., "The Growth of Bubbles in Viscous Incompressible Liquids," Rep. Inst. High Speed Mech., 40-319, 1979, pp. 23-49.

2 Lin, S. C., "Role of Microair Bubbles on Cavitation," IAHR 10th Symp. Hydraulic Machinery, 1980, pp 27-38.

3 Cramer, E., "The Dynamics and Acoustic Emission of Bubbles Driven by a Sound Field," *Cavitation and Inhomogeneities*, Springer, Berlin, 1979, pp. 54-63.

4 Prosperetti, A., "Bubble Dynamics: A Review and Some Recent Results," *Mechanics and Physics of Bubbles in Liquids*, NIJHOFF, The Hague, 1982, pp. 145-164.

5 Fujikawa, S., and Akamatsu, T., "Effects of the Nonequilibrium Condensation of Vapour on the Pressure Waves Produced by the Collapse of a Bubble in a Liquid," *J. Fluid Mech.*, Vol. 97, 1980, pp. 481-512.

6 Tomita, Y., and Shima, A., "The Effects of Heat Transfer on the Behavior of a Bubble and the Impulse Pressure in a Viscous Compressible Liquid," *ZAMM*, Vol. 59, 1979, pp. 297-306.

7 Fujikawa, S., and Akamatsu, T., "On the Mechanisms of Cavitation Bubble Collapse," IAHR 10th Symp. Hydraulic Machinery, 1980, pp. 91-102.

8 Gilmore, F. R., "The Growth or Collapse of a Spherical Bubble in a Viscous Compressible Liquid," CIT Report No. 26-4, 1952.

9 Kirkwood, J. G., and Bethe, H. A., "The Pressure Wave Produced by Underwater Explosion," ORSD Report No. 588, 1942.

10 Frenkel, J., *Kinetic Theory of Liquids*, Oxford University Press, New York, 1946.

11 Kawada, H., and Mori, Y., "A Shock Tube Study on Condensation Kinetics," *Bull. JSME*, Vol. 16, No. 97, 1973, pp. 1053-1065.

12 Hill, P. G., "Condensation of Water Vapor During Supersonic Expansion in Nozzles," *J. Fluid Mech.*, Vol. 25, 1966, pp. 593-620.

13 Schrage, R. W., *Theoretical Study of Interphase Mass Transfer*, Columbia University Press, New York, 1953.

14 Tanaka, H., "Effects of Knudsen Number on Dropwise Condensation," ASME *Journal of Heat Transfer*, Vol. 103, No. 3, 1981, pp. 606-607.

15 Tanaka, H., "Further Developments of Dropwise Condensation Theory," ASME *Journal of Heat Transfer*, Vol. 101, No. 4, 1979, pp. 603-611.

16 Matsumoto, Y., and Shirakura, M., "Mechanisms of Cavitation Nuclei Suspension," IAHR 11th Symp. Hydraulic Machinery, 1-3, 1982.

Journal of Fluids Engineering

Discussion

Turbulent Flow Over Rough Surfaces II. Turbulent Flow Parameters[1]

E. Logan.[2] This paper reports new data for fully developed pipe flow over a wide range of roughness element spacings. Reynolds number, not clearly defined, is also varied, as is roughness height. The principal result is the eddy viscosity distribution in the core region, and this is reduced to useful algebraic form. The work constitutes an extension of knowledge of turbulent flow over rough walls.

This work extends that of Nunner [1] and Siuru [2], and comparisons with their results are possible. The data given for $P/K = 19$ indicate a friction factor of 0.166, which agrees with Nunner's value of 0.16 for $P/K = 20$ and Siuru's value of 0.16 for $P/K = 17.7$.

Comparisons of turbulence levels measured by Siuru ($P/K = 17.7$) and the present authors ($P/K = 19$) are given below in tabular form. Measurements are for station X3, i.e., over the reattachment point.

	u'/u_s		v'/u_s	
Position	Present	Siuru	Present	Siuru
Centerline	.8	.86	.8	.8
$y/R = .5$	1.41	1.37	.91	.92
Element wake	1.88	1.87	1.12	1.02

These data apply to the isolated-element regime and are in excellent agreement. Centerline values for u'/u_s of 0.8 should apply to all regimes. Values presented in Fig. 2 are lower, even for the smooth-walled case. Centerline values of v'/u_s should also be 0.8, as indicated by Siuru [2] for rough pipes and Laufer [3] for smooth pipes. The present authors indicate a value of 0.459 for v_0'/u_s. This is noteworthy, as their u' and v' relations are normalized with centerline values, u_0' and v_0'.

The peaks of u', observed in element wakes, are shown in Fig. 3. These are said to diminish for P/K values of 7 and 10. Siuru and Logan [4] show significant cyclic behavior of u' for $P/K = 8.8$ in the element wake region. At station X3 it should be noted that $X/K = 5$, 8 and 11 for $P/K = 13$, 19 and 25, respectively. Reattachment probably occurs at $X/K = 8$. The u' values very close to the wall undoubtedly reflect the effect of variable wake width behind the element at the three locations.

The data of Fig. 5 show an apparent overshoot. However, $\tau_0/\rho u_0^2$ values of 0.0131, 0.0108, and 0.0114 are indicated for $P/K = 13$, 19, and 25, respectively. Linear distributions based on these values do not pass through the data points, nor does overshooting of the linear distribution occur. The source of the u_s values is not discussed in the paper, nor are values of u_s given for all cases.

Perhaps the most interesting results of this paper are the eddy viscosity distributions. Accuracy of ϵ depends on accuracy determination of the gradient dU/dr. This paper does not deal with the techniques nor the data used in this determination. Core values of ϵ shown in Figs. 7 and 8 are in line with smooth tube values and agree with those expected. The large rise of ϵ at X2 in Fig. 7 may be related to the use of the average value of u_s in calculating ϵ^+. For the isolated-element case, a sudden rise of local u_s occurs near the element. Qualitatively, use of local u_s would reduce ϵ^+ values at X2. The effect is diminished for reduced P/K, as in Fig. 8.

The very low values of ϵ^+ in Fig. 6 could be partially explained by the nature of the skimming flow at $P/K = 2$, i.e., d-type roughness in which the radius R is effectively reduced and the local u_s at X1 is probably less than the average value.

Additional References

1 Nunner, W., "Wärmeübergang und Druckabfall in rauhen Rohren," VDI-Forschungsheft 455, Ausgabe B, Band 22, 1956.

2 Siuru, W. D., "Response of a Turbulent Pipe Flow to a Change in Surface Roughness," Ph.D. thesis, Arizona State University, 1975.

3 Laufer, J., "The Structure of Turbulence in Fully Developed Pipe Flow," NACA Rept. 1174, 1954.

4 Siuru, W. D., and Logan, E., "Response of a Turbulent Pipe Flow to a Change in Roughness," ASME JOURNAL OF FLUIDS ENGINEERING, Vol. 99, 1977, pp. 548-555.

W. H. Schofield[2]. The authors discuss their data in terms of the model of Morris which the last 35 years of research on rough wall flow has shown to be inaccurate. Firstly the quasi-smooth flow regime ('d' type flow in the nomenclature of Perry et al. [5]) ceases soon after $P/_K = 2$ and certainly before $P/_K = 5$ (see Perry et al.). None of the data presented in this paper disputes this although it is stated that u'/U_s values for $P/_K = 5$ are similar to values for $P/_K = 2$ and for smooth wall flow. Wake interference flow (or 'k' type flow) starts soon after $P/_K = 2$ and theoretically extends to values of $P/_K$ of several hundred as the rate of recovery of a shear layer from a perturbation is very long (see Tillman's [6]

---

[1] By K. Nourmohammadi, P. K. Hopke, and J. J. Stukel published in the March 1985 issue of the JOURNAL OF FLUIDS ENGINEERING, Vol. 107, No. 1, pp. 55-60.

[2] Department of Mechanical and Aerospace Engineering, Arizona State University, Tempe, Ariz. 85287.

[3] Aeronautical Research Laboratories, Department of Defence, Victoria, Australia.

results or Bradshaw and Wong's [7]). In practice the layer's upstream history would not much effect flow around "isolated" elements for spacings greater than $P/_K = 20$, which is near the limit of this data.

The results presented confirm that the principles of Reynolds number similarity (Townsend [8] 1956) applies to rough wall flow for a wide range of geometries. However the results shown in Fig. 6 seem at odds with this result in that the turbulent motions that produced similarity of u'/U_s in Fig. 2 did not apparently produce similarity in the eddy viscosity profiles.

Another area of concern is the very large uncertainty bands on some of these results, up to 50 percent of reading in the case of the data presented in Fig. 3. In view of this uncertainty it is not appropriate to quote formulas for curve fits to this data to three significant places as has been done in conclusion 2 and elsewhere in the text. It is noted that these curve fits apply to both pipes which vary in diameter by a factor of 2. However the important lateral parameter that is varying is K/D and here there is only a difference of 30 percent which is quite insufficient to produce differences in the results greater than the scatter in the data. Perry et al. used differences of 800 percent in their boundary layer flows to support their conclusions.

There is room for further careful measurements in this field of research.

Additional References

5 Perry, A. E., Schofield, W. H., and Joubert, P. N., "Rough Wall Turbulent Boundary Layers," *Journal of Fluid Mechanics*, Vol. 37, 1969, pp. 383-413.

6 Tillman, W., "Investigations of Some Particularities of Turbulent Boundary Layers on Plates," British Rep. and Transl. CGD-497, MAP-VG 34-T.

7 Bradshaw, P., and Wong, F. V. F., "The Reattachment *and* Relaxation of a Turbulent Shear Layer," *Journal of Fluid Mechanics*, Vol. 52, pp. 113-135.

8 Townsend, A. A., *The Structure of Turbulent Shear Flow*, Cambridge University Press, 1956.

Authors' Closure

Response to E. Logan

Professor Logan points out many interesting comparisons between his work and ours. We are pleased that results from both studies are in agreement for comparable experimental configurations.

Response to W. H. Schofield

We agree with Dr. Schofield that given the uncertainty of the data, it is not appropriate, "to quote formulae for curved fits to this data to three significant places." We also agree that further careful measurements are need in this field.

Radial and Axial Variations in Transient Pressure Waves Transmitted Through Liquid Transmission Lines[1]

A. H. Weidermann.[2] The development of numerical methods for solutions of the Navier-Stokes equation are always useful and of interest. However, the subject title is not well served by the authors approach nor by their formulation of two relevant problems. Viscosity enters the selected flow problems in two basic ways. First, viscosity influences the transient flow field through the conservation equations and it is this characteristic which is being addressed in the paper; secondly, viscosity, for the low Reynolds number flows, establishes the flow velocity gradients in the (initial) flow field (i.e., the Poiseuille flow). In the former, the influence of viscosity is to introduce a spacial and temporal smearing effect on the flow and, perhaps, generate some additional wave systems. In the latter, viscosity introduces an energy and momentum gradient which under an appropriate stimuli will be redistributed within the flow field.

The authors selection of a finite duration (i.e., an essentially linear ramp) build-up to some step stimuli also introduces a spatial and temporal smearing effect on the transient flow field, and it is impossible, or at least difficult, to seperate the two contributions. I believe that a much more appropriate problem formulation for the waterhammer problem would have been one where the valve closes instantaneously. Additionally, the omission of viscosity in one such calculation would serve as an excellent reference problem (a two-dimension wave equation solution). The sudden stoppage of the flow at the valve location will (through momentum considerations) result in the momentary establishment of a pressure profice at this location which is proportional to the (initial) radial velocity profile; the peak pressure at the midpoint will be $2P_0$. Clearly, this early pressure distribution, together with the upstream flow gradients, will generate a radial wave system, and, of course, drive a pressure wave upstream into the fluid column. The major features of the transient flow, as shown in Fig. 1 of the paper, would certainly be present in such a reference solution. It appears, from the tabular data, that the viscosity effect is extremely small, and in some instances is of the order of the numerical uncertainties generated by the numerical methodology. I hope that the authors will have the opportunity, in the near future, to present the results of such an idealized reference solution such that we can all better understand and appreciate the proper contribution that viscosity plays in these two basic problems. Finally, in any engineering problem, the apparent minor role that viscosity plays in the transient flow will generally be masked by other system uncertainties and problem idealizations, for example, the elastic response of the containment system (i.e., pipe response).

Authors' Closure

We appreciate Dr. Wiedermann's interest in our paper; his view of the problem is somewhat different than ours. The essential point of our work is that the no-slip boundary condition can be satisfied exactly only by a simultaneous solution of both the axial and radial components of the Navier-Stokes equations. A two-dimensional non-viscous solution is not possible because the order of Euler's equations is not high enough; they cannot satisfy the no-slip condition

---

[1] By A. K. Mitra and W. T. Rouleau published in the March 1985 issue of the JOURNAL OF FLUIDS ENGINEERING, Vol. 107, pp. 105-111.

[2] AT Research Associates, Glen Ellyn, Ill. 60137.

results or Bradshaw and Wong's [7]). In practice the layer's upstream history would not much effect flow around "isolated" elements for spacings greater than $P/_K = 20$, which is near the limit of this data.

The results presented confirm that the principles of Reynolds number similarity (Townsend [8] 1956) applies to rough wall flow for a wide range of geometries. However the results shown in Fig. 6 seem at odds with this result in that the turbulent motions that produced similarity of u'/U_s in Fig. 2 did not apparently produce similarity in the eddy viscosity profiles.

Another area of concern is the very large uncertainty bands on some of these results, up to 50 percent of reading in the case of the data presented in Fig. 3. In view of this uncertainty it is not appropriate to quote formulas for curve fits to this data to three significant places as has been done in conclusion 2 and elsewhere in the text. It is noted that these curve fits apply to both pipes which vary in diameter by a factor of 2. However the important lateral parameter that is varying is K/D and here there is only a difference of 30 percent which is quite insufficient to produce differences in the results greater than the scatter in the data. Perry et al. used differences of 800 percent in their boundary layer flows to support their conclusions.

There is room for further careful measurements in this field of research.

Additional References

5 Perry, A. E., Schofield, W. H., and Joubert, P. N., "Rough Wall Turbulent Boundary Layers," *Journal of Fluid Mechanics*, Vol. 37, 1969, pp. 383–413.

6 Tillman, W., "Investigations of Some Particularities of Turbulent Boundary Layers on Plates," British Rep. and Transl. CGD-497, MAP-VG 34-T.

7 Bradshaw, P., and Wong, F. V. F., "The Reattachment *and* Relaxation of a Turbulent Shear Layer," *Journal of Fluid Mechanics*, Vol. 52, pp. 113–135.

8 Townsend, A. A., *The Structure of Turbulent Shear Flow*, Cambridge University Press, 1956.

Authors' Closure

Response to E. Logan

Professor Logan points out many interesting comparisons between his work and ours. We are pleased that results from both studies are in agreement for comparable experimental configurations.

Response to W. H. Schofield

We agree with Dr. Schofield that given the uncertainty of the data, it is not appropriate, "to quote formulae for curved fits to this data to three significant places." We also agree that further careful measurements are need in this field.

Radial and Axial Variations in Transient Pressure Waves Transmitted Through Liquid Transmission Lines[1]

A. H. Weidermann.[2] The development of numerical methods for solutions of the Navier-Stokes equation are always useful and of interest. However, the subject title is not well served by the authors approach nor by their formulation of two relevant problems. Viscosity enters the selected flow problems in two basic ways. First, viscosity influences the transient flow field through the conservation equations and it is this characteristic which is being addressed in the paper; secondly, viscosity, for the low Reynolds number flows, establishes the flow velocity gradients in the (initial) flow field (i.e., the Poiseuille flow). In the former, the influence of viscosity is to introduce a spacial and temporal smearing effect on the flow and, perhaps, generate some additional wave systems. In the latter, viscosity introduces an energy and momentum gradient which under an appropriate stimuli will be redistributed within the flow field.

The authors selection of a finite duration (i.e., an essentially linear ramp) build-up to some step stimuli also introduces a spatial and temporal smearing effect on the transient flow field, and it is impossible, or at least difficult, to seperate the two contributions. I believe that a much more appropriate problem formulation for the waterhammer problem would have been one where the valve closes instantaneously. Additionally, the omission of viscosity in one such calculation would serve as an excellent reference problem (a two-dimension wave equation solution). The sudden stoppage of the flow at the valve location will (through momentum considerations) result in the momentary establishment of a pressure profice at this location which is proportional to the (initial) radial velocity profile; the peak pressure at the midpoint will be $2P_0$. Clearly, this early pressure distribution, together with the upstream flow gradients, will generate a radial wave system, and, of course, drive a pressure wave upstream into the fluid column. The major features of the transient flow, as shown in Fig. 1 of the paper, would certainly be present in such a reference solution. It appears, from the tabular data, that the viscosity effect is extremely small, and in some instances is of the order of the numerical uncertainties generated by the numerical methodology. I hope that the authors will have the opportunity, in the near future, to present the results of such an idealized reference solution such that we can all better understand and appreciate the proper contribution that viscosity plays in these two basic problems. Finally, in any engineering problem, the apparent minor role that viscosity plays in the transient flow will generally be masked by other system uncertainties and problem idealizations, for example, the elastic response of the containment system (i.e., pipe response).

Authors' Closure

We appreciate Dr. Wiedermann's interest in our paper; his view of the problem is somewhat different than ours. The essential point of our work is that the no-slip boundary condition can be satisfied exactly only by a simultaneous solution of both the axial and radial components of the Navier-Stokes equations. A two-dimensional non-viscous solution is not possible because the order of Euler's equations is not high enough; they cannot satisfy the no-slip condition

---

[1] By A. K. Mitra and W. T. Rouleau published in the March 1985 issue of the JOURNAL OF FLUIDS ENGINEERING, Vol. 107, pp. 105–111.

[2] AT Research Associates, Glen Ellyn, Ill. 60137.

as well as the condition of zero normal velocity at a solid boundary. Thus, for inviscid flow the initial axial velocity profile will necessarily be flat and valve closure would then establish a flat pressure profile. This brings us back to classical one-dimensional water hammer.

Our choice of cubic and fourth order leading and trailing profiles is physically more realistic than jump discontinuities; it offers, in addition, the computational advantages provided by smooth functions. But we were very conservative with our smoothing: The dimensionless valve closing time we chose was of order unity, which corresponds to the order of a microsecond for the case considered in the paper. This is commensurate with experimentally attainable "instantaneous" closure, as well as being short enough to permit direct comparison with analytical solutions for instantaneous closure. In our work, the initial wave front travels only a relatively short distance before the valve is completely closed or before the pulse reaches its plateau. The agreement with Reference [5] has already been noted. Figure 1(*a*) shows that the peak centerline pressure is approximately 1.83, which compares favorably with the momentary value of 2 suggested by Dr. Wiedermann for his idealized case. From Fig. 4 it is evident that our pulse is essentially rectangular.